Search for the 6α condensed state in ^{24}Mg using ^{12}C + ^{12}C scattering with the new Si detector array SAKRA

Yuki Fujikawa

A dissertation
submitted in partial fulfillment of the requirements for
the degree of Doctor of Philosophy in Science,
Department of Physics, Kyoto University

December, 2023

Abstract

Particle clustering is an important phenomenon in atomic nuclei. In particular, the alpha cluster, comprising two protons and two neutrons, is the most essential cluster component due to its strongly bound nature. The most famous alpha-cluster state is the 0_2^+ state at $E_x = 7.65$ MeV in ^{12}C, which is called the Hoyle state. This state is proposed to be an α-condensed state in which all the alpha clusters are condensed into the lowest $0s$ orbit.

The α-condensed states with dilute density are predicted to exist even in heavier self-conjugate $A = 4k$ nuclei up to $k = 10$. We have currently achieved a certain consensus regarding the existence of the α-condensed states in ^{8}Be and ^{12}C. The ground state of ^{8}Be and the 0_2^+ state in ^{12}C are considered to be the 2α- and 3α-condensed states. The α-condensed states in ^{16}O and ^{20}Ne have not been established yet but several candidate states in those nuclei are theoretically and experimentally proposed. For ^{24}Mg, no theoretical and experimental candidate for the 6α-condensed state has been proposed.

In the present work, we searched for the 6α-condensed state in ^{24}Mg by measuring the ^{12}C + ^{12}C scattering with the SAKRA Si detector array at $E_{\rm cm} = 17.5$–25.0 MeV. SAKRA is a new Si detector array specialized for pulse shape analysis with a large solid angle, which is developed for this experiment. By using the invariant-mass method for the detected 3α particles, the inclusive cross sections for the $^{12}\mathrm{C} + {}^{12}\mathrm{C} \rightarrow {}^{12}\mathrm{C}(0_2^+) + X$ and $^{12}\mathrm{C}(3_1^-) + X$ reactions were determined. In addition, the missing-mass spectroscopy was successfully utilized to determine the excitation energy of the residual ^{12}C nucleus and the exclusive cross sections for the $^{12}\mathrm{C} + {}^{12}\mathrm{C} \rightarrow {}^{12}\mathrm{C}(0_2^+) + {}^{12}\mathrm{C}(0_1^+)$, $^{12}\mathrm{C}(0_2^+) + {}^{12}\mathrm{C}(2_1^+)$, and $^{12}\mathrm{C}(0_2^+) + {}^{12}\mathrm{C}(0_2^+)$ reactions.

In both the inclusive $^{12}\mathrm{C}(0_2^+) + X$ channel and the exclusive $^{12}\mathrm{C}(0_2^+) + {}^{12}\mathrm{C}(0_1^+)$ channel, the cross section peaked at $E_{\rm cm} = 19.4$ MeV, which correspond to the excitation energy of $E_x = 33.3$ MeV in ^{24}Mg. This 19.4-MeV state is a candidate for the 6α-condensed state because of the agreement of the excitation energy with the theoretical value and its decay property. In the exclusive $^{12}\mathrm{C}(0_2^+) + {}^{12}\mathrm{C}(0_2^+)$ channel, a broad state was observed at $E_{\rm cm} = 22.5$ MeV, which correspond to the excitation energy of $E_x = 36.4$ MeV in ^{24}Mg. From the angular distribution of the differential cross section, the spin and parity of this 22.5-MeV state was assigned to be 4^+. In addition, a 2^+ state was suggested at the low-energy side of the 22.5-MeV state. Because their excitation energies are higher than the theoretical value of the 6α-condensed state, these states might be excited states of the 6α-condensed state such as the 2_2^+ and 4_1^+ states in ^{12}C.

Contents

1 Introduction **1**

1.1 Nuclear Structure . . . 1

1.1.1 Alpha particle clustering . . . 1

1.2 α-condensed state . . . 3

1.2.1 Excitation of the Hoyle state . . . 5

1.3 α-condensed states in self-conjugate $A = 4k$ nuclei . . . 6

1.3.1 Cases in ^{8}Be–^{20}Ne . . . 7

1.3.2 Case in ^{24}Mg . . . 9

1.4 Experimental method for research into α-condensed states . . . 9

1.5 Experiment in the present work . . . 10

1.6 Contents of the thesis . . . 11

2 Development of SAKRA **13**

2.1 Motivation for the development . . . 13

2.1.1 Pulse shape discrimination . . . 14

2.2 Data acquisition system . . . 15

2.2.1 ZLE firmware . . . 17

2.3 Study of the pulse shape analysis with Si detectors . . . 18

2.3.1 NTD Si . . . 18

2.4 Performance test with mono-energetic particles . . . 20

2.5 Digital pulse processing . . . 20

2.5.1 Digital filter . . . 21

2.5.2 Pulse shape analysis . . . 22

2.6 Comparison between the experimental configurations . . . 24

2.7 Performance test with continuous energy particles . . . 26
2.8 Design of SAKRA . . . 29
2.9 Performance of SAKRA . . . 29

3 Experiment **31**
3.1 Summary of the measurement . . . 31
3.2 Facility and Beam line . . . 32
3.3 Experimental setup around the scattering chamber . . . 32
3.4 DAQ system . . . 34
3.4.1 Trigger production . . . 35
3.5 Bias voltage of SAKRA . . . 36

4 Data analysis **37**
4.1 Energy calibration . . . 37
4.2 Junction-side data reduction . . . 38
4.3 Ohmic-side data reduction . . . 39
4.3.1 Reduction of synchronous noise and cross-talk . . . 40
4.4 Hit position determination . . . 44
4.4.1 Energy validation . . . 44
4.4.2 Channel combination . . . 44
4.5 Particle identification with pulse shape analysis . . . 45
4.6 Timing gate . . . 47
4.6.1 TDC offset correction . . . 48
4.6.2 TDC reference determination . . . 49
4.7 Reconstruction of kinematics . . . 50
4.7.1 Invariant mass analysis . . . 50
4.7.2 Missing mass analysis . . . 51
4.8 Efficiency estimation . . . 52
4.9 Cross section for the ^{12}C + ^{12}C elastic scattering . . . 59

5 Result and discussion **63**
5.1 Inclusive cross section . . . 63
5.2 Exclusive cross section . . . 66

5.2.1 Angular distribution of the differential cross sections 66

6 Summary **73**

Acknowledgement **76**

References **82**

A Data tables of cross sections **83**

A.1 Inclusive cross section 83

A.2 Exclusive cross section 92

A.2.1 Angular distribution 105

List of Figures **145**

List of Tables **148**

Chapter 1

Introduction

1.1 Nuclear Structure

The atomic nucleus is a quantum many-body system consisting of nucleons, namely protons and neutrons, and its structure has been described by various models. One of the well-described models is a shell model, in which a nucleus is described by a single-particle motion in a mean-field potential generated by all nucleons. The shell model nicely explained the magic numbers, spin and parity of the ground state, and other properties of nuclei [1–4]. On the other hand, it is well known that some states have cluster structures which cannot be well described by the shell model. These states are better described by a cluster model, for example a multi-center model [5, 6], in which the nucleons within the cluster are strongly coupled and the clusters weakly interact with each other.

In order to understand the structure of atomic nuclei, it is important to examine both the shell aspect and cluster aspect, and research on each aspect has been progressing. In addition, recently, the experimental result was reported that suggests the existence of alpha clusters in the ground state [7], and the mechanism of how the cluster structures are expressed is also a topic of attention.

1.1.1 Alpha particle clustering

In the cluster structures, the alpha cluster, comprising two protons and two neutrons, is the most essential cluster component due to its strongly bound nature. The cluster structures are expected to develop around the cluster-decay threshold energies considering the weakly interaction between the clusters. This is known as "threshold rule" [8] and schematically represented by the Ikeda diagram as shown in Fig. 1.1. One of the most famous α-cluster states is the 0_2^+ state at E_x = 7.65 MeV in ^{12}C, called the Hoyle state [10], which is actually located at only 0.38 MeV above the 3α-decay threshold energy. This state was well described by the microscopic cluster model [11–13] although the shell-model calculations could not reproduce this state.

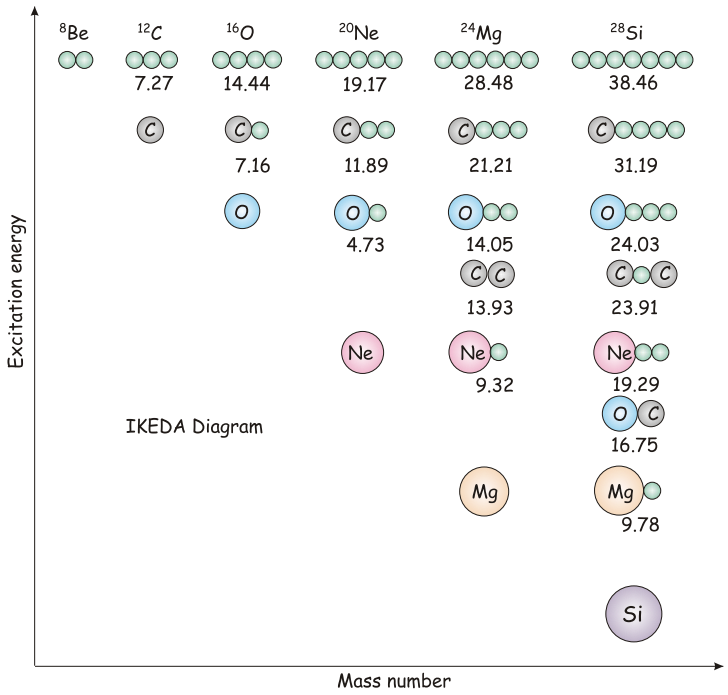

Figure 1.1: Ikeda diagram showing the relation between threshold energy to each decay mode and the cluster structure. Taken from Fig. 1 in Ref. [9]. The small circles without alphabets show alpha particles. The threshold energy from the ground state to each decay mode is shown in the unit of MeV.

The origin of these microscopic cluster model is the Brink-Bloch model [5, 6], and the wave function of $k\alpha$-cluster system is described in the Brink-Bloch model as

$$\Psi(\boldsymbol{R}_1, \boldsymbol{R}_2, \cdots, \boldsymbol{R}_k) = \mathcal{N}_0 \mathcal{A}\left[\psi(\alpha_1, \boldsymbol{R}_1)\psi(\alpha_2, \boldsymbol{R}_2)\cdots\psi(\alpha_k, \boldsymbol{R}_k)\right], \tag{1.1}$$

where $\psi(\alpha_i, \boldsymbol{R}_i)$ denotes the antisymmetrized wave function for the i-th alpha cluster at the spatial point $\boldsymbol{R}_i$. $\mathcal{N}_0$ is a normalization constant and $\mathcal{A}$ is the antisymmetrizer among the nucleons belonging to different alpha clusters. In Ref. [11], the Schrödinger equation for dynamical motion of 3α-clusters is solved by the generator-coordinate method (GCM), where $\boldsymbol{R}_1, \boldsymbol{R}_2$, and $\boldsymbol{R}_3$ are used as generator coordinates. The resonating-group method (RGM) calculation in Ref. [13] applies the 3α RGM wave function described as

$$\Psi = \mathcal{A}\left[\chi(\boldsymbol{R}_{1,2,3})\psi(\alpha_1, \boldsymbol{R}_1)\psi(\alpha_2, \boldsymbol{R}_2)\psi(\alpha_3, \boldsymbol{R}_3)\right], \tag{1.2}$$

which is similar to the Brink-Bloch model but with the addition of the wave function $\chi(\boldsymbol{R}_{1,2,3})$ for the relative motion between alpha clusters. Both in the GCM and RGM, the properties of the 0_2^+ state in ^{12}C, for example the excitation energy and the α-decay width, are well described. Therefore, this 0_2^+ state is considered to have well developed 3α-cluster structure.

1.2 α-condensed state

The 0_2^+ state in ^{12}C is proposed to be an α-condensed state in which all the alpha clusters are condensed into the lowest $0s$ orbit [14]. In Ref. [14], it was suggested that the 3α-condensed state has a dilute structure with a larger radius than the ground state by a factor of about 1.5. According to the 3α orthogonality-condition model (OCM) calculation [15], the 3α particles occupied in the single $0s$ (S_1) orbit with about 70% probability as shown in Fig. 1.2. The density distribution of the alpha clusters in the ground and 0_2^+ states obtained by this OCM calculation is shown in Fig. 1.3(a). The 0_2^+ state has spatially expanded and lower density distribution, whereas the ground state has the compact structure. Due to the dilute nature of the 0_2^+ state , the momentum distribution of the alpha clusters is concentrated at $k < 1$ fm^{-1}, resulting in an exceptionally narrow distribution as shown in Fig. 1.3(b). This δ-function-like behavior of $\rho(k)$ is similar to the momentum distribution of the dilute atomic Bose-Einstein condensation (BEC) state. Therefore, the 0_2^+ state is considered to be the ideal dilute 3α-condensed state.

The α condensation affects physical properties of the dilute nuclear matter [17–20]. When the density of the nuclear matter is decreased from the saturation density ($n_0 \approx 0.16$ fm^{-3}), the nuclear matter lowers its energy by forming localized clusters. Figure 1.4 shows the cluster fractions X_i in symmetric nuclear matter as

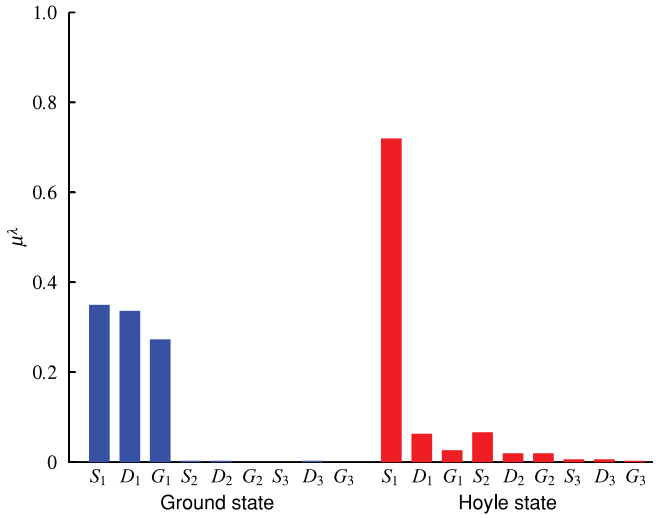

Figure 1.2: Occupation of the single-α orbitals of the Hoyle state of ^{12}C compared with the ground state [15]. Taken from Fig. 7 in Ref. [16].

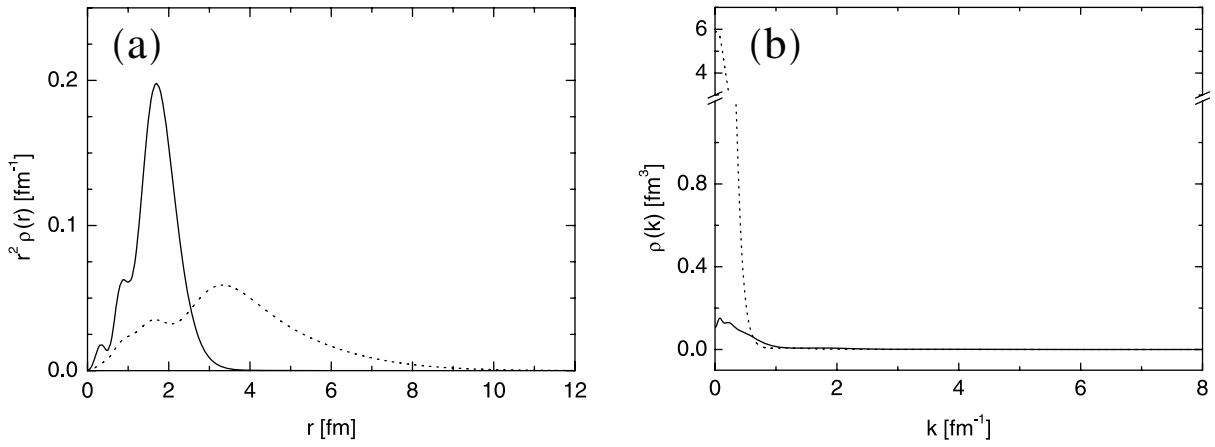

Figure 1.3: (a) Density and (b) momentum distribution of the alpha clusters in the ground state (solid lines) and the 0_2^+ state (dotted lines) in ^{12}C obtained by the 3α OCM calculation. (a) and (b) are taken from Figs. 2 and 7(a) in Ref. [15].

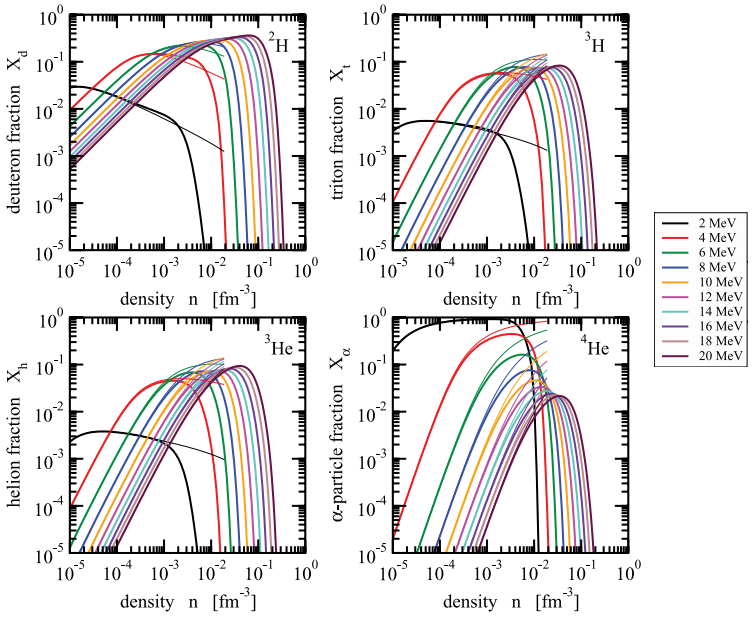

Figure 1.4: Cluster fractions X_i in symmetric nuclear matter as a function of the total density n for various temperatures T (indicated by the color code). Taken from Fig. 3 in Ref. [17].

a function of the total density n for various temperatures T. Since the alpha particle is tightly bound and has high stability, the α-particle fraction X_α is approximately 1 at low temperature of about 2 MeV. According to the generalized nonlinear relativistic mean-field (gNL-RMF) model calculation in Ref. [18], the zero-temperature symmetric nuclear matter is in the pure BEC state of alpha particles, namely α condensation state, below $n \approx 3 \times 10^{-3}$ fm^{-3}.

These theoretical calculations suggested the properties of the infinite nuclear matter, but it cannot be directly investigated. Therefore, exploring the existence of the α-condensed states in various nuclei is an intriguing endeavor to verify the theoretical predictions and to establish universal presence of dilute α-cluster states [21, 22]. Furthermore, we expect that the ubiquity of the α-condensed states will suggest that the α condensation manifests in the dilute infinite nuclear matter.

1.2.1 Excitation of the Hoyle state

The α-condensed state can be regarded as the ground state of relative motion between alpha clusters, which are dilutely distributed in space. Theoretically, the 2_2^+ state in ^{12}C has been considered to be an excitation state of the Hoyle state. According to Ref. [15], the occupation probability of the single-α orbitals for the 2_2^+ state concentrates only on the D_1 orbit with about 80%, which is quite similar to the characteristic occupation for the Hoyle state.

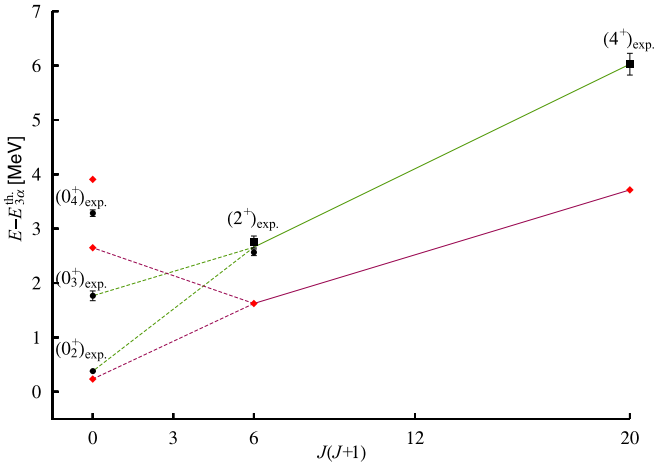

Figure 1.5: Energy levels related to the excitation states of the Hoyle state. The calculated energy levels are denoted by the red diamonds. Taken from Fig. 1 in Ref. [24].

Recently, by the multipole decomposition analysis of the ^{12}C(α,α') reaction, this 2_2^+ state and the broad 0_3^+ state were identified at $E_x = 9.84$ MeV and $E_x = 9.93$ MeV in ^{12}C [23]. Figure 1.5 shows the energy levels related to the excitation states of the Hoyle state, where the calculated energy levels are also shown by the red diamonds [24]. The 0_2^+, 2_2^+, and 4_2^+ states both in the theory and experiment roughly follow a $J(J+1)$ trajectory, although the $J^\pi = 0^+$ bandhead seems to be fragmented into the Hoyle state and the 0_3^+ state. According to Ref. [24], the 0_3^+ state is a monopole-excitation state which has the prominent ^{8}Be$(0^+) + \alpha$ structure. Furthermore, it is mentioned that the Hoyle state gains an extra binding energy compared to the ordinary ^{8}Be$(0^+) + \alpha$ rotation due to its condensed nature, resulting in the lower energy position than the $J(J+1)$ line. Therefore, the 2_2^+ state in ^{12}C is corresponding to the Hoyle rotational state where the relative motion between alpha clusters in the 3α-condensed state is excited.

1.3 α-condensed states in self-conjugate $A = 4k$ nuclei

It is theoretically expected that the $k\alpha$-condensed states are located above the $k\alpha$-decay thresholds, and alpha clusters are confined in a shallow potential pocket formed by the interplay of the short-range weak nuclear attractive interaction and the long-range repulsive Coulomb interaction. Considering the balance of these interactions, the α-condensed states with dilute density are predicted to exist even in heavier self-conjugate $A = 4k$ nuclei up to $k = 10$ [25]. Figure 1.6 shows the predicted energies of the $k\alpha$-condensed states measured from the $k\alpha$-decay threshold energies. The excitation energy of the $k\alpha$-condensed state becomes higher as the value of k increases. In a higher excitation-energy region, because the level density becomes

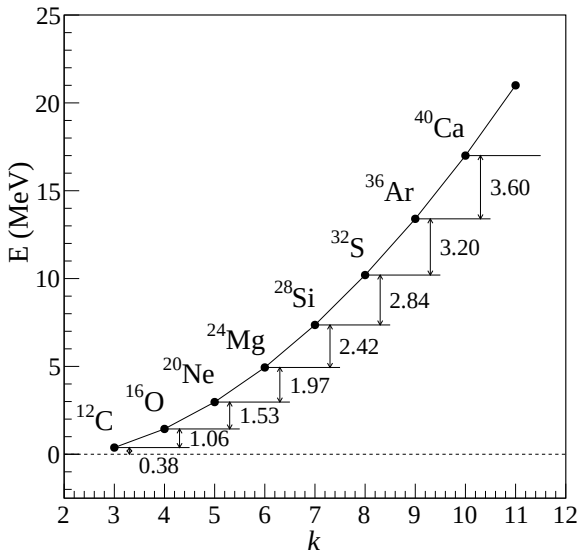

Figure 1.6: Energies of the $k\alpha$-condensed states measured from each $k\alpha$-decay threshold energy. Taken from Fig. 2 in Ref. [25].

higher, it is not easy to identify the α-condensed state in heavier nuclei.

1.3.1 Cases in ^{8}Be–^{20}Ne

We have currently achieved a certain consensus regarding the existence of the α-condensed states in ^{8}Be and ^{12}C. The ground state of ^{8}Be and the 0^+_2 state in ^{12}C are considered to be the 2α- and 3α-condensed states. These states are located slightly above the 2α- and 3α-decay thresholds, and are well described by the microscopic alpha-cluster models [11–15, 26].

The 4α-condensed state in ^{16}O is theoretically predicted to be the 0^+_6 state [27–29], and the known 0^+ state at $E_x = 15.097 \pm 0.005$ MeV [30] is a candidate for the corresponding state. We show the energy levels of 0^+ states in ^{16}O in Fig. 1.7. The energy spectra are in good agreement between the experiment and the 4α OCM calculation. In Fig. 1.8, the spectroscopic factors S^2_L are shown, which indicate the overlap between the wave function of the 4α OCM calculation and that of the $\alpha + {}^{12}\mathrm{C}(L^\pi_n)$ channels. The S^2 factor of the $\alpha + {}^{12}\mathrm{C}(0^+_2)$ channel is dominant in the 0^+_6 state as shown in Fig. 1.8(f). Because the overlap between the wave functions of the α-condensed states in different nuclei should be large, this dominance is one of the evidences for the 0^+_6 state being the 4α-condensed state. Recently, in addition, it was reported that this state decays with the almost same probability into the two ^{8}Be ground states or the $\alpha + {}^{12}\mathrm{C}(0^+_2)$ state [31]. The α-condensed states are expected to decay into the α-condensed state in lighter nuclei considering the overlap

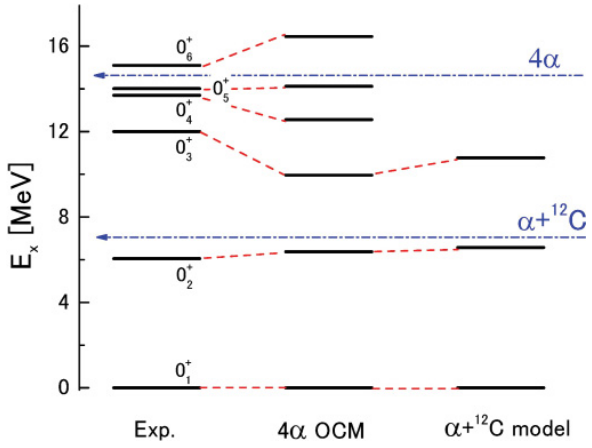

Figure 1.7: Comparison of energy spectra among experiment, the 4α OCM calculation, and the $\alpha + {}^{12}$C model calculation. Taken from Fig. 4 in Ref. [28].

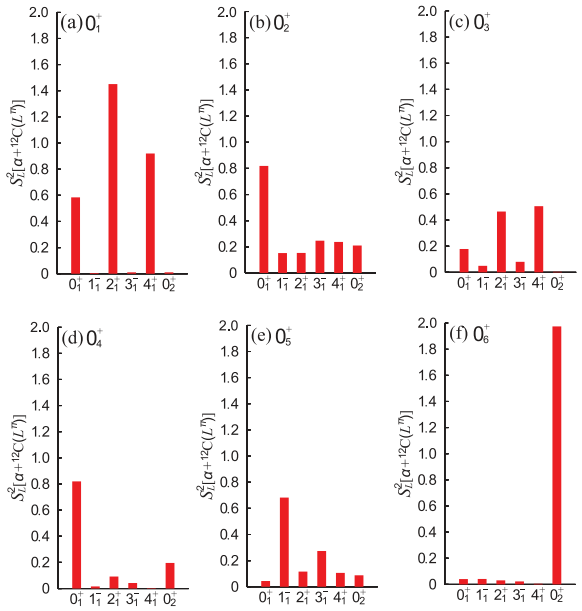

Figure 1.8: Spectroscopic factors S^2_L of the $\alpha + {}^{12}\mathrm{C}(L^\pi_n)$ channels. Taken from Fig. 5 in Ref. [28].

between the wave functions. Thus, this state in ^{16}O is a strong candidate for the 4α-condensed state.

For ^{20}Ne, several candidates for the 5α-condensed state were experimentally proposed. In Ref. [32], it was found that the three states at $E_x = 23.6$, 21.8, and 21.2 MeV in ^{20}Ne are strongly coupled to the candidate for the 4α-condensed state at $E_x = 15.097 \pm 0.005$ MeV in ^{16}O. This strong coupling between these observed states and the 4α-condensed state is the compelling evidence that they are the candidates for the 5α-condensed state. However, the spins and parities of these candidate states were not determined in Ref. [32] although they could be another strong evidence of the 5α-condensed state. The spin and parity of the α-condensed state must be 0^+ because all the alpha clusters are condensed into the $0s$ orbit. The other candidate for the 5α-condensed state was proposed to be the 0^+ state at $E_x = 22.5$ MeV in ^{20}Ne [33]. This state is not described by the shell model, and its excitation energy is close to the theoretical value of $E_x = 21.14$ MeV [25]. However, because of the high level density around the expected excitation energy, it is difficult to conclude this state to be the 5α-condensed state from the excitation energy only. In either case, theoretical efforts to interpret the experimental data are desired to pin down the 5α-condensed state.

1.3.2 Case in ^{24}Mg

For ^{24}Mg, no theoretical and experimental candidate for the 6α-condensed state has been proposed. In Ref. [34], inelastic alpha scattering was employed to search for the 6α-condensed state. Several bump structures were observed in the excitation-energy spectrum of ^{24}Mg for coincidence events where ^{8}Be, as the 2α-condensed state, was detected at the same time with an inelastically scattered alpha particle. However, it was statistically too poor to propose candidates for the 6α-condensed state.

A tentative result for the 6α-condensed state was reported in Ref. [31]. The authors of Ref. [31] analyzed events where 4α particles were detected under the assumption that those α particles were emitted from ^{16}O* excited by the $^{20}\mathrm{Ne}+\alpha \rightarrow {}^{16}\mathrm{O}^{*}+{}^{8}\mathrm{Be}$(g.s.) reaction. They reported that a peak was observed at $E_x = 34$ MeV in ^{24}Mg close to the theoretically predicted energy of the 6α-condensed state [25] when they selectively analyzed events where the invariant mass of the detected 4α particles was close to that of the candidate for the 4α-condensed state. However, the peak significance remained highly uncertain due to the statistical limitation and potential ambiguity in assumptions made in the analysis. Thus, further measurements to search for the 6α-condensed state are still needed.

1.4 Experimental method for research into α-condensed states

Although a method to identify the α-condensed states has not yet been established, experiments are being actively conducted to search for the α-condensed states based on its properties. One of the most important properties that the α-condensed states must have the spin and parity of 0^{+} and isospin of 0 since all the alpha clusters are condensed into the 0s orbit. Another important property is the decay property of the α-condensed states. The α-condensed states are expected to decay via the α-condensed states in lighter nuclei by emitting alpha particles, since the overlap between the wave functions of the α-condensed states in different nuclei should be large.

The reasonable reaction to populate isoscalar 0^{+} states is the inelastic alpha scattering off self-conjugate $A = 4k$ nuclei at forward angles. Because both the spin and isospin of the alpha particle are 0, the spin and parity of the excited state is determined by measuring the transfer angular momenta ΔL. In addition, because the inelastic alpha scattering at 0° selectively excites the isoscalar monopole ($IS\,E0$) transition which causes a density change in nuclei, it is considered that the α-condensed states is effectively excited by this reaction. However, because the $IS\,E0$ transition can populate not only the α-condensed states but the isoscalar giant monopole resonances, additional measurements are necessary to identify the α-condensed states. Therefore, the coincidence measurement of decay particles with the inelastic alpha scattering is a powerful method to

explore the α-condensed states [32, 34].

One of the difficulties in searching for the α-condensed states by measuring decay particles is angular coverage of decay-particle detectors. In the case of the inelastic alpha scattering under normal kinematic conditions, decay particles are emitted over all solid angles in the laboratory frame because the target nuclei are hardly recoiled. Therefore, the decay-particle detectors are required to cover large solid angle around the target. On the other hand, heavy-ion beams are useful for measuring decay particles because decay particles are boosted and focused on forward angles owing to the center-of-mass motion. Actually, decay-particle measurements in heavy-ion induced reactions were utilized to search for α-cluster states [31, 35–40]. In Ref. [39], the ^{12}C(^{16}O, $k\alpha$) reaction was employed to search for the $k\alpha$-condensed states up to $k = 6$, but no experimental signatures were observed. The authors of Ref. [39] suggested that $k\alpha$-condensed states might be forbidden from decaying through the $k\alpha$ channels due to their low decay energies and the Coulomb barriers. In contrast, as mentioned above, the authors of Ref. [31] attempted to determine the excitation function of ^{24}Mg in the ^{20}Ne + α reaction on the basis of the thick target method, and reported the peak at $E_x = 34$ MeV in ^{24}Mg close to the theoretically predicted energy of the 6α-condensed state [25].

1.5 Experiment in the present work

In the present work, we searched for the 6α-condensed state in ^{24}Mg by measuring the ^{12}C + ^{12}C scattering. Especially, we focused on events where 3α particles were emitted from the 0^+_2 state in ^{12}C because we expected the 6α-condensed state to decay through the 3α-condensed state. Previously, the ^{12}C + ^{12}C $\rightarrow$ ^{12}C(0^+_2) + ^{12}C(0^+_2) reaction was measured in Refs. [35, 36], and the candidate for the 6α-chain state in ^{24}Mg was proposed. Figure 1.9 shows the excitation function for the ^{12}C(^{12}C, ^{12}C[0^+_2])^{12}C(0^+_2) reaction. However, the excitation-energy range of ^{24}Mg scanned in Refs. [35, 36] ($E_x = 43.4$–49.4 MeV) was higher than that of the 6α-condensed state. In the lower excitation-energy domain, the effective excitation function of the ^{12}C + ^{12}C $\rightarrow$ 3α + X reaction was reported from the indirect measurement of 3α particles in Ref. [40, 41] as shown in Fig. 1.10. The effective 3α-emission yield was deduced using the following equation:

$$\sigma(3\alpha) = \frac{1}{3}\left[\sigma_\alpha - 2\sigma(^{16}\mathrm{O}) - \sigma(^{18}\mathrm{F}) - \sigma(^{19}\mathrm{F}) - \sigma(^{19}\mathrm{Ne}) - \sigma(^{20}\mathrm{Ne})\right]. \tag{1.3}$$

A remarkable peak structure was observed at $E_{\mathrm{cm}} \sim 19.5$ MeV, which corresponds to the theoretically predicted excitation energy of $E_x \sim 33.4$ MeV in ^{24}Mg. However, it was not compelling evidence of the 6α-condensed state because the 3α particles were not directly detected and their invariant mass was not determined. In the recent measurement of the ^{12}C + ^{12}C $\rightarrow$ 3α + ^{12}C reaction at $E_{\mathrm{cm}} = 8.9$–21 MeV [42],

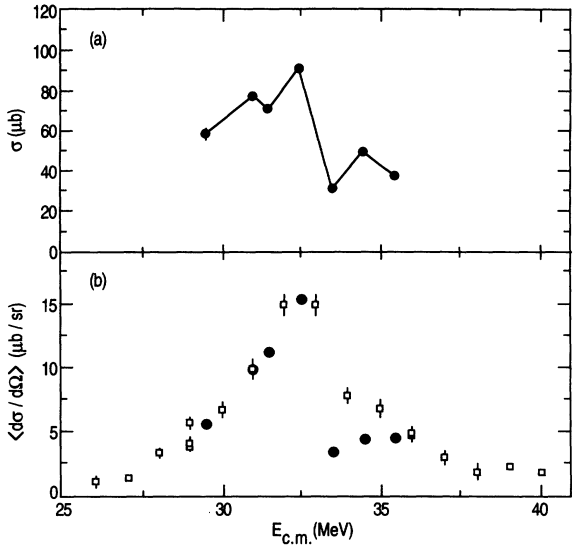

Figure 1.9: (a) Excitation function for the ^{12}C(^{12}C, ^{12}C[0^+_2])^{12}C(0^+_2) reaction. (b) Angle-averaged excitation function. Taken from Fig. 7 in Ref. [36].

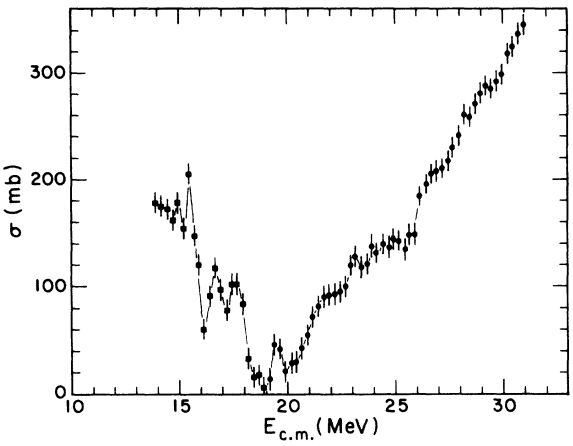

Figure 1.10: Effective 3α-emission cross section from the fused system (^{24}Mg). Taken from Fig. 9 in Ref. [41].

the 3α particles emitted from the ^{12}C + ^{12}C scattering were measured using the active-target time projection chamber. It was reported that the excitation function of the ^{12}C + ^{12}C $\rightarrow$ 3α + X reaction tended to agree with the result in Ref. [40] at energies above $E_{\rm cm}$ = 19 MeV. However, the measurement was statistically too poor to observe the peak at $E_{\rm cm} \sim$ 19.5 MeV, and the invariant mass of the 3α particles was not determined. Thus, it was strongly desired to directly measure the 3α particles emitted from the ^{12}C + ^{12}C scattering and to determine their invariant mass for examining their decay histories.

1.6 Contents of the thesis

In order to conduct this experiment, we developed a particle-identification method using pulse shape analysis (PSA) and a new Si detector array SAKRA. Firstly, we describe the detail study of PSA and the development of SAKRA in Chap. 2. The experimental details such as experimental setup, data acquisition system, and summary of the measurement are described in Chap. 3. The analysis of the SAKRA data and the efficiency estimation are explained in Chap. 4. The results of the measured cross sections are presented and discussed in Chap. 5. Finally, the summary and future perspectives are given in Chap. 6.

Chapter 2

Development of SAKRA

For low-energy decay particle measurement, we developed a new Si detector array named SAKRA (Si Array developed by Kyoto and osaka for Research into Alpha cluster states). A schematic view and photograph of SAKRA are shown in Fig. 2.1. The characteristics of SAKRA is the specialized configuration for the pulse shape analysis (PSA). In this chapter, we described the development of SAKRA and the PSA in detail. The detail of the data analysis is described in Chap. 4.

2.1 Motivation for the development

In the new experiment mentioned in Sec. 1.5, we measure decay particles emitted from the resonance state of ^{24}Mg. For the decay particle measurement, one of the most important technique is particle identification (PID). The generally-used methods for the PID using Si detectors are the E–ΔE method and the time-of-flight (TOF) method. The PID with the E–ΔE method is performed using the correlation between the energy deposit (ΔE) of the first-layer Si detector and the total energy (E) of the second-layer Si detector. Therefore, the E–ΔE method can not be applied for the low-energy particles which can not penetrate the first layer. The PID with the TOF method is performed using the correlation between the TOF and the energy of charged particles. To obtain a better resolution of TOF and the performance of PID, the flight path should be sufficiently long. However, the TOF method is not suitable for experiments that require to detect multiple decay particles because the solid angle covered by detectors becomes smaller as the flight path becomes longer, reducing the detection efficiency. Thus, we needed to develop a new PID technique and a new Si telescope for this experiment.

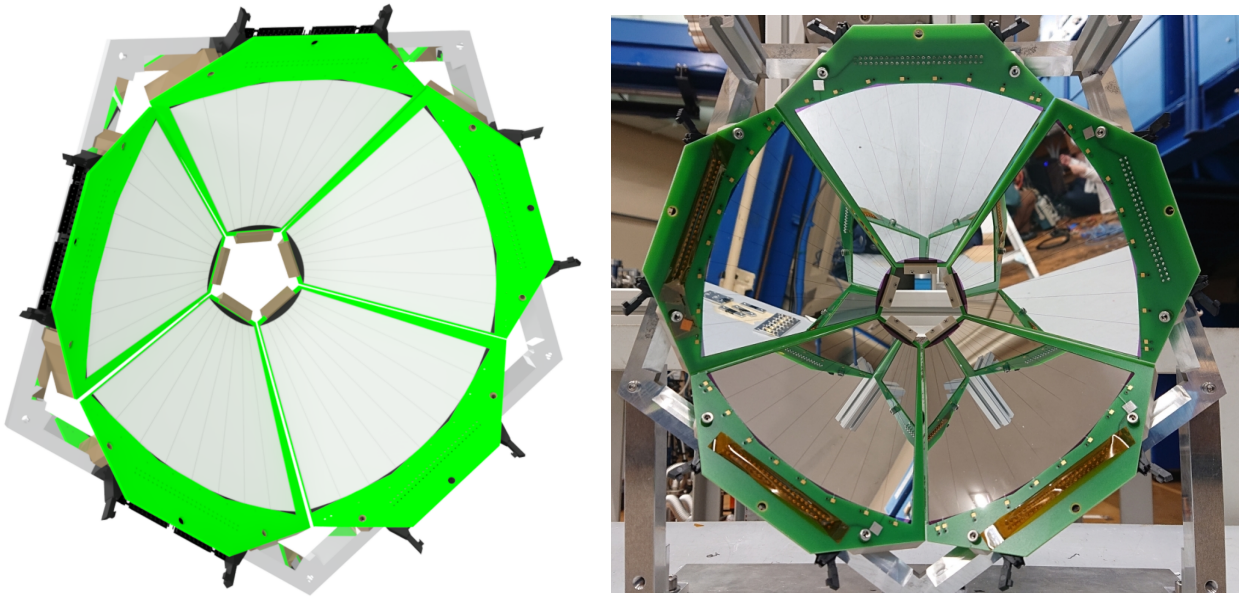

Figure 2.1: Schematic view and photograph of SAKRA.

2.1.1 Pulse shape discrimination

Recently, pulse shape discrimination (PSD) techniques have attracted attention to solve these problems. The PID with the PSD techniques is performed by using the difference of pulse shapes among different nuclides which have same energy. When a charged particle is incident on a Si detector, its energy is deposited in the Si detector and some electron-hole pairs are excited. These charge carriers (excited electrons or holes) are drifted along to the applied electric field in the Si detector and are finally read out as an electrical pulse which reflects the distribution of carriers and the drift time. According to the Bethe-Bloch formula [43], the average energy loss is roughly described as

$$-\frac{dE}{dx} \propto \frac{AZ^2}{E}, \tag{2.1}$$

where A, Z and E denote the mass number, the atomic number, and the energy of the incident particle, respectively. When incident particles have same energy, the distribution of the electron-hole pairs depends on A and Z of the incident particles. The larger A and Z of the incident particle causes the larger density of the electron-hole pairs and the shorter range of the incident particle. The difference of the range, namely the difference of the drift length directly affects its pulse shape. In addition, the applied electric field is locally distorted by the plasma which is produced by ionization, and the drift of the carriers is impeded by this plasma. Thus, the drift time of the carriers is delayed due to the plasma-erosion effect depending on the initial density of the plasma [44]. As a result of these effects, the pulse shape depends on A and Z of the

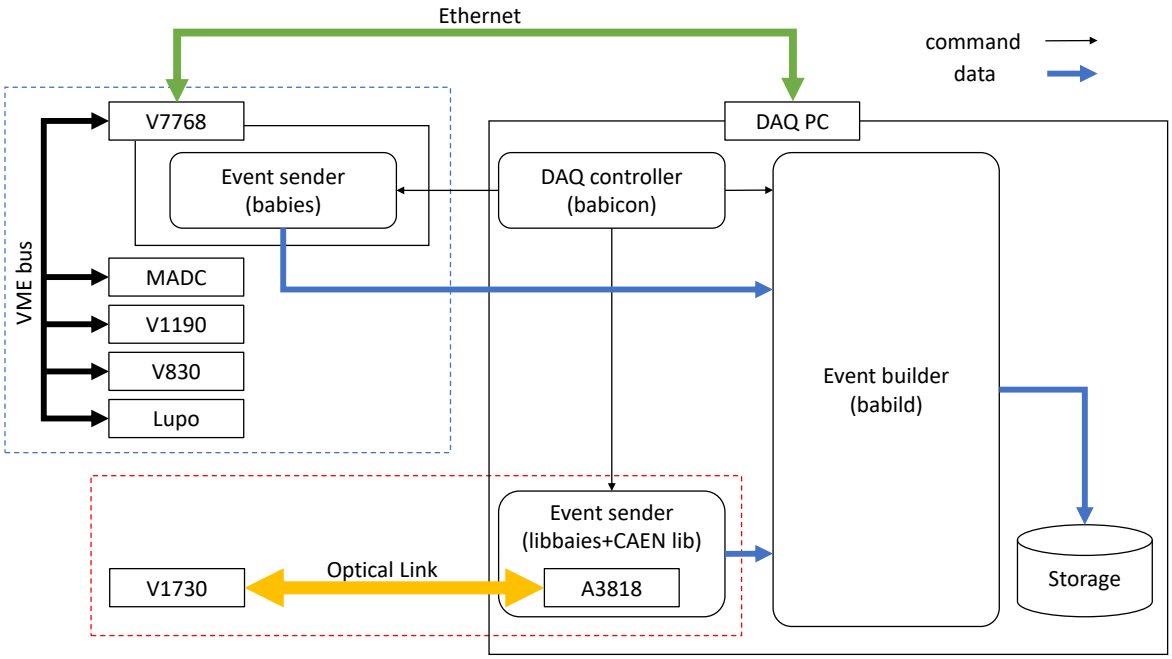

Figure 2.2: Schematic diagram of the SAKRA DAQ system. The blue-dashed box presents the system already implemented for the readout of conventional modules, and the red-dashed box indicates the newly developed part to handle the V1730 modules.

incident particle.

The PID method using the PSA with Si detectors was investigated since the 1960s [45]. In recent years, some results of the PID using the PSA for the $Z > 3$ nuclides at several MeV/u were reported [46–48]. In Ref. [49], the four light nuclides (p, d, t and α) at 3 MeV were successfully discriminated using the PSA. In addition, it is worthy to mention the PSA using machine learning techniques. It was demonstrated in Ref. [50] that the PSA using machine learning techniques is a useful method for nuclides heavier than ^{12}C.

We applied the PSA for light nuclides at lower energy and developed a new Si detector array named SAKRA which is specialized to the PSA.

2.2 Data acquisition system

For the data acquisition (DAQ) of SAKRA, we developed a new DAQ system which could handle conventional modules, for example the Mesytec MADC modules, and waveform digitizers in one system. In Fig. 2.2, we show the schematic diagram of the SAKRA DAQ system. We used the babirl DAQ system [51, 52] as the base of the new DAQ system because the babirl DAQ system has been already imple-

mented in our group for the readout of conventional modules shown as the blue-dashed box in Fig. 2.2. The babirl DAQ system is a network-distributed DAQ system used as the standard DAQ system at RIBF, which mainly consists of an event builder "babild", an event sender "babies", and a DAQ controller "babicon". We used the conventional modules listed in Table 2.1. The control and the data-readout of these conventional modules were done via VME bus and the V7768 crate controller.

Table 2.1: List of the used conventional modules.

Module type	Module name
VME CPU	Abaco V7768
Peak hold ADC	Mesytec MADC-32
TDC	CAEN V1190A
VME scaler	CAEN V830
Output register	A1100 VME Lupo

In addition to these conventional modules, in order to perform PSA, we needed to acquire waveforms from Si detectors. For a waveform digitizer, we used the CAEN V1730SB flash digitizer modules. The performances of V1730SB are summarized in Table 2.2. We used the optical link interface to handle the V1730

Table 2.2: Performances of the V1730SB module.

Number of channels	16
ADC resolution	14 bits
Sampling Rate	500 MHz
Dynamic range	0.5 V_{pp} / 2 V_{pp}

modules because the data-readout via VME bus did not have enough band width for acquiring waveforms with large data size. V1730 was directly connected to a DAQ PC via the CAEN A3818 PCIe interface bridge. Because the standard babirl DAQ system did not adapt to the optical link interface and V1730, we developed a new event sender program with libbabies which is a framework for development of a user-custom babies processes. For drivers of the CAEN modules, we used software libraries provided by CAEN. The newly developed part is shown as the red-dashed box in Fig. 2.2. Although only one V1730 module and one custom babies process are drawn in Fig. 2.2, this DAQ system is scalable for multiple V1730 modules and multiple babies processes, with the programmable number of the V1730 modules handled by one babies process.

In this DAQ system, we distribute a common trigger to all modules, and the event building is done based on its event number, which is equals to the trigger number. The V1730 modules are dead-time free while the conventional modules have some dead-time due to the conversion time. Therefore, the veto management is very important in order to avoid event slips. In addition, because the V1730 modules and the conven-

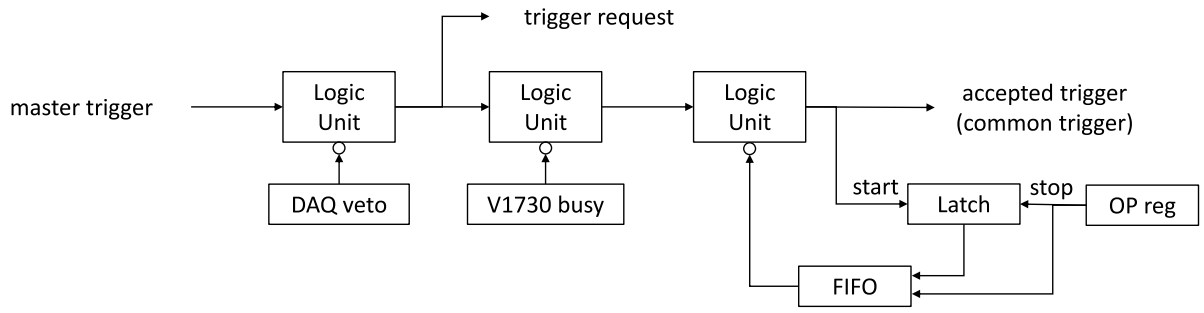

Figure 2.3: Schematic diagram of the veto circuit.

tional modules differ in the timing at which data acquisition becomes ready after the DAQ is started, we added an extra veto signal named the DAQ veto which was cleared when all modules became ready for data acquisition. The schematic diagram of the veto circuit is shown in Fig. 2.3.

2.2.1 ZLE firmware

V1730 has FPGAs for waveform recording and digital pulse processing (DPP), and several firmwares are provided by CAEN. In order to suppress the data size of waveform, we installed the DPP firmware for Zero Length Encoding Plus (DPP-ZLE*plus* firmware).

The ZLE algorithm is shown in Fig. 2.4. This algorithm discards samples which don't exceed the ZLE threshold (ZLE Thr) and suppresses the data size by recording only the number of discarded samples (N_{Sn}). In our experiments, most channels have no hits and output only baselines rather than hit-generated pulses. By properly adjusting the ZLE threshold, signals from non-hit channels are discarded and the data size is significantly suppressed. In the DPP-ZLE*plus* firmware, a baseline value is dynamically calculated at each channel. A calculated baseline value is also recorded with waveform at each channel for each event.

Additionally, we can record the baseline samples on the hit pulse using the Look Back/Forward Window (LBW/LFW). The LBW and LFW are the programmable number of samples recorded before and after ZLE threshold crossing. We set the LBW and LFW to 510 samples (maximum value) to record adequate baseline samples for evaluating its baseline value.

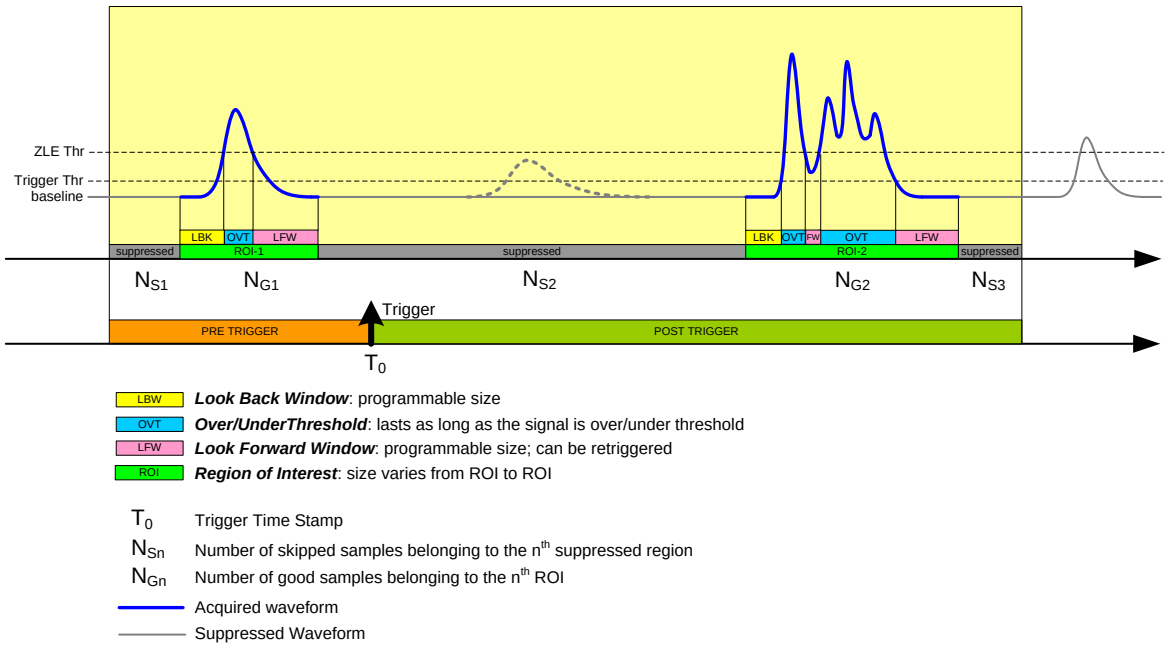

Figure 2.4: ZLE algorithm description taken from [53].

2.3 Study of the pulse shape analysis with Si detectors

In order to maximize performance of the PSA, we studied the characteristics of waveforms with various experimental setups. There are several factors that affect the characteristics of the waveforms. In this study, we investigated the effects of bias voltages applied to Si sensors, time constant of preamplifiers, uniformity of Si crystals and incident sides of charged particles. In particular, because low-energy particles stopped near the Si surface, the electric-field gradient may strongly affect pulse shapes.

2.3.1 NTD Si

We used MMM design double-sided Si strip detectors from Micron Semiconductor shown in Fig. 2.5. The junction side of the Si sensor is divided into 16-ring strips with 6.4-mm pitch, and the ohmic side is divided into 8-radial strips with 6.8° pitch. The outer radius is 135 mm, and the inner radius is 33 mm. The sector angle is 60 degrees and its thickness is 500 μm. Hit positions are determined virtually with 128-pixel granularity by reading out signals from the junction side and the ohmic side severally.

For investigating effects of uniformity of Si crystals, we compared the PSA with a Neutron Transmutation Doped (NTD) Si crystal and that with a normal Si crystal. The NTD Si crystal has good uniformity thanks to its doping method. At the neutron transmutation doping process, a natural Si crystal is irradiated with

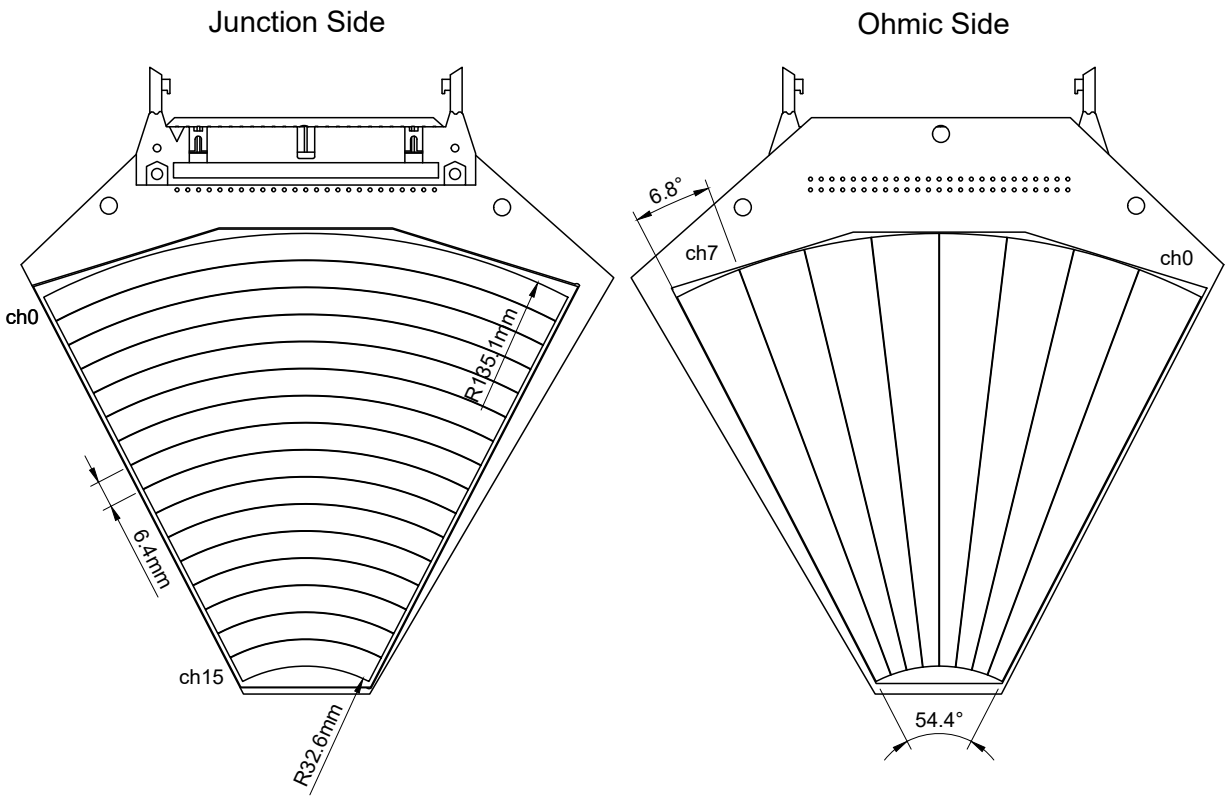

Figure 2.5: Schematic diagram of MMM design Si detector.

neurons in a nuclear reactor, and ^{31}P isotopes are created via the $^{30}\mathrm{Si}(n,\gamma)^{31}\mathrm{Si}(\beta^-)^{31}\mathrm{P}$ reactions. The created ^{31}P isotopes work as n-type donor impurities.

2.4 Performance test with mono-energetic particles

We conducted a test experiment at the tandem accelerator facility in the faculty of maritime sciences, Kobe University to acquire a dataset of nuclide-tagged waveforms of mono-energetic protons, deuterons and alpha particles. For acquiring waveforms of protons and deuterons, we used ^{1}H and ^{2}H beams accelerated to about 3 MeV by the tandem accelerator and measured Rutherford scattering off gold foil. Waveforms of alpha particles were obtained with alpha particles at 3.18 MeV emitted from ^{148}Gd isotopes in the mixed alpha source.

In this test experiment, we examined two types of preamplifiers (CAEN A1442B and Mesytec MPR), two types of Si crystals (NTD Si crystal and normal Si crystal), and two types of particle-incident sides (the ohmic side and the junction side). The specifications of two types of preamplifiers are summarized in Table. 2.3. In Table. 2.4, the configurations of the experimental setup were summarized. At each configuration, we also investigated how the performance of the PSA changed with the bias voltage applied to the Si detector.

Table 2.3: Specifications of Mesytec MPR-16/32 and CAEN A1442B preamplifiers.

	Mesytec MPR-16/32	CAEN A1442B
Energy range	25 MeV	40 MeV
Output voltage	±4 V_{diff}	±4.5 V_{diff}
Rise time	12 ns @ 0 pF	< 10 ns @ 0 pF
Decay time	25 µs	50 µs

Table 2.4: Summary of the experimental configurations. k is the index of the configuration.

k	Preamplifier	Si crystal	incident side
1	CAEN A1442B	NTD	ohmic
2	CAEN A1442B	normal	ohmic
3	CAEN A1442B	NTD	junction
4	Mesytec MPR	NTD	ohmic

2.5 Digital pulse processing

A waveform data contains ADC values at each clock and a baseline value calculated by the DPP-ZLE*plus* firmware. The peak ADC value in each event is calculated from the maximum amplitude of the waveform

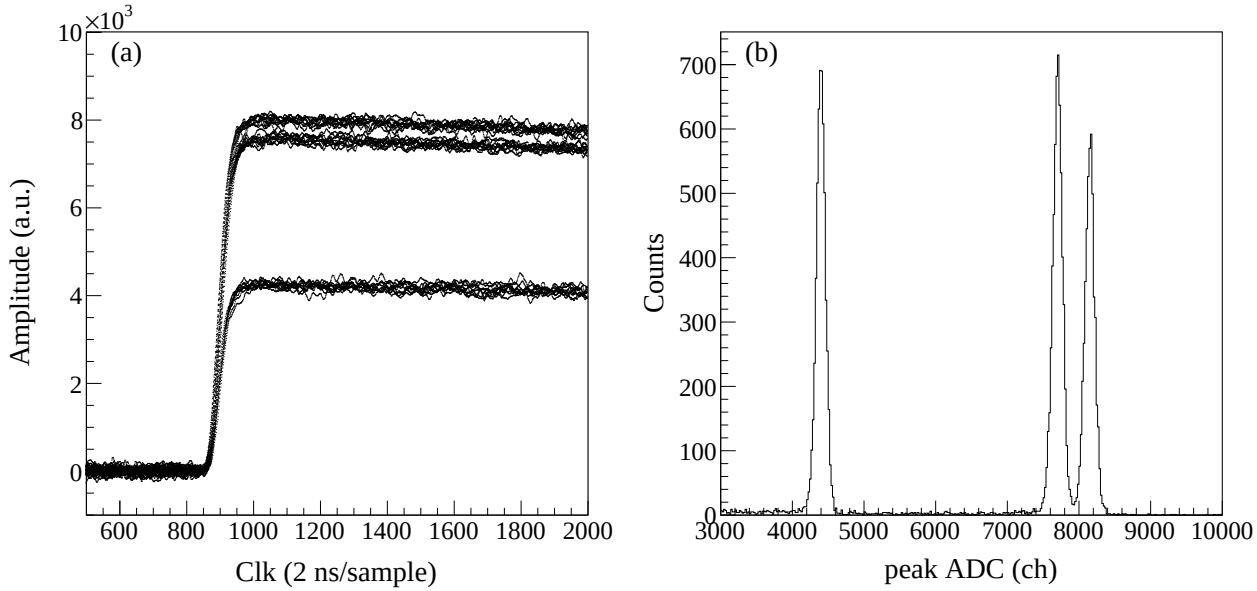

Figure 2.6: Data of the mixed alpha source. (a) Typical baseline-subtracted waveforms. (b) Peak ADC histogram.

after subtracting the baseline, and the clock value when the ADC value peaks is also saved as PeakClk.

2.5.1 Digital filter

Typical baseline-subtracted waveforms of the mixed (^{241}Am, ^{244}Cm, ^{148}Gd) alpha source at $k = 1$ configuration are shown in Fig. 2.6(a), and the peak ADC histogram is shown in Fig. 2.6(b). The three types of waveforms and peaks correspond to the alpha particles of 5.46 MeV emitted from ^{241}Am, 5.78 MeV emitted from ^{244}Cm, and 3.18 MeV emitted from ^{148}Gd, respectively. In Fig. 2.6(b), the peak ADC resolution for the 3.18-MeV alpha particles emitted from ^{148}Gd was 1.49% (sigma). In order to improve the peak ADC resolution, we applied the Finite Impulse Response (FIR) filter described as

$$y_n = \sum_{k=0}^{L} h_k x_{n-k}, \tag{2.2}$$

where y_i and x_i are the output and input values for the FIR filter, h_k is a filter parameter. The passband of the FIR filter are determined by the parameter set $\{h_0 \ldots h_L\}$. We calculated FIR parameter sets with the Digital Filter Design Services on the Web page [54]. To reduce a high-frequency noise, we designed a low-pass filter (LPF) with a cutoff frequency of 1.5 MHz and a filter length of 401. Figure 2.7(a) shows the filtered waveforms of the same samples as in Fig. 2.6. The peak ADC histogram calculated from the filtered waveforms is shown in Fig. 2.7(b), and the peak ADC resolution for the alpha particles at 3.18 MeV was slightly improved to 1.38% (sigma).

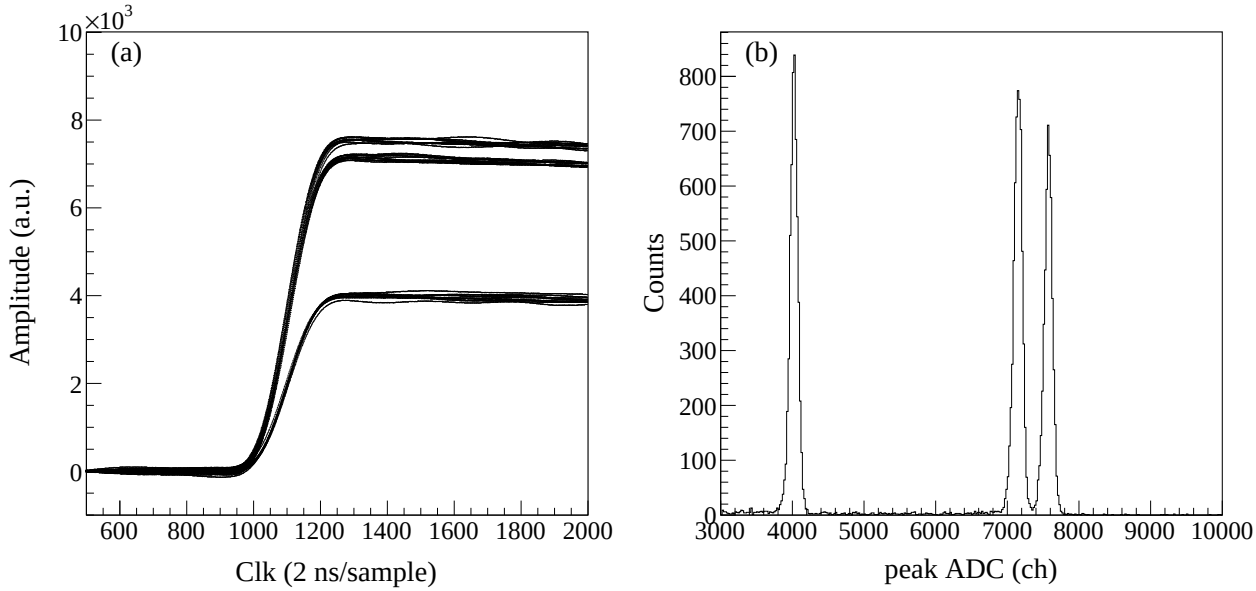

Figure 2.7: Data of the mixed alpha source. (a) Typical filtered waveforms. (b) Peak ADC histogram.

In addition, we designed a digital shaping filter by imitating the analog circuit of a shaping amplifier. The analog circuit of the shaping amplifier consists of a CR–RC^n circuit, The CR/RC circuit is a high-pass/low-pass filter and a differentiation/integration circuit. Therefore, we constructed the digital shaping filter with one numerical differentiation section and the three LPFs designed above. The waveforms filtered by the LPF and the shaping filter are shown in Fig. 2.8(a). The peak ADC resolution of ^{148}Gd peak in Fig. 2.8(b) was 1.14% (sigma), and the improvement from the resolution in Fig. 2.7(b) was 17%. For energy calibration, we used this peak ADC value calculated from a shaped waveform.

2.5.2 Pulse shape analysis

For the PSA, we used the waveform read out from the junction side of the Si detector. We show typical waveforms at the $k = 4$ configuration in Fig. 2.9(a) and those averaged over 2000 events at the same configuration in Fig. 2.9(b). Each waveform after subtracting each baseline was normalized to have a maximum amplitude of 1. The time was aligned such that the clock corresponding to an amplitude of 0.1 was set to $t = 0$. The blue, black, and red dots correspond to the waveforms of proton, deuteron, and alpha, respectively. As the PSA parameter, we used the peak-to-peak amplitude of the differential waveform, named $A_{\max}$. To differentiate the waveform, we use the triangle filter described as

$$y_n = \frac{\sum_{k=1}^{L} x_{n+k} - \sum_{k=-L}^{-1} x_{n+k}}{L}, \tag{2.3}$$

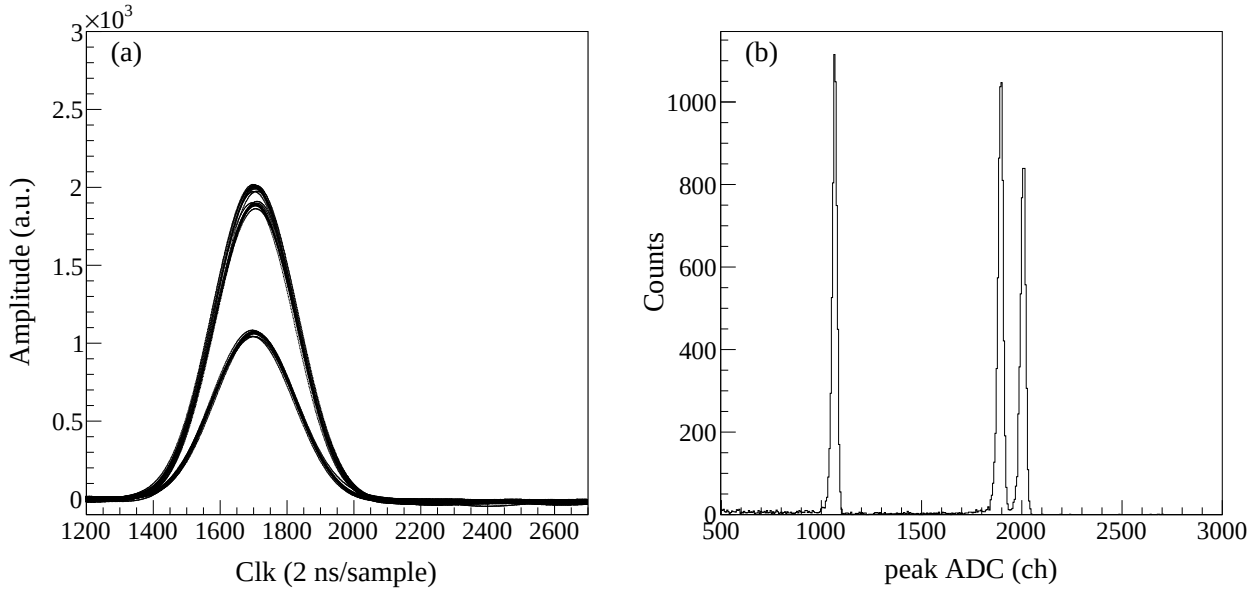

Figure 2.8: Data of the mixed alpha source. (a) Typical waveforms filtered by the LPF and the shaping filter. (b) Peak ADC histogram.

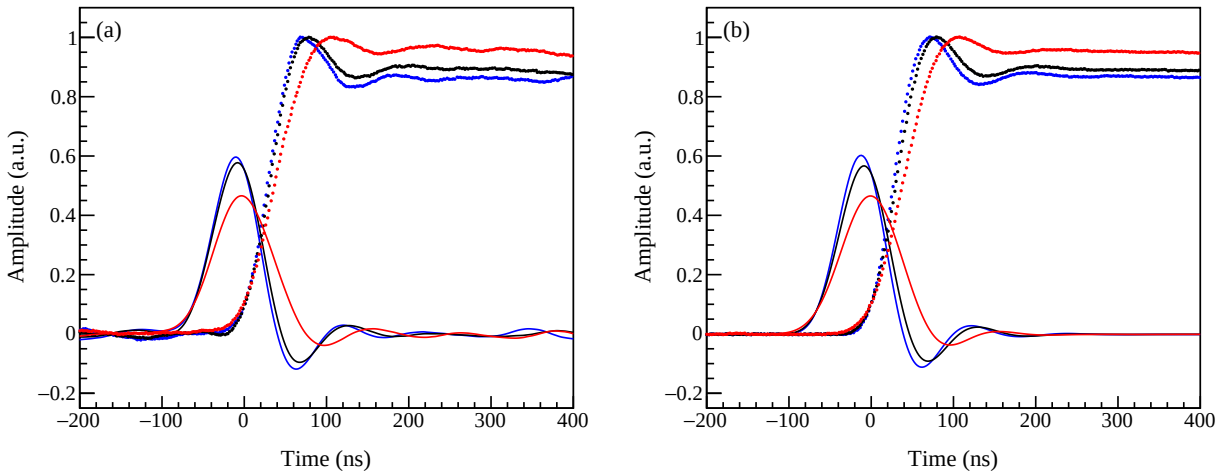

Figure 2.9: Waveforms at the $k = 4$ configuration. (a) Typical one-event waveforms. (b) Averaged waveforms over 2000 events. The blue, black, and red dots correspond to the waveforms of proton, deuteron, and alpha, respectively. The each differential waveform is shown by the solid lines.

where y_i, x_i, and L denote the output value, the input value, and the length of the triangle filter, respectively. The differential waveforms are shown in Fig. 2.9 by the solid lines.

2.6 Comparison between the experimental configurations

We show the waveforms at various k configurations averaged over 2000 events as the dotted lines and their differential waveforms as the solid lines in Fig. 2.10(k-a). The normalization, the time alignment, and the notation of the colors are same in Fig. 2.9. The $A_{\max}$ spectra are shown in Fig. 2.10(k-b) with the same color notation. Each $A_{\max}$ spectrum was scaled to an integrated value of 1.

In order to compare the PID capability, we evaluated the figure of merit (FoM) defined as

$$\mathrm{FoM}_{i-j} = \frac{\left|\mu_i - \mu_j\right|}{2.35\left(\sigma_i + \sigma_j\right)}, \tag{2.4}$$

where μ_i and σ_i are the mean and the sigma of the Gaussian function fitted to the $A_{\max}$ spectrum at each k configuration. Generally, the PID capability is thought to be sufficient at FoM > 0.75 [46]. In Table 2.5, we summarized the FoM for various nuclides pair at each configuration. For example, the $\mathrm{FoM}_{p-\alpha}$ in Fig. 2.10(1-b) is 1.55, and it suggests that this PSA has sufficient capability for the p–α discrimination. Comparing Figs. 2.10(1-b) and (2-b), it corresponds to the comparison of Si crystals, and the $A_{\max}$ distribution of each nuclide in Fig. 2.10(1-b) is narrower than that in Fig. 2.10(2-b). It is considered that the better uniformity of the NTD Si crystal results in its small position dependence of the electric field and good PID performance than the normal Si crystal. In regards to the $k = 3$ configuration, the waveforms in Fig. 2.10(3-a) and the $A_{\max}$ spectra in Fig. 2.10(3-b) have little difference among the three nuclides. Near the junction side, the electric-field gradient is larger than the ohmic side, and the drift time and the collection time of carriers become shorter. As a result, it is considered that the difference in the initial distributions of carriers produced by different nuclides is inefficiently reflected in the pulse shape. In particular, low-energy particles such as those in this study stop at a few μm from the Si surface, so the junction-side incidence has no PID capability. As shown in Fig. 2.10(4-b), at the $k = 4$ configuration, the difference in the $A_{\max}$ peak positions among the

Table 2.5: FoM for various nuclides pair at each configuration.

k	p–α	p–d	d–α
1	1.55	0.47	1.04
2	0.49	0.14	0.33
3	0.06	0.03	0.03
4	3.41	0.95	2.40

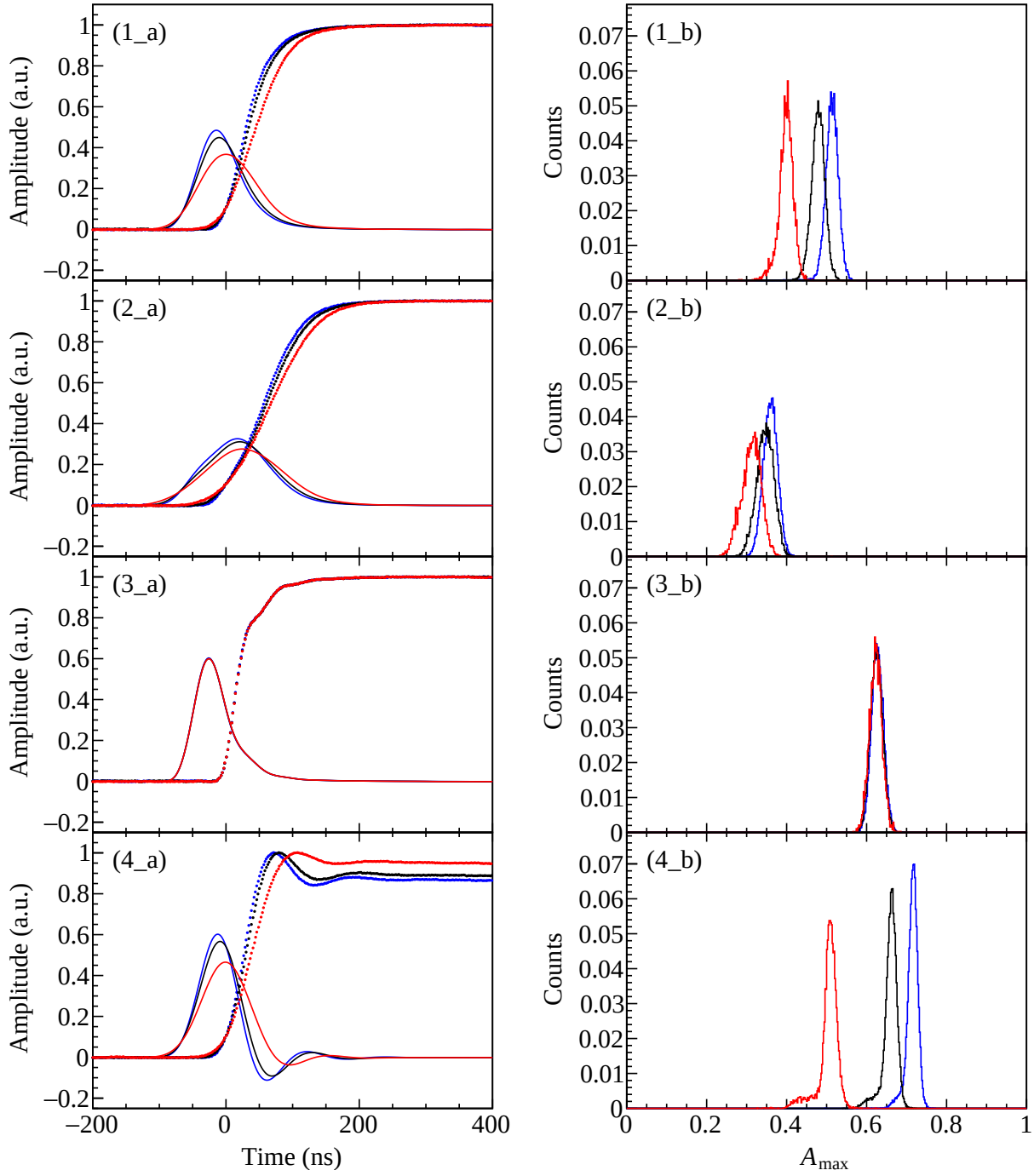

Figure 2.10: Comparison between the experimental configurations. (k-a) Waveforms averaged over 2000 events and their differential waveform are shown by the dotted and solid lines, respectively. (k-b) A_{max} spectra. The notation of the colors are same as Fig. 2.9.

three nuclides is the largest, and the FoM is also the largest. In Fig. 2.10(4-a), the difference in the pulse shape between the nuclides appears not only in the rise shape but also in the decay shape. This difference in the decay shape does not appear at other configurations using the CAEN A1442B preamplifier, thus it is considered that the decay-time constant of the preamplifier strongly affects the PID capability. In addition, the $\mathrm{FoM}_{p\text{–}d}$ at only the $k = 4$ configuration is larger than 0.75. Since the $\mathrm{FoM}_{p\text{–}d}$ is smaller than the $\mathrm{FoM}_{p\text{–}\alpha}$ and the $\mathrm{FoM}_{d\text{–}\alpha}$ in any configurations, the isotopic identification is considered to be more difficult than the atomic number identification.

According to the above results, we concluded that the $k = 4$ configuration was the most suitable experimental setup for our measurements. For all subsequent measurements, we utilized the $k = 4$ configuration.

2.7 Performance test with continuous energy particles

Following the investigation of the PID performance for mono-energetic particles in Sec. 2.4, we studied the energy dependence of the PID performance. A test experiment was conducted at the CYRIC cyclotron facility in Tohoku University to acquire a continuous energy dataset of nuclide-tagged waveforms containing several nuclides. In order to produce several nucllides with continuous energy, we used a $^{11}\mathrm{B} + ^{12}\mathrm{C}$ breakup reaction with a $^{11}\mathrm{B}$ beam at 83 MeV bombarding a 100-μg/cm^2-thick $^{\mathrm{nat}}\mathrm{C}$ target. Emitted decay particles were detected with a two-layer Si detectors array. The first layer was a 100-μm-thick ΔE detector and the second layer was a 500-μm-thick E detector. The waveforms of the output signals from the second-layer Si detector were used as the continuous energy dataset. According to the results in Sec. 2.6, we utilized the MPR-16 preamplifier, the ohmic-side injection, and the NTD Si crystal.

In order to tag each waveform by the nuclides, the PID by the E–ΔE method was performed at each event. We show the E–ΔE correlation in Fig. 2.11. The loci corresponding to each nuclide which stopped in the second layer were clearly identified, and punch-through events which particles penetrated the second layer were observed. We identified the following nuclides in Fig. 2.11(a): p, d, t, ^{3}He, ^{4}He, ^{6}He, ^{6}Li, and ^{7}Li. The PID functions described as $E = [0] + [1]/\Delta E$ for each nuclide are also shown in Fig. 2.11(a) by the solid lines. To avoid contamination of the punch-through events, we decided the energy cutoff for each nuclide to be 6.0, 7.0, 8.0, 20.0, 25.0, and 25.0 MeV for p, d, t, ^{3,4}He, ^{6}He, and ^{6,7}Li, respectively. In Fig. 2.11(b), the selected events for each nuclide to perform the PSA are plotted on the E–ΔE correlation using the same colors as the each PID function.

We applied the triangle filter given by Eq. (2.3) to nuclide-tagged waveforms and obtained the correlation between A_{max} and energies for each nuclide. The A_{max}–E correlations are shown in Fig. 2.12 using the same

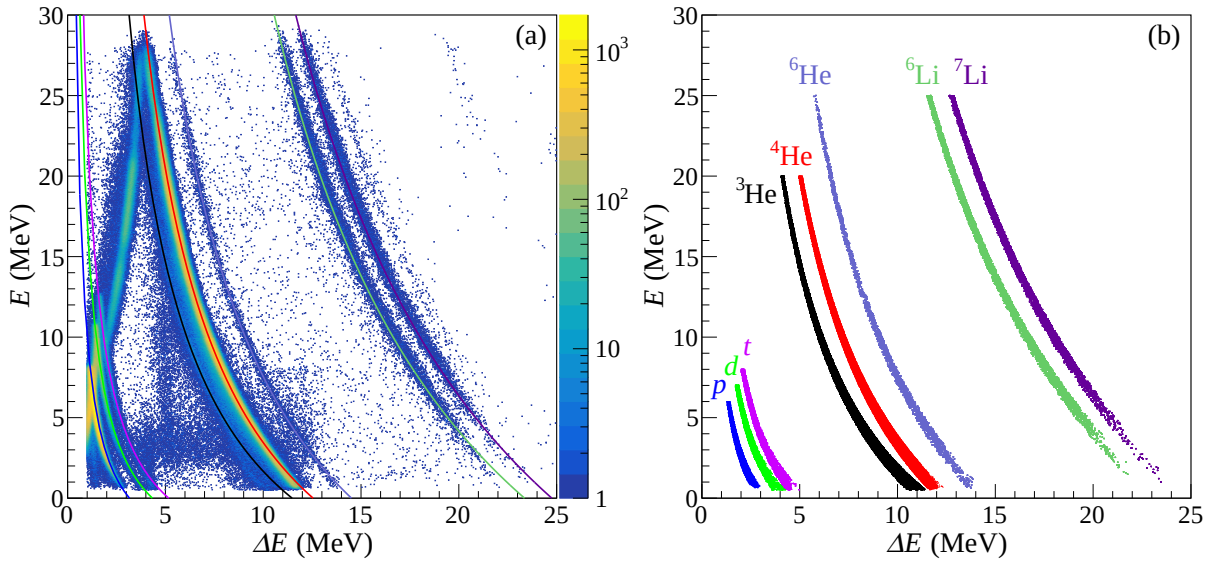

Figure 2.11: Correlation between the measured energies in the first layer (ΔE) and the second layer (E). (a) Overlaid with the PID functions described as $E = [0] + [1]/\Delta E$. (b) Scatter plots of selected events for each nuclide to perform the PSA.

colors as the PID functions. The yields of protons and α particles are much higher than other nuclides, and that of ^{3}He, ^{6}He, ^{6}Li, and ^{7}Li are very low. However, it is possible to find out the energy-dependence trend of A_{max} and its difference among the different nuclides. For any nuclide, A_{max} decreases with energy in the low-energy region, and after a certain energy, it turns to increase with energy. The minimum value of A_{max} and the associated energy depend on the nuclide, and this energy tends to be smaller as the atomic number is smaller. The energy dependence of the decreasing part is almost the same for all nuclides, thus two low-energy nuclides that are both in the decreasing region, for example ^{4}He and ^{6}Li at 3 MeV, can not be distinguished by our PSA. The energy dependence of the increasing part differs among nuclides. However, the difference in this dependence is small among isotopes with the same atomic number, which may make the isotopic identification more difficult.

We quantitatively evaluated the energy dependence of the p–α discrimination capability based on the FoM$_{p-\alpha}$. We show the A_{max} spectra at $E = 2.0, 2.5, 3.0 \pm 0.05$ MeV in Fig. 2.13(a)–(c). Each A_{max} spectrum was scaled to a integrated value of 1. The FoM$_{p-\alpha}$s are also indicated in Fig. 2.13. The FoM$_{p-\alpha}$ decreases with energy, and the FoM$_{p-\alpha}$ at $E = 2.0$ MeV is 0.87. In Fig. 2.12, A_{max} of proton is almost the same as that of alpha below 2.0 MeV. Therefore, the lower-energy limit for p–α discrimination using A_{max} is around 2.0 MeV.

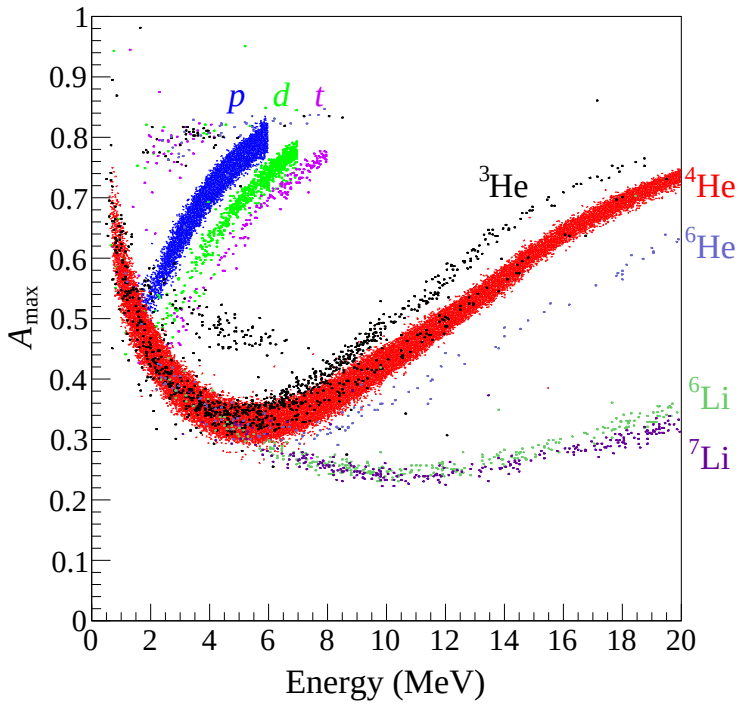

Figure 2.12: Scatter plots of $A_{\max}$ versus energies. A display threshold of > 1 is imposed for proton and α. The notation of the colors is same as Fig. 2.11.

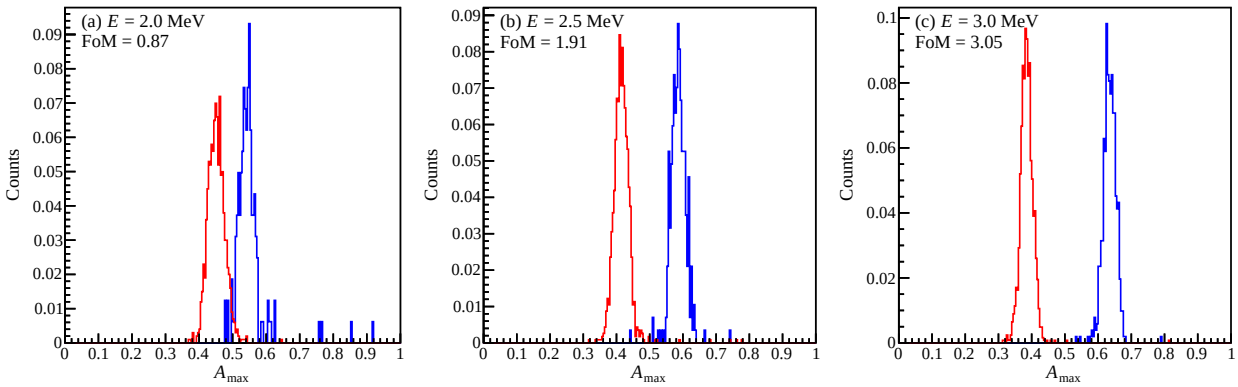

Figure 2.13: $A_{\max}$ spectra at (a) $E = 2.0 \pm 0.05$ MeV, (b) $E = 2.5 \pm 0.05$ MeV, and (c) $E = 3.0 \pm 0.05$ MeV. The $\mathrm{FoM}_{p-\alpha}$ at each energy is indicated in each panel. The blue and red spectra correspond to proton and α.

2.8 Design of SAKRA

The schematic view of SAKRA was shown in Fig. 2.1. SAKRA has a lampshade configuration and consists of 5 segments MMM design Si detectors from Micron Semiconductor described in Sec. 2.3.1. The total number of the read-out strips is 80 (16×5) on the junction sides and 40 (8×5) on the ohmic sides. The configuration of SAKRA is similar to CAKE at iThemba Labs [55] and SABRE at Florida State University's John D. Fox accelerator laboratory [56], but SAKRA is specialized for the PSA based on the results in Sec. 2.6. SAKRA is constructed with the NTD Si detectors and the ohmic-side incidence configuration. In addition, SAKRA can be used in various facilities or scattering chambers, and in consideration of extensibility to multi-layered configurations in future experiments, its frame was designed not to interfere with punch-through particles.

2.9 Performance of SAKRA

In order to evaluate the PID performance at all junction-side strips of SAKRA, we conducted a test experiment at the JAEA tandem accelerator facility (mentioned in detail in the next chapter). Nuclide-tagged data were obtained by measuring the Rutherford scattering off gold foil using the four-nuclide ($p \cdot d \cdot {}^{3}\mathrm{He} \cdot {}^{4}\mathrm{He}$) beams at 5 MeV and 9 MeV. We had planned to obtain four nuclides with several energies between 1 MeV and 9 MeV using gold foils of several different thicknesses. However, since the thickness of the gold foil was different from the nominal value, the obtained p and d energies became in a narrower range than expected. Fortunately, the acquired data contained a continuous energy distribution, probably due to scattering from the aluminum target frame, and we also used this continuous energy data as nuclide-tagged data.

We show the A_{max}–E correlations at Ch. 7 on the junction side of segment 0 and segment 1 in Figs. 2.14(a) and (b). Comparing Figs. 2.14(a) and (b), although the minimum value of A_{max} for each nuclide depends on the individual segment, the energy-dependence trend and the energy with minimum A_{max} are almost the same between the two segments. We checked the A_{max}–E correlations at all 80 channels of SAKRA, and confirmed that the lower-energy limit for the p–α discrimination using A_{max} is around 2 MeV at all channels.

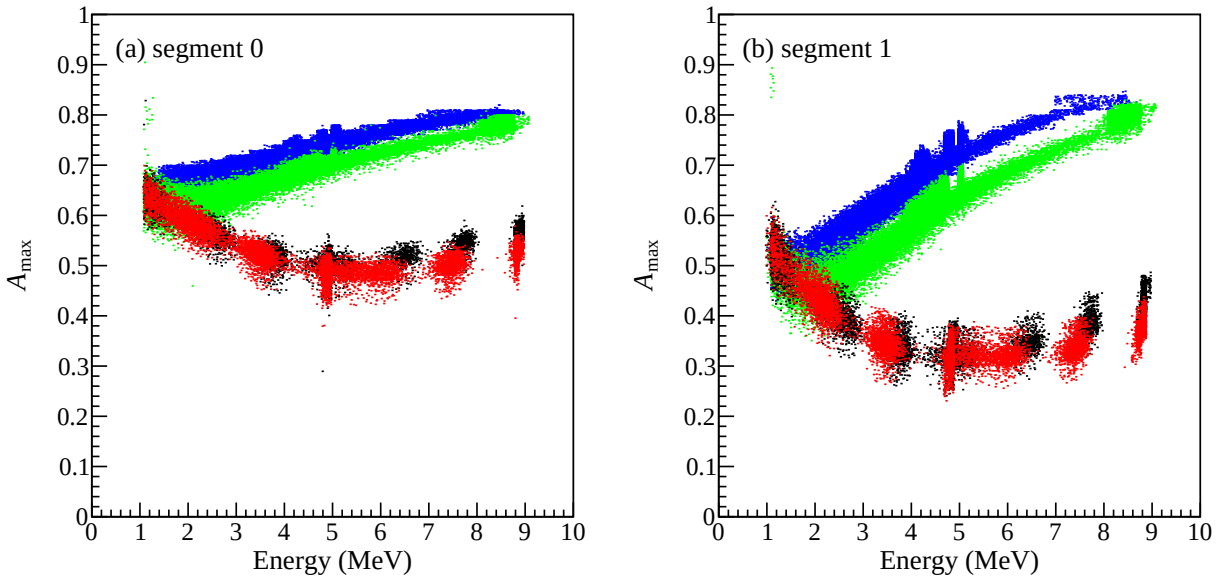

Figure 2.14: Scatter plots of A_{max} versus the energy at Ch. 7 on the junction side of (a) segment 0 and (b) segment 1 of SAKRA. The blue, green, black, and red dots correspond to the data of proton, deuteron, ^{3}He, and α, respectively.

Chapter 3

Experiment

We measured the ^{12}C + ^{12}C resonance scattering at the energy range of E_{beam} = 35.0–50.0 MeV. The experiment was conducted at the R5 beam line in the Tokai Tandem accelerator facility of the Japan Atomic Energy Agency (JAEA). A ^{12}C beam bombarded the $^{\mathrm{nat}}$C target with a thickness of 100 μg/cm^2, and decay particles were emitted from ^{24}Mg resonance states. We detected the decay particles by the Si detector array SAKRA.

3.1 Summary of the measurement

This experiment was conducted in the two periods, March (March 29–April 1, 2022) and April (April 18–21, 2022). In the first beam-time period, we scanned the beam energy in 1.0 MeV steps from 35.0 MeV to 50.0 MeV, corresponding to the excitation energy in ^{24}Mg from 31.4 MeV to 38.9 MeV. The beam energies utilized in the second beam-time period were selected within the region where structures were observed in the preliminary results of the first beam-time period. We summarize the utilized beam energy and the rough measurement time of the physics run in Table 3.1. At E_{beam} = 35.0–40.0 MeV in the first beam-time period and at all beam energies in the second beam-time period, we acquired data with the minimum-bias trigger for about 10 minutes.

Table 3.1: Summary of the measurement.

Period	Beam Energy (MeV)	Energy step (MeV)	Measurement time (hours)
Mar.	35.0–37.0	1.0	2.0
	38.0–50.0	1.0	2.5
Apr.	38.4–39.6	0.4	4.0
	40.5–46.5	1.0	3.5
	40.0–46.0	2.0	1.0

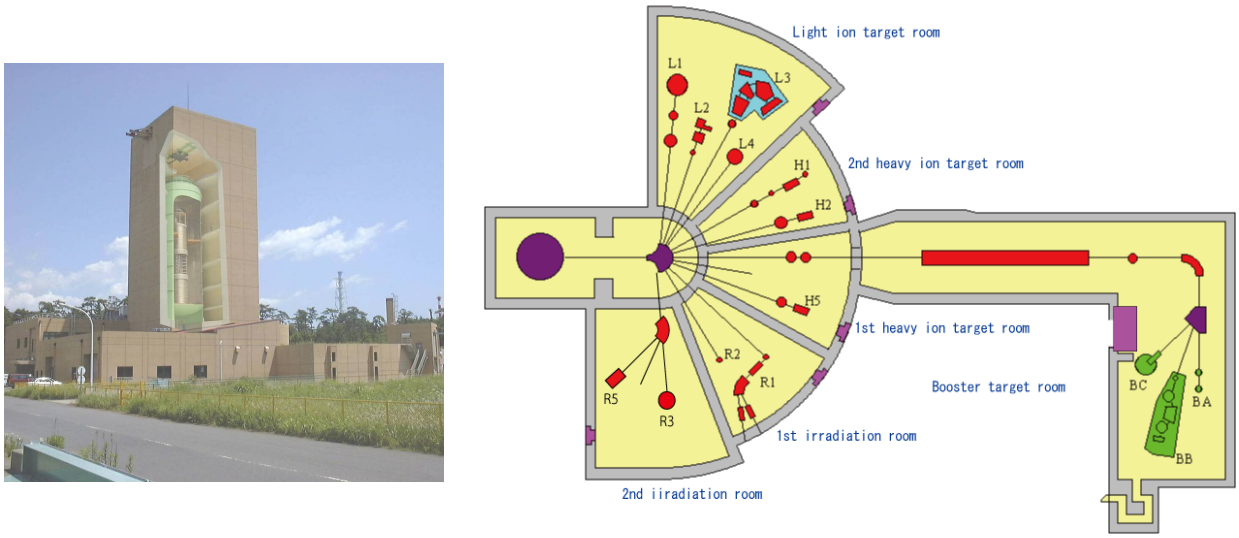

Figure 3.1: Schematic exterior and plane view of the JAEA tandem accelerator facility. Taken from Ref. [57].

3.2 Facility and Beam line

The JAEA tandem accelerator facility is located in Tokai-mura, Ibaragi prefecture, Japan. A schematic exterior and a plane view of the JAEA tandem accelerator facility are shown in Fig. 3.1. In this tandem accelerator, negative ions from the ion source were accelerated through a negative ion (low-energy) accelerator tube for the positive high voltage terminal. At the end of the negative ion accelerator tube, the ions through an electron stripper and the charge stae of the ions were transformed to positive. The positive ions were accelerated again at a positive ion (high-energy) accelerator tube for the ground terminal. Finally, in our experiment, a $^{12}C^{5+}$ beam was transported to the target in the R5 beam line. It is an advantage of the tandem accelerator that the tuning of the accelerator is relatively easy when we changed the beam energies because the tandem accelerator is a linear and electrostatic accelarator. Because we needed to frequently change the beam energies for scanning the excitation energy of ^{24}Mg, we conducted this experiment at this facility.

3.3 Experimental setup around the scattering chamber

A schematic view and a photograph of the setup in the scattering chamber are shown in Fig. 3.2. A ^{12}C beam came from the left side and bombarded a target mounted on the target ladder at the center of the scattering chamber. In order to detect decay particles effectively, we placed SAKRA at the forward angle because decay particles emitted from ^{24}Mg resonance state are boosted and focused on forward angles. By applying

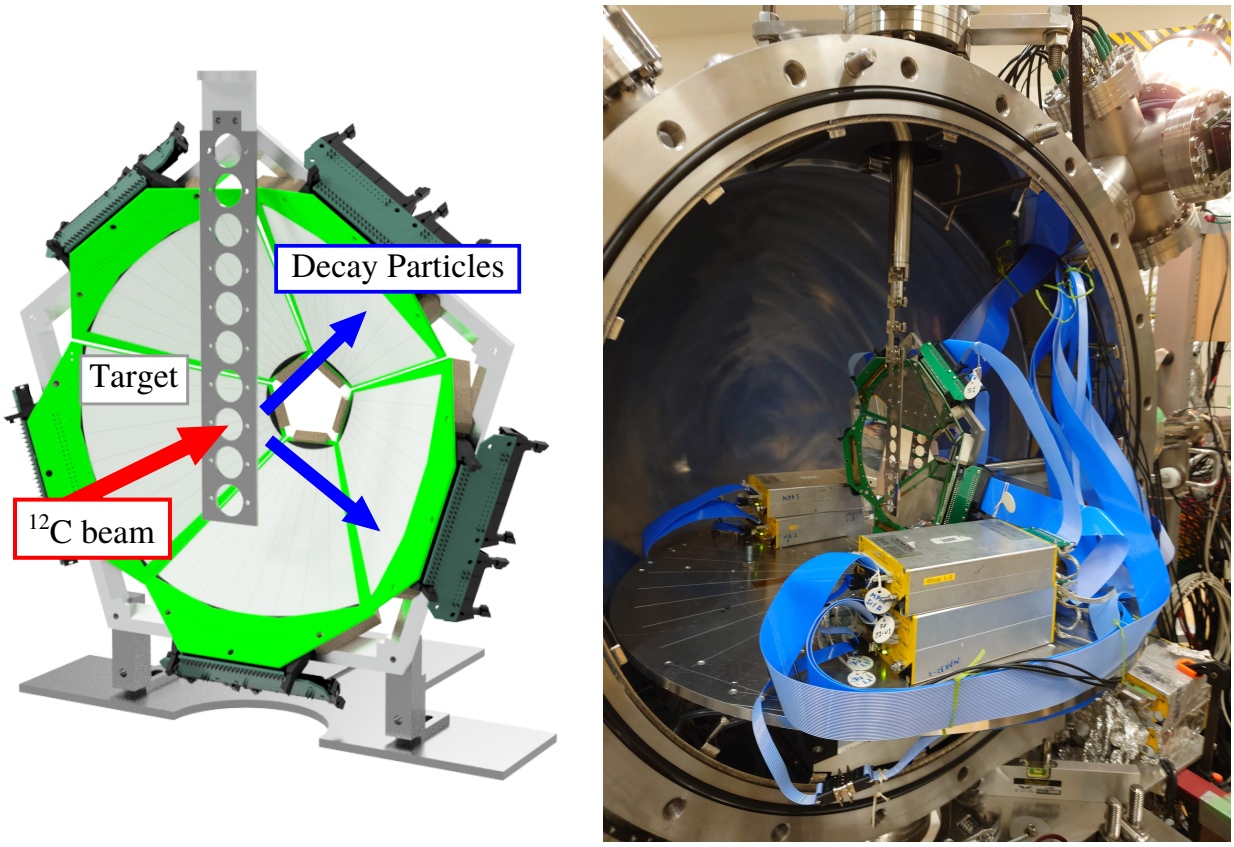

Figure 3.2: Schematic view and photograph of the setup in the scattering chamber.

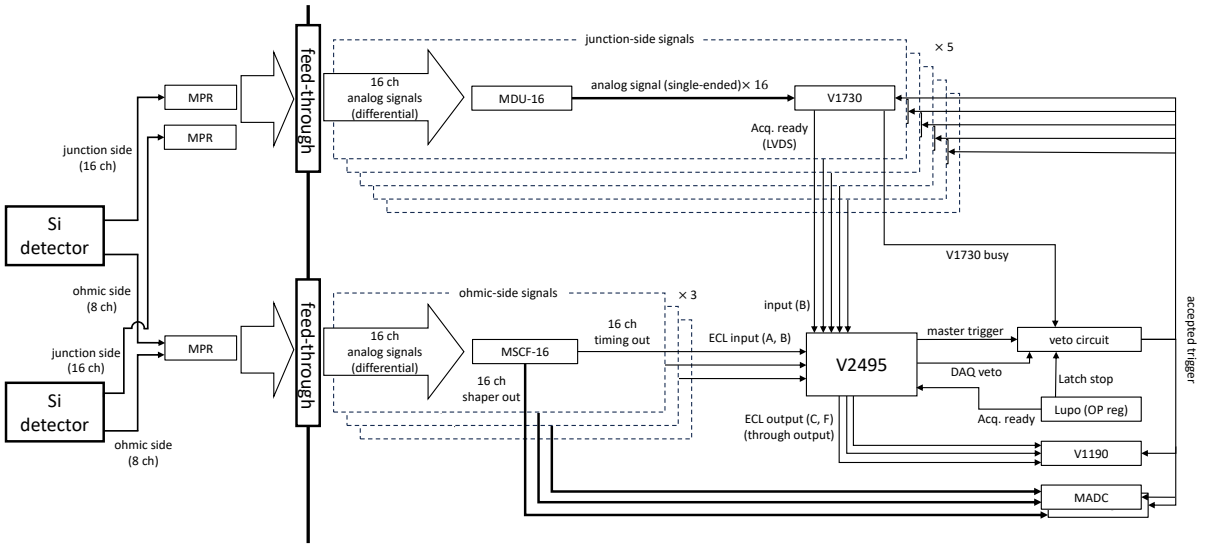

Figure 3.3: Schematic diagram of the signal processing.

the PID method with the PSA, SAKRA could be installed closer to the target and cover a large solid angle. The design value of the horizontal distance between the target and SAKRA's pentagonal frame was 20 mm.

In order to suppress electrical noises, the MPR-16/32 preamplifiers were also installed in the scattering chamber. The signals from the Si detectors were separated to the junction-side signals (16 ch) and the ohmic-side signals (8 ch) immediately after the read-out connector on each Si detector. The junction-side signals and the ohmic-side signals were amplified by respective preamplifiers. Output signals from the preamplifiers were taken out of the scattering chamber via feed-through flanges.

We had prepared two ^{nat}C targets with different thicknesses, which were 100 μg/cm^2 and 30 μg/cm^2, to control the event rate during the beam time. However, we used the 100-μg/cm^2-thick target only in the all measurement. The isotope abundance of ^{12}C was assumued 98.9% (natural abundance).

3.4 DAQ system

The DAQ system used in this experiment was described in Sec. 2.2. A schematic diagram of the signal processing is shown in Fig. 3.3. The junction-side signals were converted to single-ended signals with the MDU-16 modules and digitized by V1730s. The ohmic-side signals were sent to the Mesytec MSCF-16 shaping amplifiers. The peak heights of shaper-out signals were recorded by the MADC-32 peak-hold ADCs. In the first beam-time period, because we made a mistake in the configuration of MADC-32, the input dynamic range of MADC-32 was insufficient. Therefore, we modified it in the second beam-time period,

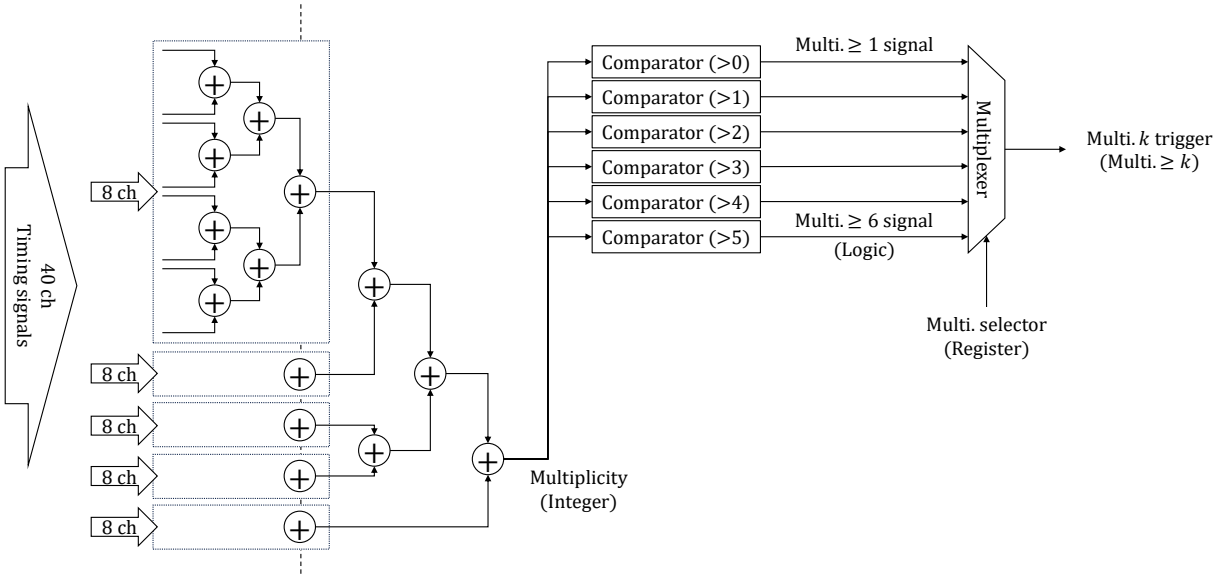

Figure 3.4: Schematic diagram of the trigger production in V2495.

and thus the input dynamic range of MADC-32 was different in the two beam-time periods. The MSCF-16 modules were also equipped with timing-filter amplifiers and constant-fraction discriminators. The timing-out signals were recorded by the V1190 TDC, and were sent to the CAEN V2495 FPGA module for the trigger production.

3.4.1 Trigger production

The trigger signal was generated from the timing signals from the ohmic side using V2495. In Fig. 3.4, we show the schematic diagram of the trigger production in V2495. All 40 timing signals were input to V2495 and added by 6-stages of 8-bits adders. The output value of the last adder was the multiplicity of the timing signals at those time. In order to generate logical signals, the multiplicity value was input into the comparators with threshold values from 0 to 5. The output signals of the comparators (Multi. $\geq$ 1–6 signals) were output from V2495 as NIM signals for monitoring these rates and sent to the multiplexer for generating the multiplicity trigger. The trigger multiplicity k was selected by the Multi. selector, which was the programmable register and could be changed remotely. During the beam time, we used the Multi. 1 trigger for the minimum-bias measurement and the Multi. 3 trigger for the physics measurement.

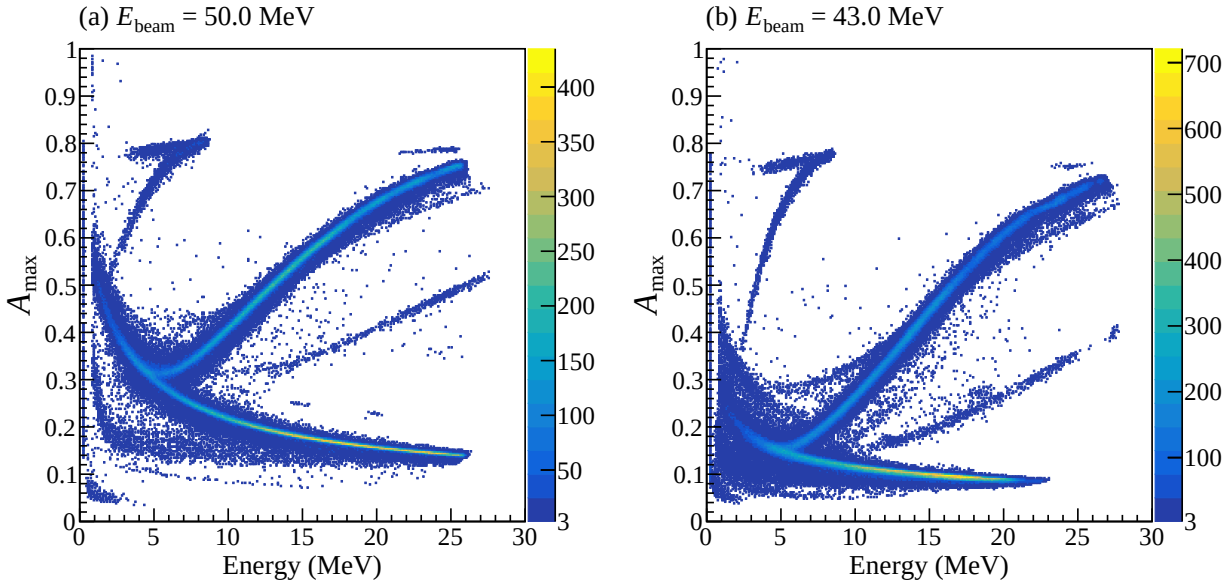

Figure 3.5: A_{max} variation due to the bias shortage comparing at (a) E_{beam} = 50.0 MeV and (b) E_{beam} = 43.0 MeV in the first beam-time period.

3.5 Bias voltage of SAKRA

The bias voltage was applied to each of SAKRA's 5 Si detectors separately via respective preamplifiers. For improving the PID performance, the bias voltages were tuned to be just slightly above the full-depletion voltage, avoiding excessive voltage, for each Si detector. However, in the middle of the first beam-time period, we noticed the shortage of the bias voltages. Figures 3.5(a) and (b) show the correlations between A_{max} and energies for the same junction-side strip at (a) E_{beam} = 50.0 MeV and (b) E_{beam} = 43.0 MeV in the first beam-time period. The measurement at E_{beam} = 50.0 MeV was taken at the beginning of the first beam-time period, and the measurement at E_{beam} = 43.0 MeV was later. Comparing Figs. 3.5(a) and (b), the A_{max} value actually became lower at E_{beam} = 43.0 MeV. This is probably because SAKRA was placed at the forward angle, which caused radiation damage and increased the leak current. As a result, because the rising edge of waveform became dull, the A_{max} value varied and the low-energy particles could not cross over the trigger threshold.

Due to this bias shortage, the experimental data from some Si sensors were unreliable at some beam energies in the first beam-time period. After realizing this bias shortage, we verified the bias voltages by cautiously monitoring A_{max} on every run, and increased the bias voltage if it was deficient.

Chapter 4

Data analysis

4.1 Energy calibration

The energy calibration was performed with a mixed alpha source, which contains ^{241}Am (5.46 MeV), ^{244}Cm (5.78 MeV) and ^{148}Gd (3.18 MeV). The junction-side channels were calibrated using the peak ADC value calculated from shaped waveforms as described in Sec. 2.5.1. Figure 4.1(a) shows the total energy spectrum of a total of the 16 junction-side channels in the segment 0. The calibration of the ohmic-side channels was simply performed using the peak ADC value recorded by MADC-32, but the calibration parameters differed in the two beam-time periods due to the difference in the input dynamic range. Figure 4.1(b) shows the energy spectrum of a total of the 8 ohmic-side channels in the segment 0. To quantify the resolution of SAKRA, the ^{148}Gd peak was analyzed at all the junction-side and ohmic-side channels. Table 4.1 summarizes the energy resolution of all the channels at sigma, the best and worst resolution for the junction and ohmic sides of each segment.

One concern is energy shifts due to the bias voltage change during the beam time. To investigate energy shifts, we acquired calibration data using the mixed alpha source at all bias voltages used during beam time. As a result of analyzing these data, no energy shift was confirmed at least for the ^{148}Gd peak at 3.18 MeV.

Table 4.1: Summary of the energy resolution of the ^{148}Gd peak at sigma.

	Junction side					Ohmic side				
Segment	total (keV)	best (keV)	ch	worst (keV)	ch	total (keV)	best (keV)	ch	worst (keV)	ch
0	21.71	18.27	14	23.23	0	25.92	24.31	0	27.31	6
1	21.52	19.21	11	23.89	14	26.39	22.93	4	27.79	7
2	21.90	20.02	13	23.76	15	28.28	22.33	6	54.09	7
3	22.34	19.00	11	24.57	0	42.05	30.17	0	45.24	5
4	21.56	18.67	11	23.20	1	36.70	31.85	6	41.58	4

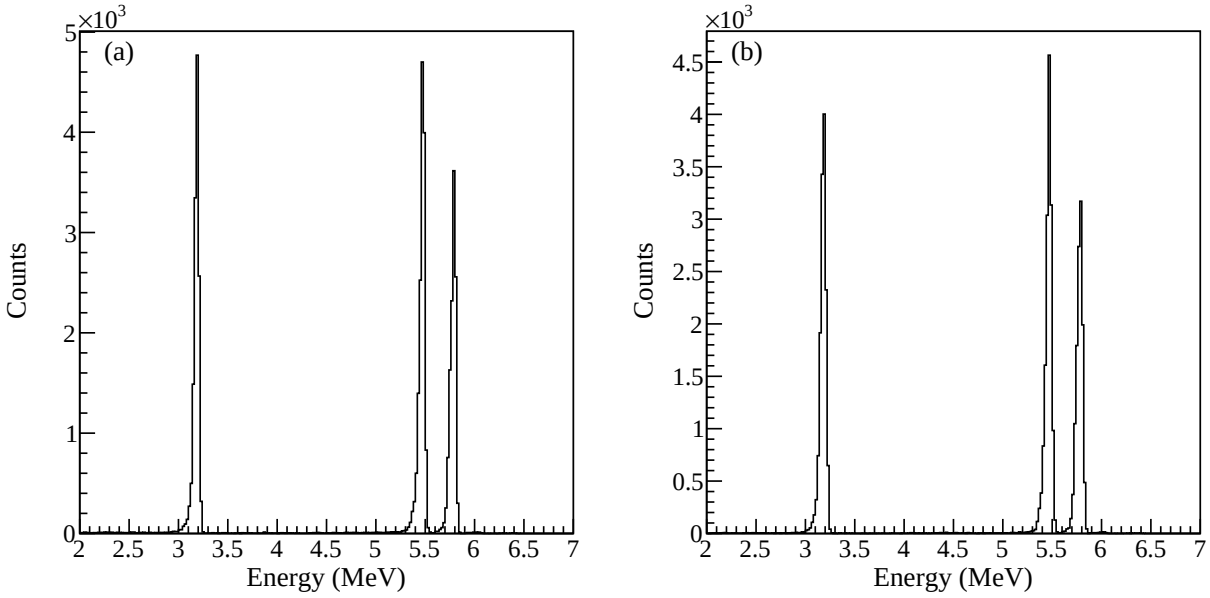

Figure 4.1: Energy spectra of the mixed alpha source. (a) Junction side and (b) ohmic side.

4.2 Junction-side data reduction

Examples of raw waveforms and baseline-subtracted waveforms are shown in Figs. 4.2(a) and (b). Waveform data were processed as described in Sec. 2.5, and several values (Peak ADC, PeakClk, Baseline, Energy, and $A_{\max}$) were obtained for each waveform. Figure 4.2 contains the following types of the waveforms: Prompt (Black), Accidental (Red), Noise or Cross-talk (Blue), Pileup (Magenta), Overflow (Green), and Falling (Cyan) events. Falling events are waveform tails of hit pulses outside the recording period and are easily eliminated by PeakClk. We identified events with a PeakClk of less than 100 as the Falling events. Overflow events are also easily identified. Peak ADC values for the overflow events are close to or about the same as baseline values. Events with a difference of less than 200 between baseline and peak ADC values were identified as the Overflow events.

In order to distinguish the other types of waveforms, we used the integrated value of each waveform (I). We show the correlation between the integral and the peak ADC in Fig. 4.3(a). Figure 4.3(b) is the enlarged view of the dashed-box region in Fig. 4.3(a). The vertical locus around 15000 ch of the peak ADC in Fig. 4.3(a) corresponds to the Overflow events. The two oblique loci in Fig. 4.3(a), and the upper one corresponds to the Pileup or Falling events because these types of waveforms have larger amplitude at earlier clocks than the Prompt events. This locus with $I > 1.5 \times 10^3 \times$ peak ADC was selected as the Pileup events. Because the waveform of Noise or Cross-talk event oscillates around its baseline, the integral value is about

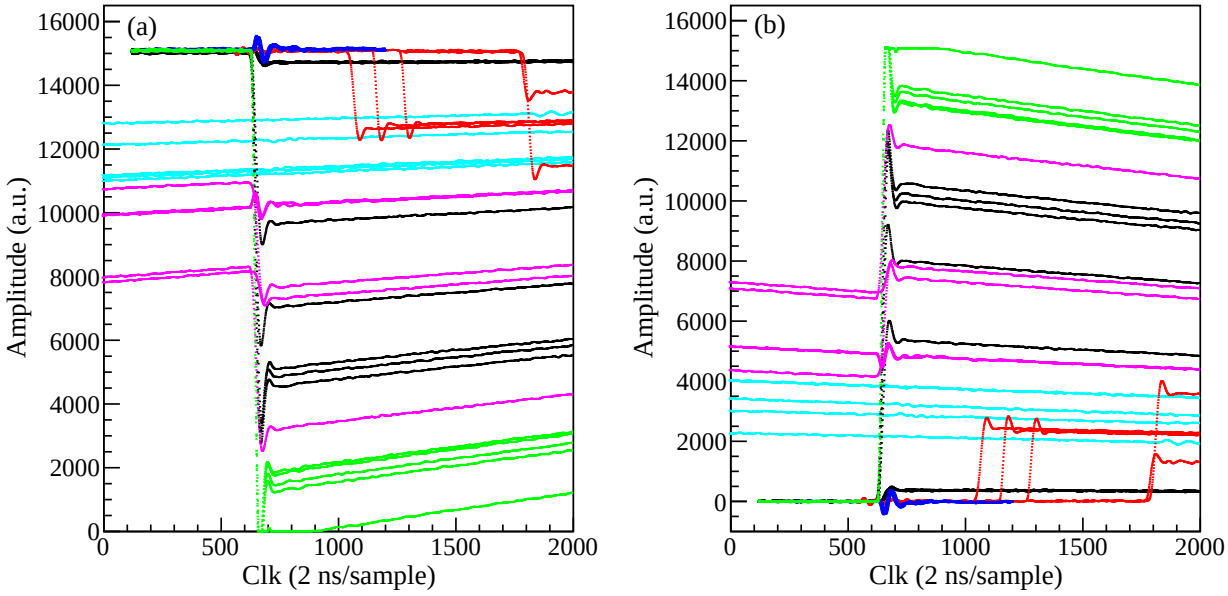

Figure 4.2: Examples of acquired waveforms. (a) Raw waveforms and (b) baseline-subtracted waveforms.

0. Therefore, the locus around 0 of the integral in Fig. 4.3(b) corresponds to the Noise or Cross-talk events. We identified events with an integral value less than 2×10^5 as the Noise or Cross-talk events. Events that were not identified as the Falling, Overflow, Pileup and Noise or Cross-talk event were identified as the Prompt and Accidental events. The event types and the gate conditions are summarized in Table. 4.2.

Table 4.2: Summary of the event types and the gate conditions.

Event type	Gate condition
Falling	PeakClk $<$ 100
Overflow	Baseline $-$ peak ADC $<$ 200
Pileup	Integral $> 1.5 \times 10^3 \times$ peak ADC
Noise or Cross-talk	Integral $< 2 \times 10^5$
Prompt and Accidental	otherwise

4.3 Ohmic-side data reduction

The data from the ohmic sides is only the ADC and TDC information for each channel. To eliminate events due to low-energy noise or cross-talk, we needed to decide the low-energy threshold. In addition, because the dynamic range of MADC-32 was insufficient in the first beam-time period, we had to lower the high-energy threshold compared to the second beam-time period. Figures 4.4(a) and (b) show an example of the ohmic-side energy spectra at $E_{\mathrm{beam}} = 38.0$ MeV taken in the first and second beam-time periods. The

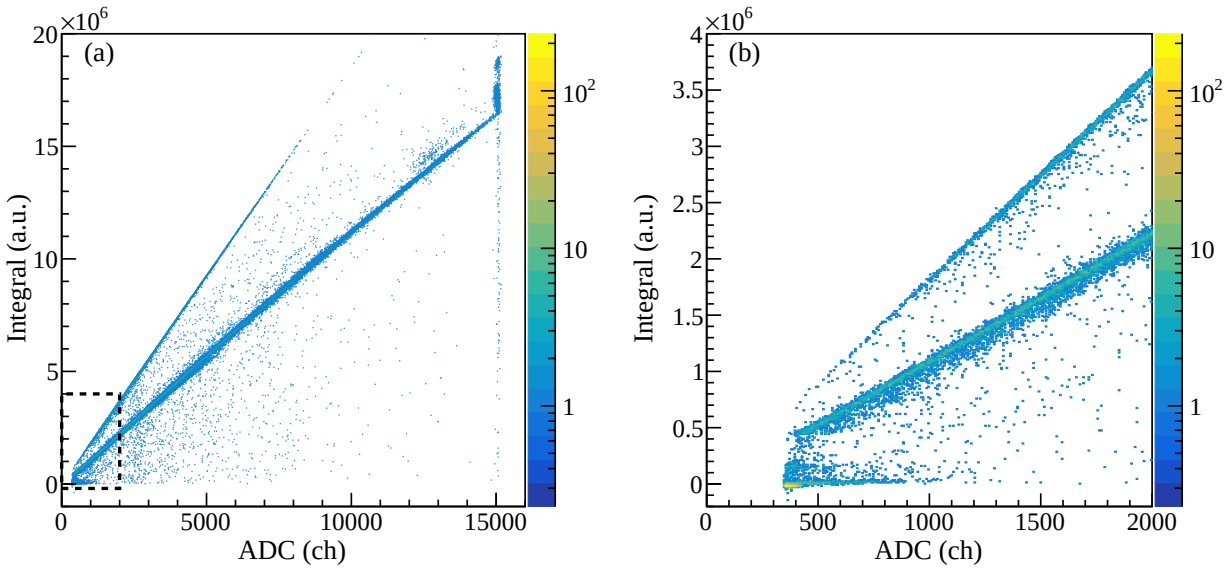

Figure 4.3: Correlation between integral and peak ADC. (b) Enlarged view of the dashed-box region in (a).

black and red spectra represent all the events and the TDC-hit gated events, respectively. Since the dip around 0.5 MeV in the TDC-hit gated spectrum corresponds to the energy threshold set to the MSCF-16 modules, we decided the low-energy threshold at 0.5 MeV. The overflow peak is observed around 15 MeV in Fig. 4.4(a), and the overflow energies vary channel by channel depending on the gain. Therefore, the high-energy threshold for the first beam-time period was determined to be the lowest overflow energy of 14.8 MeV. For the second beam-time period, the high-energy threshold was determined by the energy range of MPR-16/32 preamplifier, which was nominally 25 MeV. Because it was found that the preamplifiers were not saturated even above 25 MeV as seen in Fig. 4.4(b), the high-energy threshold for the second beam-time period was determined to be 30.0 MeV.

4.3.1 Reduction of synchronous noise and cross-talk

We eliminated low-energy noises using the TDC-hit gate and the low-energy threshold, but some events with high multiplicity remained. Figure 4.5 shows a typical energy correlation between neighbor strips in the segment 0. The wedge-shaped locus corresponds to true events because alpha particles emitted from same ^{12}C are considered to have similar energy.

In Fig. 4.6, we show another energy correlation in the segment 3. Although the wedge-shaped locus is observed also in Fig. 4.6, almost all the events are concentrated in the very low-energy region with the same energy. One of the origins of the high-multiplicity events is these synchronous noises which occur in many

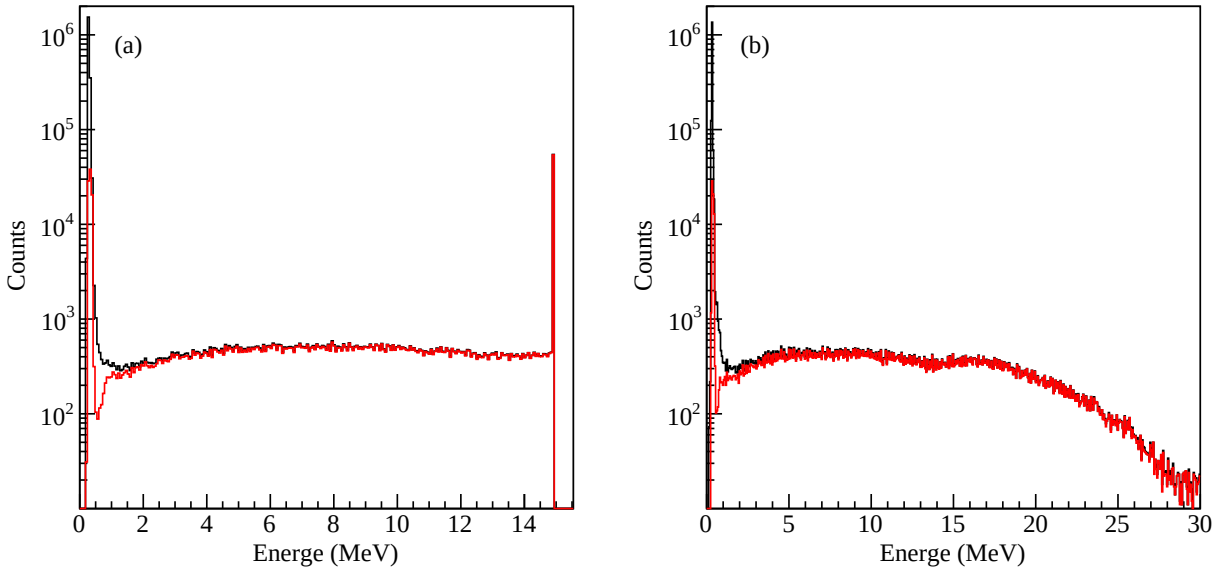

Figure 4.4: Example of the ohmic-side energy spectra in the (a) first and (b) second beam-time periods. The black and red spectra represent all the events and the TDC-hit gated events, respectively.

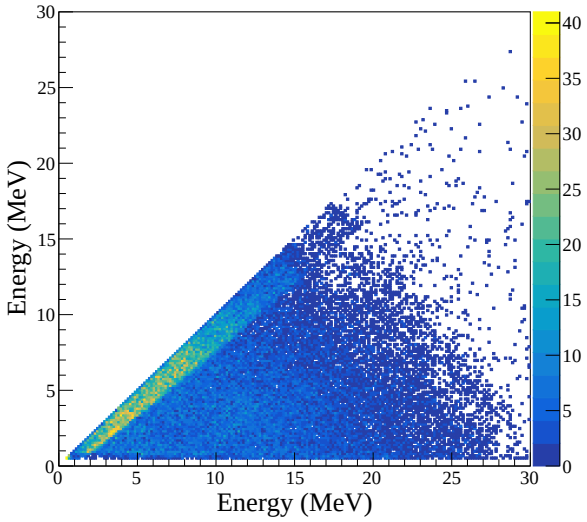

Figure 4.5: Typical energy correlation between neighbor strips at the ohmic side in the segment 0.

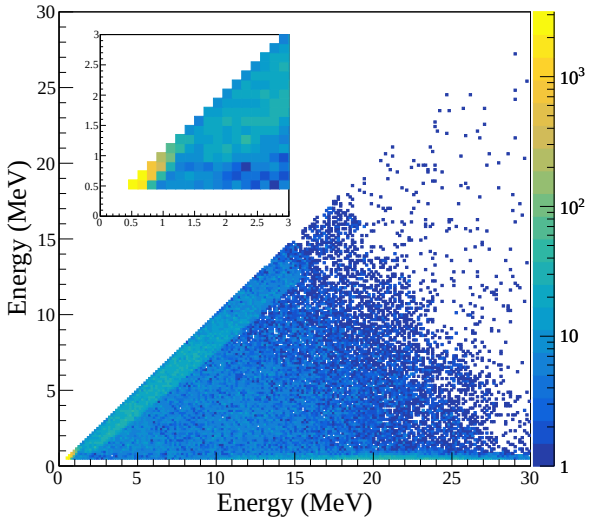

Figure 4.6: Energy correlation between neighboring strips at the ohmic side including the synchronous noises in the segment 3. The enlarged view of E = 0–3 MeV is also shown.

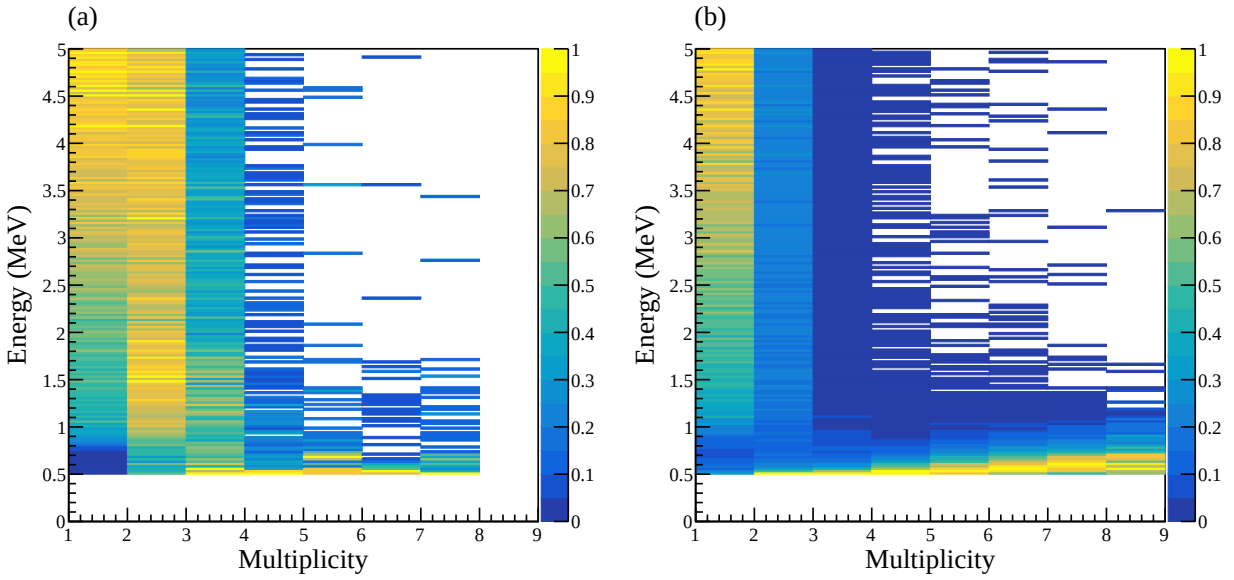

Figure 4.7: Energy distributions at each multiplicity in (a) the segment 0 and (b) the segment 3.

strips at the same time with almost same pulse height. We consider that the synchronous noise is attributed to data transfer. The energy distributions at various multiplicities in the segments 0 and 3 are shown in Fig. 4.7. The maximum entry at each multiplicity is normalized to 1 for comparing among different multiplicities. In the multiplicity = 1 events in the both segments and the multiplicity = 2 events on the segment 0, the energy distributions are uniform over wide energy range. However, in the higher multiplicity events, the energy distributions are concentrated at very low energies, especially in the segment. 3. These events are due to the synchronous noises. In order to remove the synchronous noises, we excluded the rear-side hits if energies on multiple strips are similar ($|E_i - E_j| < 0.12$ MeV) and both of the energies are lower than 1.5 MeV. The result of the synchronous-noise reduction is shown in Fig. 4.8. Because the concentration at low energies in Fig. 4.8(a) and the high multiplicity events in Fig. 4.8(b) are hardly found, the synchronous-noise reduction was successfully worked. However, in Fig. 4.8(b), low-energy events remained at multiplicity = 2–4.

These low-energy events are considered to be cross-talk events. In the analysis, we observed two types of cross-talk events as seen in Fig. 4.9. In Figs. 4.8(a) and 4.9(a), the well-known cross-talk events are seen at very low energy in the y-axis and relatively higher energy in the x-axis. These cross-talk events are induced on the Si sensor or circuit board by incident particles with higher energies. Therefore, we excluded hits with energies below 1 MeV if hits with high energy ($E > 10$ MeV) were included in the same segment. The other type of the cross-talk events between Ch. 0 and Ch. 7 in the segment 0 is seen in Fig. 4.9(b). Because Ch. 0 and Ch. 7 are located at both edges of the rear side of the Si sensor, these cross-talk events are considered

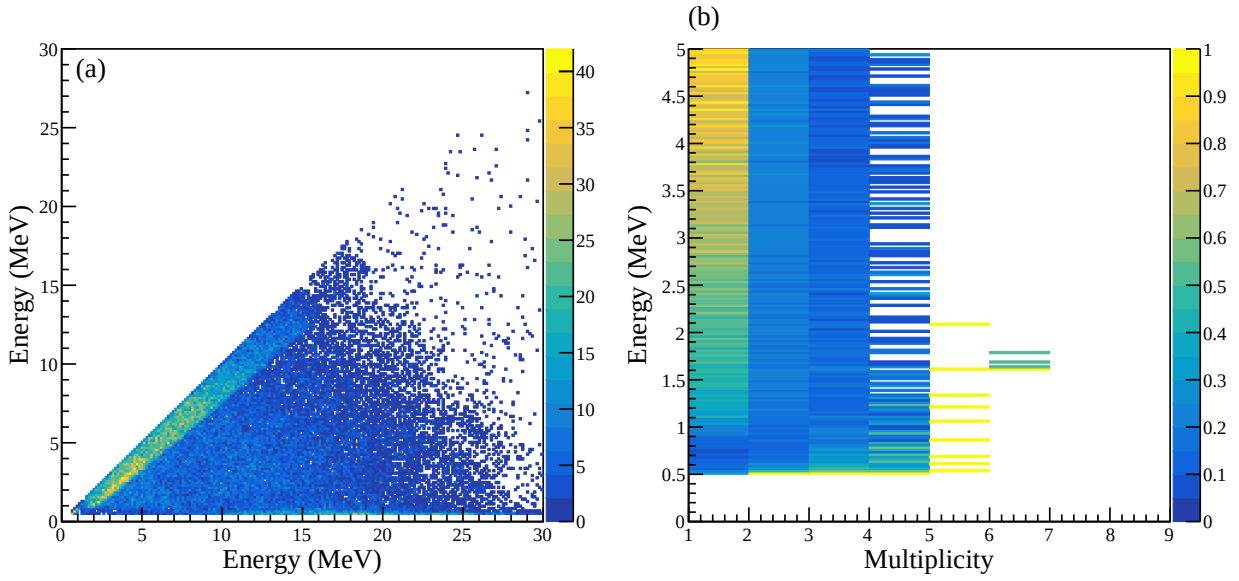

Figure 4.8: Result of the synchronous-noise reduction in the segment 3. (a) Energy correlation. (b) Energy distribution.

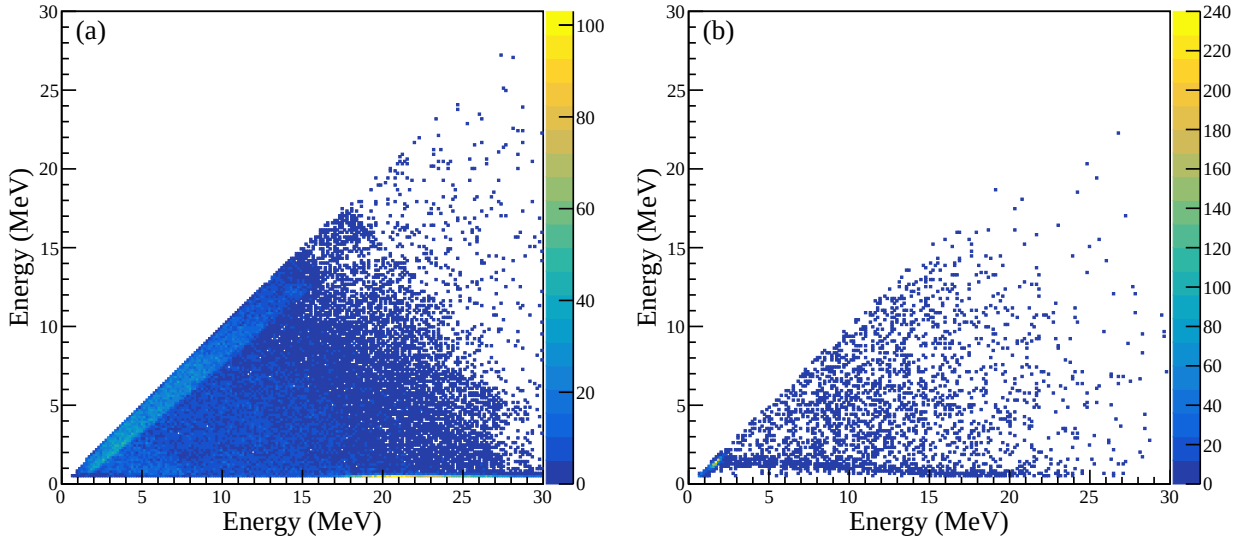

Figure 4.9: Energy correlation after the synchronous-noise reduction. (a) Correlation between neighboring strips in the segment 2. (b) Correlation between Ch. 0 and Ch. 7 of the rear side in the segment 0.

to be induced through the guard ring on the Si sensor. However, these events could not be reliably separated from true events, thus we didn't exclude this type of the cross-talk events.

4.4 Hit position determination

In Sec. 4.2 and Sec. 4.3, we analyzed front-side and rear-side hits separately, and created lists of strips on the both sides excluding invalid hits. In this section, we will combine the strips on both sides in the same segment to determine the hit position and energy of particles.

4.4.1 Energy validation

When multiple particles are incident on the same segment detector, the number of the hit strips on front and rear sides may be different, but the summed energy detected on each side should be the same. Considering the energy resolution of SAKRA, we set the following restriction to validate the consistency in energy on the front and rear sides:

$$\left| \sum E_{\mathrm{front}} - \sum E_{\mathrm{rear}} \right| < \mathrm{Max}(N_{\mathrm{front}}, N_{\mathrm{rear}}) \times 0.21 \text{ MeV}, \tag{4.1}$$

where $\sum E_{\mathrm{front}}$ and $\sum E_{\mathrm{rear}}$ are the summed energy detected on the front and rear sides, and N_i denotes the length of the list for each side, respectively. Figure 4.10 shows the correlation between total energy in the front- and rear-side strip lists, where Figs. 4.10(a) and (b) are data from the first and second beam-time periods. In Fig. 4.10(a), the events in the red-dashed box contain overflow strips of the rear side.

4.4.2 Channel combination

Data sorting to search for channel combinations between the front and rear sides was conducted by considering the 6 types of strip combinations shown in Fig. 4.11. The red pixels are the hit positions, and the yellow strips are the hit channels on the front or rear side. Figure 4.11(a) is named FR hit, where a pair of front and rear channels is triggered by 1 particle only. In Fig. 4.11(b) or (c), named FRR hit or FFR hit, 2 particles hit the same strip on the front or rear side and hit separate strips on the other side. Figure 4.11(d) or (e), named FRRR hit or FFFR hit, is similar to the FRR or FFR hit, but 3 particles hit the same strip on the front or rear side. With these 5 types, we can decode the multi-hit strips and determine the energies of the particles from individual hit strips. On the other hand, we cannot logically resolve the hit pattern shown in Fig. 4.11(f), named FFRR hit. On a FFRR hit, 2 front strips and 2 rear strips are triggered, but it is not possible to discern whether there are 3 or 4 particles, and even assuming there are 3 particles, the hit pixels and particle energies cannot be assigned correctly.

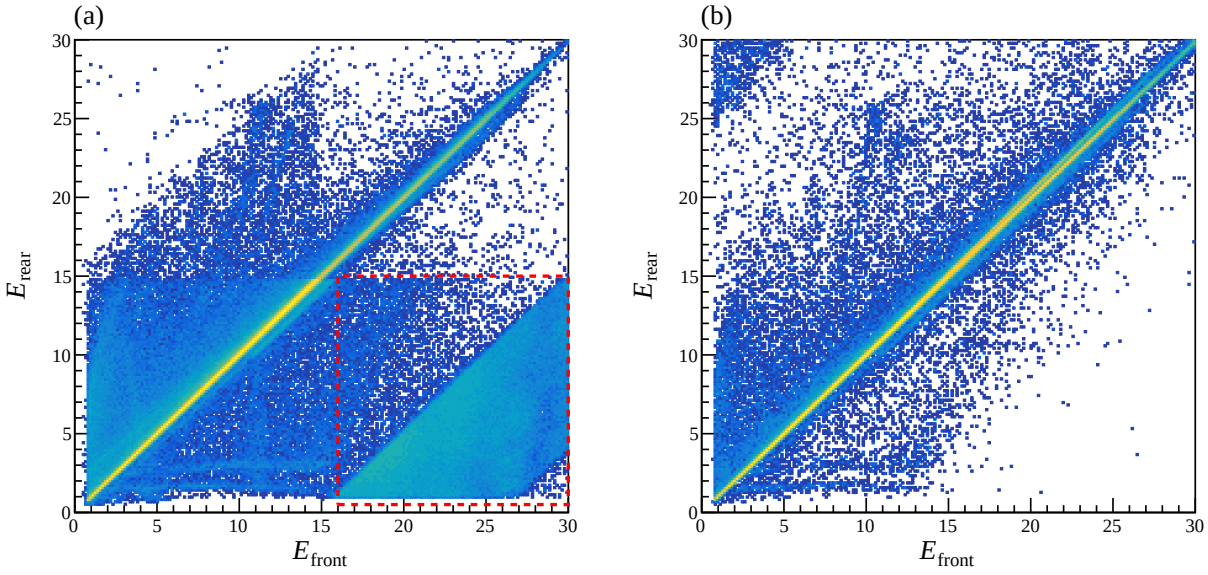

Figure 4.10: Energy correlation between total energy contained in the front- and rear-side strip lists (log scale). (a) Data of the first beam-time period. (b) Data of the second beam-time period.

At first, the FR hit pattern was searched in the front and rear strip lists, and energy differences between the front and rear strips was calculated. If a combination of front and rear strips satisfying the energy restriction,

$$\left| \sum E_{\mathrm{front}} - \sum E_{\mathrm{rear}} \right| < 0.21 \text{ MeV}, \tag{4.2}$$

it was determined that a single particle had hit both the front and rear strips. If no FR hit satisfying Eq. (4.2) was found in the front and rear strip lists, the remaining 5 types of the combination in Fig. 4.11 were applied to the lists. If the strip combination with the smallest energy difference between $\sum E_{\mathrm{front}}$ and $\sum E_{\mathrm{rear}}$ among the 5 types satisfied Eq. (4.2), the combination was adopted. If the adopted combination was not in FFRR hit, the decomposed pixels were used as the hit positions and energies of the particles. After that, the front and rear strips included in the adopted combination were removed from the front and rear strip lists, and the data sorting was iterated from the first step until the length of the front or rear strip list became zero.

4.5 Particle identification with pulse shape analysis

As described in Sec. 2.5.2, we used A_{max} as a PID parameter and performed PID by the correlation between A_{max} and kinetic energies of decay particles. Typical examples of the correlation are shown in Fig. 4.12. As we can see in Fig. 4.12, there are mainly 3 types of loci, and the value of A_{max} differs for each channel even for the same type of locus. Thus, we choose these loci manually for all the segments and all the channels of

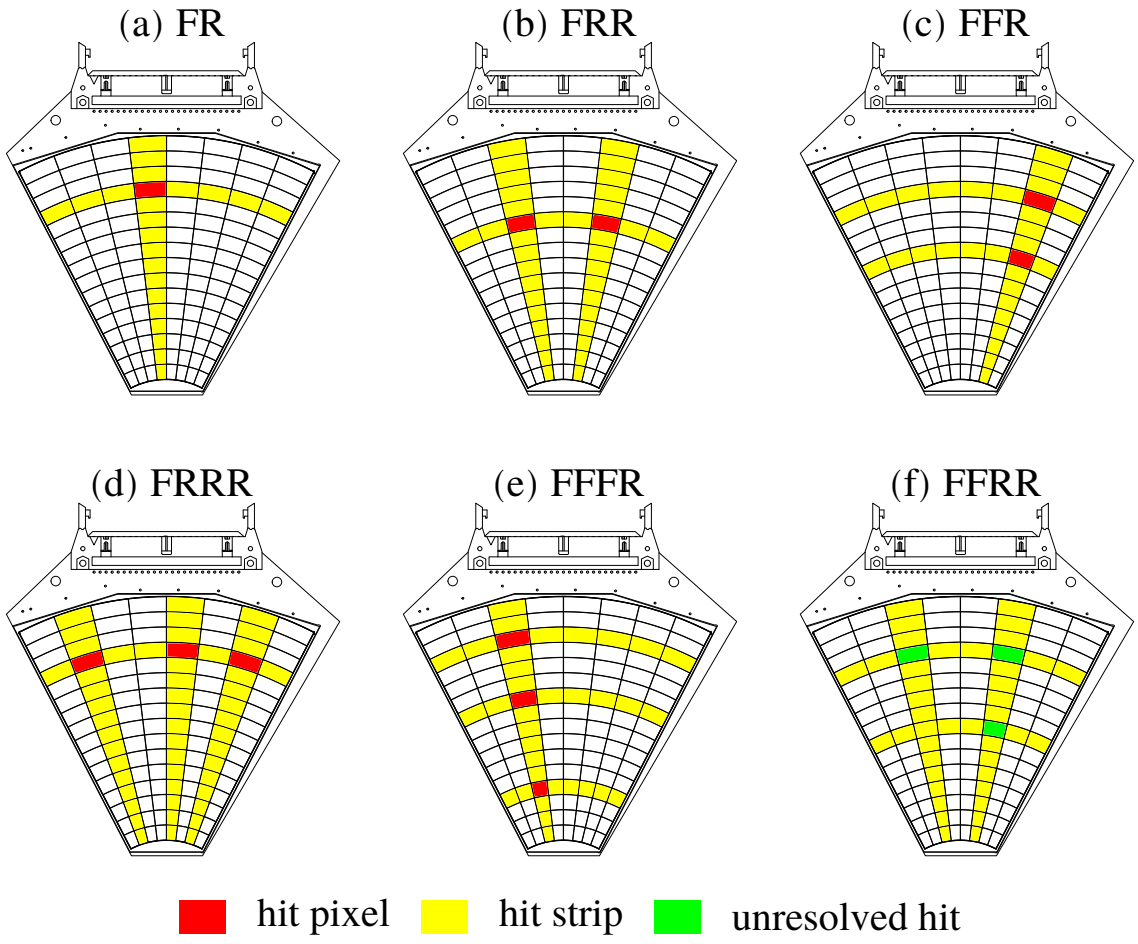

Figure 4.11: Schematic diagrams of the 6 types of combinations. (a) FR hit, (b) FRR hit, (c) FFR hit, (d) FRRR hit, (e) FFFR hit, and (f) FFRR hit (not decomposed).

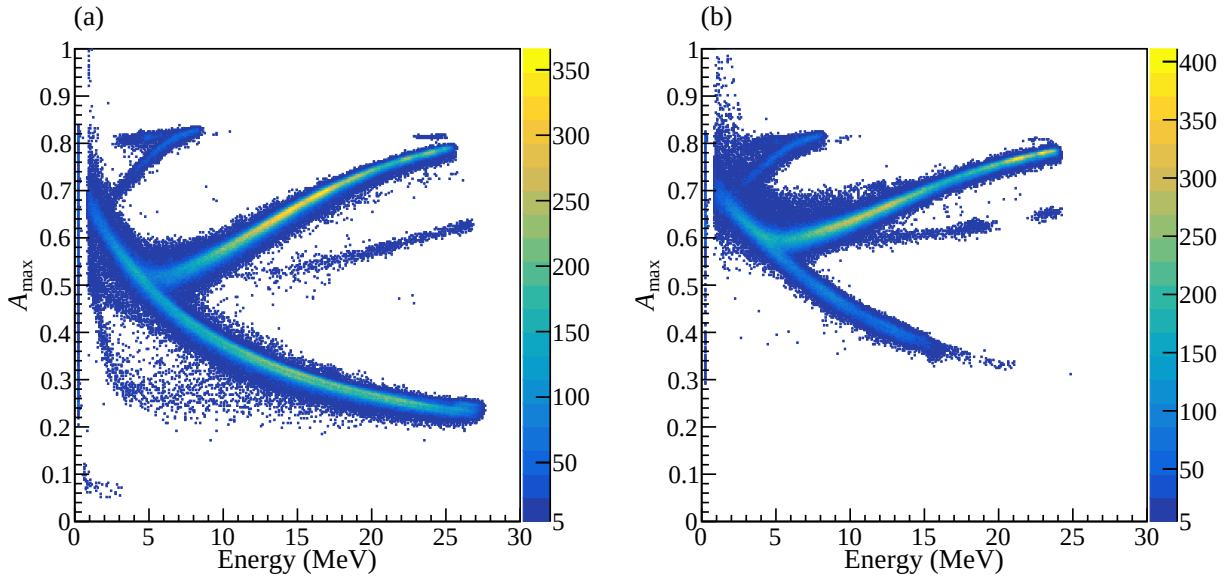

Figure 4.12: Correlation between A_{max} and kinetic energies of decay particles at (a) Ch. 14 in Seg. 0, and (b) Ch. 10 in Seg. 0.

SAKRA. Figure 4.13(a) shows manually drawn lines for each channel, and the boxes in Fig. 4.13(b) present the PID region determined based on the drawn lines. The loci in the blue, red, and green boxes correspond to charged particles with $Z = 1$, $Z = 2$, and $Z \geq 3$, and the dominant isotopes in the individual loci are proton, alpha, and ^{12}C, respectively. The red-dashed line in Fig. 4.13(a) is calculated by scaling the x-axis twice from the red-solid line, and the locus in the red-dashed box in Fig. 4.13(b) is precisely on the red-dashed line. It means that this locus is corresponding to ^{8}Be, namely, 2α particles detected in the same junction-side strip with almost same energy. At lower kinetic energy than 5 MeV, alpha particles cannot be separated from ^{12}C. In this PID procedure with the PSA, we identified particles that belong to only one PID region as p, α, or ^{12}C, and particles that belong to several PID regions were identified as multi-PID particles, tagged as $\{\alpha, ^{12}\text{C}\}$ or $\{p, \alpha, ^{12}\text{C}\}$.

4.6 Timing gate

In order to reduce accidental coincidence events, we employed the timing gate. However, there were some problems in TDC data, and we corrected these problems.

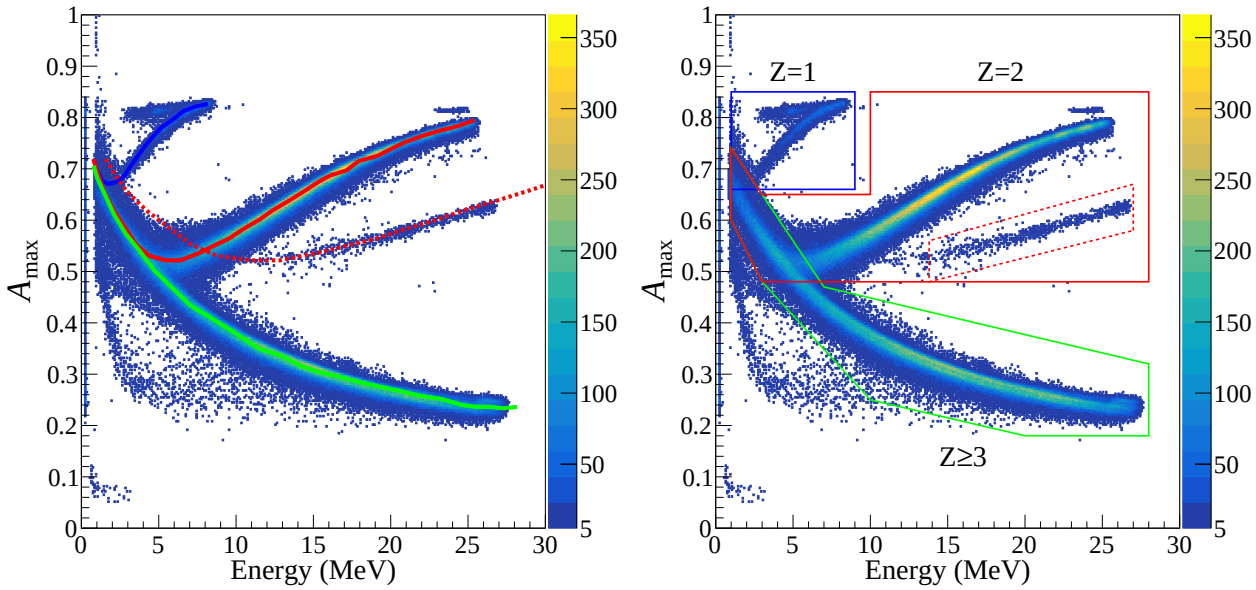

Figure 4.13: PID using the correlation between A_{max} and kinetic energies of decay particles. (a) Overlaid with the manually drawn lines for the individual loci. (b) Overlaid with the boxes presenting the PID region. The blue, red, and green lines or boxes correspond to charged particles with $Z = 1$, $Z = 2$, and $Z \geq 3$, respectively.

4.6.1 TDC offset correction

At first, we found that the TDC data had different offsets for individual channels. We show the TDC data taken with a pulse generator in Fig. 4.14(a), where the x-axis denotes the channel of TDC and the y-axis denotes the difference between the TDC value at each channel and that at Ch. 0. A pulse was input to the test pulser input of the preamplifiers, and the output signals of the preamplifiers were amplified by the MSCF-16 timing filter amplifiers, and the timing out signals were recorded by the V1190 TDC. Because the test pulse was internally distributed to each channel, the output timings should be almost the same. However, as shown in Fig. 4.14(a), the timings differed for each channel. After the all beam times had finished, we tried to find the cause of the timing differences by observing the signals with an oscilloscope. As a result, we found that the analog signals from the preamplifiers were output at the same timing but the timing outputs from the MSCF-16 were different for individual channels. Although we used the same configuration of the CFD plug in modules in the MSCF-16, it might be considered that there were individual differences in the CFD circuit of each channel. Therefore, we adjusted the TDC offsets for each channel as shown in Fig. 4.14(b).

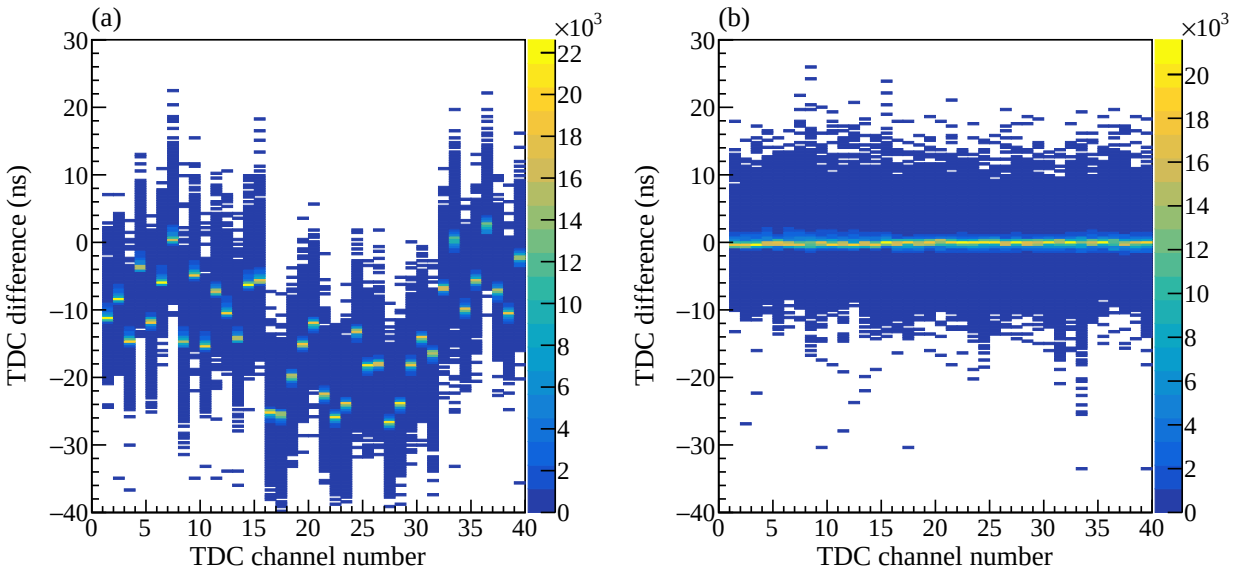

Figure 4.14: TDC data taken with a pulse generator. The y-axis shown the difference between the TDC value at each channel and that at Ch. 0. (a) Before the offset correction. (b) After the offset correction.

4.6.2 TDC reference determination

The V1190 TDC module needs a timing reference channel because V1190 has a jitter with width of about 25 ns, and we usually use the same signal as the trigger signal for the reference. However, because the trigger signal was generated using the timing signals, the trigger signal had different offset depending on the channel that generated the trigger. Therefore, it was necessary to determine the TDC reference by analysis using the TDC data of each channel.

We decided to use the TDC value closest to the average of TDC values as a reference. In order to reduce the accidental hits, we discarded these hits using a statistical measure, the interquartile range (IQR). The IQR is calculated by $Q_3 - Q_1$, where the Q_1 and Q_3 denote the first and third quartiles, respectively. Data below $Q_1 - 1.5 \times \mathrm{IQR}$ or above $Q_3 + 1.5 \times \mathrm{IQR}$ are typically identified as outliers. Also in our case, outliers were identified with the same restriction, and the average of the TDC values was calculated excluding outliers. Since we were interested in the multi-α particle events, the TDC reference was selected from particles tagged as the FR hit and identified as α or multi-PID particles.

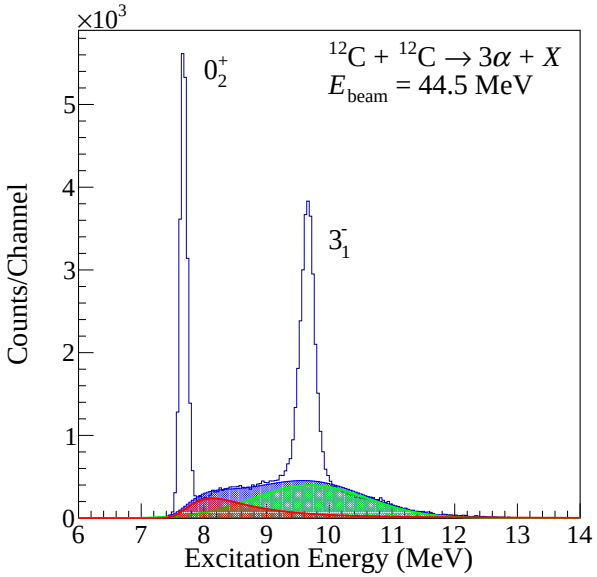

Figure 4.15: Excitation-energy spectrum of ^{12}C reconstructed from the detected 3α particles in the $^{12}C + ^{12}C \rightarrow 3\alpha + X$ reaction at E_{beam} = 44.5 MeV. The green spectrum shows the Gaussian function representing the broad states in ^{12}C whereas the red spectrum is the Landau distribution function representing the other backgrounds. The sum of two spectra is also shown by the blue spectrum.

4.7 Reconstruction of kinematics

Assuming that the reaction point was at the center of the target, we obtained 4-vectors of decay particles. In the reconstruction of kinematics, only decay particles identified not to be alpha particles were deliberately excluded from the analysis in order to prevent loss of low-energy alpha particles.

4.7.1 Invariant mass analysis

In the event involving 3α particles emitted from the same ^{12}C nucleus, these particles were boosted along the velocity of the center of mass, and likely to hit a single Si segment. In order to identify the decay events via the 3α-condensed state in ^{12}C, we reconstructed the invariant mass of the 3α particles detected in the single Si segment, and determined the excitation energy of the parent ^{12}C. Figure 4.15 shows the excitation-energy spectrum of ^{12}C reconstructed from the detected 3α particles in the $^{12}C + ^{12}C \rightarrow 3\alpha + X$ reaction at E_{beam} = 44.5 MeV. In Fig. 4.15, the two prominent peaks due to the 0_2^+ state at E_x = 7.65 MeV and the 3_1^- state at E_x = 9.64 MeV are observed on the continuous spectrum due to the broad 0_3^+ and 2_2^+ states in ^{12}C [23] and the other backgrounds. The backgrounds were mainly originated from events in which the PID was incorrect, while contribution from accidental coincidence events was negligible. The continuous

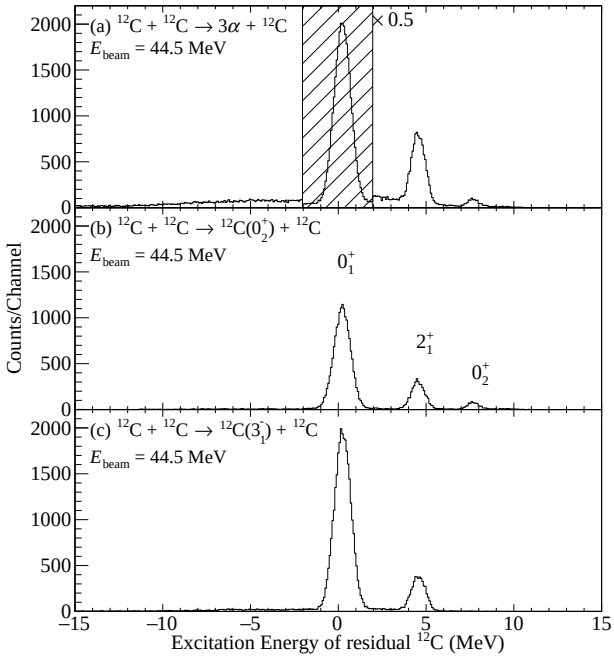

Figure 4.16: Excitation-energy spectra of the residual ^{12}C for (a) ^{12}C + ^{12}C → 3α + ^{12}C, (b) ^{12}C + ^{12}C → ^{12}C(0^+_2) + ^{12}C, and (c) ^{12}C + ^{12}C → ^{12}C(3^-_1) + ^{12}C reactions. The spectrum in the hatched area is downscaled by a factor of 0.5.

spectrum was fitted by the combination of a Gaussian function representing the broad ^{12}C states and a Landau distribution function representing the backgrounds. The green and red spectra show the Gaussian and Landau distribution functions, respectively, whereas the blue spectrum is the sum of them. The parameters of the two functions were determined to reproduce the experimental spectrum. The yields for the ^{12}C + ^{12}C → ^{12}C(0^+_2) + X and ^{12}C + ^{12}C → ^{12}C(3^-_1) + X reactions were estimated by subtracting the blue spectrum from the measured spectrum.

4.7.2 Missing mass analysis

In addition, in order to exclusively identify reaction channels, we determined the excitation energy of the residual ^{12}C nucleus by estimating the missing mass of the reaction from momenta of the detected 3α particles. Figure 4.16(a) shows the excitation-energy spectra of the residual ^{12}C for all the events presented in Fig. 4.15, whereas Figs. 4.16(b) and (c) are the excitation-energy spectra for the selected events in which the excitation energy in Fig. 4.15 is close to those of the 0^+_2 and 3^-_1 states, respectively. Although a little continuous background was observed below the prominent 3 peaks corresponding to the 0^+_1, 2^+_1, and 0^+_2 states of the residual ^{12}C nuclei in Fig. 4.16(a), there was almost no continuum background in

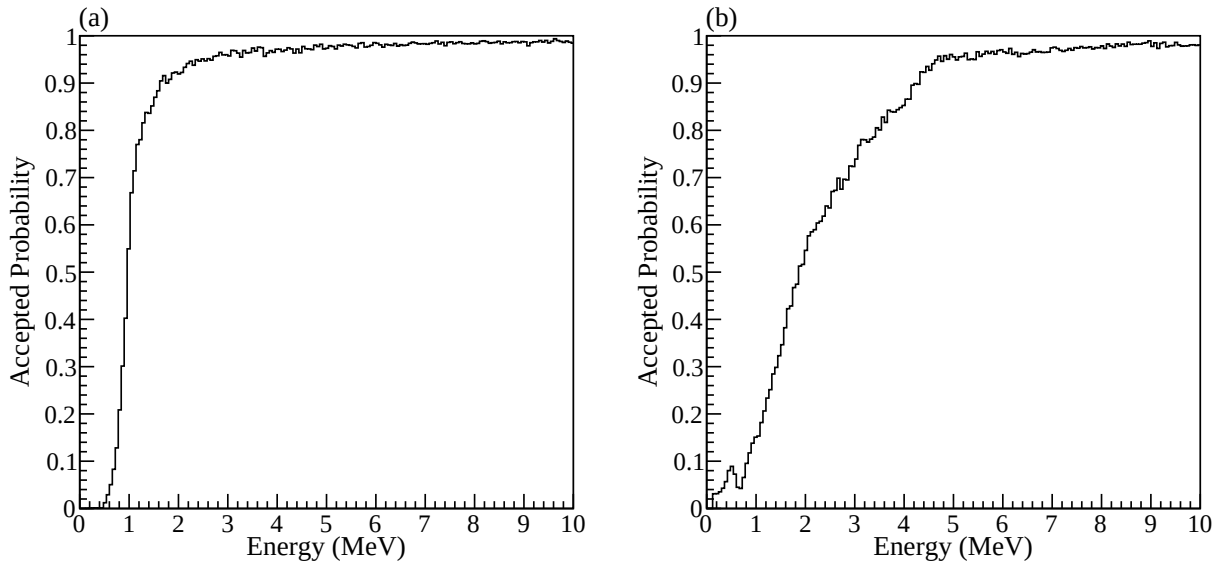

Figure 4.17: Accepted (not ignored) probability as the function of rear-side energies. (a) Typical channel and (b) another channel under the bias shortage.

Figs. 4.16(b) and (c) after the invariant masses of the detected 3α particles were selected. The yields for the $^{12}C + {}^{12}C \rightarrow {}^{12}C(0^+_2) + {}^{12}C(0^+_1)$, $^{12}C(0^+_2) + {}^{12}C(2^+_1)$, and $^{12}C(0^+_2) + {}^{12}C(0^+_2)$ reactions were determined from Fig. 4.16(b).

4.8 Efficiency estimation

To estimate the detection efficiency for each reaction channel, the Monte Carlo simulations were performed in the following three steps. In all the steps of the simulation, we assumed that two ^{12}C nuclei were emitted from the $^{12}C + {}^{12}C$ reaction. If the ^{12}C nucleus was excited to the 0^+_2 or 3^-_1 states, it would sequentially decayed to 3α particles via the $\alpha + {}^8Be$(g.s.) channel. The two-body decay in each step isotropically occurred in the rest frame of the parent nucleus. The simulations took into account the energy resolution of SAKRA, and recorded the generated events when the multiplicity was larger than 2, similar to the experimental trigger condition. In addition, to reflect the effect of bias shortages (described in Sec. 3.5), generated particles were ignored according to the energy- and channel-dependent probabilities obtained from the experimental data. Examples of the probability are shown in Fig. 4.17. We analyzed the simulated data in the same manner as the experimental data, and estimated the efficiency of 3α detection and ^{12}C reconstruction for each reaction channel.

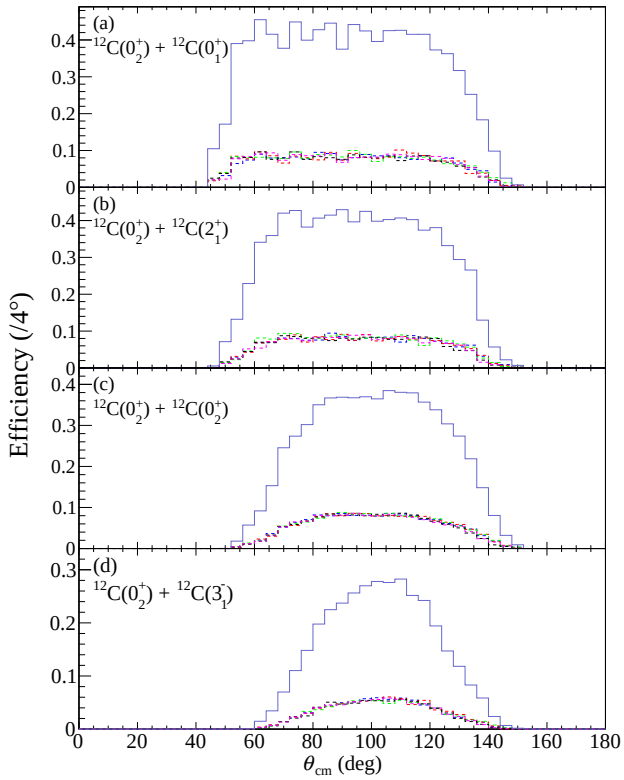

Figure 4.18: Efficiency at each angular bin for $^{12}C + {}^{12}C \rightarrow$ (a) $^{12}C(0^+_2) + {}^{12}C(0^+_1)$, (b) $^{12}C(0^+_2) + {}^{12}C(2^+_1)$, (c) $^{12}C(0^+_2) + {}^{12}C(0^+_2)$, and (d) $^{12}C(0^+_2) + {}^{12}C(3^-_1)$ reactions at $E_{beam} = 44.5$ MeV. The efficiency using all 5 segments and each single segment of SAKRA is shown by solid and dashed lines.

Step 1: Efficiency at each angle for individual reaction channels

In the first step, all the solid angles were divided into polar angular bins with a width of $\theta_{cm} = 4.0°$, and the efficiency for individual reaction channels at every beam energy was estimated in each angular bin in order to determine the differential cross section. We assumed that the differential cross section was constant within one angular bin. For example, we show the efficiency for $^{12}C + {}^{12}C \rightarrow {}^{12}C(0^+_2) + {}^{12}C(0^+_1)$, $^{12}C(0^+_2) + {}^{12}C(2^+_1)$, $^{12}C(0^+_2) + {}^{12}C(0^+_2)$, and $^{12}C(0^+_2) + {}^{12}C(3^-_1)$ reactions at $E_{beam} = 44.5$ MeV in Figs. 4.18(a)–(d). The efficiency using all 5 segments and each single segment of SAKRA is shown by the solid and dashed lines.

In each reaction channel, experimental data at beam energies where the maximum value of the efficiency at each angular bin using reliable segments of SAKRA was below 5% were excluded from the analysis due to large statistical errors. If the number of the reliable segments was 4 or 3, this threshold was downscaled to 4% or 3%. Figure 4.19 shows the maximum value of the efficiency at each angular bin as a function of E_{cm}. The parent ^{12}C that decays into 3α particles is in the (left) 0^+_2 and (right) 3^-_1 states, and the residual ^{12}C

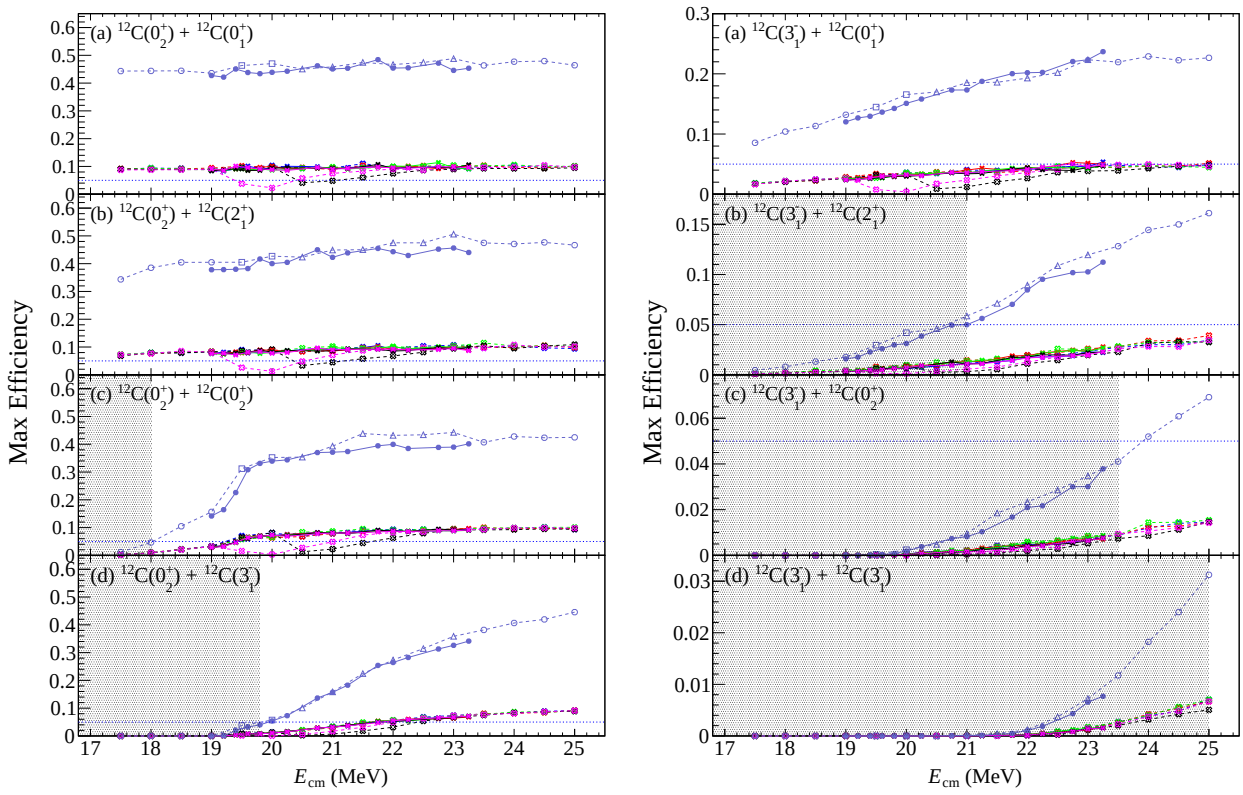

Figure 4.19: Maximum value of the efficiency at each angular bin as a function of $E_{\rm cm}$. The parent ^{12}C that decays into 3α particles is in the (left) 0^+_2 and (right) 3^-_1 states, and the residual ^{12}C is in the (a) 0^+_1, (b) 2^+_1, (c) 0^+_2, and (d) 3^-_1 states, respectively. The dashed lines and open symbols correspond to the results from the first beam-time period, and the solid lines and solid symbols represent those from the second beam-time period. The cross symbols represent the results using each single segment of SAKRA. The circle, rectangle, and triangle symbols denote that the number of the used reliable segments was 5, 4, and 3, respectively. The beam energies in the hatched areas were excluded from the analysis.

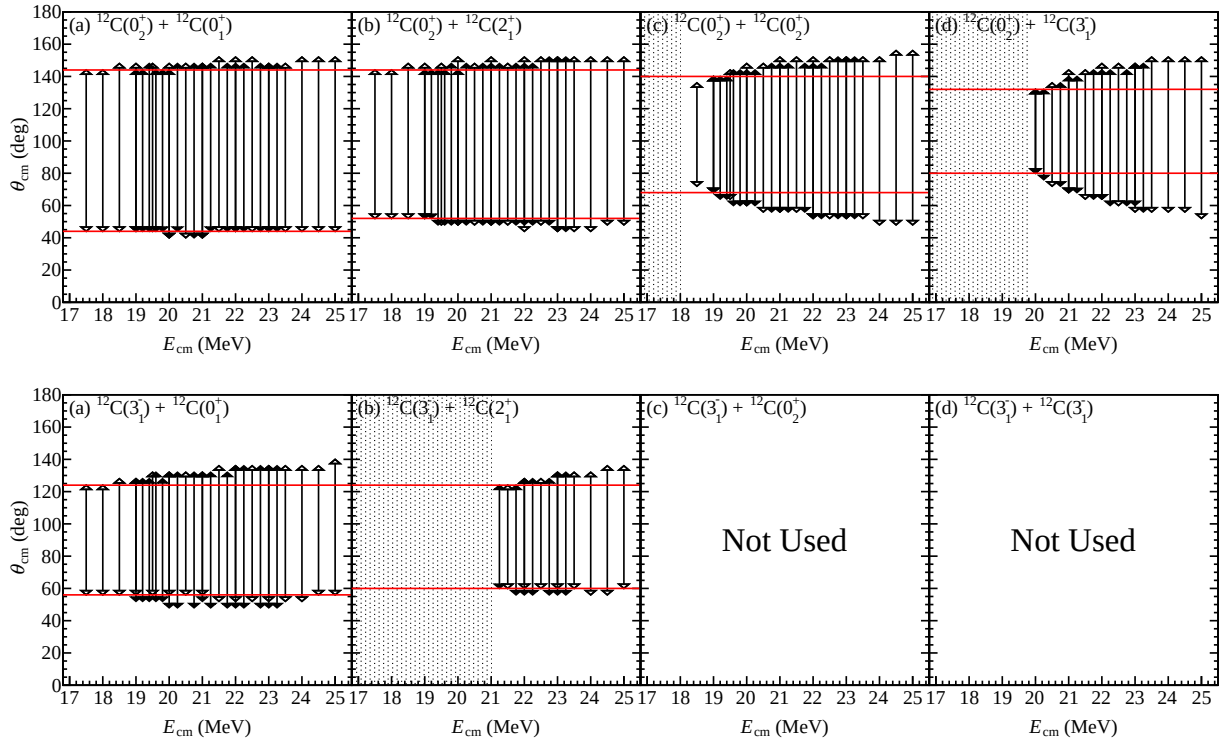

Figure 4.20: Angular acceptance for each reaction channel at each beam energy. The parent ^{12}C that decays into 3α particles is in the (top) 0^+_2 and (bottom) 3^-_1 states, and the residual ^{12}C is in the (a) 0^+_1, (b) 2^+_1, (c) 0^+_2, and (d) 3^-_1 states, respectively. The open arrows correspond to the results from the first beam-time period, and the solid arrows represent those from the second beam-time period. The red-horizontal lines represent the angular acceptance of each reaction channel.

is in the (a) 0^+_1, (b) 2^+_1, (c) 0^+_2, and (d) 3^-_1 states, respectively. The dashed lines and open symbols correspond to the results from the first beam-time period, and the solid lines and solid symbols represent those from the second beam-time period. The cross symbols represent the results using each single segment of SAKRA. The circle, rectangle, and triangle symbols denote that the number of the used reliable segments was 5, 4, and 3, respectively. For comparison with the threshold value of 5%, which is shown by the dotted-horizontal lines, the maximum values in the measurement with the number of the reliable segments was 4 or 3 are multiplied by a factor of 5/4 or 5/3. The beam energies in the hatched areas were excluded from the analysis. With this restriction, the ^{12}C(3^-_1) + ^{12}C(3^-_1) channel was excluded at all beam energies, and the ^{12}C(3^-_1) + ^{12}C(0^+_2) channel was accepted only at a few beam energies. Considering this low efficiency, we decided to exclude the ^{12}C(3^-_1) + ^{12}C(0^+_2) channel at all beam energies.

The angular acceptance was determined to include only those angular bins where their efficiency exceeded 1%. Figure 4.20 shows the angular acceptance of each reaction channel at each beam energy. The

red-horizontal lines in Fig. 4.20 represent the angular acceptance for each reaction channel. In general, the angular acceptance in the center-of-mass frame declines as the beam energy decreases because the decay particles are emitted over a wider angular range in the laboratory frame at the lower center-of-mass energy. Thus the angular acceptance of each reaction channel was determined at the lowest beam energy. It should be noted that the $^{12}C(0^+_2)+^{12}C(0^+_2)$ reaction at E_{cm} = 18.5 MeV was excluded in order to enlarge the angular acceptance for this reaction. For example, the angular acceptance for the $^{12}C + ^{12}C \rightarrow ^{12}C(0^+_2) + ^{12}C(0^+_1)$, $^{12}C(0^+_2) + ^{12}C(2^+_1)$, and $^{12}C(0^+_2) + ^{12}C(0^+_2)$ reactions were $44^\circ \leq \theta_{cm} \leq 144^\circ$, $52^\circ \leq \theta_{cm} \leq 144^\circ$, and $68^\circ \leq \theta_{cm} \leq 140^\circ$, respectively.

Step 2: Averaged efficiency over the angular acceptance for the exclusive reactions

In the second step, the averaged efficiency over the angular acceptance $\Delta\Omega_{cm}$ for individual reaction channels was estimated at each beam energy. The second simulation was conducted using the measured angular distributions of the differential cross sections for the individual reaction channels obtained in the first step. Figure 4.21 shows as an example the measured angular distribution of the differential cross sections for the $^{12}C(0^+_2) + ^{12}C(0^+_1)$ channel at E_{cm} = 25.0 MeV and the simulation data generated based on the measured angular distribution. In the simulation, the differential cross sections between the data points were estimated by the spline interpolation functions, and the experimental data outside the angular acceptance decided in the first step were also used to determine the spline interpolation functions.

The angular averaged efficiency is shown in Fig. 4.22. For comparison between beam energies, the efficiency for the measurements with the 3 or 4 reliable segments are multiplied by a factor of 5/4 or 5/3, similar to Fig. 4.19. At some energies, even though these energies were not excluded in the previous step, the efficiency for the $^{12}C(0^+_2)+^{12}C(3^-_1)$ channel was 0 because there was no yield for this channel at these energies in our experiments. The efficiency of all reaction channels depends almost smoothly on E_{cm}, whereas some fluctuations or dips are seen in the $^{12}C(0^+_2) + ^{12}C(0^+_1)$ and $^{12}C(0^+_2) + ^{12}C(2^+_1)$ channels. This is considered to depend on whether a peak of the angular distribution overlaps the boundary of the angular acceptance.

The cross sections integrated over the angular acceptances were obtained by using the total yields determined from Fig. 4.16(b) and the angular averaged efficiency. For comparing the cross sections of various reaction channels with the different angular acceptances, the obtained cross sections were normalized by a factor of $4\pi/\Delta\Omega_{cm}$.

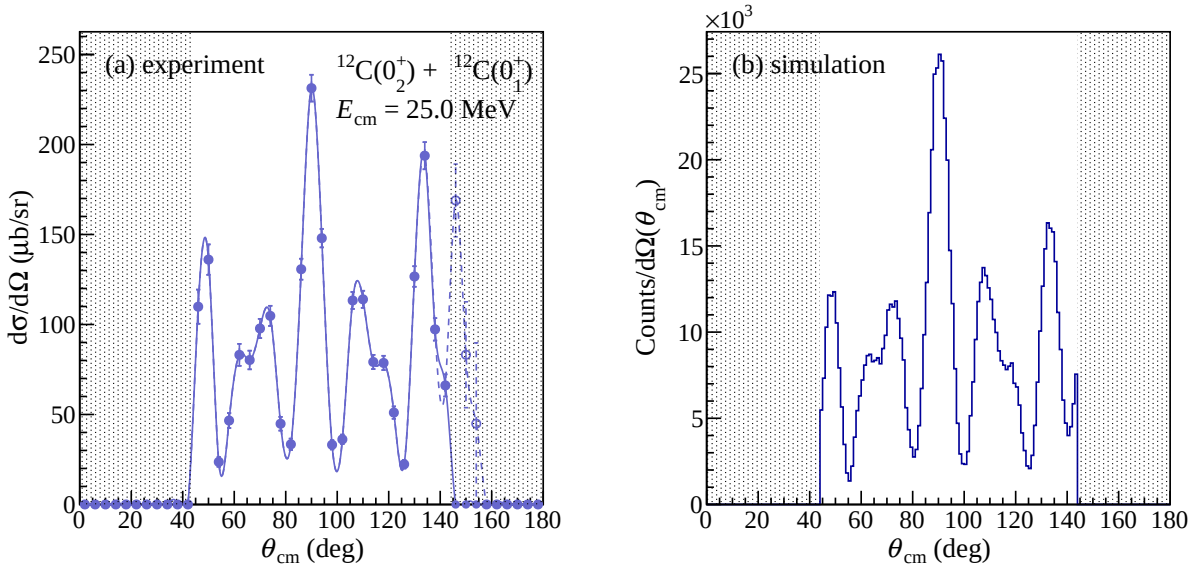

Figure 4.21: Example of (a) the measured angular distribution of the differential cross sections and (b) the generated simulation data. The hatched areas show the outside of the angular acceptance, and the open circles in (a) represent the differential cross sections outside the angular acceptance. The solid and dashed lines in (a) show the spline interpolation functions without and with the differential cross sections outside the acceptance.

Step 3: Averaged efficiency over all the solid angles for the inclusive reactions

In the third step, the averaged efficiency over all the solid angles for the inclusive $^{12}C + ^{12}C \rightarrow ^{12}C(0_2^+, 3_1^-) + X \rightarrow 3\alpha + X$ reactions was estimated. In this simulation, the 0_1^+, 2_1^+, and 0_2^+ states were taken into account as the final states of the residual ^{12}C nuclei. The population of the residual states was determined from the exclusive cross sections for the various reaction channels obtained in the second step. However, unlike in the second step, the angular distributions of the differential exclusive cross sections were assumed to be isotropic, because the angular acceptances $\Delta\Omega_{cm}$ were different between the reaction channels. The averaged efficiency over all the solid angles for the inclusive reactions is shown in Fig. 4.23. In Fig. 4.23(b), a kink structure is seen at $E_{cm} \sim 21.0$ MeV because the $^{12}C(3_1^-) + ^{12}C(2_1^+)$ channel was taken into account only at beam energies larger than $E_{cm} = 21.0$ MeV, but the energy dependence of the efficiency for the $^{12}C(3_1^-) + X$ channel is monotonous, and in Fig. 4.23(a), the efficiency for the $^{12}C(0_2^-) + X$ channel is almost constant. Finally, the total cross sections of the inclusive reactions were obtained by using the yields estimated from Fig. 4.15 and the averaged efficiency over all the solid angles.

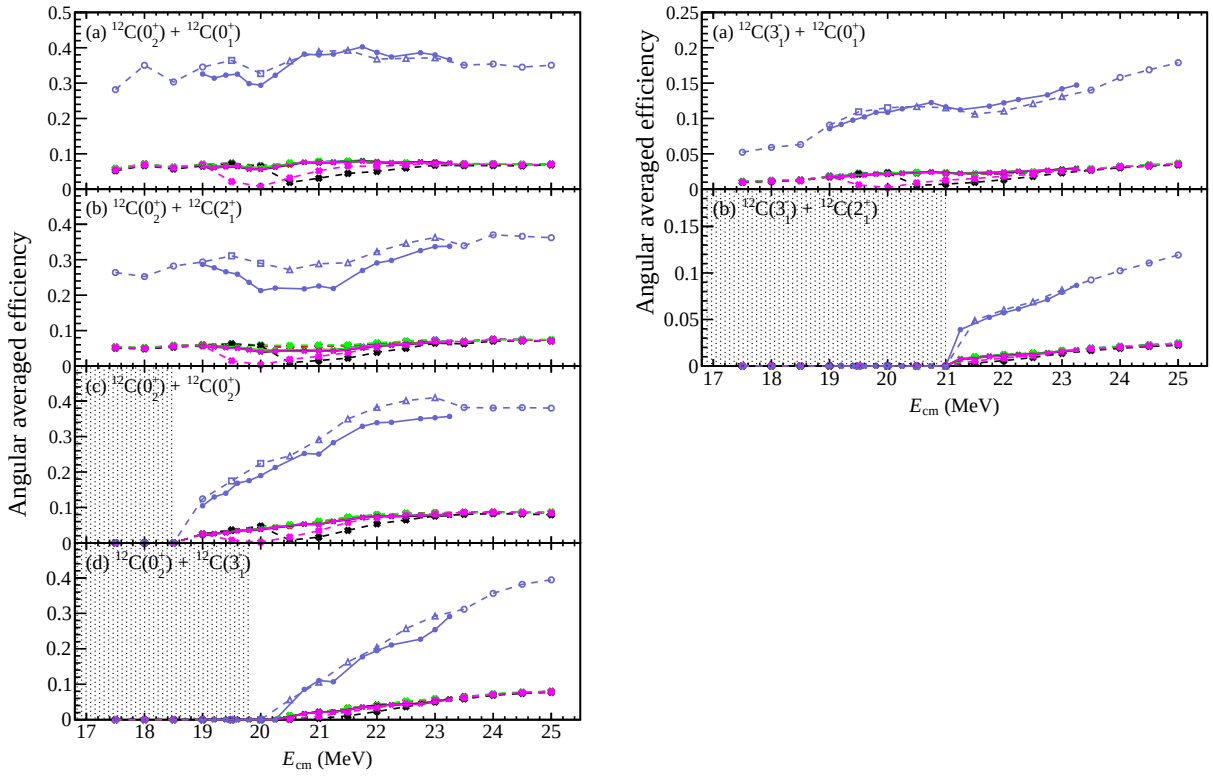

Figure 4.22: Angular averaged efficiency. The reaction channels in each panel and the notation of the symbols are same as Fig. 4.19. The beam energies in the hatched areas were excluded from the analysis. The $^{12}C(3^-_1) + {}^{12}C(0^+_2)$ and $^{12}C(3^-_1) + {}^{12}C(3^-_1)$ channels were omitted because these channels were not used in the analysis.

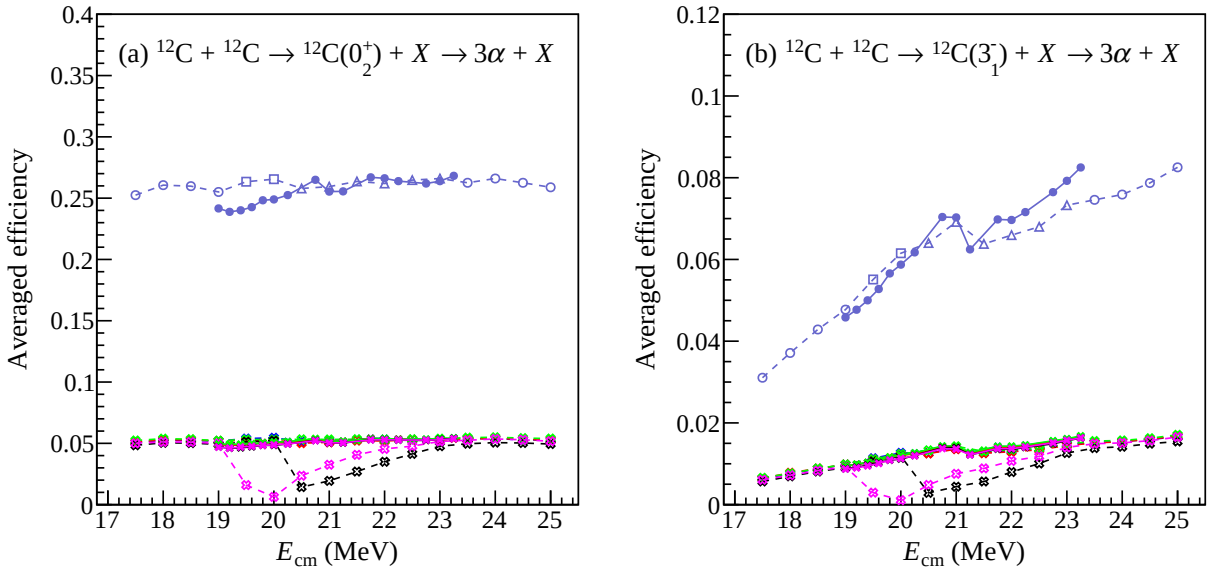

Figure 4.23: Averaged efficiency over all the solid angles for the inclusive (a) ^{12}C + ^{12}C → ^{12}C(0^+_2) + X → 3α + X and (b) ^{12}C + ^{12}C → ^{12}C(3^-_1) + X → 3α + X reactions. The notation of the symbols are same as Fig. 4.19.

4.9 Cross section for the ^{12}C + ^{12}C elastic scattering

In order to evaluate the accuracy of the present analysis, we compared the differential cross sections for the ^{12}C + ^{12}C elastic scattering at $\theta_{cm} = 90°$ with the previous result reported in Ref. [58] shown in Fig. 4.24. In our experiment, because the physics measurement was conducted with the trigger condition of Multi. ≥ 3, the ^{12}C + ^{12}C elastic scattering could not be measured in the physics run. Thus, we analyzed the data from the minimum bias measurement for obtaining the cross sections for the ^{12}C + ^{12}C elastic scattering. If two detected particles were identified as ^{12}C and they satisfied the two-body kinematics, the event was identified as the ^{12}C + ^{12}C elastic scattering. In case of the elastic scattering at $\theta_{cm} = 90°$, both ^{12}C nuclei are scattered on the same angle of $\theta_{cm} = 90°$. Therefore, considering the angular straggling, we selected the events which both ^{12}C nuclei were scattered on $85° \leq \theta_{cm} \leq 95°$. Figure 4.25 shows the present result of the differential cross sections for the ^{12}C + ^{12}C elastic scattering at $\theta_{cm} = 90°$. Comparing Figs. 4.24 and 4.25, the energy dependence of the cross sections, for example two peak structure around $E_{cm} = 20$ MeV, is similar between the present and previous result, but the absolute value of the present result is about 10 times smaller than that of the previous result.

We considered that this inconsistent result was caused by excessive trigger rate during the minimum bias measurements. Figure 4.26 shows the event time stamp distribution at (a) minimum bias measurement (Trig.

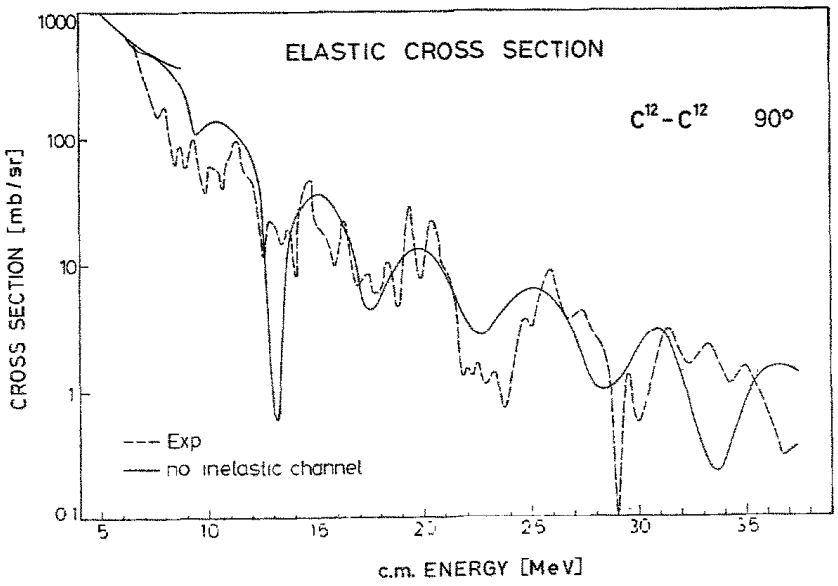

Figure 4.24: Previous result of the differential cross sections for the $^{12}C+^{12}C$ elastic scattering at $\theta_{cm} = 90°$. Taken from Fig. 7 in Ref. [58].

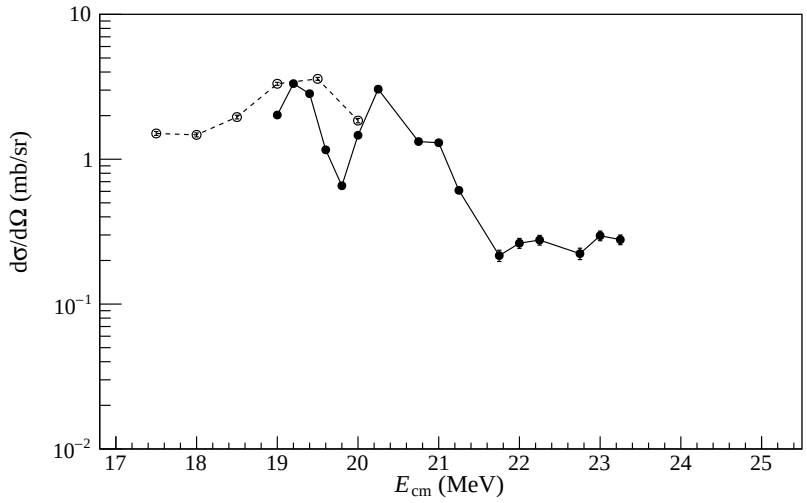

Figure 4.25: Present result of the differential cross sections for the $^{12}C + ^{12}C$ elastic scattering at $\theta_{cm} = 90°$. The notation of the open and solid symbols is same as Fig. 4.19.

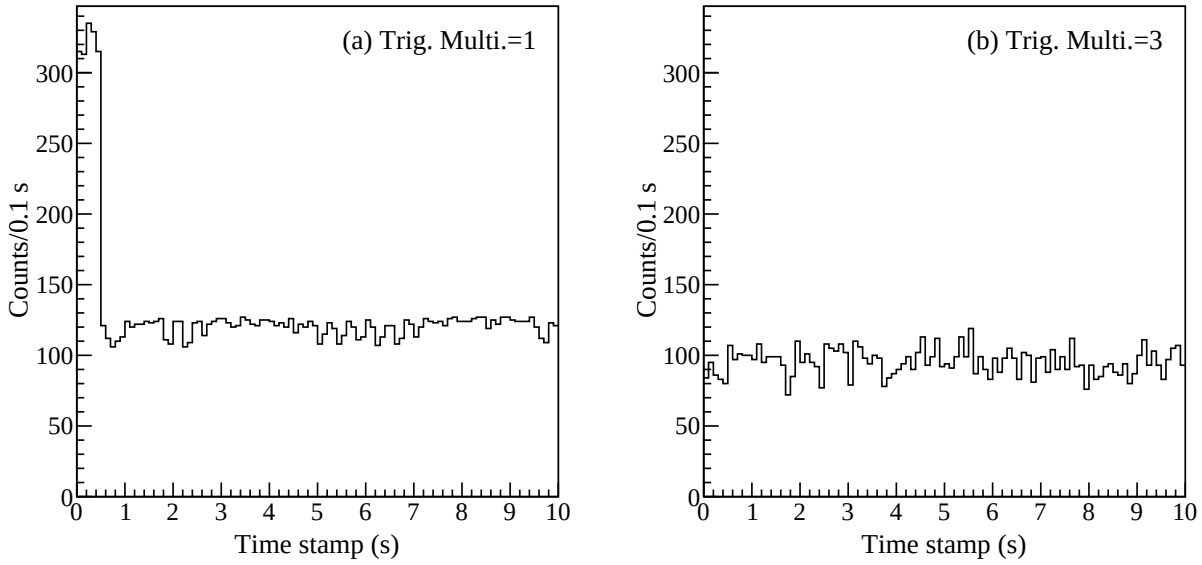

Figure 4.26: Event time stamp distribution at the (a) minimum bias measurement (Trig. Multi. = 1) and (b) physics measurement (Trig. Multi. = 3).

Multi. = 1, see Sec. 3.4.1) and (b) physics measurement (Trig. Multi. = 3). In Fig. 4.26(a), the event rate was approximately 300 counts/0.1 s for the first 0.5 seconds, then suddenly dropped to about 100 counts/0.1 s and was limited to this event rate. This limitation was due to the V1730 busy, which was issued when the data buffer of V1730 was full. For the minimum bias measurements, the event rate was so high that the data transfer rate of V1730 was insufficient, and V1730 could not maintain data acquisition without dead time. On the other hand, in case of the physics measurement shown in Fig. 4.26(b), these drop-off in the event rate did not occur. Therefore, we concluded that this discrepancy was peculiar to the minimum bias measurements and that normalization based on the cross section of the elastic scattering was not necessary for the results of the physics measurements.

Chapter 5

Result and discussion

5.1 Inclusive cross section

Figure 5.1 shows the inclusive cross sections for the $^{12}C + ^{12}C \rightarrow ^{12}C(0^+_2, 3^-_1) + X \rightarrow 3\alpha + X$ reactions as a function of the center-of-mass energy E_{cm} of the initial $^{12}C + ^{12}C$ system. The open symbols correspond to the results from the first beam-time period, and the solid symbols represent those from the second beam-time period. The cross symbols on the dotted line denote the cross sections acquired with each single segment of SAKRA. The cross sections acquired by using the reliable segments of SAKRA at each beam energy are also shown. The circle, rectangle, and triangle symbols on the solid line indicate that the number of the used segments was 5, 4, and 3, respectively. The vertical error bars include the statistical errors only. It was found that the absolute values of the cross sections systematically fluctuated among the five segments of SAKRA although the energy dependence of the cross section obtained by each single segment was similar. Therefore, we took the cross sections with all reliable segments of SAKRA as the result values and treated these fluctuations among the single segments as the systematic uncertainties. In Fig. 5.2, we show the results of the inclusive cross sections as the symbols and the systematic uncertainties as the gray bands. The horizontal axis of Fig. 5.2 takes into account the energy loss of the ^{12}C beam within the target at each beam energy, and this ambiguity is shown as the horizontal error bar.

A relatively narrow peak structure is observed at $E_{cm} = 19.4$ MeV in both Figs. 5.2(a) and (b), while the broad structure is observed at $E_{cm} = 20.0$–22.0 MeV in Fig. 5.2(a) only. It should be noted that the narrower state at $E_{cm} = 19.4$ MeV had been previously observed in indirect measurements of the 3α emission from the $^{12}C + ^{12}C$ reaction [40] as shown in Fig. 1.10. The present work showed that this state decayed to the 3α particles via the 0^+_2 and 3^-_1 states in ^{12}C by the direct measurement. This is strong evidence that this narrower state is a multi-α cluster state because the 0^+_2 and 3^-_1 states are known as the spatially developed 3α-cluster states. This 19.4-MeV state actually couples with the 0^+_2 state as the 3α-condensed state, and its

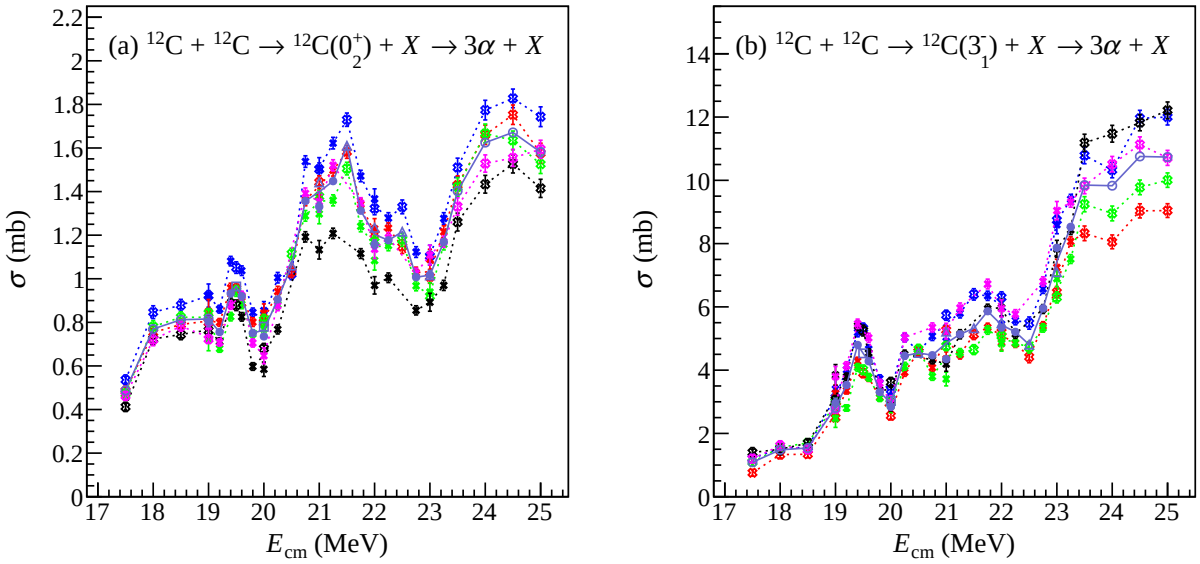

Figure 5.1: Inclusive cross sections for the (a) ^{12}C + ^{12}C → ^{12}C(0^+_2) + X → 3α + X and (b) ^{12}C + ^{12}C → ^{12}C(3^-_1) + X → 3α + X reactions. The open symbols corresponding to the results from the first beam-time period, and the solid symbols represent those from the second beam-time period. The cross symbols on the dotted line denote the cross sections acquired with each single segment of SAKRA. The circle, square, and triangle symbols on the solid line indicate the cross sections obtained using the 5, 4, and 3 reliable segments, respectively. The dotted and solid lines are shown to guide the eye.

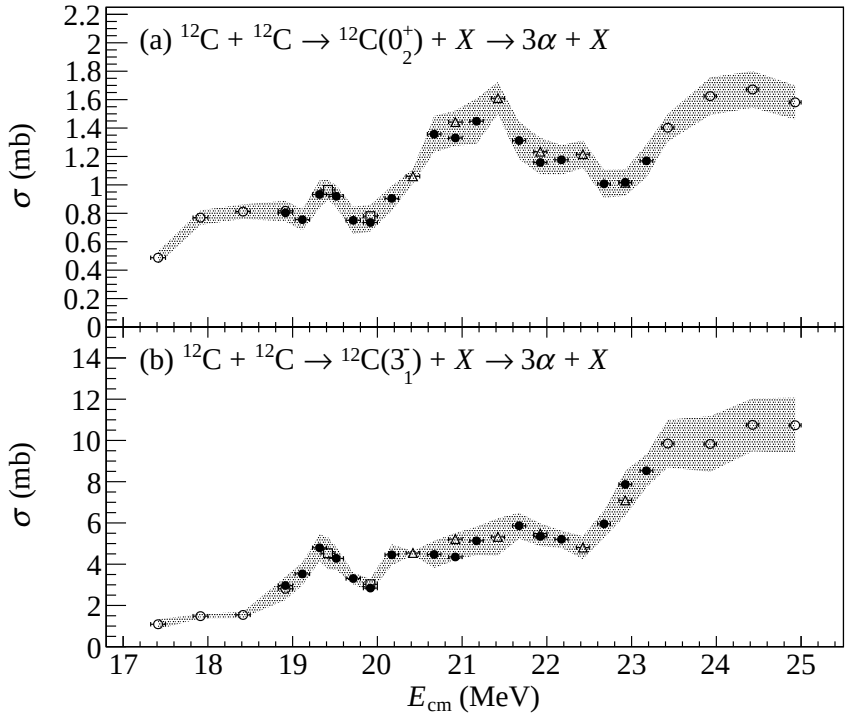

Figure 5.2: Inclusive cross sections for the (a) ^{12}C + ^{12}C → ^{12}C(0^+_2) + X → 3α + X and (b) ^{12}C + ^{12}C → ^{12}C(3^-_1) + X → 3α + X reactions. The notation of the symbols is same as Fig. 5.1.

energy of $E_{\mathrm{cm}} = 19.4$ MeV, corresponding to the excitation energy of $E_x = 33.3$ MeV in ^{24}Mg, is close to the theoretical value of the 6α-condensed state predicted in Ref. [25]. It is, therefore, reasonable to consider this state as a candidate for the 6α-condensed state. However, we could not determine the spin and parity of this candidate in this analysis.

5.2 Exclusive cross section

As in Sec. 5.1, the exclusive cross sections acquired by using each single segment or the reliable segments of SAKRA are shown in Fig. 5.3, and the results of the exclusive cross sections are shown in Fig. 5.4 along with the gray bands of the systematic uncertainties. Figures 5.4(a), (b), and (c) show the exclusive cross sections for the $^{12}\mathrm{C} + {}^{12}\mathrm{C} \rightarrow {}^{12}\mathrm{C}(0^+_2) + {}^{12}\mathrm{C}(0^+_1)$, $^{12}\mathrm{C}(0^+_2) + {}^{12}\mathrm{C}(2^+_1)$, and $^{12}\mathrm{C}(0^+_2) + {}^{12}\mathrm{C}(0^+_2)$ reactions, respectively, as in Fig. 5.3. The energy dependence of the measured cross sections exhibits different behavior for each reaction channel. This indicates the successful separation of the reaction channels in the present analysis.

The peak at $E_{\mathrm{cm}} = 19.4$ MeV, which is a candidate for the 6α-condensed state, is observed in the $^{12}\mathrm{C}(0^+_2)+{}^{12}\mathrm{C}(0^+_1)$ channel in Fig. 5.4(a), but is not in the $^{12}\mathrm{C}(0^+_2)+{}^{12}\mathrm{C}(0^+_2)$ channel in Fig. 5.4(c). This result appears to contradict the expectation that the overlap of the wave functions between the 6α-condensed state and $^{12}\mathrm{C}(0^+_2)+{}^{12}\mathrm{C}(0^+_2)$ should be larger rather than that between the 6α-condensed state and $^{12}\mathrm{C}(0^+_2)+{}^{12}\mathrm{C}(0^+_1)$. A plausible explanation of this result is that the $^{12}\mathrm{C}(0^+_2)+{}^{12}\mathrm{C}(0^+_2)$ channel is hindered by the Coulomb barrier due to the low decay energy as pointed out in Ref. [39].

A broad peak is observed around $E_{\mathrm{cm}} = 22.5$ MeV in the cross-section spectrum for the $^{12}\mathrm{C} + {}^{12}\mathrm{C} \rightarrow {}^{12}\mathrm{C}(0^+_2) + {}^{12}\mathrm{C}(0^+_2)$ reaction shown in Fig. 5.4(c). This energy corresponds to the excitation energy of 36.4 MeV in ^{24}Mg. This broad state ought to be a multi-α cluster state as well as the narrow state found at $E_{\mathrm{cm}} = 19.4$ MeV. Because the $^{12}\mathrm{C}(0^+_2) + {}^{12}\mathrm{C}(0^+_2)$ channel should be strongly coupled with the 6α-condensed state, this broad state should be akin to the 6α-condensed state. This state is inferred to be an excited state of the 6α-condensed state such as the 2^+_2 and 4^+_1 states in ^{12}C [24] since its excitation energy is 3.1 MeV higher than the theoretical value of the 6α-condensed state [25]. In the ^{12}C case, the excited states of the 3α-condensed state with $J^\pi = 2^+$ and 4^+ were theoretically predicted at 1.4 and 3.5 MeV above the 3α-condensed state [24], and their experimental counterparts were reported in Refs. [23, 59, 60].

5.2.1 Angular distribution of the differential cross sections

To investigate the spins and parities of the observed states, the angular distributions of the differential cross sections were analyzed. In the present analysis, because the spins and parities of the two ^{12}C nuclei were

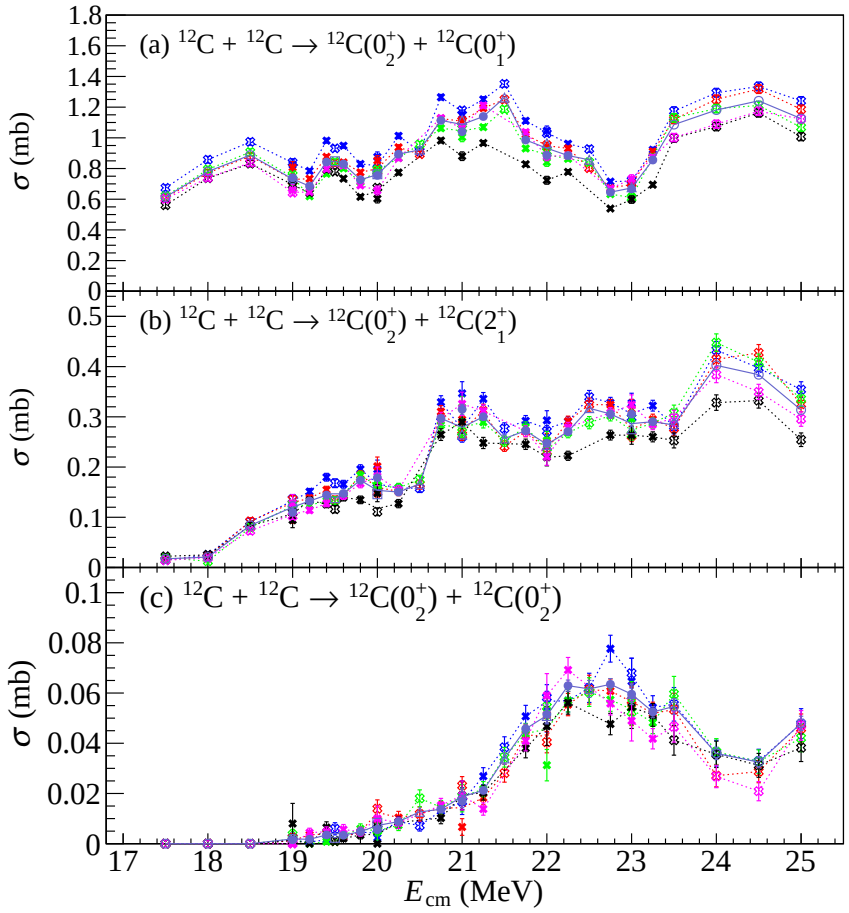

Figure 5.3: Exclusive cross sections for the ^{12}C + ^{12}C → (a) ^{12}C(0^+_2) + ^{12}C(0^+_1), (b) ^{12}C(0^+_2) + ^{12}C(2^+_1), and (c) ^{12}C(0^+_2) + ^{12}C(0^+_2) reactions with each single segment or the reliable segments of SAKRA. The notation of the symbols and the lines are same as Fig. 5.1.

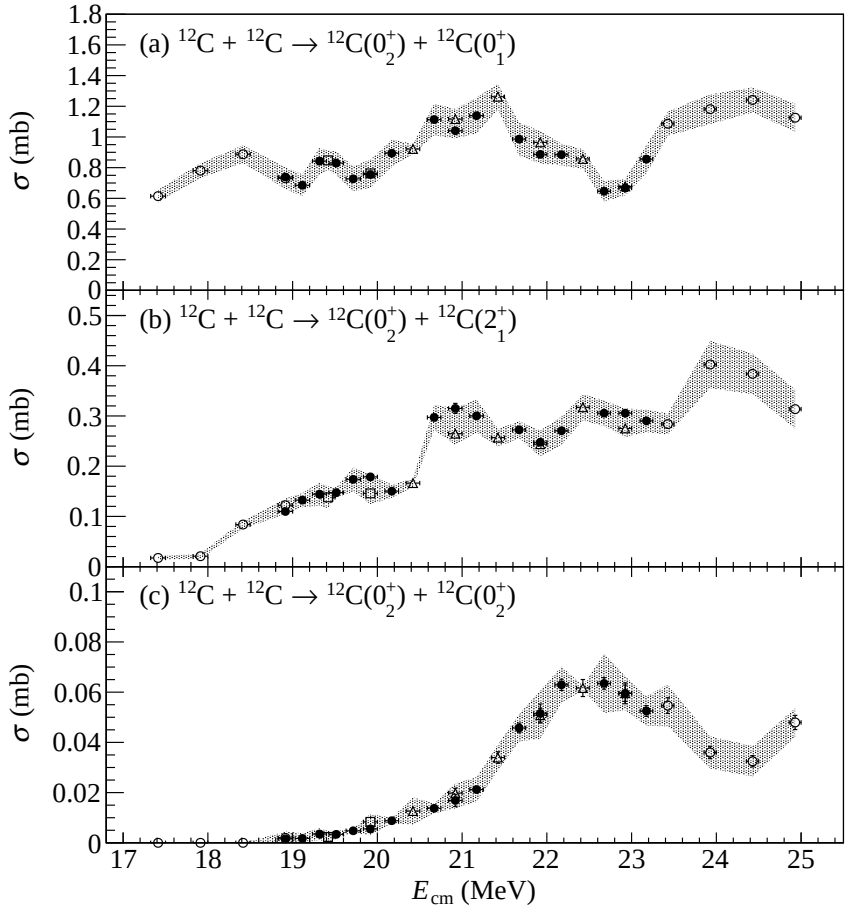

Figure 5.4: Exclusive cross sections for the ^{12}C + ^{12}C → (a) ^{12}C(0^+_2) + ^{12}C(0^+_1), (b) ^{12}C(0^+_2) + ^{12}C(2^+_1), and (c) ^{12}C(0^+_2) + ^{12}C(0^+_2) reactions. The notation of the symbols are same as Fig. 5.1.

determined to be 0^+ by the invariant mass analysis and the missing mass analysis, the relative angular momentum L between the two ^{12}C nuclei was equal to the angular momentum transfer ΔL. ΔL might be extracted from the angular distributions of the differential cross sections for the ^{12}C + ^{12}C reaction. Assuming an existence of 0^+ resonance state in ^{24}Mg, it is expected that the contribution of $L = 0$ component will be large at that resonant energy and the angular distribution might be constant with $\theta_{\rm cm}$.

In Ref. [36], the similar analysis was performed by fitting the angular distributions with the formula

$$\frac{d\sigma}{d\Omega}(\theta_{\rm cm}) = \left| \sum_l a_l e^{i\phi(l)} P_l(\cos\theta_{\rm cm}) \right|^2, \tag{5.1}$$

where $P_l(x)$ denotes the Legendre polynomial of order l, and the partial-wave amplitudes a_l and their phases $\phi(l)$ were the fit parameters. Following Ref. [36], we used this formula (5.1) as a fitting function. Figure 5.5 shows the angular distributions of the differential cross sections for the ^{12}C + ^{12}C $\rightarrow$ ^{12}C(0^+_2) + ^{12}C(0^+_1) reaction at the five energies around $E_{\rm cm}$ = 19.4 MeV as the symbols and the best-fit results as the red lines. The left and right panels of Fig. 5.5 show the fitting results using a single l value and multiple l values up to five, respectively. If the reaction process is classical two-body scattering, the angular distribution should be dominated by the grazing angular momentum $l_{\rm gr}$ given implicitly by

$$E = \frac{l_{\rm gr}(l_{\rm gr}+1)\hbar^2}{2\mu R_{\rm gr}^2} + \frac{Z_1 Z_2 e^2}{R_{\rm gr}}, \tag{5.2}$$

where $R_{\rm gr}$ is the sum of the nuclear radii, namely $r_0(A_1^{1/3} + A_2^{1/3})$. However, the experimental results varied irregularly with $E_{\rm cm}$ as shown in the left panels of Fig. 5.5, and these results may suggest that there exist complicated reaction processes. At $E_{\rm cm}$ = 19.4 MeV, its diffraction pattern is best fitted by the Legendre polynomial of order 8 although the enhancement of the diffraction amplitude at $\theta_{\rm cm} = 90^\circ$ is not reproduced. This result means that the cross section around $E_{\rm cm}$ = 19.4 MeV is dominated by the L = 8 component which is very close to the grazing angular moment of l_{gr} = 8.8, and it does not suggest the L = 0 component populating the 6α-condensed state with $J^\pi = 0^+$. This is due to the fact that contamination from continuous components was quite large as seen in Fig 5.4(a), and it obscures the L = 0 component even if the 19.4-MeV state is the 6α-condensed state. The enhancement of the differential cross section around $\theta_{\rm cm} = 90^\circ$ also indicates that the cross section around $E_{\rm cm}$ = 19.4 MeV is dominated by the continuous components with several multipolarities components because this enhancement is not reproduced with a single Legendre polynomial but only by introducing several partial waves. The best-fit results with Eq. (5.1) using up to five contributing partial waves (l = 0–8) are shown in the right panels of Fig. 5.5. The contribution from the L = 0 component was suggested at $E_{\rm cm}$ = 19.4 MeV, but its fraction was so small that we could not explicitly

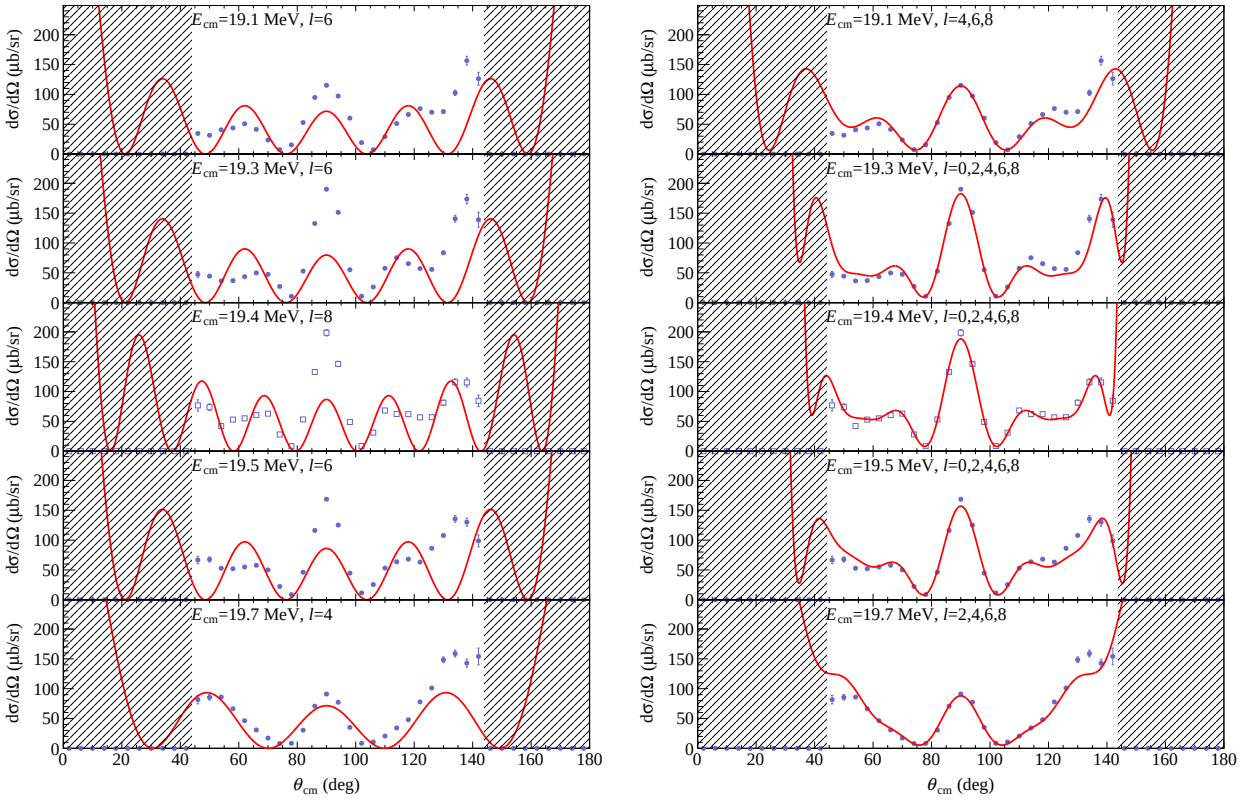

Figure 5.5: Angular distributions of the differential cross sections for the $^{12}C + {}^{12}C \rightarrow {}^{12}C(0_2^+) + {}^{12}C(0_1^+)$ reaction at the five energies around $E_{cm} = 19.4$ MeV shown as the symbols. The notation of the symbols are same as Fig. 5.1. The best-fit results with the single and multiple l values in Eq. (5.1) are shown by the red line in the left and right panels, respectively. The l values taken into account are indicated in each panel.

demonstrate the existence of the 0^+ resonance. Therefore, the subtraction of the continuous components is necessary to determine the spin and parity of the small peak on the continuous spectrum. However, its yield was statistically too poor to reliably perform this analysis, and we could not determine the spin and parity of this state.

On the other hand, as shown in Fig. 5.6, the angular distributions of the cross sections for the $^{12}C+^{12}C \rightarrow {}^{12}C(0_2^+) + {}^{12}C(0_2^+)$ reaction at the four energies around $E_{cm} = 22.5$ MeV were well represented with a single Legendre polynomial of order 4. It is reasonable to consider that the spin and parity of the broad state around $E_{cm} = 22.5$ MeV is 4^+. At lower energies, it is difficult to reproduce the angular distributions with a single Legendre polynomial due to the enhancement around $\theta_{cm} = 90°$. In the left panels of Fig. 5.7, the best-fit l value is indicated in each panel, and the squared Legendre polynomials of order 2 or 4 are plotted by the dashed or thin solid lines, respectively. The angular distributions at $E_{cm} = 21.4$, 21.7, and 21.9 MeV were fitted with Eq. (5.1) taking contributions from $l = 2$ and 4 into account as shown in the right panels of Fig. 5.7 by the thick solid lines. The angular distributions are better fitted by incorporating both the $L = 2$ and $L = 4$ components into account than by utilizing a single Legendre polynomial. It is a signature that a 2^+ state exists at the low-energy side of the broad state around $E_{cm} = 22.5$ MeV although the 2^+ resonance could not be separated from the broad 4^+ state in the energy spectrum in Fig. 5.4(c). These spin-parity assignments are consistent with our speculation that this broad structure is due to excited states of the 6α-condensed state. Considering the difference of the excitation energy and their spins and parities, these states might be excited states of the 6α-condensed state in similar to the 2_2^+ and 4_1^+ states in ^{12}C.

It is also essential to compare the present results with theoretical calculations for further clarification regarding the internal structures of the observed states. However no microscopic calculations for the 6α-condensed state are available at present. Therefore, theoretical efforts are strongly desired to properly interpret the present results and to establish the 6α-condensed state.

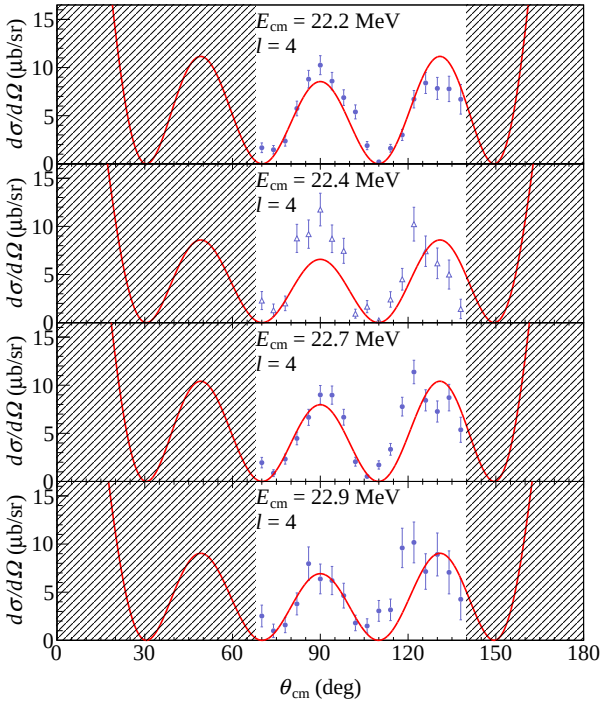

Figure 5.6: Same as Fig. 5.5, but for the $^{12}C + {}^{12}C \rightarrow {}^{12}C(0_2^+) + {}^{12}C(0_2^+)$ reaction around $E_{cm} = 22.5$ MeV.

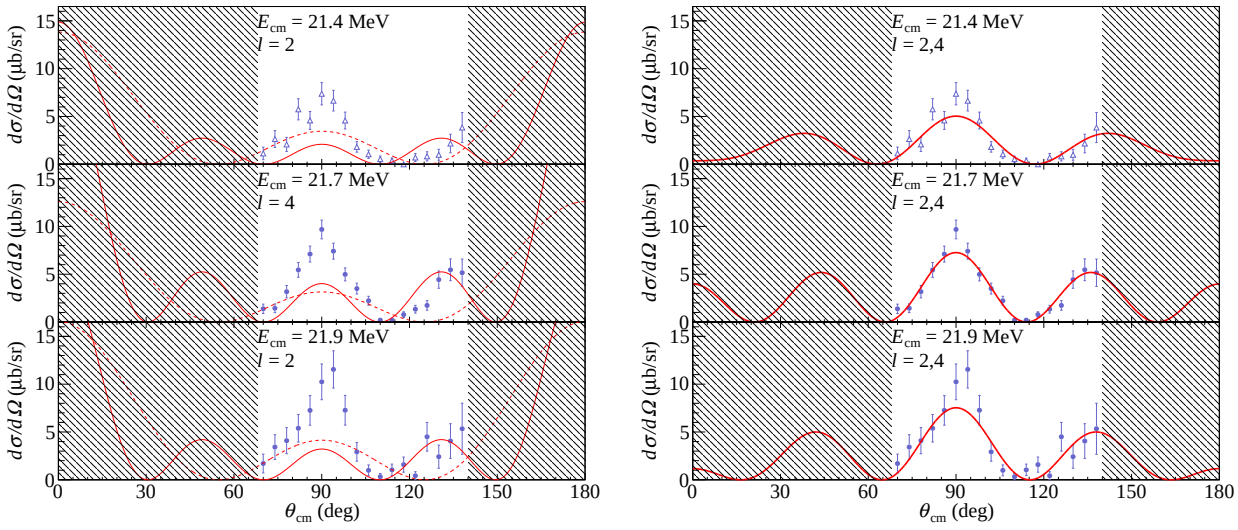

Figure 5.7: Same as Fig. 5.5, but for the $^{12}C+{}^{12}C \rightarrow {}^{12}C(0_2^+)+{}^{12}C(0_2^+)$ reaction at the low-energy side of the 22.5-MeV state. (Left panel) Squared Legendre polynomials of order 2 and 4 are plotted by the dashed and thin solid lines. (Right panel) Legendre polynomial fits taking contributions from $l = 2$ and 4 into account are plotted by the thick solid lines.

Chapter 6

Summary

Structures of atomic nuclei have been described with various nuclear pictures. One of the successful models is a shell model, in which nucleons occupy single-particle orbits in the mean-field potential generated by all nucleons. On the other hand, it is known that there exist cluster states in which several nucleons atrongly correlate with each other to form clusters. These states are described by a cluster model where the clusters weakly interact with each other. In the cluster structure, one of the most interesting states is the α-condensed states in which all the alpha clusters are condensed into the lowest s orbit, and the α-condensed states have a dilute structure with a larger radius.

The α-condensed states are predicted to exist in the self-conjugate $A = 4k$ nuclei up to $k = 10$. It is theoretically expected that the $k\alpha$-condensed states are located above the $k\alpha$-decay thresholds, and alpha clusters are confined in a shallow potential pocket formed by the interplay of the short-range weak nuclear attractive interaction and the long-range repulsive Coulomb interaction. Exploring the existence of the α-condensed states in various nuclei is an intriguing endeavor to verify the theoretical predictions and to establish universal presence of dilute α-cluster states. The ubiquity of the α-condensed states will suggest that the α condensation manifests in the dilute nuclear matter. In the present situation, the existence of the α-condensed states is established only in ^{8}Be and ^{12}C. In case of ^{16}O and ^{20}Ne, several candidate states are theoretically and experimentally proposed although they have not been established yet. However, for ^{24}Mg and heavier nuclei, no candidates of the α-condensed states have not been proposed.

In the present work, we measured the ^{12}C + ^{12}C scattering using the SAKRA detector in order to search for the 6α-condensed state in ^{24}Mg. The Si detector array SAKRA was newly developed for this experiment and specialized for the PSA. The experiment was conducted at the JAEA tandem accelerator facility. We utilized a ^{12}C beam with an incident energy of $E_{\rm cm}$ = 17.5–25.0 MeV to survey the excitation-energy range of 31.4–38.9 MeV in ^{24}Mg. For identifying the decay events of the excited states of ^{24}Mg via the 0^{+}_{2} or 3^{-}_{1}

state in ^{12}C, we reconstructed invariant mass of ^{12}C with 3α particles detected in one segment of SAKRA, and successfully identified 3α particles emitted from the 0^+_2 or 3^-_1 state. Then, we obtained the inclusive cross sections for the ^{12}C + ^{12}C $\rightarrow$ ^{12}C(0^+_2 or 3^-_1) + X $\rightarrow$ 3α + X reactions. In addition, we determined the excitation energy of the residual ^{12}C nucleus using the missing mass method, and exclusively obtained the cross sections for the ^{12}C + ^{12}C $\rightarrow$ ^{12}C(0^+_2) + ^{12}C(0^+_1), ^{12}C(0^+_2) + ^{12}C(2^+_1), and ^{12}C(0^+_2) + ^{12}C(0^+_2) channels.

The inclusive cross sections for the ^{12}C + ^{12}C $\rightarrow$ ^{12}C(0^+_2 or 3^-_1) + X $\rightarrow$ 3α + X reactions peaked at $E_{\rm cm}$ = 19.4 MeV, which corresponds to the excitation energy of 33.3 MeV in ^{24}Mg. This 19.4-MeV state was observed in the direct measurement of the 3α emission from the ^{12}C + ^{12}C reaction for the first time, and was found to decay via the 0^+_2 and 3^-_1 states in ^{12}C. This fact is strong evidence that the 19.4-MeV state is a multi-α cluster state. This 19.4-MeV state actually couples with the 0^+_2 state as the 3α-condensed state, and its energy is close to the theoretical value of the 6α-condensed state. These results suggest that this state is a candidate for the 6α-condensed state. This peak was also observed in the exclusive ^{12}C + ^{12}C $\rightarrow$ ^{12}C(0^+_2)+^{12}C(0^+_1) reaction, but not in the ^{12}C+^{12}C $\rightarrow$ ^{12}C(0^+_2)+^{12}C(0^+_2) reaction although the 6α-condensed state should have a larger overlap with the ^{12}C(0^+_2)+^{12}C(0^+_2) channel than with the ^{12}C(0^+_2)+^{12}C(0^+_1) channel. This could be explained by an inference that the ^{12}C(0^+_2) + ^{12}C(0^+_2) channel is suppressed by the Coulomb barrier due to its low decay energy. In the ^{12}C(0^+_2) + ^{12}C(0^+_2) channel, we found a broad structure around $E_{\rm cm}$ = 22.5 MeV, corresponding to E_x = 36.4 MeV in ^{24}Mg. This broad state ought to be a multi-α cluster state as well as the narrow state found at $E_{\rm cm}$ = 19.4 MeV.

To provide further clarification regarding the internal structure of these observed states, the spins and parities of these states are required. The angular distributions of the cross sections were analyzed to gain an insight into the spin and parity. Although the spin and parity of the 19.4-MeV state could not be resolved due to the continuous components, those of the broad 22.5-MeV state were assigned to be 4^+. In addition, a signature of the 2^+ state was suggested at lower-energy side of the broad state. Considering the excitation energy which is 3.1 MeV higher than the theoretical value of the 6α-condensed state, this broad state might be akin to the α-condensed state like the Hoyle band states known as the 2^+_2 and 4^+_1 states in ^{12}C.

It is also essential to compare the present results with theoretical calculations. However no microscopic calculations for the 6α-condensed state are available at present. Therefore, theoretical efforts are strongly desired to properly interpret the present results and to establish the 6α-condensed state.

Acknowledgement

First and foremost, I would like to express my deepest gratitude to my supervisor, Prof. Takahiro Kawabata. He introduced me to the research field of the nuclear-cluster physics and the α-condensed state when I was an undergraduate student of KADAIKENKYU P4. Fortunately, I was given interesting research themes, which led to important results, in both P4 and the master's course. In the doctor's course, he provided me the challenging project to develop a new Si detector array and its DAQ system specialized for pulse shape analysis. For eight years, he has been continuously supporting and encouraging me in the experiments, data analysis, and thesis writing. I would like to sincerely thank him taking the time out of his busy schedule to publish my work and complete my doctoral thesis on the search for the 6α-condensed state in ^{24}Mg.

I gratefully acknowledge the present and past members of our research group. This experiment could not be carried out without the support of our group members: Prof. Satoshi Adachi, Prof. Tatsuya Furuno, Mr. Motoki Murata, Dr. Kento Inaba, Mr. Shintaro Okamoto, Mr. Kohsuke Sakanashi, Ms. Kanako Himi, Mr. Seiya Tsuji, Mr. Yuya Honda, and Mr. Kenshin Miyamoto. I really enjoyed working on many experiments together and the daily conversations. Thanks to them, I was able to spend an exciting research life.

The experiment of the ^{12}C + ^{12}C scattering was carried out at the JAEA tandem accelerator facility. I would like to thank the JAEA collaborators: Prof. Katsuhisa Nisio, Prof. Hiroyuki Makii, Prof. Kentaro Hirose, Prof. Riccardo Orlandi, and Dr. Fumi Suzaki for their enthusiastic and professional supports. I also acknowledge the JAEA tandem accelerator crews for providing a high-quality beam.

I would like to appreciate all of the members of Experimental Nuclear and Hadronic Physics Laboratory (NH) at Kyoto University. Prof. Tomofumi Nagae, the leader of NH, has always guided and encouraged me. I thank Prof. Juzo Zenihiro, Ms. Shiyo Enyo, Mr. Yuto Hijikata, and Mr. Kanta Yahiro for their cooperation in the experiment. I would also like to acknowledge all the NH members who made my days so enjoyable, and the office staffs who provided a comfortable working environment.

Finally, I would like to express my deepest appreciation to my parents, brother, and grand parents for always supporting me. Thanks to their patient support and understanding, I was able to continue and complete my present work and dissertation.

References

[1] M. G. Mayer, Physical Review **75** (1949) 1969. doi:10.1103/PhysRev.74.1547.

[2] M. G. Mayer, Physical Review **78** (1950) 16–21. doi:10.1103/PhysRev.78.16.

[3] O. Haxel, J. H. D. Jensen, H. E. Suess, Physical Review **75** (1949) 1766. doi:10.1103/PhysRev.75.1766.2.

[4] O. Haxel, J. H. D. Jensen, H. E. Suess, Zeitschrift für Physik **128** (1950) 295–311. doi:10.1007/BF00585103.

[5] D. M. Brink, Proceedings of the International School of Physics "Enrico Fermi" course **36** (1965), ed. by C. Bloch, (Academic Press, 1966) p. 247.

[6] H. Margenau, Physical Review **59** (1941) 37. doi:10.1103/PhysRev.59.37.

[7] J. Tanaka, Z. Yang, S. Typel, S. Adachi, S. Bai, P. V. Beek, D. Beaumel, Y. Fujikawa, J. Han, S. Heil, S. Huang, A. Inoue, Y. Jiang, N. Kobayashi, Y. Kubota, W. Liu, J. Lou, Y. Maeda, Y. Matsuda, K. Miki, S. Nakamura, K. Ogata, V. Panin, H. Scheit, F. Schindler, P. Schrock, D. Symochko, A. Tamii, T. Uesaka, V. Wagner, K. Yoshida, J. Zenihiro, T. Aumann, *Science* **371** (2021) 260–264. doi:10.1126/science.abe4688.

[8] K. Ikeda, N. Takigawa, H. Horiuchi, Progress of Theoretical Physics Supplement **E68** (1968) 464. doi:10.1143/PTPS.E68.464.

[9] M. Freer, H. O. Fynbo, Progress in Particle and Nuclear Physics **78** (2014) 1–23. doi:10.1016/j.ppnp.2014.06.001.

[10] F. Hoyle, D. N.F.Dunbar, W. Wenzel, W. Whaling, Physical Review C **92** (1953) 1095.

[11] E. Uegaki, Y. Abe, S. Okabe, H. Tanaka, Progress of Theoretical Physics **62** (6) (1979) 1621–1640. doi:10.1143/ptp.62.1621.

[12] Y. Fujiwara, H. Horiuchi, K. Ikeda, M. Kamimura, K. Kato, Y. Suzuki, E. Uegaki, Progress of Theoretical Physics Supplement **68** (1980) 29. doi:10.1143/PTPS.68.29.

[13] M. Kamimura, Nuclear Physics A **351** (1981) 456–480. doi:10.1016/0375-9474(81)90182-2.

[14] A. Tohsaki, H. Horiuchi, P. Schuck, G. Röpke, Physical Review Letters **87** (2001) 192501. doi:10.1103/PhysRevLett.87.192501.

[15] T. Yamada, P. Schuck, European Physical Journal A **26** (2005) 185–199. doi:10.1140/epja/i2005-10168-1.

[16] Y. Funaki, H. Horiuchi, W. Von Oertzen, G. Röpke, P. Schuck, A. Tohsaki, T. Yamada, Physical Review C **80** (2009) 064326. doi:10.1103/PhysRevC.80.064326.

[17] S. Typel, G. Röpke, T. Klähn, D. Blaschke, H. H. Wolter, Physical Review C **81** (2010) 015803. doi:10.1103/PhysRevC.81.015803.

[18] Z. W. Zhang, L. W. Chen, Physical Review C **100** (2019) 054304. doi:10.1103/PhysRevC.100.054304.

[19] L. M. Satarov, R. V. Poberezhnyuk, I. N. Mishustin, H. Stoecker, Physical Review C **103** (2021) 024301. doi:10.1103/PhysRevC.103.024301.

[20] J. P. Ebran, M. Girod, E. Khan, R. D. Lasseri, P. Schuck, Physical Review C **102** (2020) 014305. doi:10.1103/PhysRevC.102.014305.

[21] W. von Oertzen, Alpha-cluster Condensations in Nuclei and Experimental Approaches for their Studies, Vol. 818 of Lecture Notes in Physics, Springer Berlin Heidelberg, Berlin, Heidelberg, 2010, pp. 109–128. doi:10.1007/978-3-642-13899-7_3.

[22] T. Yamada, Y. Funaki, H. Horiuchi, G. Röpke, P. Schuck, A. Tohsaki, Nuclear Alpha-Particle Condensates, Vol. 848 of Lecture Notes in Physics, Springer Berlin Heidelberg, Berlin, Heidelberg, 2012, pp. 229–298. doi:10.1007/978-3-642-24707-1_5.

[23] M. Itoh, H. Akimune, M. Fujiwara, U. Garg, N. Hashimoto, T. Kawabata, K. Kawase, S. Kishi, T. Murakami, K. Nakanishi, Y. Nakatsugawa, B. K. Nayak, S. Okumura, H. Sakaguchi, H. Takeda,

S. Terashima, M. Uchida, Y. Yasuda, M. Yosoi, J. Zenihiro, Physical Review C **84** (2011) 054308. doi:10.1103/PhysRevC.84.054308.

[24] Y. Funaki, Physical Review C **92** (2015) 021302(R). doi:10.1103/PhysRevC.92.021302.

[25] T. Yamada, P. Schuck, Physical Review C **69** (2004) 024309. doi:10.1103/PhysRevC.69.024309.

[26] Y. Funaki, H. Horiuchi, A. Tohsaki, P. Schuck, G. Röpke, Progress of Theoretical Physics **108** (2) (2002) 297–322. doi:10.1143/PTP.108.297.

[27] Y. Funaki, T. Yamada, H. Horiuchi, G. Röpke, P. Schuck, A. Tohsaki, Physical Review Letters **101** (2008) 082502. doi:10.1103/PhysRevLett.101.082502.

[28] T. Yamada, Y. Funaki, T. Myo, H. Horiuchi, K. Ikeda, R. Gerd, Physical Review C **85** (2012) 034315. doi:10.1103/PhysRevC.85.034315.

[29] Y. Funaki, Physical Review C **97** (2018) 021304(R). doi:10.1103/PhysRevC.97.021304.

[30] D. R. Tilley, H. R. Weller, C. M. Cheves, Nuclear Physics A **565** (1993) 1–184. doi:10.1016/0375-9474(93)90073-7.

[31] M. Barbui, K. Hagel, J. Gauthier, S. Wuenschel, R. Wada, V. Z. Goldberg, R. T. Desouza, S. Hudan, D. Fang, X. G. Cao, J. B. Natowitz, Physical Review C **98** (2018) 044601. doi:10.1103/PhysRevC.98.044601.

[32] S. Adachi, Y. Fujikawa, T. Kawabata, H. Akimune, T. Doi, T. Furuno, T. Harada, K. Inaba, S. Ishida, M. Itoh, C. Iwamoto, N. Kobayashi, Y. Maeda, Y. Matsuda, M. Murata, S. Okamoto, A. Sakaue, R. Sekiya, A. Tamii, M. Tsumura, Physics Letters B **819** (2021) 136411. doi:10.1016/j.physletb.2021.136411.

[33] J. A. Swartz, B. A. Brown, P. Papka, F. D. Smit, R. Neveling, E. Z. Buthelezi, S. V. Förtsch, M. Freer, T. Kokalova, J. P. Mira, F. Nemulodi, J. N. Orce, W. A. Richter, G. F. Steyn, Physical Review C **91** (2015) 034317. doi:10.1103/PhysRevC.91.034317.

[34] T. Kawabata, T. Adachi, M. Fujiwara, K. Hatanaka, Y. Ishiguro, M. Itoh, Y. Maeda, H. Matsubara, H. Miyasako, Y. Nozawa, T. Saito, S. Sakaguchi, Y. Sasamoto, Y. Shimizu, T. Takahashi, A. Tamii, S. Terashima, H. Tokieda, N. Tomida, T. Uesaka, M. Uchida, Y. Yasuda, N. Yokota, H. P.

Yoshida, J. Zenihiro, Journal of Physics: Conference Series **436** (2013) 012009. doi:10.1088/1742-6596/436/1/012009.

[35] A. H. Wuosmaa, B. B. Back, I. G. Bearden, R. R. Betts, M. Freer, J. Gehring, B. G. Glagola, T. Happ, D. J. Henderson, P. Wilt, Physical Review Letters **68** (1992) 1295. doi:10.1103/PhysRevLett.68.1295.

[36] A. H. Wuosmaa, M. Freer, B. B. Back, R. R. Betts, J. C. Gehring, B. G. Glagola, T. Happ, D. J. Henderson, P. Wilt, I. G. Bearden, Physical Review C **50** (1994) 2909. doi:10.1103/PhysRevC.50.2909.

[37] M. Freer, A. C. Merchant, Journal of Physics G: Nuclear and Particle Physics **23** (1997) 261–323. doi:10.1088/0954-3899/23/3/002.

[38] J. Vadas, T. K. Steinbach, J. Schmidt, V. Singh, C. Haycraft, S. Hudan, R. T. Desouza, L. T. Baby, S. A. Kuvin, I. Wiedenhöver, Physical Review C **92** (2015) 064610. doi:10.1103/PhysRevC.92.064610.

[39] J. Bishop, T. Kokalova, M. Freer, L. Acosta, M. Assié, S. Bailey, G. Cardella, N. Curtis, E. De Filippo, D. Dell'Aquila, S. De Luca, L. Francalanza, B. Gnoffo, G. Lanzalone, I. Lombardo, N. S. Martorana, S. Norella, A. Pagano, E. V. Pagano, M. Papa, S. Pirrone, G. Politi, F. Rizzo, P. Russotto, L. Quattrocchi, R. Smith, I. Stefan, A. Trifirò, M. Trimarchì, G. Verde, M. Vigilante, C. Wheldon, Physical Review C **100** (2019) 034320. doi:10.1103/PhysRevC.100.034320.

[40] J. J. Kolata, R. E. Malmin, P. A. DeYoung, S. Davis, R. Luhn, Physical Review C **21** (1980) 776–778. doi:10.1103/PhysRevC.21.776.

[41] J. J. Kolata, Physical Review C **21** (1980) 579. doi:10.1103/PhysRevC.21.579.

[42] X. Y. Wang, N. T. Zhang, Z. C. Zhang, C. G. Lu, T. L. Pu, J. L. Zhang, L. M. Duan, B. S. Gao, K. A. Li, Y. T. Li, Y. Qian, L. H. Ru, B. Wang, X. D. Xu, H. Y. Zhao, W. P. Lin, Z. W. Cai, B. F. Ji, Q. T. Li, J. Y. Xu, X. D. Tang, Chinese Physics C **46** (2022) 104001. doi:10.1088/1674-1137/ac7a1d.

[43] W. Leo, Techniques for Nuclear an Particle Physics Experiments, Springer-Verlag, 1993.

[44] G. Pausch, W. Bohne, D. Hilscher, Nuclear Instruments and Methods in Physics Research A **337** (1994) 573–587. doi:10.1016/0168-9002(94)91129-0.

[45] C. A. Ammerlaan, R. F. Rumphorst, L. A. Koerts, Nuclear Instruments and Methods **22** (1963) 189–200. doi:10.1016/0029-554X(63)90248-9.

[46] S. Barlini, R. Bougault, P. Laborie, O. Lopez, D. Mercier, M. Parlog, B. Tamain, E. Vient, E. Chevallier, A. Chbihi, B. Jacquot, V. L. Kravchuk, Nuclear Instruments and Methods in Physics Research A **600** (2009) 644–650. doi:10.1016/j.nima.2008.12.200.

[47] G. Pastore, D. Gruyer, P. Ottanelli, N. Le Neindre, G. Pasquali, R. Alba, S. Barlini, M. Bini, E. Bonnet, B. Borderie, R. Bougault, M. Bruno, G. Casini, A. Chbihi, D. Dell'Aquila, J. A. Dueñas, D. Fabris, L. Francalanza, J. D. Frankland, F. Gramegna, M. Henri, A. Kordyasz, T. Kozik, I. Lombardo, O. Lopez, L. Morelli, A. Olmi, M. Pârlog, S. Piantelli, G. Poggi, D. Santonocito, A. A. Stefanini, S. Valdré, G. Verde, E. Vient, M. Vigilante, Nuclear Instruments and Methods in Physics Research A **860** (2017) 42–50. doi:10.1016/j.nima.2017.01.048.

[48] K. Mahata, A. Shrivastava, J. A. Gore, S. K. Pandit, V. V. Parkar, K. Ramachandran, A. Kumar, S. Gupta, P. Patale, Nuclear Instruments and Methods in Physics Research A **894** (2018) 20–24. doi:10.1016/j.nima.2018.03.052.

[49] J. A. Dueñas, D. Mengoni, V. V. Parkar, R. Berjillos, M. Assie, D. Beaumel, A. M. Sánchez-Benítez, I. Martel, Nuclear Instruments and Methods in Physics Research A **676** (2012) 70–73. doi:10.1016/j.nima.2012.02.032.

[50] J. L. Flores, I. Martel, R. Jiménez, J. Galán, P. Salmerón, Nuclear Instruments and Methods in Physics Research A **830** (2016) 287–293. doi:10.1016/j.nima.2016.05.107.

[51] H. Baba, T. Ichihara, T. Ohnishi, S. Takeuchi, K. Yoshida, Y. Watanabe, S. Ota, S. Shimoura, Nuclear Instruments and Methods in Physics Research A **616** (2010) 65–68. doi:10.1016/j.nima.2010.02.120.

[52] RIBFDAQ web site, https://ribf.riken.jp/RIBFDAQ/index.php.

[53] CAEN, User Manual UM6064, 725-730 DPP-ZLE*plus*, Digital Pulse Processing for Zero Length Encoding, Rev. 2 (2020).

[54] Digital filter design services, http://dsp.jpn.org/dfdesign/.

[55] P. Adsley, R. Neveling, P. Papka, Z. Dyers, J. W. Brümmer, C. A. Diget, N. J. Hubbard, K. C. Li, A. Long, D. J. Marin-Lambarri, L. Pellegri, V. Pesudo, L. C. Pool, F. D. Smit, S. Triambak, Journal of Instrumentation **12** (2017) T02004. doi:10.1088/1748-0221/12/02/T02004.

[56] E. C. Good, B. Sudarsan, K. T. Macon, C. M. Deibel, L. T. Baby, J. C. Blackmon, C. Benetti, J. C. Esparza, N. Gerken, K. Hanselman, G. W. McCann, A. B. Morelock, J. F. Perello, K. H. Pham, E. Rubino, E. Temanson, I. Wiedenhöver, Nuclear Instruments and Methods in Physics Research A **1003** (2021) 165299. doi:10.1016/j.nima.2021.165299.

[57] JAEA tandem accelerator facility web site, https://ttandem.jaea.go.jp/.

[58] H.-J. Fink, W. Scheid, W. Greiner, Nuclear Physics A **188** (1972) 259–288. doi:10.1016/0375-9474(72)90059-0.

[59] W. R. Zimmerman, M. W. Ahmed, B. Bromberger, S. C. Stave, A. Breskin, V. Dangendorf, T. Delbar, M. Gai, S. S. Henshaw, J. M. Mueller, C. Sun, K. Tittelmeier, H. R. Weller, Y. K. Wu, Physical Review Letters **110** (2013) 152502. doi:10.1103/PhysRevLett.110.152502.

[60] M. Freer, S. Almaraz-Calderon, A. Aprahamian, N. I. Ashwood, M. Barr, B. Bucher, P. Copp, M. Couder, N. Curtis, X. Fang, F. Jung, S. Lesher, W. Lu, J. D. Malcolm, A. Roberts, W. P. Tan, C. Wheldon, V. A. Ziman, Physical Review C **83** (2011) 034314. doi:10.1103/PhysRevC.83.034314.

Appendix A

Data tables of cross sections

A.1 Inclusive cross section

Table A.1: $^{12}C(^{12}C, ^{12}C[0_2^+] \rightarrow 3\alpha)X$ reaction at the first beam-time period.

E_{cm} (MeV)	Seg.	σ (mb)	error (mb)
17.5	0	5.36×10^{-1}	2.27×10^{-2}
	1	4.85×10^{-1}	2.15×10^{-2}
	2	4.72×10^{-1}	2.21×10^{-2}
	3	4.12×10^{-1}	2.14×10^{-2}
	4	4.63×10^{-1}	2.08×10^{-2}
18.0	0	8.47×10^{-1}	2.95×10^{-2}
	1	7.53×10^{-1}	2.83×10^{-2}
	2	7.80×10^{-1}	2.69×10^{-2}
	3	7.24×10^{-1}	2.70×10^{-2}
	4	7.20×10^{-1}	2.75×10^{-2}
18.5	0	8.78×10^{-1}	2.69×10^{-2}
	1	7.90×10^{-1}	2.49×10^{-2}
	2	8.23×10^{-1}	2.47×10^{-2}
	3	7.44×10^{-1}	2.39×10^{-2}
	4	7.83×10^{-1}	2.33×10^{-2}
19.0	0	9.23×10^{-1}	2.30×10^{-2}
	1	7.99×10^{-1}	2.18×10^{-2}
	2	8.42×10^{-1}	2.17×10^{-2}
	3	7.62×10^{-1}	2.08×10^{-2}
	4	7.23×10^{-1}	2.05×10^{-2}
19.5	0	1.05	2.65×10^{-2}
	1	9.56×10^{-1}	2.50×10^{-2}
	2	9.44×10^{-1}	2.50×10^{-2}
	3	8.78×10^{-1}	2.44×10^{-2}
	4	–	–
20.0	0	7.97×10^{-1}	2.55×10^{-2}
	1	8.01×10^{-1}	2.57×10^{-2}
	2	8.11×10^{-1}	2.56×10^{-2}
	3	6.80×10^{-1}	2.31×10^{-2}
	4	–	–
20.5	0	1.02	2.55×10^{-2}
	1	1.03	2.60×10^{-2}
	2	1.11	2.57×10^{-2}
	3	–	–
	4	–	–
21.0	0	1.50	2.91×10^{-2}
	1	1.44	2.93×10^{-2}
	2	1.38	2.78×10^{-2}
	3	–	–
	4	–	–
21.5	0	1.73	3.06×10^{-2}

Continued.

Table A.1 : (Continued)

Continued.

Table A.1 : (Continued)

E_{cm} (MeV)	Seg.	σ (mb)	error (mb)
	1	1.58	2.98×10^{-2}
	2	1.51	2.89×10^{-2}
	3	–	–
	4	–	–
22.0	0	1.32	2.87×10^{-2}
	1	1.20	2.88×10^{-2}
	2	1.17	2.70×10^{-2}
	3	–	–
	4	–	–
22.5	0	1.33	3.17×10^{-2}
	1	1.15	3.13×10^{-2}
	2	1.18	3.04×10^{-2}
	3	–	–
	4	–	–
23.0	0	1.10	3.00×10^{-2}
	1	1.01	2.95×10^{-2}
	2	9.20×10^{-1}	2.79×10^{-2}
	3	–	–
	4	–	–
23.5	0	1.51	4.28×10^{-2}
	1	1.43	4.22×10^{-2}
	2	1.42	4.27×10^{-2}
	3	1.26	4.10×10^{-2}
	4	1.33	3.99×10^{-2}
24.0	0	1.77	4.51×10^{-2}
	1	1.66	4.43×10^{-2}
	2	1.67	4.31×10^{-2}
	3	1.43	4.07×10^{-2}
	4	1.53	3.96×10^{-2}
24.5	0	1.83	4.27×10^{-2}
	1	1.75	4.46×10^{-2}

Continued.

Table A.1 : (Continued)

E_{cm} (MeV)	Seg.	σ (mb)	error (mb)
	2	1.63	4.30×10^{-2}
	3	1.53	4.13×10^{-2}
	4	1.55	3.92×10^{-2}
25.0	0	1.74	4.53×10^{-2}
	1	1.58	4.58×10^{-2}
	2	1.53	4.29×10^{-2}
	3	1.41	4.17×10^{-2}
	4	1.59	4.14×10^{-2}

Table A.2: $^{12}C(^{12}C, ^{12}C[0^+_2] \rightarrow 3\alpha)X$ reaction at the second beam-time period.

E_{cm} (MeV)	Seg.	σ (mb)	error (mb)
19.0	0	9.23×10^{-1}	5.31×10^{-2}
	1	8.50×10^{-1}	5.47×10^{-2}
	2	7.21×10^{-1}	5.10×10^{-2}
	3	7.81×10^{-1}	4.90×10^{-2}
	4	7.80×10^{-1}	4.78×10^{-2}
19.2	0	8.60×10^{-1}	1.80×10^{-2}
	1	8.00×10^{-1}	1.78×10^{-2}
	2	6.79×10^{-1}	1.64×10^{-2}
	3	7.12×10^{-1}	1.68×10^{-2}
	4	7.08×10^{-1}	1.68×10^{-2}
19.4	0	1.08	2.17×10^{-2}
	1	9.58×10^{-1}	2.14×10^{-2}
	2	8.26×10^{-1}	1.96×10^{-2}
	3	8.92×10^{-1}	1.96×10^{-2}
	4	8.80×10^{-1}	1.97×10^{-2}

Continued.

Table A.2 : (Continued)

E_{cm} (MeV)	Seg.	σ (mb)	error (mb)
19.6	0	1.04	2.20×10^{-2}
	1	9.16×10^{-1}	2.10×10^{-2}
	2	8.82×10^{-1}	1.99×10^{-2}
	3	8.25×10^{-1}	1.96×10^{-2}
	4	9.22×10^{-1}	2.07×10^{-2}
19.8	0	8.45×10^{-1}	2.03×10^{-2}
	1	8.01×10^{-1}	1.98×10^{-2}
	2	7.47×10^{-1}	1.92×10^{-2}
	3	5.97×10^{-1}	1.74×10^{-2}
	4	7.05×10^{-1}	1.86×10^{-2}
20.0	0	8.54×10^{-1}	4.15×10^{-2}
	1	8.42×10^{-1}	4.26×10^{-2}
	2	7.69×10^{-1}	3.81×10^{-2}
	3	5.85×10^{-1}	3.30×10^{-2}
	4	6.47×10^{-1}	3.64×10^{-2}
20.2	0	1.00	2.41×10^{-2}
	1	9.41×10^{-1}	2.42×10^{-2}
	2	8.81×10^{-1}	2.30×10^{-2}
	3	7.67×10^{-1}	2.08×10^{-2}
	4	8.76×10^{-1}	2.29×10^{-2}
20.8	0	1.54	2.65×10^{-2}
	1	1.36	2.60×10^{-2}
	2	1.29	2.44×10^{-2}
	3	1.19	2.35×10^{-2}
	4	1.39	2.51×10^{-2}
21.0	0	1.51	4.80×10^{-2}
	1	1.38	4.82×10^{-2}
	2	1.30	4.52×10^{-2}
	3	1.13	4.25×10^{-2}
	4	1.35	4.67×10^{-2}
21.2	0	1.62	2.65×10^{-2}
	1	1.50	2.66×10^{-2}
	2	1.36	2.53×10^{-2}
	3	1.21	2.38×10^{-2}
	4	1.52	2.57×10^{-2}
21.8	0	1.47	2.62×10^{-2}
	1	1.34	2.55×10^{-2}
	2	1.24	2.50×10^{-2}
	3	1.12	2.25×10^{-2}
	4	1.35	2.54×10^{-2}
22.0	0	1.37	4.60×10^{-2}
	1	1.23	4.66×10^{-2}
	2	1.08	4.39×10^{-2}
	3	9.70×10^{-1}	3.99×10^{-2}
	4	1.14	4.30×10^{-2}
22.2	0	1.28	2.47×10^{-2}
	1	1.23	2.47×10^{-2}
	2	1.15	2.37×10^{-2}
	3	1.00	2.21×10^{-2}
	4	1.19	2.34×10^{-2}
22.8	0	1.12	2.46×10^{-2}
	1	1.03	2.49×10^{-2}
	2	9.68×10^{-1}	2.30×10^{-2}
	3	8.55×10^{-1}	2.11×10^{-2}
	4	1.03	2.30×10^{-2}
23.0	0	1.11	4.55×10^{-2}
	1	1.09	4.58×10^{-2}
	2	9.39×10^{-1}	4.27×10^{-2}
	3	8.92×10^{-1}	4.12×10^{-2}
	4	1.11	4.50×10^{-2}
23.2	0	1.28	2.65×10^{-2}
	1	1.22	2.74×10^{-2}

Continued.

Table A.2 : (Continued)

Continued.

Table A.2 : (Continued)

E_{cm} (MeV)	Seg.	σ (mb)	error (mb)
	2	1.16	2.59×10^{-2}
	3	9.70×10^{-1}	2.33×10^{-2}
	4	1.17	2.57×10^{-2}

Table A.3: $^{12}C(^{12}C, ^{12}C[3^-_1] \rightarrow 3\alpha)X$ reaction at the first beam-time period.

E_{cm} (MeV)	Seg.	σ (mb)	error (mb)
17.5	0	1.21	1.32×10^{-1}
	1	7.56×10^{-1}	1.09×10^{-1}
	2	1.10	1.24×10^{-1}
	3	1.40	1.55×10^{-1}
	4	1.20	1.35×10^{-1}
18.0	0	1.53	1.52×10^{-1}
	1	1.33	1.35×10^{-1}
	2	1.56	1.50×10^{-1}
	3	1.50	1.77×10^{-1}
	4	1.61	1.54×10^{-1}
18.5	0	1.56	1.39×10^{-1}
	1	1.34	1.14×10^{-1}
	2	1.70	1.26×10^{-1}
	3	1.69	1.46×10^{-1}
	4	1.49	1.37×10^{-1}
19.0	0	3.13	1.35×10^{-1}
	1	2.50	1.15×10^{-1}
	2	3.00	1.26×10^{-1}
	3	3.06	1.40×10^{-1}
	4	2.78	1.34×10^{-1}

Continued.

Table A.3 : (Continued)

E_{cm} (MeV)	Seg.	σ (mb)	error (mb)
19.5	0	5.32	1.67×10^{-1}
	1	3.90	1.43×10^{-1}
	2	4.01	1.52×10^{-1}
	3	5.25	1.71×10^{-1}
	4	–	–
20.0	0	3.38	1.49×10^{-1}
	1	2.56	1.32×10^{-1}
	2	2.96	1.40×10^{-1}
	3	3.61	1.56×10^{-1}
	4	–	–
20.5	0	4.58	1.54×10^{-1}
	1	4.58	1.55×10^{-1}
	2	4.66	1.53×10^{-1}
	3	–	–
	4	–	–
21.0	0	5.74	1.61×10^{-1}
	1	5.26	1.55×10^{-1}
	2	4.76	1.46×10^{-1}
	3	–	–
	4	–	–
21.5	0	6.39	1.80×10^{-1}
	1	5.13	1.61×10^{-1}
	2	4.65	1.55×10^{-1}
	3	–	–
	4	–	–
22.0	0	6.30	1.76×10^{-1}
	1	5.20	1.67×10^{-1}
	2	5.08	1.61×10^{-1}
	3	–	–
	4	–	–
22.5	0	5.49	1.93×10^{-1}

Continued.

Table A.3 : (Continued)

E_{cm} (MeV)	Seg.	σ (mb)	error (mb)
	1	4.42	1.82×10^{-1}
	2	4.72	1.81×10^{-1}
	3	–	–
	4	–	–
23.0	0	8.74	2.01×10^{-1}
	1	6.46	1.79×10^{-1}
	2	6.30	1.75×10^{-1}
	3	–	–
	4	–	–
23.5	0	1.08×10^{1}	2.64×10^{-1}
	1	8.32	2.32×10^{-1}
	2	9.24	2.39×10^{-1}
	3	1.12×10^{1}	2.72×10^{-1}
	4	9.82	2.47×10^{-1}
24.0	0	1.03×10^{1}	2.44×10^{-1}
	1	8.06	2.18×10^{-1}
	2	8.95	2.34×10^{-1}
	3	1.15×10^{1}	2.65×10^{-1}
	4	1.05×10^{1}	2.44×10^{-1}
24.5	0	1.20×10^{1}	2.53×10^{-1}
	1	9.03	2.24×10^{-1}
	2	9.78	2.32×10^{-1}
	3	1.18×10^{1}	2.57×10^{-1}
	4	1.11×10^{1}	2.43×10^{-1}
25.0	0	1.20×10^{1}	2.51×10^{-1}
	1	9.04	2.17×10^{-1}
	2	1.00×10^{1}	2.28×10^{-1}
	3	1.22×10^{1}	2.64×10^{-1}
	4	1.07×10^{1}	2.38×10^{-1}

Table A.4: $^{12}C(^{12}C, ^{12}C[3_1^-] \rightarrow 3\alpha)X$ reaction at the second beam-time period.

E_{cm} (MeV)	Seg.	σ (mb)	error (mb)
19.0	0	3.40	3.36×10^{-1}
	1	3.27	2.71×10^{-1}
	2	2.48	2.86×10^{-1}
	3	3.85	3.30×10^{-1}
	4	3.80	3.21×10^{-1}
19.2	0	4.01	1.18×10^{-1}
	1	3.35	1.07×10^{-1}
	2	2.80	1.00×10^{-1}
	3	3.79	1.21×10^{-1}
	4	4.14	1.25×10^{-1}
19.4	0	5.19	1.38×10^{-1}
	1	4.29	1.23×10^{-1}
	2	4.09	1.24×10^{-1}
	3	5.40	1.44×10^{-1}
	4	5.46	1.48×10^{-1}
19.6	0	4.66	1.37×10^{-1}
	1	3.77	1.22×10^{-1}
	2	3.77	1.21×10^{-1}
	3	4.54	1.37×10^{-1}
	4	5.02	1.44×10^{-1}
19.8	0	3.73	1.23×10^{-1}
	1	3.14	1.13×10^{-1}
	2	3.12	1.14×10^{-1}
	3	3.37	1.21×10^{-1}
	4	3.59	1.24×10^{-1}
20.0	0	3.15	2.38×10^{-1}
	1	2.89	2.23×10^{-1}
	2	2.87	2.15×10^{-1}
	3	2.93	2.18×10^{-1}

Continued.

Table A.4 : (Continued)

E_{cm} (MeV)	Seg.	σ (mb)	error (mb)
	4	2.97	2.26×10^{-1}
20.2	0	5.03	1.42×10^{-1}
	1	3.93	1.26×10^{-1}
	2	4.12	1.25×10^{-1}
	3	4.50	1.37×10^{-1}
	4	5.04	1.48×10^{-1}
20.8	0	5.08	1.38×10^{-1}
	1	4.08	1.25×10^{-1}
	2	3.80	1.21×10^{-1}
	3	4.33	1.27×10^{-1}
	4	5.35	1.43×10^{-1}
21.0	0	4.91	2.43×10^{-1}
	1	4.35	2.21×10^{-1}
	2	3.72	2.17×10^{-1}
	3	4.19	2.27×10^{-1}
	4	5.23	2.49×10^{-1}
21.2	0	5.80	1.51×10^{-1}
	1	4.49	1.37×10^{-1}
	2	4.55	1.33×10^{-1}
	3	5.13	1.45×10^{-1}
	4	5.97	1.57×10^{-1}
21.8	0	6.35	1.47×10^{-1}
	1	5.35	1.37×10^{-1}
	2	5.27	1.34×10^{-1}
	3	5.94	1.44×10^{-1}
	4	6.72	1.54×10^{-1}
22.0	0	5.45	2.66×10^{-1}
	1	4.88	2.46×10^{-1}
	2	4.84	2.41×10^{-1}
	3	5.97	2.68×10^{-1}
	4	5.95	2.72×10^{-1}

Continued.

Table A.4 : (Continued)

E_{cm} (MeV)	Seg.	σ (mb)	error (mb)
22.2	0	5.57	1.39×10^{-1}
	1	4.85	1.33×10^{-1}
	2	4.87	1.33×10^{-1}
	3	5.14	1.36×10^{-1}
	4	5.77	1.43×10^{-1}
22.8	0	6.57	1.45×10^{-1}
	1	5.40	1.34×10^{-1}
	2	5.33	1.32×10^{-1}
	3	5.93	1.40×10^{-1}
	4	6.80	1.49×10^{-1}
23.0	0	8.60	2.84×10^{-1}
	1	7.24	2.62×10^{-1}
	2	6.89	2.60×10^{-1}
	3	7.83	2.69×10^{-1}
	4	9.04	2.88×10^{-1}
23.2	0	9.40	1.57×10^{-1}
	1	8.07	1.47×10^{-1}
	2	7.51	1.41×10^{-1}
	3	8.43	1.49×10^{-1}
	4	9.31	1.60×10^{-1}

Table A.5: ^{12}C(^{12}C, ^{12}C[0^+_2] $\rightarrow 3\alpha$)X reaction using reliable segments of SAKRA.

E_{cm} (MeV)	E'_{cm} (MeV)	$\Delta E'_{\mathrm{cm}}$ (MeV)	σ (mb)	$\Delta\sigma_{\mathrm{stat}}$ (mb)	$\Delta\sigma_{\mathrm{syst}}$ (mb)
17.5	17.41	8.75×10^{-2}	4.87×10^{-1}	9.47×10^{-3}	4.71×10^{-2}
18.0	17.91	8.75×10^{-2}	7.69×10^{-1}	1.24×10^{-2}	5.21×10^{-2}
18.5	18.41	8.50×10^{-2}	8.12×10^{-1}	1.10×10^{-2}	5.12×10^{-2}
19.0	18.91	8.50×10^{-2}	8.15×10^{-1}	8.85×10^{-3}	7.30×10^{-2}
	(Mar.)		8.17×10^{-1}	9.57×10^{-3}	–
	(Apr.)		8.03×10^{-1}	2.33×10^{-2}	–
19.2	19.11	8.50×10^{-2}	7.55×10^{-1}	7.66×10^{-3}	7.58×10^{-2}
19.4	19.32	8.25×10^{-2}	9.33×10^{-1}	9.09×10^{-3}	9.81×10^{-2}
19.5	19.42	8.25×10^{-2}	9.64×10^{-1}	1.25×10^{-2}	7.17×10^{-2}
19.6	19.51	8.50×10^{-2}	9.20×10^{-1}	9.20×10^{-3}	7.76×10^{-2}
19.8	19.72	8.47×10^{-2}	7.51×10^{-1}	8.42×10^{-3}	9.63×10^{-2}
20.0	19.92	8.25×10^{-2}	7.65×10^{-1}	1.01×10^{-2}	9.48×10^{-2}
	(Mar.)		7.80×10^{-1}	1.24×10^{-2}	–
	(Apr.)		7.35×10^{-1}	1.74×10^{-2}	–
20.2	20.17	8.00×10^{-2}	9.05×10^{-1}	1.02×10^{-2}	8.89×10^{-2}
20.5	20.42	8.00×10^{-2}	1.06	1.48×10^{-2}	5.13×10^{-2}
20.8	20.67	8.00×10^{-2}	1.36	1.12×10^{-2}	1.28×10^{-1}
21.0	20.92	8.00×10^{-2}	1.40	1.30×10^{-2}	1.25×10^{-1}
	(Mar.)		1.44	1.66×10^{-2}	–
	(Apr.)		1.33	2.08×10^{-2}	–
21.2	21.17	8.00×10^{-2}	1.45	1.14×10^{-2}	1.61×10^{-1}
21.5	21.42	7.75×10^{-2}	1.61	1.71×10^{-2}	1.14×10^{-1}
21.8	21.67	7.75×10^{-2}	1.31	1.11×10^{-2}	1.33×10^{-1}
22.0	21.92	7.75×10^{-2}	1.20	1.26×10^{-2}	1.29×10^{-1}
	(Mar.)		1.23	1.63×10^{-2}	–
	(Apr.)		1.16	1.99×10^{-2}	–
22.2	22.17	7.75×10^{-2}	1.18	1.07×10^{-2}	1.05×10^{-1}
22.5	22.43	7.50×10^{-2}	1.22	1.81×10^{-2}	9.76×10^{-2}
22.8	22.68	7.50×10^{-2}	1.01	1.05×10^{-2}	9.85×10^{-2}
23.0	22.93	7.50×10^{-2}	1.02	1.29×10^{-2}	9.31×10^{-2}
	(Mar.)		1.02	1.68×10^{-2}	–
	(Apr.)		1.02	2.02×10^{-2}	–

Continued.

Table A.5 : (Continued)

E_{cm} (MeV)	E'_{cm} (MeV)	$\Delta E'_{cm}$ (MeV)	σ (mb)	$\Delta\sigma_{stat}$ (mb)	$\Delta\sigma_{syst}$ (mb)
23.2	23.18	7.50×10^{-2}	1.17	1.15×10^{-2}	1.16×10^{-1}
23.5	23.43	7.25×10^{-2}	1.40	1.87×10^{-2}	9.75×10^{-2}
24.0	23.93	7.25×10^{-2}	1.62	1.91×10^{-2}	1.33×10^{-1}
24.5	24.43	7.25×10^{-2}	1.67	1.89×10^{-2}	1.29×10^{-1}
25.0	24.93	7.00×10^{-2}	1.58	1.96×10^{-2}	1.20×10^{-1}

Table A.6: ^{12}C(^{12}C, ^{12}C[3^-_1] $\rightarrow 3\alpha$)X reaction using reliable segments of SAKRA.

E_{cm} (MeV)	E'_{cm} (MeV)	$\Delta E'_{cm}$ (MeV)	σ (mb)	$\Delta\sigma_{stat}$ (mb)	$\Delta\sigma_{syst}$ (mb)
17.5	17.41	8.75×10^{-2}	1.09	5.90×10^{-2}	2.42×10^{-1}
18.0	17.91	8.75×10^{-2}	1.48	6.89×10^{-2}	1.09×10^{-1}
18.5	18.41	8.50×10^{-2}	1.54	5.94×10^{-2}	1.51×10^{-1}
19.0	18.91	8.50×10^{-2}	2.83	5.47×10^{-2}	5.67×10^{-1}
	(Mar.)		2.81	5.89×10^{-2}	–
	(Apr.)		2.97	1.46×10^{-1}	–
19.2	19.11	8.50×10^{-2}	3.53	5.16×10^{-2}	5.56×10^{-1}
19.4	19.32	8.25×10^{-2}	4.80	6.10×10^{-2}	6.58×10^{-1}
19.5	19.42	8.25×10^{-2}	4.53	8.02×10^{-2}	7.77×10^{-1}
19.6	19.51	8.50×10^{-2}	4.28	5.94×10^{-2}	5.67×10^{-1}
19.8	19.72	8.47×10^{-2}	3.31	5.37×10^{-2}	2.84×10^{-1}
20.0	19.92	8.25×10^{-2}	2.96	5.94×10^{-2}	3.18×10^{-1}
	(Mar.)		3.03	7.30×10^{-2}	–
	(Apr.)		2.84	1.02×10^{-1}	–
20.2	20.17	8.00×10^{-2}	4.45	6.11×10^{-2}	5.15×10^{-1}
20.5	20.42	8.00×10^{-2}	4.54	8.94×10^{-2}	9.23×10^{-2}
20.8	20.67	8.00×10^{-2}	4.47	5.88×10^{-2}	6.64×10^{-1}
21.0	20.92	8.00×10^{-2}	4.85	6.78×10^{-2}	6.63×10^{-1}
	(Mar.)		5.22	8.90×10^{-2}	–
	(Apr.)		4.35	1.05×10^{-1}	–
21.2	21.17	8.00×10^{-2}	5.13	6.49×10^{-2}	6.89×10^{-1}
21.5	21.42	7.75×10^{-2}	5.32	9.60×10^{-2}	9.06×10^{-1}

Continued.

Table A.6 : (Continued)

E_{cm} (MeV)	E'_{cm} (MeV)	$\Delta E'_{cm}$ (MeV)	σ (mb)	$\Delta\sigma_{stat}$ (mb)	$\Delta\sigma_{syst}$ (mb)
21.8	21.67	7.75×10^{-2}	5.86	6.43×10^{-2}	6.33×10^{-1}
22.0	21.92	7.75×10^{-2}	5.43	7.46×10^{-2}	5.54×10^{-1}
	(Mar.)		5.48	9.73×10^{-2}	–
	(Apr.)		5.35	1.16×10^{-1}	–
22.2	22.17	7.75×10^{-2}	5.21	6.13×10^{-2}	4.18×10^{-1}
22.5	22.43	7.50×10^{-2}	4.81	1.08×10^{-1}	5.59×10^{-1}
22.8	22.68	7.50×10^{-2}	5.95	6.28×10^{-2}	6.70×10^{-1}
23.0	22.93	7.50×10^{-2}	7.43	8.08×10^{-2}	1.09
	(Mar.)		7.10	1.08×10^{-1}	–
	(Apr.)		7.87	1.23×10^{-1}	–
23.2	23.18	7.50×10^{-2}	8.53	6.75×10^{-2}	8.10×10^{-1}
23.5	23.43	7.25×10^{-2}	9.85	1.12×10^{-1}	1.16
24.0	23.93	7.25×10^{-2}	9.83	1.08×10^{-1}	1.35
24.5	24.43	7.25×10^{-2}	1.08×10^{1}	1.08×10^{-1}	1.29
25.0	24.93	7.00×10^{-2}	1.07×10^{1}	1.07×10^{-1}	1.34

A.2 Exclusive cross section

Table A.7: $^{12}C(^{12}C, ^{12}C[0_2^+] \rightarrow 3\alpha)^{12}C(0_1^+)$ reaction at the first beam-time period.

E_{cm} (MeV)	Seg.	σ (mb)	error (mb)
17.5	0	6.74×10^{-1}	1.92×10^{-2}
	1	6.08×10^{-1}	1.82×10^{-2}
	2	6.21×10^{-1}	1.83×10^{-2}
	3	5.61×10^{-1}	1.85×10^{-2}
	4	6.02×10^{-1}	1.87×10^{-2}
18.0	0	8.57×10^{-1}	2.21×10^{-2}
	1	7.71×10^{-1}	2.09×10^{-2}
	2	7.94×10^{-1}	2.12×10^{-2}
	3	7.37×10^{-1}	2.12×10^{-2}
	4	7.40×10^{-1}	2.09×10^{-2}
18.5	0	9.74×10^{-1}	2.18×10^{-2}
	1	8.80×10^{-1}	2.09×10^{-2}
	2	9.07×10^{-1}	2.09×10^{-2}
	3	8.32×10^{-1}	2.10×10^{-2}
	4	8.38×10^{-1}	2.05×10^{-2}
19.0	0	8.40×10^{-1}	1.65×10^{-2}
	1	7.17×10^{-1}	1.52×10^{-2}
	2	7.57×10^{-1}	1.56×10^{-2}
	3	6.92×10^{-1}	1.55×10^{-2}
	4	6.43×10^{-1}	1.46×10^{-2}
19.5	0	9.32×10^{-1}	1.84×10^{-2}
	1	8.33×10^{-1}	1.75×10^{-2}
	2	8.44×10^{-1}	1.76×10^{-2}
	3	7.79×10^{-1}	1.71×10^{-2}
	4	–	–
20.0	0	8.00×10^{-1}	1.88×10^{-2}
	1	7.81×10^{-1}	1.87×10^{-2}
	2	7.92×10^{-1}	1.88×10^{-2}
	3	6.75×10^{-1}	1.76×10^{-2}
	4	–	–
20.5	0	9.12×10^{-1}	1.75×10^{-2}
	1	8.93×10^{-1}	1.73×10^{-2}
	2	9.58×10^{-1}	1.75×10^{-2}
	3	–	–
	4	–	–
21.0	0	1.18	1.92×10^{-2}
	1	1.11	1.87×10^{-2}
	2	1.06	1.80×10^{-2}
	3	–	–
	4	–	–
21.5	0	1.35	2.05×10^{-2}
	1	1.25	1.97×10^{-2}
	2	1.19	1.92×10^{-2}
	3	–	–
	4	–	–
22.0	0	1.03	1.91×10^{-2}
	1	9.52×10^{-1}	1.83×10^{-2}
	2	9.12×10^{-1}	1.80×10^{-2}
	3	–	–
	4	–	–
22.5	0	9.27×10^{-1}	2.05×10^{-2}
	1	8.03×10^{-1}	1.91×10^{-2}
	2	8.42×10^{-1}	1.94×10^{-2}
	3	–	–
	4	–	–
23.0	0	7.22×10^{-1}	1.78×10^{-2}
	1	7.02×10^{-1}	1.76×10^{-2}
	2	6.09×10^{-1}	1.63×10^{-2}

Table A.7 : (Continued)

Continued.

Table A.7 : (Continued)

E_{cm} (MeV)	Seg.	σ (mb)	error (mb)
	3	–	–
	4	–	–
23.5	0	1.17	2.89×10^{-2}
	1	1.12	2.84×10^{-2}
	2	1.13	2.87×10^{-2}
	3	9.98×10^{-1}	2.78×10^{-2}
	4	1.00	2.71×10^{-2}
24.0	0	1.29	2.92×10^{-2}
	1	1.25	2.88×10^{-2}
	2	1.19	2.80×10^{-2}
	3	1.07	2.76×10^{-2}
	4	1.09	2.70×10^{-2}
24.5	0	1.34	2.89×10^{-2}
	1	1.32	2.89×10^{-2}
	2	1.21	2.74×10^{-2}
	3	1.16	2.79×10^{-2}
	4	1.17	2.75×10^{-2}
25.0	0	1.24	2.86×10^{-2}
	1	1.19	2.85×10^{-2}
	2	1.07	2.67×10^{-2}
	3	1.01	2.62×10^{-2}
	4	1.12	2.73×10^{-2}

Table A.8: $^{12}C(^{12}C, ^{12}C[0_2^+] \rightarrow 3\alpha)^{12}C(0_1^+)$ reaction at the second beam-time period.

E_{cm} (MeV)	Seg.	σ (mb)	error (mb)
19.0	0	8.25×10^{-1}	3.89×10^{-2}

Continued.

Table A.8 : (Continued)

E_{cm} (MeV)	Seg.	σ (mb)	error (mb)
	1	8.07×10^{-1}	3.86×10^{-2}
	2	6.79×10^{-1}	3.55×10^{-2}
	3	7.19×10^{-1}	3.76×10^{-2}
	4	6.60×10^{-1}	3.57×10^{-2}
19.2	0	7.85×10^{-1}	1.32×10^{-2}
	1	7.33×10^{-1}	1.27×10^{-2}
	2	6.19×10^{-1}	1.16×10^{-2}
	3	6.39×10^{-1}	1.22×10^{-2}
	4	6.47×10^{-1}	1.22×10^{-2}
19.4	0	9.81×10^{-1}	1.59×10^{-2}
	1	8.76×10^{-1}	1.49×10^{-2}
	2	7.66×10^{-1}	1.39×10^{-2}
	3	7.91×10^{-1}	1.45×10^{-2}
	4	7.96×10^{-1}	1.44×10^{-2}
19.6	0	9.49×10^{-1}	1.60×10^{-2}
	1	8.40×10^{-1}	1.50×10^{-2}
	2	8.01×10^{-1}	1.47×10^{-2}
	3	7.35×10^{-1}	1.43×10^{-2}
	4	8.20×10^{-1}	1.50×10^{-2}
19.8	0	8.30×10^{-1}	1.56×10^{-2}
	1	7.75×10^{-1}	1.50×10^{-2}
	2	7.13×10^{-1}	1.44×10^{-2}
	3	6.16×10^{-1}	1.40×10^{-2}
	4	6.90×10^{-1}	1.47×10^{-2}
20.0	0	8.76×10^{-1}	3.22×10^{-2}
	1	8.52×10^{-1}	3.18×10^{-2}
	2	7.70×10^{-1}	2.99×10^{-2}
	3	6.03×10^{-1}	2.78×10^{-2}
	4	6.57×10^{-1}	2.88×10^{-2}
20.2	0	1.01	1.79×10^{-2}
	1	9.38×10^{-1}	1.71×10^{-2}

Continued.

Table A.8 : (Continued)

E_{cm} (MeV)	Seg.	σ (mb)	error (mb)
	2	8.69×10^{-1}	1.65×10^{-2}
	3	7.74×10^{-1}	1.61×10^{-2}
	4	8.68×10^{-1}	1.68×10^{-2}
20.8	0	1.26	1.82×10^{-2}
	1	1.13	1.72×10^{-2}
	2	1.06	1.67×10^{-2}
	3	9.83×10^{-1}	1.62×10^{-2}
	4	1.13	1.73×10^{-2}
21.0	0	1.15	3.15×10^{-2}
	1	1.10	3.10×10^{-2}
	2	1.00	2.97×10^{-2}
	3	8.80×10^{-1}	2.82×10^{-2}
	4	1.06	3.10×10^{-2}
21.2	0	1.25	1.76×10^{-2}
	1	1.19	1.74×10^{-2}
	2	1.07	1.63×10^{-2}
	3	9.66×10^{-1}	1.58×10^{-2}
	4	1.21	1.77×10^{-2}
21.8	0	1.11	1.67×10^{-2}
	1	1.02	1.61×10^{-2}
	2	9.31×10^{-1}	1.53×10^{-2}
	3	8.28×10^{-1}	1.45×10^{-2}
	4	1.04	1.64×10^{-2}
22.0	0	1.05	3.09×10^{-2}
	1	9.40×10^{-1}	2.90×10^{-2}
	2	8.42×10^{-1}	2.76×10^{-2}
	3	7.24×10^{-1}	2.57×10^{-2}
	4	8.79×10^{-1}	2.85×10^{-2}
22.2	0	9.61×10^{-1}	1.59×10^{-2}
	1	9.31×10^{-1}	1.58×10^{-2}
	2	8.63×10^{-1}	1.52×10^{-2}

Continued.

Table A.8 : (Continued)

E_{cm} (MeV)	Seg.	σ (mb)	error (mb)
	3	7.78×10^{-1}	1.46×10^{-2}
	4	8.84×10^{-1}	1.55×10^{-2}
22.8	0	7.15×10^{-1}	1.41×10^{-2}
	1	6.73×10^{-1}	1.37×10^{-2}
	2	6.33×10^{-1}	1.33×10^{-2}
	3	5.39×10^{-1}	1.22×10^{-2}
	4	6.69×10^{-1}	1.37×10^{-2}
23.0	0	7.08×10^{-1}	2.65×10^{-2}
	1	6.82×10^{-1}	2.60×10^{-2}
	2	6.17×10^{-1}	2.50×10^{-2}
	3	5.98×10^{-1}	2.45×10^{-2}
	4	7.32×10^{-1}	2.72×10^{-2}
23.2	0	9.22×10^{-1}	1.70×10^{-2}
	1	9.11×10^{-1}	1.69×10^{-2}
	2	8.77×10^{-1}	1.67×10^{-2}
	3	6.94×10^{-1}	1.48×10^{-2}
	4	8.74×10^{-1}	1.66×10^{-2}

Table A.9: $^{12}C(^{12}C, ^{12}C[0^+_2] \rightarrow 3\alpha)^{12}C(2^+_1)$ reaction at the first beam-time period.

E_{cm} (MeV)	Seg.	σ (mb)	error (mb)
17.5	0	1.47×10^{-2}	3.06×10^{-3}
	1	1.57×10^{-2}	3.14×10^{-3}
	2	1.95×10^{-2}	3.51×10^{-3}
	3	2.23×10^{-2}	3.88×10^{-3}
	4	1.43×10^{-2}	3.06×10^{-3}
18.0	0	2.51×10^{-2}	4.66×10^{-3}

Continued.

Table A.9 : (Continued)

E_{cm} (MeV)	Seg.	σ (mb)	error (mb)
	1	2.20×10^{-2}	4.32×10^{-3}
	2	1.24×10^{-2}	3.21×10^{-3}
	3	2.52×10^{-2}	4.76×10^{-3}
	4	1.92×10^{-2}	4.10×10^{-3}
18.5	0	9.10×10^{-2}	7.15×10^{-3}
	1	9.19×10^{-2}	7.20×10^{-3}
	2	7.95×10^{-2}	6.67×10^{-3}
	3	8.32×10^{-2}	7.13×10^{-3}
	4	7.29×10^{-2}	6.52×10^{-3}
19.0	0	1.36×10^{-1}	7.49×10^{-3}
	1	1.35×10^{-1}	7.39×10^{-3}
	2	1.26×10^{-1}	7.22×10^{-3}
	3	1.09×10^{-1}	6.83×10^{-3}
	4	1.02×10^{-1}	6.59×10^{-3}
19.5	0	1.68×10^{-1}	8.77×10^{-3}
	1	1.34×10^{-1}	7.94×10^{-3}
	2	1.33×10^{-1}	7.83×10^{-3}
	3	1.16×10^{-1}	7.35×10^{-3}
	4	–	–
20.0	0	1.59×10^{-1}	9.24×10^{-3}
	1	1.49×10^{-1}	9.08×10^{-3}
	2	1.63×10^{-1}	9.32×10^{-3}
	3	1.11×10^{-1}	7.83×10^{-3}
	4	–	–
20.5	0	1.58×10^{-1}	8.74×10^{-3}
	1	1.65×10^{-1}	9.07×10^{-3}
	2	1.75×10^{-1}	8.80×10^{-3}
	3	–	–
	4	–	–
21.0	0	2.60×10^{-1}	1.09×10^{-2}
	1	2.64×10^{-1}	1.10×10^{-2}

Continued.

Table A.9 : (Continued)

E_{cm} (MeV)	Seg.	σ (mb)	error (mb)
	2	2.70×10^{-1}	1.08×10^{-2}
	3	–	–
	4	–	–
21.5	0	2.77×10^{-1}	1.12×10^{-2}
	1	2.42×10^{-1}	1.05×10^{-2}
	2	2.52×10^{-1}	1.05×10^{-2}
	3	–	–
	4	–	–
22.0	0	2.72×10^{-1}	1.09×10^{-2}
	1	2.31×10^{-1}	1.01×10^{-2}
	2	2.29×10^{-1}	9.87×10^{-3}
	3	–	–
	4	–	–
22.5	0	3.39×10^{-1}	1.32×10^{-2}
	1	3.24×10^{-1}	1.31×10^{-2}
	2	2.88×10^{-1}	1.22×10^{-2}
	3	–	–
	4	–	–
23.0	0	2.98×10^{-1}	1.19×10^{-2}
	1	2.62×10^{-1}	1.13×10^{-2}
	2	2.65×10^{-1}	1.13×10^{-2}
	3	–	–
	4	–	–
23.5	0	2.81×10^{-1}	1.49×10^{-2}
	1	2.77×10^{-1}	1.49×10^{-2}
	2	3.08×10^{-1}	1.56×10^{-2}
	3	2.53×10^{-1}	1.49×10^{-2}
	4	2.98×10^{-1}	1.55×10^{-2}
24.0	0	4.33×10^{-1}	1.70×10^{-2}
	1	4.14×10^{-1}	1.67×10^{-2}
	2	4.48×10^{-1}	1.75×10^{-2}

Continued.

Table A.9 : (Continued)

E_{cm} (MeV)	Seg.	σ (mb)	error (mb)
	3	3.28×10^{-1}	1.54×10^{-2}
	4	3.84×10^{-1}	1.62×10^{-2}
24.5	0	3.97×10^{-1}	1.58×10^{-2}
	1	4.27×10^{-1}	1.65×10^{-2}
	2	4.09×10^{-1}	1.61×10^{-2}
	3	3.32×10^{-1}	1.49×10^{-2}
	4	3.50×10^{-1}	1.51×10^{-2}
25.0	0	3.54×10^{-1}	1.57×10^{-2}
	1	3.25×10^{-1}	1.50×10^{-2}
	2	3.36×10^{-1}	1.51×10^{-2}
	3	2.54×10^{-1}	1.35×10^{-2}
	4	2.96×10^{-1}	1.45×10^{-2}

Table A.10: $^{12}C(^{12}C, ^{12}C[0_2^+] \rightarrow 3\alpha)^{12}C(2_1^+)$ reaction at the second beam-time period.

E_{cm} (MeV)	Seg.	σ (mb)	error (mb)
19.0	0	1.16×10^{-1}	1.63×10^{-2}
	1	1.03×10^{-1}	1.52×10^{-2}
	2	1.08×10^{-1}	1.56×10^{-2}
	3	9.42×10^{-2}	1.49×10^{-2}
	4	1.28×10^{-1}	1.74×10^{-2}
19.2	0	1.51×10^{-1}	6.33×10^{-3}
	1	1.38×10^{-1}	6.06×10^{-3}
	2	1.24×10^{-1}	5.77×10^{-3}
	3	1.34×10^{-1}	6.15×10^{-3}
	4	1.14×10^{-1}	5.65×10^{-3}
19.4	0	1.80×10^{-1}	7.72×10^{-3}

Continued.

Table A.10 : (Continued)

E_{cm} (MeV)	Seg.	σ (mb)	error (mb)
	1	1.55×10^{-1}	7.14×10^{-3}
	2	1.32×10^{-1}	6.56×10^{-3}
	3	1.26×10^{-1}	6.58×10^{-3}
	4	1.28×10^{-1}	6.62×10^{-3}
19.6	0	1.66×10^{-1}	7.79×10^{-3}
	1	1.43×10^{-1}	7.14×10^{-3}
	2	1.46×10^{-1}	7.14×10^{-3}
	3	1.40×10^{-1}	7.24×10^{-3}
	4	1.43×10^{-1}	7.40×10^{-3}
19.8	0	1.96×10^{-1}	8.89×10^{-3}
	1	1.85×10^{-1}	8.54×10^{-3}
	2	1.83×10^{-1}	8.46×10^{-3}
	3	1.35×10^{-1}	7.57×10^{-3}
	4	1.67×10^{-1}	8.47×10^{-3}
20.0	0	1.95×10^{-1}	1.85×10^{-2}
	1	2.01×10^{-1}	1.85×10^{-2}
	2	1.64×10^{-1}	1.66×10^{-2}
	3	1.48×10^{-1}	1.71×10^{-2}
	4	1.81×10^{-1}	1.86×10^{-2}
20.2	0	1.58×10^{-1}	8.80×10^{-3}
	1	1.51×10^{-1}	8.59×10^{-3}
	2	1.59×10^{-1}	8.75×10^{-3}
	3	1.27×10^{-1}	8.23×10^{-3}
	4	1.54×10^{-1}	8.97×10^{-3}
20.8	0	3.29×10^{-1}	1.27×10^{-2}
	1	3.10×10^{-1}	1.22×10^{-2}
	2	2.84×10^{-1}	1.17×10^{-2}
	3	2.65×10^{-1}	1.16×10^{-2}
	4	2.97×10^{-1}	1.25×10^{-2}
21.0	0	3.47×10^{-1}	2.34×10^{-2}
	1	2.94×10^{-1}	2.12×10^{-2}

Continued.

Table A.10 : (Continued)

E_{cm} (MeV)	Seg.	σ (mb)	error (mb)
	2	3.19×10^{-1}	2.21×10^{-2}
	3	2.90×10^{-1}	2.20×10^{-2}
	4	3.26×10^{-1}	2.33×10^{-2}
21.2	0	3.36×10^{-1}	1.25×10^{-2}
	1	3.13×10^{-1}	1.19×10^{-2}
	2	2.89×10^{-1}	1.15×10^{-2}
	3	2.48×10^{-1}	1.11×10^{-2}
	4	3.11×10^{-1}	1.26×10^{-2}
21.8	0	2.92×10^{-1}	1.06×10^{-2}
	1	2.71×10^{-1}	1.04×10^{-2}
	2	2.79×10^{-1}	1.05×10^{-2}
	3	2.45×10^{-1}	1.03×10^{-2}
	4	2.72×10^{-1}	1.07×10^{-2}
22.0	0	2.93×10^{-1}	1.92×10^{-2}
	1	2.49×10^{-1}	1.80×10^{-2}
	2	2.53×10^{-1}	1.80×10^{-2}
	3	2.20×10^{-1}	1.71×10^{-2}
	4	2.21×10^{-1}	1.71×10^{-2}
22.2	0	2.90×10^{-1}	1.01×10^{-2}
	1	2.91×10^{-1}	1.02×10^{-2}
	2	2.68×10^{-1}	9.76×10^{-3}
	3	2.22×10^{-1}	9.10×10^{-3}
	4	2.79×10^{-1}	1.01×10^{-2}
22.8	0	3.28×10^{-1}	1.06×10^{-2}
	1	3.24×10^{-1}	1.06×10^{-2}
	2	3.02×10^{-1}	1.03×10^{-2}
	3	2.64×10^{-1}	9.77×10^{-3}
	4	3.08×10^{-1}	1.05×10^{-2}
23.0	0	3.27×10^{-1}	1.97×10^{-2}
	1	3.15×10^{-1}	1.97×10^{-2}
	2	2.97×10^{-1}	1.88×10^{-2}

Continued.

Table A.10 : (Continued)

E_{cm} (MeV)	Seg.	σ (mb)	error (mb)
	3	2.63×10^{-1}	1.80×10^{-2}
	4	3.24×10^{-1}	1.99×10^{-2}
23.2	0	3.22×10^{-1}	1.08×10^{-2}
	1	2.95×10^{-1}	1.04×10^{-2}
	2	2.88×10^{-1}	1.01×10^{-2}
	3	2.60×10^{-1}	9.96×10^{-3}
	4	2.85×10^{-1}	1.02×10^{-2}

Table A.11: $^{12}C(^{12}C, ^{12}C[0_2^+] \rightarrow 3\alpha)^{12}C(0_2^+)$ reaction at the first beam-time period.

E_{cm} (MeV)	Seg.	σ (mb)	error (mb)
17.5	0	–	–
	1	–	–
	2	–	–
	3	–	–
	4	–	–
18.0	0	–	–
	1	–	–
	2	–	–
	3	–	–
	4	–	–
18.5	0	–	–
	1	–	–
	2	–	–
	3	–	–
	4	–	–
19.0	0	2.45×10^{-3}	1.73×10^{-3}

Continued.

Table A.11 : (Continued)

E_{cm} (MeV)	Seg.	σ (mb)	error (mb)
	1	2.38×10^{-3}	1.69×10^{-3}
	2	3.61×10^{-3}	2.09×10^{-3}
	3	1.24×10^{-3}	1.24×10^{-3}
	4	0.00	0.00
19.5	0	5.93×10^{-3}	2.42×10^{-3}
	1	1.01×10^{-3}	1.01×10^{-3}
	2	1.03×10^{-3}	1.03×10^{-3}
	3	1.03×10^{-3}	1.03×10^{-3}
	4	–	–
20.0	0	5.83×10^{-3}	2.20×10^{-3}
	1	1.40×10^{-2}	3.49×10^{-3}
	2	5.23×10^{-3}	2.14×10^{-3}
	3	7.68×10^{-3}	2.56×10^{-3}
	4	–	–
20.5	0	7.22×10^{-3}	2.18×10^{-3}
	1	1.18×10^{-2}	2.79×10^{-3}
	2	1.81×10^{-2}	3.36×10^{-3}
	3	–	–
	4	–	–
21.0	0	1.67×10^{-2}	3.05×10^{-3}
	1	2.31×10^{-2}	3.57×10^{-3}
	2	1.90×10^{-2}	3.16×10^{-3}
	3	–	–
	4	–	–
21.5	0	3.84×10^{-2}	4.19×10^{-3}
	1	2.81×10^{-2}	3.60×10^{-3}
	2	3.44×10^{-2}	3.92×10^{-3}
	3	–	–
	4	–	–
22.0	0	5.83×10^{-2}	5.07×10^{-3}
	1	4.04×10^{-2}	4.24×10^{-3}

Continued.

Table A.11 : (Continued)

E_{cm} (MeV)	Seg.	σ (mb)	error (mb)
	2	5.46×10^{-2}	4.92×10^{-3}
	3	–	–
	4	–	–
22.5	0	6.21×10^{-2}	5.81×10^{-3}
	1	6.14×10^{-2}	5.75×10^{-3}
	2	6.04×10^{-2}	5.71×10^{-3}
	3	–	–
	4	–	–
23.0	0	6.79×10^{-2}	5.91×10^{-3}
	1	5.70×10^{-2}	5.43×10^{-3}
	2	5.25×10^{-2}	5.23×10^{-3}
	3	–	–
	4	–	–
23.5	0	5.55×10^{-2}	6.68×10^{-3}
	1	5.34×10^{-2}	6.52×10^{-3}
	2	5.97×10^{-2}	6.94×10^{-3}
	3	4.12×10^{-2}	5.95×10^{-3}
	4	4.66×10^{-2}	6.12×10^{-3}
24.0	0	3.61×10^{-2}	5.15×10^{-3}
	1	2.71×10^{-2}	4.45×10^{-3}
	2	3.66×10^{-2}	5.23×10^{-3}
	3	3.56×10^{-2}	5.25×10^{-3}
	4	2.68×10^{-2}	4.46×10^{-3}
24.5	0	3.29×10^{-2}	4.74×10^{-3}
	1	2.87×10^{-2}	4.43×10^{-3}
	2	3.26×10^{-2}	4.71×10^{-3}
	3	3.12×10^{-2}	4.76×10^{-3}
	4	2.09×10^{-2}	3.82×10^{-3}
25.0	0	4.78×10^{-2}	5.98×10^{-3}
	1	4.59×10^{-2}	5.78×10^{-3}
	2	4.21×10^{-2}	5.53×10^{-3}

Continued.

Table A.11 : (Continued)

E_{cm} (MeV)	Seg.	σ (mb)	error (mb)
	3	3.82×10^{-2}	5.52×10^{-3}
	4	4.71×10^{-2}	5.93×10^{-3}

Table A.12: $^{12}C(^{12}C, ^{12}C[0_2^+] \rightarrow 3\alpha)^{12}C(0_2^+)$ reaction at the second beam-time period.

E_{cm} (MeV)	Seg.	σ (mb)	error (mb)
19.0	0	0.00	0.00
	1	0.00	0.00
	2	0.00	0.00
	3	8.02×10^{-3}	8.02×10^{-3}
	4	0.00	0.00
19.2	0	7.10×10^{-4}	7.10×10^{-4}
	1	3.53×10^{-3}	1.58×10^{-3}
	2	0.00	0.00
	3	0.00	0.00
	4	4.38×10^{-3}	1.79×10^{-3}
19.4	0	1.53×10^{-3}	1.08×10^{-3}
	1	3.89×10^{-3}	1.74×10^{-3}
	2	7.79×10^{-4}	7.79×10^{-4}
	3	6.43×10^{-3}	2.27×10^{-3}
	4	4.76×10^{-3}	1.94×10^{-3}
19.6	0	2.75×10^{-3}	1.37×10^{-3}
	1	2.73×10^{-3}	1.37×10^{-3}
	2	3.40×10^{-3}	1.52×10^{-3}
	3	2.09×10^{-3}	1.21×10^{-3}
	4	5.65×10^{-3}	2.00×10^{-3}
19.8	0	4.62×10^{-3}	1.74×10^{-3}
	1	4.63×10^{-3}	1.75×10^{-3}
	2	5.92×10^{-3}	1.97×10^{-3}
	3	3.46×10^{-3}	1.55×10^{-3}
	4	4.78×10^{-3}	1.81×10^{-3}
20.0	0	2.36×10^{-3}	2.36×10^{-3}
	1	9.70×10^{-3}	4.85×10^{-3}
	2	4.82×10^{-3}	3.41×10^{-3}
	3	0.00	0.00
	4	1.00×10^{-2}	5.00×10^{-3}
20.2	0	8.77×10^{-3}	2.34×10^{-3}
	1	1.04×10^{-2}	2.51×10^{-3}
	2	7.35×10^{-3}	2.12×10^{-3}
	3	8.47×10^{-3}	2.35×10^{-3}
	4	8.29×10^{-3}	2.30×10^{-3}
20.8	0	1.30×10^{-2}	2.61×10^{-3}
	1	1.42×10^{-2}	2.69×10^{-3}
	2	1.45×10^{-2}	2.69×10^{-3}
	3	1.02×10^{-2}	2.29×10^{-3}
	4	1.53×10^{-2}	2.79×10^{-3}
21.0	0	1.70×10^{-2}	5.37×10^{-3}
	1	6.65×10^{-3}	3.32×10^{-3}
	2	1.82×10^{-2}	5.47×10^{-3}
	3	1.92×10^{-2}	5.80×10^{-3}
	4	1.92×10^{-2}	5.79×10^{-3}
21.2	0	2.69×10^{-2}	3.41×10^{-3}
	1	1.83×10^{-2}	2.79×10^{-3}
	2	2.17×10^{-2}	3.04×10^{-3}
	3	2.03×10^{-2}	2.97×10^{-3}
	4	1.38×10^{-2}	2.44×10^{-3}
21.8	0	5.07×10^{-2}	4.37×10^{-3}
	1	4.33×10^{-2}	4.04×10^{-3}

Continued.

Table A.12 : (Continued)

E_{cm} (MeV)	Seg.	σ (mb)	error (mb)

Continued.

Table A.12 : (Continued)

E_{cm} (MeV)	Seg.	σ (mb)	error (mb)
	2	4.38×10^{-2}	4.05×10^{-3}
	3	3.80×10^{-2}	3.82×10^{-3}
	4	4.09×10^{-2}	3.96×10^{-3}
22.0	0	5.26×10^{-2}	8.11×10^{-3}
	1	5.13×10^{-2}	8.02×10^{-3}
	2	3.13×10^{-2}	6.26×10^{-3}
	3	4.68×10^{-2}	7.69×10^{-3}
	4	5.90×10^{-2}	8.70×10^{-3}
22.2	0	5.70×10^{-2}	4.52×10^{-3}
	1	5.54×10^{-2}	4.44×10^{-3}
	2	5.69×10^{-2}	4.50×10^{-3}
	3	5.61×10^{-2}	4.52×10^{-3}
	4	6.92×10^{-2}	4.99×10^{-3}
22.8	0	7.77×10^{-2}	5.35×10^{-3}
	1	6.08×10^{-2}	4.76×10^{-3}
	2	5.73×10^{-2}	4.62×10^{-3}
	3	4.76×10^{-2}	4.26×10^{-3}
	4	5.58×10^{-2}	4.54×10^{-3}
23.0	0	6.47×10^{-2}	9.24×10^{-3}
	1	5.55×10^{-2}	8.46×10^{-3}
	2	5.60×10^{-2}	8.55×10^{-3}
	3	5.44×10^{-2}	8.49×10^{-3}
	4	4.90×10^{-2}	8.05×10^{-3}
23.2	0	5.43×10^{-2}	4.65×10^{-3}
	1	5.19×10^{-2}	4.45×10^{-3}
	2	4.82×10^{-2}	4.36×10^{-3}
	3	5.13×10^{-2}	4.53×10^{-3}
	4	4.18×10^{-2}	4.04×10^{-3}

Table A.13: ^{12}C(^{12}C, ^{12}C[0^+_2] → 3α)^{12}C(0^+_1) reaction using reliable segments of SAKRA.

E_{cm} (MeV)	E'_{cm} (MeV)	$\Delta E'_{cm}$ (MeV)	σ (mb)	$\Delta\sigma_{stat}$ (mb)	$\Delta\sigma_{syst}$ (mb)
17.5	17.41	8.75×10^{-2}	6.14×10^{-1}	8.32×10^{-3}	4.08×10^{-2}
18.0	17.91	8.75×10^{-2}	7.81×10^{-1}	9.51×10^{-3}	4.94×10^{-2}
18.5	18.41	8.50×10^{-2}	8.87×10^{-1}	9.41×10^{-3}	5.80×10^{-2}
19.0	18.91	8.50×10^{-2}	7.32×10^{-1}	6.40×10^{-3}	7.04×10^{-2}
	(Mar.)		7.30×10^{-1}	6.93×10^{-3}	–
	(Apr.)		7.39×10^{-1}	1.67×10^{-2}	–
19.2	19.11	8.50×10^{-2}	6.85×10^{-1}	5.54×10^{-3}	7.10×10^{-2}
19.4	19.32	8.25×10^{-2}	8.43×10^{-1}	6.59×10^{-3}	8.81×10^{-2}
19.5	19.42	8.25×10^{-2}	8.48×10^{-1}	8.84×10^{-3}	6.32×10^{-2}
19.6	19.51	8.50×10^{-2}	8.30×10^{-1}	6.71×10^{-3}	7.77×10^{-2}
19.8	19.72	8.47×10^{-2}	7.27×10^{-1}	6.61×10^{-3}	8.19×10^{-2}
20.0	19.92	8.25×10^{-2}	7.60×10^{-1}	7.64×10^{-3}	9.18×10^{-2}
	(Mar.)		7.63×10^{-1}	9.25×10^{-3}	–
	(Apr.)		7.55×10^{-1}	1.35×10^{-2}	–
20.2	20.17	8.00×10^{-2}	8.94×10^{-1}	7.56×10^{-3}	8.91×10^{-2}
20.5	20.42	8.00×10^{-2}	9.22×10^{-1}	1.01×10^{-2}	3.31×10^{-2}
20.8	20.67	8.00×10^{-2}	1.11	7.67×10^{-3}	1.04×10^{-1}
21.0	20.92	8.00×10^{-2}	1.09	8.42×10^{-3}	9.57×10^{-2}
	(Mar.)		1.12	1.07×10^{-2}	–
	(Apr.)		1.04	1.36×10^{-2}	–
21.2	21.17	8.00×10^{-2}	1.14	7.60×10^{-3}	1.18×10^{-1}
21.5	21.42	7.75×10^{-2}	1.26	1.14×10^{-2}	8.38×10^{-2}
21.8	21.67	7.75×10^{-2}	9.86×10^{-1}	7.07×10^{-3}	1.09×10^{-1}
22.0	21.92	7.75×10^{-2}	9.32×10^{-1}	8.18×10^{-3}	1.06×10^{-1}
	(Mar.)		9.65×10^{-1}	1.07×10^{-2}	–
	(Apr.)		8.86×10^{-1}	1.27×10^{-2}	–
22.2	22.17	7.75×10^{-2}	8.85×10^{-1}	6.89×10^{-3}	7.06×10^{-2}
22.5	22.43	7.50×10^{-2}	8.57×10^{-1}	1.14×10^{-2}	6.36×10^{-2}
22.8	22.68	7.50×10^{-2}	6.46×10^{-1}	6.00×10^{-3}	6.63×10^{-2}
23.0	22.93	7.50×10^{-2}	6.73×10^{-1}	7.55×10^{-3}	5.49×10^{-2}
	(Mar.)		6.78×10^{-1}	9.96×10^{-3}	–
	(Apr.)		6.68×10^{-1}	1.16×10^{-2}	–

Continued.

Table A.13 : (Continued)

$E_{\rm cm}$ (MeV)	$E'_{\rm cm}$ (MeV)	$\Delta E'_{\rm cm}$ (MeV)	σ (mb)	$\Delta\sigma_{\rm stat}$ (mb)	$\Delta\sigma_{\rm syst}$ (mb)
23.2	23.18	7.50×10^{-2}	8.56×10^{-1}	7.33×10^{-3}	9.26×10^{-2}
23.5	23.43	7.25×10^{-2}	1.09	1.26×10^{-2}	8.01×10^{-2}
24.0	23.93	7.25×10^{-2}	1.18	1.26×10^{-2}	9.71×10^{-2}
24.5	24.43	7.25×10^{-2}	1.24	1.26×10^{-2}	8.12×10^{-2}
25.0	24.93	7.00×10^{-2}	1.13	1.23×10^{-2}	9.22×10^{-2}

Table A.14: ^{12}C(^{12}C, ^{12}C[0^+_2] $\rightarrow 3\alpha$)^{12}C(2^+_1) reaction using reliable segments of SAKRA.

$E_{\rm cm}$ (MeV)	$E'_{\rm cm}$ (MeV)	$\Delta E'_{\rm cm}$ (MeV)	σ (mb)	$\Delta\sigma_{\rm stat}$ (mb)	$\Delta\sigma_{\rm syst}$ (mb)
17.5	17.41	8.75×10^{-2}	1.73×10^{-2}	1.49×10^{-3}	3.47×10^{-3}
18.0	17.91	8.75×10^{-2}	2.07×10^{-2}	1.89×10^{-3}	5.28×10^{-3}
18.5	18.41	8.50×10^{-2}	8.38×10^{-2}	3.11×10^{-3}	7.98×10^{-3}
19.0	18.91	8.50×10^{-2}	1.20×10^{-1}	2.91×10^{-3}	1.55×10^{-2}
	(Mar.)		1.22×10^{-1}	3.19×10^{-3}	–
	(Apr.)		1.10×10^{-1}	7.10×10^{-3}	–
19.2	19.11	8.50×10^{-2}	1.32×10^{-1}	2.68×10^{-3}	1.40×10^{-2}
19.4	19.32	8.25×10^{-2}	1.44×10^{-1}	3.11×10^{-3}	2.31×10^{-2}
19.5	19.42	8.25×10^{-2}	1.38×10^{-1}	4.00×10^{-3}	2.17×10^{-2}
19.6	19.51	8.50×10^{-2}	1.47×10^{-1}	3.28×10^{-3}	1.05×10^{-2}
19.8	19.72	8.47×10^{-2}	1.74×10^{-1}	3.77×10^{-3}	2.38×10^{-2}
20.0	19.92	8.25×10^{-2}	1.54×10^{-1}	3.89×10^{-3}	2.94×10^{-2}
	(Mar.)		1.46×10^{-1}	4.45×10^{-3}	–
	(Apr.)		1.79×10^{-1}	8.02×10^{-3}	–
20.2	20.17	8.00×10^{-2}	1.50×10^{-1}	3.88×10^{-3}	1.31×10^{-2}
20.5	20.42	8.00×10^{-2}	1.66×10^{-1}	5.12×10^{-3}	8.50×10^{-3}
20.8	20.67	8.00×10^{-2}	2.97×10^{-1}	5.43×10^{-3}	2.48×10^{-2}
21.0	20.92	8.00×10^{-2}	2.79×10^{-1}	5.33×10^{-3}	3.66×10^{-2}
	(Mar.)		2.65×10^{-1}	6.29×10^{-3}	–
	(Apr.)		3.15×10^{-1}	1.00×10^{-2}	–
21.2	21.17	8.00×10^{-2}	3.00×10^{-1}	5.34×10^{-3}	3.32×10^{-2}
21.5	21.42	7.75×10^{-2}	2.57×10^{-1}	6.20×10^{-3}	1.81×10^{-2}

Continued.

Table A.14 : (Continued)

E_{cm} (MeV)	E'_{cm} (MeV)	$\Delta E'_{cm}$ (MeV)	σ (mb)	$\Delta\sigma_{stat}$ (mb)	$\Delta\sigma_{syst}$ (mb)
21.8	21.67	7.75×10^{-2}	2.72×10^{-1}	4.70×10^{-3}	1.71×10^{-2}
22.0	21.92	7.75×10^{-2}	2.45×10^{-1}	4.77×10^{-3}	2.61×10^{-2}
	(Mar.)		2.44×10^{-1}	5.94×10^{-3}	–
	(Apr.)		2.48×10^{-1}	8.02×10^{-3}	–
22.2	22.17	7.75×10^{-2}	2.71×10^{-1}	4.42×10^{-3}	2.83×10^{-2}
22.5	22.43	7.50×10^{-2}	3.17×10^{-1}	7.41×10^{-3}	2.62×10^{-2}
22.8	22.68	7.50×10^{-2}	3.06×10^{-1}	4.65×10^{-3}	2.56×10^{-2}
23.0	22.93	7.50×10^{-2}	2.86×10^{-1}	5.26×10^{-3}	2.87×10^{-2}
	(Mar.)		2.75×10^{-1}	6.65×10^{-3}	–
	(Apr.)		3.05×10^{-1}	8.61×10^{-3}	–
23.2	23.18	7.50×10^{-2}	2.90×10^{-1}	4.61×10^{-3}	2.23×10^{-2}
23.5	23.43	7.25×10^{-2}	2.84×10^{-1}	6.79×10^{-3}	2.10×10^{-2}
24.0	23.93	7.25×10^{-2}	4.02×10^{-1}	7.45×10^{-3}	4.73×10^{-2}
24.5	24.43	7.25×10^{-2}	3.84×10^{-1}	7.04×10^{-3}	4.04×10^{-2}
25.0	24.93	7.00×10^{-2}	3.14×10^{-1}	6.61×10^{-3}	3.90×10^{-2}

Table A.15: $^{12}C(^{12}C, ^{12}C[0^+_2] \rightarrow 3\alpha)^{12}C(0^+_2)$ reaction using reliable segments of SAKRA.

E_{cm} (MeV)	E'_{cm} (MeV)	$\Delta E'_{cm}$ (MeV)	σ (mb)	$\Delta\sigma_{stat}$ (mb)	$\Delta\sigma_{syst}$ (mb)
17.5	17.41	8.75×10^{-2}	–	–	–
18.0	17.91	8.75×10^{-2}	–	–	–
18.5	18.41	8.50×10^{-2}	–	–	–
19.0	18.91	8.50×10^{-2}	1.90×10^{-3}	6.35×10^{-4}	2.57×10^{-3}
	(Mar.)		1.96×10^{-3}	6.94×10^{-4}	–
	(Apr.)		1.57×10^{-3}	1.57×10^{-3}	–
19.2	19.11	8.50×10^{-2}	1.75×10^{-3}	5.05×10^{-4}	2.08×10^{-3}
19.4	19.32	8.25×10^{-2}	3.49×10^{-3}	7.45×10^{-4}	2.32×10^{-3}
19.5	19.42	8.25×10^{-2}	2.32×10^{-3}	7.73×10^{-4}	2.46×10^{-3}
19.6	19.51	8.50×10^{-2}	3.38×10^{-3}	6.90×10^{-4}	1.38×10^{-3}
19.8	19.72	8.47×10^{-2}	4.80×10^{-3}	8.11×10^{-4}	8.84×10^{-4}
20.0	19.92	8.25×10^{-2}	7.24×10^{-3}	1.05×10^{-3}	4.29×10^{-3}

Continued.

Table A.15 : (Continued)

E_{cm} (MeV)	E'_{cm} (MeV)	$\Delta E'_{cm}$ (MeV)	σ (mb)	$\Delta\sigma_{stat}$ (mb)	$\Delta\sigma_{syst}$ (mb)
	(Mar.)		8.34×10^{-3}	1.35×10^{-3}	–
	(Apr.)		5.55×10^{-3}	1.67×10^{-3}	–
20.2	20.17	8.00×10^{-2}	8.81×10^{-3}	1.07×10^{-3}	1.11×10^{-3}
20.5	20.42	8.00×10^{-2}	1.27×10^{-2}	1.66×10^{-3}	5.46×10^{-3}
20.8	20.67	8.00×10^{-2}	1.37×10^{-2}	1.21×10^{-3}	2.00×10^{-3}
21.0	20.92	8.00×10^{-2}	1.87×10^{-2}	1.51×10^{-3}	4.97×10^{-3}
	(Mar.)		1.98×10^{-2}	1.92×10^{-3}	–
	(Apr.)		1.69×10^{-2}	2.46×10^{-3}	–
21.2	21.17	8.00×10^{-2}	2.12×10^{-2}	1.40×10^{-3}	4.91×10^{-3}
21.5	21.42	7.75×10^{-2}	3.40×10^{-2}	2.30×10^{-3}	5.20×10^{-3}
21.8	21.67	7.75×10^{-2}	4.57×10^{-2}	1.95×10^{-3}	5.42×10^{-3}
22.0	21.92	7.75×10^{-2}	5.11×10^{-2}	2.24×10^{-3}	9.65×10^{-3}
	(Mar.)		5.08×10^{-2}	2.79×10^{-3}	–
	(Apr.)		5.15×10^{-2}	3.79×10^{-3}	–
22.2	22.17	7.75×10^{-2}	6.29×10^{-2}	2.23×10^{-3}	7.31×10^{-3}
22.5	22.43	7.50×10^{-2}	6.16×10^{-2}	3.39×10^{-3}	9.62×10^{-4}
22.8	22.68	7.50×10^{-2}	6.35×10^{-2}	2.28×10^{-3}	1.18×10^{-2}
23.0	22.93	7.50×10^{-2}	5.96×10^{-2}	2.56×10^{-3}	6.77×10^{-3}
	(Mar.)		5.96×10^{-2}	3.26×10^{-3}	–
	(Apr.)		5.95×10^{-2}	4.15×10^{-3}	–
23.2	23.18	7.50×10^{-2}	5.25×10^{-2}	2.13×10^{-3}	5.87×10^{-3}
23.5	23.43	7.25×10^{-2}	5.46×10^{-2}	3.14×10^{-3}	8.27×10^{-3}
24.0	23.93	7.25×10^{-2}	3.60×10^{-2}	2.45×10^{-3}	6.41×10^{-3}
24.5	24.43	7.25×10^{-2}	3.25×10^{-2}	2.24×10^{-3}	6.11×10^{-3}
25.0	24.93	7.00×10^{-2}	4.79×10^{-2}	2.82×10^{-3}	5.77×10^{-3}

A.2.1 Angular distribution

Table A.16: Angular distribution for the $^{12}C(^{12}C, ^{12}C[0^+_2] \rightarrow 3\alpha)^{12}C(0^+_1)$ reaction using reliable segments of SAKRA.

E'_{cm} (MeV)	θ_{cm} (deg)	$d\sigma/d\Omega$ (μb/sr)	$\Delta d\sigma/d\Omega_{stat}$ (μb/sr)
17.41	46	7.23×10^1	1.26×10^1
	50	8.12×10^1	7.09
	54	5.26×10^1	4.12
	58	6.67×10^1	3.83
	62	4.88×10^1	3.01
	66	2.75×10^1	1.98
	70	6.31	9.74×10^{-1}
	74	7.55	1.04
	78	8.53	1.04
	82	2.50×10^1	1.84
	86	5.13×10^1	2.60
	90	7.23×10^1	3.05
	94	6.29×10^1	2.94
	98	2.78×10^1	1.95
	102	9.69	1.14
	106	9.30	1.16
	110	9.57	1.21
	114	2.76×10^1	2.08
	118	6.48×10^1	3.31
	122	8.57×10^1	4.05
	126	6.90×10^1	4.00
	130	8.90×10^1	4.99
	134	1.43×10^2	7.76
	138	1.49×10^2	1.05×10^1
	142	1.08×10^2	1.61×10^1
17.91	46	3.60×10^1	8.74
	50	6.81×10^1	7.03
	54	6.00×10^1	4.87
	58	8.32×10^1	4.86
	62	7.32×10^1	4.19
	66	5.86×10^1	3.27
	70	4.05×10^1	2.75
	74	1.68×10^1	1.73
	78	1.37×10^1	1.50
	82	4.74×10^1	2.81
	86	1.12×10^2	4.32
	90	1.24×10^2	4.45
	94	1.07×10^2	4.34
	98	5.07×10^1	2.89
	102	1.45×10^1	1.55
	106	2.09×10^1	1.90
	110	4.49×10^1	2.88
	114	6.97×10^1	3.69
	118	8.41×10^1	4.15
	122	8.38×10^1	4.44
	126	8.50×10^1	4.78
	130	1.14×10^2	6.22
	134	9.24×10^1	6.63
	138	6.57×10^1	7.49
	142	6.40×10^1	1.33×10^1
18.41	46	1.16×10^2	1.23×10^1
	50	1.30×10^2	7.76
	54	9.71×10^1	5.35
	58	1.02×10^2	4.82
	62	9.07×10^1	4.06
	66	4.38×10^1	2.49
	70	1.24×10^1	1.29

Continued.

Table A.16 : (Continued)

Continued.

Table A.16 : (Continued)

E'_{cm} (MeV)	θ_{cm} (deg)	$d\sigma/d\Omega$ (μb/sr)	$\Delta d\sigma/d\Omega_{stat}$ (μb/sr)
	74	2.04	5.09×10^{-1}
	78	9.10	1.05
	82	3.93×10^{1}	2.22
	86	7.95×10^{1}	3.10
	90	1.09×10^{2}	3.66
	94	8.07×10^{1}	3.17
	98	4.30×10^{1}	2.31
	102	1.06×10^{1}	1.16
	106	1.94	5.01×10^{-1}
	110	1.17×10^{1}	1.30
	114	4.07×10^{1}	2.39
	118	8.47×10^{1}	3.63
	122	1.10×10^{2}	4.26
	126	1.15×10^{2}	4.72
	130	1.48×10^{2}	5.97
	134	1.90×10^{2}	7.89
	138	2.32×10^{2}	1.19×10^{1}
	142	8.15×10^{1}	1.06×10^{1}
18.91	46	5.67×10^{1}	6.73
(Mar.)	50	5.88×10^{1}	4.31
	54	5.58×10^{1}	3.45
	58	5.28×10^{1}	2.95
	62	4.33×10^{1}	2.46
	66	3.09×10^{1}	1.86
	70	2.50×10^{1}	1.64
	74	1.10×10^{1}	1.02
	78	1.37×10^{1}	1.13
	82	5.97×10^{1}	2.41
	86	1.24×10^{2}	3.42
	90	1.64×10^{2}	3.91
	94	1.27×10^{2}	3.49

Continued.

Table A.16 : (Continued)

E'_{cm} (MeV)	θ_{cm} (deg)	$d\sigma/d\Omega$ (μb/sr)	$\Delta d\sigma/d\Omega_{stat}$ (μb/sr)
	98	6.37×10^{1}	2.43
	102	1.55×10^{1}	1.22
	106	1.12×10^{1}	1.04
	110	2.64×10^{1}	1.64
	114	3.76×10^{1}	2.00
	118	4.17×10^{1}	2.23
	122	5.47×10^{1}	2.64
	126	7.15×10^{1}	3.28
	130	8.81×10^{1}	3.90
	134	1.10×10^{2}	5.13
	138	1.27×10^{2}	7.40
	142	8.87×10^{1}	9.85
18.91	46	4.52×10^{1}	1.43×10^{1}
(Apr.)	50	5.15×10^{1}	9.56
	54	5.04×10^{1}	7.13
	58	4.34×10^{1}	5.85
	62	2.70×10^{1}	4.27
	66	3.62×10^{1}	4.45
	70	2.15×10^{1}	3.54
	74	7.48	2.00
	78	1.60×10^{1}	2.92
	82	6.08×10^{1}	5.85
	86	1.49×10^{2}	8.96
	90	1.61×10^{2}	9.29
	94	1.26×10^{2}	8.34
	98	7.25×10^{1}	6.24
	102	1.41×10^{1}	2.83
	106	9.68	2.35
	110	2.43×10^{1}	3.84
	114	4.34×10^{1}	5.23
	118	3.84×10^{1}	5.23

Continued.

Table A.16 : (Continued)

E'_{cm} (MeV)	θ_{cm} (deg)	$d\sigma/d\Omega$ (μb/sr)	$\Delta d\sigma/d\Omega_{stat}$ (μb/sr)
	122	6.42×10^{1}	7.13
	126	8.33×10^{1}	8.88
	130	1.02×10^{2}	1.08×10^{1}
	134	1.00×10^{2}	1.28×10^{1}
	138	1.35×10^{2}	2.03×10^{1}
	142	1.08×10^{2}	3.00×10^{1}
19.11	46	3.46×10^{1}	4.05
	50	3.15×10^{1}	2.57
	54	4.07×10^{1}	2.14
	58	4.37×10^{1}	2.01
	62	5.08×10^{1}	1.96
	66	4.15×10^{1}	1.62
	70	2.36×10^{1}	1.26
	74	7.41	6.71×10^{-1}
	78	1.54×10^{1}	9.73×10^{-1}
	82	5.28×10^{1}	1.83
	86	9.49×10^{1}	2.41
	90	1.15×10^{2}	2.70
	94	9.73×10^{1}	2.49
	98	6.02×10^{1}	1.94
	102	1.93×10^{1}	1.12
	106	7.13	6.89×10^{-1}
	110	2.92×10^{1}	1.43
	114	5.11×10^{1}	1.96
	118	6.63×10^{1}	2.31
	122	7.62×10^{1}	2.64
	126	7.01×10^{1}	2.71
	130	7.12×10^{1}	3.10
	134	1.03×10^{2}	4.39
	138	1.57×10^{2}	7.35
	142	1.26×10^{2}	1.07×10^{1}

Continued.

Table A.16 : (Continued)

E'_{cm} (MeV)	θ_{cm} (deg)	$d\sigma/d\Omega$ (μb/sr)	$\Delta d\sigma/d\Omega_{stat}$ (μb/sr)
19.32	46	4.74×10^{1}	4.83
	50	4.44×10^{1}	3.34
	54	3.65×10^{1}	2.26
	58	3.70×10^{1}	2.04
	62	4.36×10^{1}	1.96
	66	4.98×10^{1}	1.87
	70	4.74×10^{1}	1.91
	74	2.72×10^{1}	1.40
	78	1.06×10^{1}	8.85×10^{-1}
	82	5.28×10^{1}	2.01
	86	1.33×10^{2}	3.01
	90	1.90×10^{2}	3.83
	94	1.51×10^{2}	3.44
	98	5.51×10^{1}	1.96
	102	1.07×10^{1}	9.31×10^{-1}
	106	2.63×10^{1}	1.46
	110	5.76×10^{1}	2.19
	114	7.53×10^{1}	2.61
	118	6.54×10^{1}	2.56
	122	5.71×10^{1}	2.46
	126	5.57×10^{1}	2.67
	130	8.37×10^{1}	3.61
	134	1.41×10^{2}	5.68
	138	1.74×10^{2}	7.97
	142	1.39×10^{2}	1.25×10^{1}
19.42	46	7.68×10^{1}	9.38
	50	7.38×10^{1}	5.73
	54	4.22×10^{1}	3.86
	58	5.30×10^{1}	3.76
	62	5.51×10^{1}	3.32
	66	6.05×10^{1}	3.20

Continued.

Table A.16 : (Continued)

E'_{cm} (MeV)	θ_{cm} (deg)	$d\sigma/d\Omega$ (μb/sr)	$\Delta d\sigma/d\Omega_{stat}$ (μb/sr)
	70	6.30×10^{1}	3.30
	74	2.80×10^{1}	2.02
	78	8.44	1.09
	82	5.32×10^{1}	2.84
	86	1.33×10^{2}	4.15
	90	1.99×10^{2}	5.40
	94	1.46×10^{2}	4.44
	98	4.90×10^{1}	2.50
	102	8.74	1.07
	106	3.11×10^{1}	2.13
	110	6.83×10^{1}	3.21
	114	6.23×10^{1}	2.97
	118	6.21×10^{1}	3.32
	122	5.68×10^{1}	3.19
	126	5.70×10^{1}	3.40
	130	8.13×10^{1}	4.38
	134	1.16×10^{2}	5.72
	138	1.15×10^{2}	7.49
	142	8.45×10^{1}	9.69
19.51	46	6.67×10^{1}	6.31
	50	6.76×10^{1}	4.23
	54	5.28×10^{1}	2.70
	58	5.20×10^{1}	2.46
	62	5.50×10^{1}	2.24
	66	5.78×10^{1}	2.11
	70	5.01×10^{1}	2.03
	74	2.23×10^{1}	1.29
	78	8.66	8.54×10^{-1}
	82	4.62×10^{1}	1.94
	86	1.16×10^{2}	2.89
	90	1.69×10^{2}	3.77

Continued.

Table A.16 : (Continued)

E'_{cm} (MeV)	θ_{cm} (deg)	$d\sigma/d\Omega$ (μb/sr)	$\Delta d\sigma/d\Omega_{stat}$ (μb/sr)
	94	1.25×10^{2}	3.15
	98	4.47×10^{1}	1.83
	102	1.16×10^{1}	9.90×10^{-1}
	106	2.55×10^{1}	1.51
	110	5.31×10^{1}	2.17
	114	6.37×10^{1}	2.39
	118	6.81×10^{1}	2.65
	122	6.32×10^{1}	2.74
	126	8.63×10^{1}	3.36
	130	1.08×10^{2}	4.15
	134	1.36×10^{2}	5.51
	138	1.30×10^{2}	6.62
	142	9.87×10^{1}	9.92
19.72	46	8.16×10^{1}	7.11
	50	8.54×10^{1}	4.59
	54	8.60×10^{1}	3.56
	58	6.64×10^{1}	2.70
	62	4.63×10^{1}	2.02
	66	3.08×10^{1}	1.56
	70	1.72×10^{1}	1.18
	74	8.17	8.01×10^{-1}
	78	8.34	8.14×10^{-1}
	82	3.05×10^{1}	1.58
	86	7.08×10^{1}	2.30
	90	9.11×10^{1}	2.72
	94	7.73×10^{1}	2.50
	98	3.51×10^{1}	1.66
	102	8.46	8.30×10^{-1}
	106	1.07×10^{1}	9.40×10^{-1}
	110	2.06×10^{1}	1.33
	114	3.42×10^{1}	1.73

Continued.

Table A.16 : (Continued)

E'_{cm} (MeV)	θ_{cm} (deg)	$d\sigma/d\Omega$ (μb/sr)	$\Delta d\sigma/d\Omega_{stat}$ (μb/sr)
	118	4.80×10^{1}	2.16
	122	7.78×10^{1}	2.91
	126	1.01×10^{2}	3.44
	130	1.48×10^{2}	4.75
	134	1.59×10^{2}	5.74
	138	1.43×10^{2}	6.85
	142	1.54×10^{2}	1.40×10^{1}
19.92	46	1.15×10^{2}	1.18×10^{1}
(Mar.)	50	1.36×10^{2}	8.11
	54	1.10×10^{2}	6.00
	58	9.35×10^{1}	4.89
	62	4.87×10^{1}	3.30
	66	2.95×10^{1}	2.39
	70	1.65×10^{1}	1.81
	74	5.28	9.06×10^{-1}
	78	1.50×10^{1}	1.58
	82	4.21×10^{1}	2.72
	86	5.93×10^{1}	2.90
	90	7.19×10^{1}	3.28
	94	6.35×10^{1}	3.05
	98	3.52×10^{1}	2.23
	102	1.24×10^{1}	1.31
	106	6.82	1.02
	110	1.42×10^{1}	1.45
	114	3.43×10^{1}	2.36
	118	4.74×10^{1}	2.90
	122	8.34×10^{1}	3.98
	126	1.26×10^{2}	4.93
	130	1.89×10^{2}	7.00
	134	1.41×10^{2}	6.55
	138	9.15×10^{1}	6.04

Continued.

Table A.16 : (Continued)

E'_{cm} (MeV)	θ_{cm} (deg)	$d\sigma/d\Omega$ (μb/sr)	$\Delta d\sigma/d\Omega_{stat}$ (μb/sr)
	142	8.75×10^{1}	8.98
19.92	46	7.01×10^{1}	1.26×10^{1}
(Apr.)	50	1.12×10^{2}	1.07×10^{1}
	54	9.59×10^{1}	7.09
	58	7.04×10^{1}	5.45
	62	4.46×10^{1}	4.04
	66	2.19×10^{1}	2.63
	70	1.94×10^{1}	2.55
	74	4.13	1.10
	78	9.95	1.79
	82	2.91×10^{1}	3.17
	86	6.60×10^{1}	4.40
	90	7.56×10^{1}	4.96
	94	6.22×10^{1}	4.38
	98	3.49×10^{1}	3.24
	102	1.67×10^{1}	2.29
	106	8.65	1.70
	110	9.12	1.69
	114	4.04×10^{1}	3.78
	118	4.98×10^{1}	4.42
	122	9.10×10^{1}	6.34
	126	1.30×10^{2}	7.72
	130	1.88×10^{2}	1.10×10^{1}
	134	1.66×10^{2}	1.19×10^{1}
	138	1.30×10^{2}	1.31×10^{1}
	142	1.75×10^{2}	2.67×10^{1}
20.17	46	4.07×10^{1}	5.04
	50	8.73×10^{1}	5.05
	54	8.50×10^{1}	3.55
	58	7.89×10^{1}	3.14
	62	7.16×10^{1}	2.68

Continued.

Table A.16 : (Continued)

E'_{cm} (MeV)	θ_{cm} (deg)	$d\sigma/d\Omega$ (μb/sr)	$\Delta d\sigma/d\Omega_{stat}$ (μb/sr)
	66	8.20×10^{1}	2.79
	70	4.84×10^{1}	2.18
	74	8.68	8.86×10^{-1}
	78	1.58×10^{1}	1.23
	82	5.57×10^{1}	2.33
	86	7.61×10^{1}	2.48
	90	9.50×10^{1}	3.05
	94	8.87×10^{1}	2.94
	98	5.48×10^{1}	2.17
	102	2.10×10^{1}	1.40
	106	8.46	8.91×10^{-1}
	110	5.44×10^{1}	2.29
	114	9.54×10^{1}	3.07
	118	9.90×10^{1}	3.44
	122	8.75×10^{1}	3.27
	126	1.29×10^{2}	4.26
	130	1.41×10^{2}	4.80
	134	9.35×10^{1}	4.66
	138	1.03×10^{2}	6.04
	142	2.89×10^{2}	1.99×10^{1}
20.42	46	1.24×10^{1}	3.74
	50	3.33×10^{1}	4.37
	54	7.63×10^{1}	5.37
	58	4.88×10^{1}	3.78
	62	6.19×10^{1}	3.90
	66	9.50×10^{1}	4.84
	70	7.10×10^{1}	3.91
	74	2.64×10^{1}	2.27
	78	1.15×10^{1}	1.46
	82	5.59×10^{1}	3.20
	86	1.20×10^{2}	4.32

Continued.

Table A.16 : (Continued)

E'_{cm} (MeV)	θ_{cm} (deg)	$d\sigma/d\Omega$ (μb/sr)	$\Delta d\sigma/d\Omega_{stat}$ (μb/sr)
	90	1.34×10^{2}	4.79
	94	1.19×10^{2}	4.33
	98	7.08×10^{1}	3.34
	102	1.63×10^{1}	1.67
	106	2.57×10^{1}	2.10
	110	8.23×10^{1}	3.74
	114	1.27×10^{2}	4.84
	118	1.07×10^{2}	4.51
	122	8.35×10^{1}	4.11
	126	1.18×10^{2}	5.41
	130	9.41×10^{1}	5.04
	134	5.63×10^{1}	4.29
	138	8.47×10^{1}	6.46
	142	1.58×10^{2}	1.42×10^{1}
20.67	46	2.12×10^{1}	3.35
	50	6.21×10^{1}	4.21
	54	4.94×10^{1}	2.62
	58	3.71×10^{1}	2.04
	62	7.96×10^{1}	2.68
	66	1.57×10^{2}	3.72
	70	1.40×10^{2}	3.63
	74	4.86×10^{1}	2.04
	78	1.25×10^{1}	1.06
	82	7.13×10^{1}	2.51
	86	1.39×10^{2}	3.26
	90	1.93×10^{2}	4.15
	94	1.61×10^{2}	3.62
	98	7.63×10^{1}	2.52
	102	1.18×10^{1}	1.02
	106	4.28×10^{1}	1.91
	110	1.57×10^{2}	3.93

Continued.

Table A.16 : (Continued)

E'_{cm} (MeV)	θ_{cm} (deg)	$d\sigma/d\Omega$ (μb/sr)	$\Delta d\sigma/d\Omega_{stat}$ (μb/sr)
	114	1.96×10^2	4.53
	118	1.19×10^2	3.51
	122	4.65×10^1	2.24
	126	7.59×10^1	3.12
	130	8.63×10^1	3.55
	134	4.40×10^1	2.98
	138	5.87×10^1	4.05
	142	1.85×10^2	1.13×10^1
20.92	46	9.37	3.12
(Mar.)	50	1.55×10^1	3.03
	54	2.65×10^1	3.08
	58	1.77×10^1	2.25
	62	8.53×10^1	4.50
	66	1.94×10^2	7.01
	70	1.53×10^2	6.01
	74	6.14×10^1	3.51
	78	1.25×10^1	1.51
	82	7.08×10^1	3.64
	86	1.67×10^2	5.05
	90	2.14×10^2	6.03
	94	1.99×10^2	5.83
	98	9.62×10^1	3.96
	102	1.40×10^1	1.54
	106	5.01×10^1	2.87
	110	1.67×10^2	5.41
	114	2.13×10^2	6.15
	118	1.32×10^2	5.05
	122	3.55×10^1	2.69
	126	2.71×10^1	2.40
	130	4.50×10^1	3.44
	134	2.31×10^1	2.67

Continued.

Table A.16 : (Continued)

E'_{cm} (MeV)	θ_{cm} (deg)	$d\sigma/d\Omega$ (μb/sr)	$\Delta d\sigma/d\Omega_{stat}$ (μb/sr)
	138	5.31×10^1	4.91
	142	8.91×10^1	8.38
20.92	46	8.09	3.62
(Apr.)	50	3.06×10^1	5.50
	54	1.71×10^1	2.67
	58	2.01×10^1	2.69
	62	8.16×10^1	4.90
	66	1.72×10^2	7.31
	70	1.52×10^2	7.03
	74	4.70×10^1	3.60
	78	9.28	1.67
	82	6.00×10^1	4.24
	86	1.48×10^2	6.27
	90	2.00×10^2	7.85
	94	1.70×10^2	7.07
	98	8.18×10^1	4.90
	102	1.22×10^1	1.96
	106	4.27×10^1	3.54
	110	1.53×10^2	6.99
	114	2.07×10^2	8.31
	118	1.17×10^2	6.52
	122	3.74×10^1	3.78
	126	2.76×10^1	3.37
	130	4.21×10^1	4.59
	134	2.66×10^1	4.20
	138	4.89×10^1	7.14
	142	1.24×10^2	1.79×10^1
21.17	46	8.24	1.94
	50	2.50×10^1	2.68
	54	1.48×10^1	1.33
	58	1.70×10^1	1.34

Continued.

Table A.16 : (Continued)

E'_{cm} (MeV)	θ_{cm} (deg)	$d\sigma/d\Omega$ (μb/sr)	$\Delta d\sigma/d\Omega_{stat}$ (μb/sr)
	62	9.79×10^{1}	2.89
	66	1.90×10^{2}	4.19
	70	1.61×10^{2}	4.02
	74	6.09×10^{1}	2.17
	78	1.49×10^{1}	1.19
	82	6.37×10^{1}	2.31
	86	1.68×10^{2}	3.64
	90	2.34×10^{2}	4.57
	94	1.80×10^{2}	3.87
	98	7.72×10^{1}	2.57
	102	9.81	9.11×10^{-1}
	106	5.96×10^{1}	2.22
	110	1.73×10^{2}	3.92
	114	2.29×10^{2}	4.70
	118	1.40×10^{2}	3.81
	122	3.51×10^{1}	1.95
	126	1.86×10^{1}	1.45
	130	4.59×10^{1}	2.59
	134	3.37×10^{1}	2.65
	138	2.90×10^{1}	2.80
	142	1.35×10^{2}	1.09×10^{1}
21.42	46	1.21×10^{1}	3.50
	50	2.52×10^{1}	3.71
	54	7.01	1.50
	58	1.83×10^{1}	2.27
	62	1.07×10^{2}	5.13
	66	2.08×10^{2}	7.51
	70	1.99×10^{2}	7.06
	74	1.01×10^{2}	4.75
	78	2.61×10^{1}	2.32
	82	8.03×10^{1}	3.76

Continued.

Table A.16 : (Continued)

E'_{cm} (MeV)	θ_{cm} (deg)	$d\sigma/d\Omega$ (μb/sr)	$\Delta d\sigma/d\Omega_{stat}$ (μb/sr)
	86	1.91×10^{2}	5.35
	90	2.77×10^{2}	6.96
	94	2.20×10^{2}	5.96
	98	7.65×10^{1}	3.53
	102	1.90×10^{1}	1.77
	106	9.78×10^{1}	4.14
	110	2.00×10^{2}	5.80
	114	2.26×10^{2}	6.51
	118	1.25×10^{2}	4.83
	122	3.38×10^{1}	2.66
	126	1.49×10^{1}	1.78
	130	3.61×10^{1}	2.97
	134	2.52×10^{1}	2.72
	138	1.77×10^{1}	2.67
	142	7.78×10^{1}	9.05
21.67	46	2.21×10^{1}	3.41
	50	3.18×10^{1}	2.91
	54	8.59	1.01
	58	2.67×10^{1}	1.70
	62	1.14×10^{2}	3.14
	66	1.69×10^{2}	3.99
	70	1.47×10^{2}	3.98
	74	6.19×10^{1}	2.29
	78	2.30×10^{1}	1.43
	82	6.58×10^{1}	2.39
	86	1.06×10^{2}	2.79
	90	1.52×10^{2}	3.71
	94	1.24×10^{2}	3.18
	98	7.03×10^{1}	2.48
	102	2.56×10^{1}	1.46
	106	5.59×10^{1}	2.21

Continued.

Table A.16 : (Continued)

E'_{cm} (MeV)	θ_{cm} (deg)	$d\sigma/d\Omega$ (μb/sr)	$\Delta d\sigma/d\Omega_{stat}$ (μb/sr)
	110	1.37×10^2	3.54
	114	1.95×10^2	4.34
	118	1.44×10^2	3.73
	122	5.38×10^1	2.42
	126	1.39×10^1	1.25
	130	3.66×10^1	2.22
	134	4.10×10^1	2.67
	138	3.80×10^1	3.34
	142	7.30×10^1	6.96
21.92	46	4.01×10^1	6.19
(Mar.)	50	4.68×10^1	5.17
	54	1.30×10^1	2.08
	58	6.98×10^1	4.32
	62	1.78×10^2	6.94
	66	1.87×10^2	7.47
	70	9.52×10^1	5.18
	74	3.83×10^1	3.01
	78	2.86×10^1	2.51
	82	6.24×10^1	3.47
	86	6.08×10^1	3.15
	90	6.63×10^1	3.55
	94	6.13×10^1	3.22
	98	5.15×10^1	2.96
	102	3.55×10^1	2.51
	106	3.58×10^1	2.53
	110	1.01×10^2	4.18
	114	2.19×10^2	6.68
	118	2.10×10^2	6.59
	122	8.67×10^1	4.35
	126	1.68×10^1	1.97
	130	5.47×10^1	3.92

Continued.

Table A.16 : (Continued)

E'_{cm} (MeV)	θ_{cm} (deg)	$d\sigma/d\Omega$ (μb/sr)	$\Delta d\sigma/d\Omega_{stat}$ (μb/sr)
	134	6.22×10^1	4.50
	138	3.99×10^1	3.86
	142	6.50×10^1	7.36
21.92	46	3.44×10^1	7.51
(Apr.)	50	4.24×10^1	6.54
	54	1.31×10^1	2.28
	58	5.10×10^1	4.22
	62	1.65×10^2	7.18
	66	1.57×10^2	7.09
	70	1.00×10^2	5.98
	74	2.98×10^1	2.92
	78	2.32×10^1	2.66
	82	4.48×10^1	3.54
	86	5.39×10^1	3.82
	90	6.34×10^1	4.57
	94	5.66×10^1	3.99
	98	5.09×10^1	3.80
	102	3.14×10^1	3.08
	106	2.52×10^1	2.75
	110	9.24×10^1	5.33
	114	1.93×10^2	8.21
	118	1.98×10^2	8.26
	122	9.14×10^1	5.96
	126	2.36×10^1	3.10
	130	4.99×10^1	4.99
	134	7.01×10^1	6.87
	138	6.67×10^1	8.61
	142	1.08×10^2	1.64×10^1
22.17	46	5.89×10^1	5.22
	50	4.37×10^1	3.41
	54	1.17×10^1	1.14

Continued.

Table A.16 : (Continued)

E'_{cm} (MeV)	θ_{cm} (deg)	$d\sigma/d\Omega$ (μb/sr)	$\Delta d\sigma/d\Omega_{stat}$ (μb/sr)
	58	8.03×10^{1}	2.89
	62	1.79×10^{2}	3.95
	66	1.60×10^{2}	3.84
	70	7.49×10^{1}	2.72
	74	1.14×10^{1}	9.62×10^{-1}
	78	2.86×10^{1}	1.60
	82	3.90×10^{1}	1.80
	86	3.63×10^{1}	1.69
	90	3.42×10^{1}	1.79
	94	3.56×10^{1}	1.68
	98	4.21×10^{1}	1.87
	102	3.33×10^{1}	1.74
	106	1.18×10^{1}	1.00
	110	6.14×10^{1}	2.32
	114	1.72×10^{2}	3.98
	118	2.16×10^{2}	4.53
	122	1.25×10^{2}	3.72
	126	2.48×10^{1}	1.72
	130	4.42×10^{1}	2.52
	134	9.69×10^{1}	4.32
	138	1.01×10^{2}	5.37
	142	1.17×10^{2}	8.23
22.43	46	5.55×10^{1}	8.28
	50	4.03×10^{1}	5.43
	54	1.72×10^{1}	2.68
	58	5.88×10^{1}	4.51
	62	1.48×10^{2}	7.33
	66	1.81×10^{2}	8.82
	70	9.37×10^{1}	5.63
	74	1.53×10^{1}	2.16
	78	1.45×10^{1}	2.16

Continued.

Table A.16 : (Continued)

E'_{cm} (MeV)	θ_{cm} (deg)	$d\sigma/d\Omega$ (μb/sr)	$\Delta d\sigma/d\Omega_{stat}$ (μb/sr)
	82	3.43×10^{1}	2.83
	86	6.61×10^{1}	3.80
	90	1.02×10^{2}	4.92
	94	7.99×10^{1}	4.16
	98	3.80×10^{1}	2.84
	102	1.84×10^{1}	2.08
	106	1.50×10^{1}	1.92
	110	7.15×10^{1}	3.95
	114	1.64×10^{2}	6.15
	118	1.75×10^{2}	6.68
	122	8.22×10^{1}	4.78
	126	1.66×10^{1}	2.20
	130	4.48×10^{1}	3.77
	134	6.64×10^{1}	4.96
	138	6.28×10^{1}	5.30
	142	5.90×10^{1}	7.05
22.68	46	2.50×10^{1}	3.47
	50	2.31×10^{1}	2.57
	54	1.36×10^{1}	1.26
	58	6.36×10^{1}	2.61
	62	1.19×10^{2}	3.48
	66	9.90×10^{1}	3.35
	70	5.31×10^{1}	2.33
	74	1.20×10^{1}	9.97×10^{-1}
	78	4.62	6.54×10^{-1}
	82	2.76×10^{1}	1.56
	86	6.31×10^{1}	2.28
	90	9.33×10^{1}	3.02
	94	6.69×10^{1}	2.38
	98	3.14×10^{1}	1.72
	102	7.33	8.14×10^{-1}

Continued.

Table A.16 : (Continued)

E'_{cm} (MeV)	θ_{cm} (deg)	$d\sigma/d\Omega$ (μb/sr)	$\Delta d\sigma/d\Omega_{stat}$ (μb/sr)
	106	1.27×10^1	1.08
	110	4.92×10^1	2.13
	114	1.04×10^2	3.18
	118	1.36×10^2	3.86
	122	8.76×10^1	3.12
	126	3.14×10^1	1.93
	130	2.60×10^1	1.97
	134	3.88×10^1	2.74
	138	5.84×10^1	4.09
	142	9.90×10^1	7.59
22.93	46	2.78×10^1	5.93
(Mar.)	50	1.99×10^1	3.97
	54	1.62×10^1	2.59
	58	1.05×10^2	6.00
	62	1.62×10^2	8.47
	66	9.49×10^1	6.42
	70	3.70×10^1	3.51
	74	8.37	1.61
	78	8.35	1.58
	82	3.38×10^1	3.14
	86	5.74×10^1	3.62
	90	8.84×10^1	4.51
	94	6.38×10^1	3.57
	98	3.67×10^1	2.69
	102	1.53×10^1	1.88
	106	5.15	1.07
	110	2.73×10^1	2.37
	114	8.21×10^1	4.25
	118	1.68×10^2	6.59
	122	1.39×10^2	6.43
	126	3.73×10^1	3.16

Continued.

Table A.16 : (Continued)

E'_{cm} (MeV)	θ_{cm} (deg)	$d\sigma/d\Omega$ (μb/sr)	$\Delta d\sigma/d\Omega_{stat}$ (μb/sr)
	130	1.44×10^1	2.03
	134	2.93×10^1	3.18
	138	4.70×10^1	4.40
	142	9.88×10^1	8.70
22.93	46	3.21×10^1	7.79
(Apr.)	50	1.33×10^1	3.69
	54	1.74×10^1	2.72
	58	8.37×10^1	5.58
	62	1.27×10^2	6.77
	66	8.33×10^1	5.79
	70	2.82×10^1	3.19
	74	5.26	1.28
	78	1.06×10^1	1.84
	82	3.54×10^1	3.30
	86	5.37×10^1	4.00
	90	9.00×10^1	5.51
	94	6.67×10^1	4.52
	98	2.91×10^1	3.08
	102	1.70×10^1	2.35
	106	7.36	1.57
	110	2.89×10^1	3.06
	114	9.24×10^1	5.68
	118	1.52×10^2	7.56
	122	1.33×10^2	7.63
	126	4.05×10^1	4.20
	130	1.64×10^1	3.04
	134	5.41×10^1	6.16
	138	7.71×10^1	8.73
	142	1.22×10^2	1.53×10^1
23.18	46	6.84×10^1	5.78
	50	4.52×10^1	3.55

Continued.

Table A.16 : (Continued)

E'_{cm} (MeV)	θ_{cm} (deg)	$d\sigma/d\Omega$ (μb/sr)	$\Delta d\sigma/d\Omega_{stat}$ (μb/sr)
	54	2.09×10^{1}	1.61
	58	1.20×10^{2}	3.70
	62	1.62×10^{2}	4.13
	66	9.00×10^{1}	3.24
	70	2.66×10^{1}	1.71
	74	4.69	6.57×10^{-1}
	78	1.58×10^{1}	1.26
	82	3.09×10^{1}	1.69
	86	6.29×10^{1}	2.40
	90	7.73×10^{1}	2.75
	94	7.17×10^{1}	2.58
	98	3.80×10^{1}	1.91
	102	1.85×10^{1}	1.39
	106	7.12	8.52×10^{-1}
	110	2.10×10^{1}	1.46
	114	1.02×10^{2}	3.26
	118	1.97×10^{2}	4.71
	122	1.79×10^{2}	4.80
	126	4.89×10^{1}	2.67
	130	4.06×10^{1}	2.61
	134	9.44×10^{1}	4.29
	138	1.17×10^{2}	5.96
	142	1.75×10^{2}	9.69
23.43	46	9.15×10^{1}	9.70
	50	1.06×10^{2}	8.14
	54	3.12×10^{1}	3.43
	58	1.69×10^{2}	7.73
	62	2.43×10^{2}	9.93
	66	1.35×10^{2}	6.97
	70	3.48×10^{1}	3.36
	74	1.65×10^{1}	2.38

Continued.

Table A.16 : (Continued)

E'_{cm} (MeV)	θ_{cm} (deg)	$d\sigma/d\Omega$ (μb/sr)	$\Delta d\sigma/d\Omega_{stat}$ (μb/sr)
	78	2.30×10^{1}	2.64
	82	4.22×10^{1}	3.34
	86	6.09×10^{1}	3.61
	90	9.09×10^{1}	4.47
	94	6.87×10^{1}	3.68
	98	4.56×10^{1}	3.12
	102	2.70×10^{1}	2.42
	106	1.81×10^{1}	1.98
	110	2.55×10^{1}	2.29
	114	1.31×10^{2}	5.41
	118	2.37×10^{2}	7.33
	122	1.90×10^{2}	7.04
	126	4.48×10^{1}	3.35
	130	7.47×10^{1}	4.88
	134	1.47×10^{2}	7.08
	138	1.06×10^{2}	6.76
	142	1.37×10^{2}	1.03×10^{1}
23.93	46	1.03×10^{2}	9.45
	50	1.09×10^{2}	7.68
	54	3.01×10^{1}	3.16
	58	1.44×10^{2}	6.89
	62	2.20×10^{2}	9.16
	66	1.42×10^{2}	7.00
	70	5.57×10^{1}	4.10
	74	5.81×10^{1}	4.34
	78	3.26×10^{1}	3.05
	82	3.57×10^{1}	3.08
	86	8.92×10^{1}	4.56
	90	1.39×10^{2}	5.49
	94	9.24×10^{1}	4.01
	98	2.83×10^{1}	2.35

Continued.

Table A.16 : (Continued)

E'_{cm} (MeV)	θ_{cm} (deg)	$d\sigma/d\Omega$ (μb/sr)	$\Delta d\sigma/d\Omega_{stat}$ (μb/sr)
	102	2.84×10^{1}	2.34
	106	5.23×10^{1}	3.13
	110	5.90×10^{1}	3.42
	114	1.21×10^{2}	4.86
	118	2.20×10^{2}	6.83
	122	1.60×10^{2}	5.99
	126	3.13×10^{1}	2.75
	130	1.03×10^{2}	5.18
	134	1.73×10^{2}	7.22
	138	1.21×10^{2}	7.23
	142	1.13×10^{2}	8.21
24.43	46	1.36×10^{2}	1.10×10^{1}
	50	1.64×10^{2}	9.08
	54	3.96×10^{1}	3.44
	58	1.09×10^{2}	6.12
	62	1.79×10^{2}	8.66
	66	1.14×10^{2}	5.98
	70	9.80×10^{1}	5.35
	74	7.85×10^{1}	4.80
	78	2.61×10^{1}	2.75
	82	3.21×10^{1}	2.83
	86	1.09×10^{2}	5.10
	90	1.79×10^{2}	6.19
	94	1.05×10^{2}	4.10
	98	3.13×10^{1}	2.46
	102	2.36×10^{1}	2.05
	106	7.14×10^{1}	3.62
	110	9.62×10^{1}	4.28
	114	1.18×10^{2}	4.71
	118	1.56×10^{2}	5.56
	122	1.17×10^{2}	4.89

Continued.

Table A.16 : (Continued)

E'_{cm} (MeV)	θ_{cm} (deg)	$d\sigma/d\Omega$ (μb/sr)	$\Delta d\sigma/d\Omega_{stat}$ (μb/sr)
	126	4.09×10^{1}	3.08
	130	1.35×10^{2}	5.76
	134	2.40×10^{2}	8.54
	138	1.34×10^{2}	7.01
	142	1.16×10^{2}	8.33
24.93	46	1.10×10^{2}	9.49
	50	1.36×10^{2}	8.45
	54	2.36×10^{1}	2.71
	58	4.66×10^{1}	4.15
	62	8.31×10^{1}	6.11
	66	8.03×10^{1}	5.18
	70	9.78×10^{1}	5.36
	74	1.05×10^{2}	5.59
	78	4.48×10^{1}	3.82
	82	3.34×10^{1}	3.16
	86	1.31×10^{2}	5.82
	90	2.31×10^{2}	7.43
	94	1.48×10^{2}	5.12
	98	3.31×10^{1}	2.59
	102	3.62×10^{1}	2.66
	106	1.13×10^{2}	4.72
	110	1.14×10^{2}	4.75
	114	7.92×10^{1}	3.95
	118	7.86×10^{1}	3.97
	122	5.10×10^{1}	3.43
	126	2.23×10^{1}	2.34
	130	1.27×10^{2}	5.71
	134	1.94×10^{2}	7.53
	138	9.73×10^{1}	6.24
	142	6.61×10^{1}	6.17

Table A.17: Angular distribution for the $^{12}C(^{12}C, ^{12}C[0_2^+] \rightarrow 3\alpha)^{12}C(2_1^+)$ reaction using reliable segments of SAKRA.

E'_{cm} (MeV)	θ_{cm} (deg)	$d\sigma/d\Omega$ (μb/sr)	$\Delta d\sigma/d\Omega_{stat}$ (μb/sr)
17.41	54	0.00	0.00
	58	1.78	1.78
	62	8.30×10^{-1}	8.30×10^{-1}
	66	1.89	9.47×10^{-1}
	70	0.00	0.00
	74	2.10	7.41×10^{-1}
	78	1.29	5.28×10^{-1}
	82	2.71	7.25×10^{-1}
	86	3.02	7.32×10^{-1}
	90	2.44	6.30×10^{-1}
	94	3.11	7.13×10^{-1}
	98	1.49	4.98×10^{-1}
	102	1.15	4.35×10^{-1}
	106	1.73	5.47×10^{-1}
	110	1.43	5.06×10^{-1}
	114	8.07×10^{-1}	4.03×10^{-1}
	118	4.33×10^{-1}	3.06×10^{-1}
	122	8.14×10^{-1}	4.70×10^{-1}
	126	3.33×10^{-1}	3.33×10^{-1}
	130	1.02	7.19×10^{-1}
	134	1.95	1.38
	138	2.13	2.13
	142	0.00	0.00
17.91	54	4.59	4.59
	58	3.07	2.17
	62	0.00	0.00
	66	3.29	1.24
	70	2.52	8.91×10^{-1}

Continued.

Table A.17 : (Continued)

E'_{cm} (MeV)	θ_{cm} (deg)	$d\sigma/d\Omega$ (μb/sr)	$\Delta d\sigma/d\Omega_{stat}$ (μb/sr)
	74	1.99	7.52×10^{-1}
	78	1.63	6.17×10^{-1}
	82	2.20	6.94×10^{-1}
	86	2.05	6.50×10^{-1}
	90	1.33	5.03×10^{-1}
	94	9.62×10^{-1}	4.30×10^{-1}
	98	2.22	6.42×10^{-1}
	102	1.55	5.47×10^{-1}
	106	2.03	6.41×10^{-1}
	110	2.03	6.78×10^{-1}
	114	4.71×10^{-1}	3.33×10^{-1}
	118	1.56	6.36×10^{-1}
	122	2.99×10^{-1}	2.99×10^{-1}
	126	3.65×10^{-1}	3.65×10^{-1}
	130	9.93×10^{-1}	7.02×10^{-1}
	134	5.15	2.31
	138	0.00	0.00
	142	0.00	0.00
18.41	54	5.40	3.82
	58	7.86	2.62
	62	4.88	1.47
	66	5.30	1.18
	70	1.93	6.42×10^{-1}
	74	5.29	9.82×10^{-1}
	78	5.82	9.57×10^{-1}
	82	8.70	1.14
	86	9.68	1.17
	90	1.32×10^{1}	1.31
	94	9.21	1.13
	98	8.83	1.10
	102	6.65	9.80×10^{-1}

Continued.

Table A.17 : (Continued)

E'_{cm} (MeV)	θ_{cm} (deg)	$d\sigma/d\Omega$ (μb/sr)	$\Delta d\sigma/d\Omega_{stat}$ (μb/sr)
	106	3.28	6.98×10^{-1}
	110	2.38	6.13×10^{-1}
	114	2.05	5.90×10^{-1}
	118	3.17	7.69×10^{-1}
	122	8.23	1.32
	126	8.33	1.43
	130	1.23×10^{1}	2.00
	134	9.08	2.27
	138	1.17×10^{1}	3.70
	142	1.11×10^{1}	5.54
18.91	54	9.46	3.35
(Mar.)	58	6.06	1.75
	62	5.32	1.25
	66	5.58	9.86×10^{-1}
	70	7.31	1.07
	74	7.74	9.91×10^{-1}
	78	6.62	8.41×10^{-1}
	82	1.18×10^{1}	1.11
	86	1.53×10^{1}	1.25
	90	1.73×10^{1}	1.33
	94	1.43×10^{1}	1.19
	98	1.19×10^{1}	1.11
	102	1.12×10^{1}	1.10
	106	7.03	9.00×10^{-1}
	110	6.24	8.56×10^{-1}
	114	4.92	7.79×10^{-1}
	118	5.28	8.35×10^{-1}
	122	7.65	1.09
	126	9.60	1.31
	130	1.23×10^{1}	1.64
	134	1.97×10^{1}	2.82

Continued.

Table A.17 : (Continued)

E'_{cm} (MeV)	θ_{cm} (deg)	$d\sigma/d\Omega$ (μb/sr)	$\Delta d\sigma/d\Omega_{stat}$ (μb/sr)
	138	1.73×10^{1}	3.77
	142	1.55×10^{1}	5.16
18.91	54	0.00	0.00
(Apr.)	58	5.76	4.07
	62	3.35	2.37
	66	4.02	2.01
	70	3.58	1.79
	74	8.73	2.52
	78	8.58	2.29
	82	1.13×10^{1}	2.60
	86	1.12×10^{1}	2.58
	90	2.14×10^{1}	3.56
	94	1.53×10^{1}	2.95
	98	1.16×10^{1}	2.66
	102	1.08×10^{1}	2.62
	106	6.25	2.08
	110	5.61	1.98
	114	5.16	1.95
	118	3.19	1.60
	122	7.94	2.81
	126	1.15×10^{1}	3.64
	130	9.95	3.76
	134	2.62×10^{1}	8.73
	138	6.39	6.39
	142	1.50×10^{1}	1.50×10^{1}
19.11	54	3.40	1.52
	58	1.69	6.88×10^{-1}
	62	5.95	1.02
	66	5.24	7.64×10^{-1}
	70	5.11	7.16×10^{-1}
	74	7.50	7.86×10^{-1}

Continued.

Table A.17 : (Continued)

E'_{cm} (MeV)	θ_{cm} (deg)	$d\sigma/d\Omega$ (μb/sr)	$\Delta d\sigma/d\Omega_{stat}$ (μb/sr)
	78	1.03×10^{1}	8.42×10^{-1}
	82	1.21×10^{1}	9.25×10^{-1}
	86	1.63×10^{1}	1.04
	90	1.81×10^{1}	1.10
	94	1.85×10^{1}	1.10
	98	1.45×10^{1}	1.02
	102	1.06×10^{1}	8.93×10^{-1}
	106	8.52	8.09×10^{-1}
	110	6.17	7.03×10^{-1}
	114	5.81	7.00×10^{-1}
	118	7.03	8.07×10^{-1}
	122	1.05×10^{1}	1.09
	126	1.15×10^{1}	1.24
	130	1.84×10^{1}	1.76
	134	2.10×10^{1}	2.50
	138	2.38×10^{1}	4.14
	142	1.61×10^{1}	5.10
19.32	54	7.24	2.29
	58	5.81	1.37
	62	7.63	1.25
	66	5.93	8.47×10^{-1}
	70	9.01	1.03
	74	1.09×10^{1}	9.87×10^{-1}
	78	1.33×10^{1}	1.03
	82	1.23×10^{1}	9.90×10^{-1}
	86	1.37×10^{1}	1.02
	90	1.41×10^{1}	1.04
	94	1.53×10^{1}	1.12
	98	1.19×10^{1}	9.83×10^{-1}
	102	1.12×10^{1}	9.92×10^{-1}
	106	1.04×10^{1}	9.60×10^{-1}

Continued.

Table A.17 : (Continued)

E'_{cm} (MeV)	θ_{cm} (deg)	$d\sigma/d\Omega$ (μb/sr)	$\Delta d\sigma/d\Omega_{stat}$ (μb/sr)
	110	9.74	9.65×10^{-1}
	114	6.72	8.27×10^{-1}
	118	7.23	8.83×10^{-1}
	122	8.16	1.03
	126	1.15×10^{1}	1.33
	130	1.57×10^{1}	1.73
	134	2.35×10^{1}	2.77
	138	3.08×10^{1}	5.13
	142	2.78×10^{1}	6.96
19.42	54	6.53	2.92
	58	8.42	2.11
	62	3.84	1.16
	66	6.52	1.21
	70	1.31×10^{1}	1.68
	74	1.07×10^{1}	1.35
	78	1.22×10^{1}	1.35
	82	1.14×10^{1}	1.33
	86	1.18×10^{1}	1.32
	90	1.26×10^{1}	1.35
	94	1.16×10^{1}	1.30
	98	1.17×10^{1}	1.31
	102	1.25×10^{1}	1.41
	106	1.31×10^{1}	1.43
	110	9.90	1.25
	114	8.39	1.20
	118	6.77	1.10
	122	5.73	1.06
	126	1.10×10^{1}	1.65
	130	1.64×10^{1}	2.11
	134	1.51×10^{1}	2.54
	138	2.20×10^{1}	4.24

Continued.

Table A.17 : (Continued)

E'_{cm} (MeV)	θ_{cm} (deg)	$d\sigma/d\Omega$ (μb/sr)	$\Delta d\sigma/d\Omega_{stat}$ (μb/sr)
	142	3.03×10^{1}	7.83
19.51	54	5.74	1.91
	58	7.23	1.54
	62	5.11	1.00
	66	7.83	9.64×10^{-1}
	70	1.18×10^{1}	1.19
	74	1.11×10^{1}	1.01
	78	1.15×10^{1}	9.87×10^{-1}
	82	1.04×10^{1}	9.68×10^{-1}
	86	1.11×10^{1}	9.77×10^{-1}
	90	8.30	8.17×10^{-1}
	94	9.44	8.96×10^{-1}
	98	9.36	9.05×10^{-1}
	102	1.22×10^{1}	1.04
	106	1.35×10^{1}	1.13
	110	1.27×10^{1}	1.11
	114	1.08×10^{1}	1.05
	118	6.31	8.43×10^{-1}
	122	8.07	1.03
	126	1.25×10^{1}	1.39
	130	1.83×10^{1}	1.87
	134	2.65×10^{1}	2.93
	138	3.54×10^{1}	5.06
	142	3.59×10^{1}	6.66
19.72	54	8.06	2.33
	58	8.48	1.63
	62	7.90	1.13
	66	9.65	1.09
	70	1.44×10^{1}	1.27
	74	1.39×10^{1}	1.10
	78	9.72	9.11×10^{-1}

Continued.

Table A.17 : (Continued)

E'_{cm} (MeV)	θ_{cm} (deg)	$d\sigma/d\Omega$ (μb/sr)	$\Delta d\sigma/d\Omega_{stat}$ (μb/sr)
	82	9.18	8.92×10^{-1}
	86	7.26	7.97×10^{-1}
	90	6.68	7.09×10^{-1}
	94	6.19	7.19×10^{-1}
	98	8.16	8.47×10^{-1}
	102	1.11×10^{1}	9.70×10^{-1}
	106	1.31×10^{1}	1.07
	110	1.48×10^{1}	1.19
	114	1.18×10^{1}	1.10
	118	9.80	1.04
	122	7.80	1.01
	126	1.01×10^{1}	1.21
	130	2.20×10^{1}	2.09
	134	3.07×10^{1}	2.91
	138	6.51×10^{1}	7.24
	142	7.54×10^{1}	1.15×10^{1}
19.92	54	6.67	2.72
(Mar.)	58	4.68	1.56
	62	7.14	1.52
	66	7.09	1.29
	70	1.27×10^{1}	1.62
	74	1.30×10^{1}	1.50
	78	1.01×10^{1}	1.30
	82	9.65	1.27
	86	5.35	9.46×10^{-1}
	90	3.15	6.86×10^{-1}
	94	6.00	9.87×10^{-1}
	98	8.76	1.16
	102	1.39×10^{1}	1.47
	106	1.31×10^{1}	1.48
	110	1.16×10^{1}	1.42

Continued.

Table A.17 : (Continued)

E'_{cm} (MeV)	θ_{cm} (deg)	$d\sigma/d\Omega$ (μb/sr)	$\Delta d\sigma/d\Omega_{stat}$ (μb/sr)
	114	1.04×10^{1}	1.40
	118	5.89	1.02
	122	4.67	1.04
	126	7.07	1.29
	130	1.74×10^{1}	2.22
	134	3.08×10^{1}	3.48
	138	5.21×10^{1}	6.52
	142	4.54×10^{1}	8.44
19.92	54	0.00	0.00
(Apr.)	58	5.63	2.52
	62	8.16	2.35
	66	6.22	1.72
	70	1.06×10^{1}	2.11
	74	1.12×10^{1}	1.97
	78	1.66×10^{1}	2.40
	82	8.59	1.72
	86	5.34	1.33
	90	2.17	8.22×10^{-1}
	94	3.74	1.13
	98	9.26	1.75
	102	9.07	1.75
	106	1.13×10^{1}	2.03
	110	1.61×10^{1}	2.52
	114	9.95	2.03
	118	4.04	1.28
	122	6.81	1.89
	126	1.15×10^{1}	2.57
	130	1.79×10^{1}	3.66
	134	4.47×10^{1}	7.16
	138	1.03×10^{2}	1.85×10^{1}
	142	8.74×10^{1}	2.26×10^{1}

Continued.

Table A.17 : (Continued)

E'_{cm} (MeV)	θ_{cm} (deg)	$d\sigma/d\Omega$ (μb/sr)	$\Delta d\sigma/d\Omega_{stat}$ (μb/sr)
20.17	54	7.73	2.33
	58	4.63	1.24
	62	6.72	1.08
	66	5.08	8.47×10^{-1}
	70	7.34	9.48×10^{-1}
	74	6.27	7.60×10^{-1}
	78	8.00	8.78×10^{-1}
	82	1.03×10^{1}	1.00
	86	8.42	8.97×10^{-1}
	90	7.01	7.94×10^{-1}
	94	8.13	8.92×10^{-1}
	98	8.36	8.92×10^{-1}
	102	9.68	9.83×10^{-1}
	106	6.97	8.39×10^{-1}
	110	6.09	8.07×10^{-1}
	114	5.85	8.36×10^{-1}
	118	6.51	8.85×10^{-1}
	122	5.15	8.58×10^{-1}
	126	6.81	1.05
	130	1.61×10^{1}	1.82
	134	2.71×10^{1}	2.68
	138	7.73×10^{1}	7.51
	142	8.53×10^{1}	1.15×10^{1}
20.42	54	2.30	1.62
	58	3.43	1.30
	62	7.28	1.46
	66	5.36	1.20
	70	5.54	1.07
	74	7.42	1.13
	78	6.68	1.16
	82	7.67	1.17

Continued.

Table A.17 : (Continued)

E'_{cm} (MeV)	θ_{cm} (deg)	$d\sigma/d\Omega$ (μb/sr)	$\Delta d\sigma/d\Omega_{stat}$ (μb/sr)
	86	1.13×10^{1}	1.42
	90	1.66×10^{1}	1.72
	94	1.51×10^{1}	1.65
	98	9.64	1.31
	102	6.06	1.01
	106	4.33	8.66×10^{-1}
	110	4.59	9.17×10^{-1}
	114	8.67	1.34
	118	9.78	1.51
	122	9.90	1.53
	126	1.49×10^{1}	2.03
	130	2.69×10^{1}	2.92
	134	3.41×10^{1}	3.63
	138	7.58×10^{1}	8.58
	142	6.76×10^{1}	1.03×10^{1}
20.67	54	2.75×10^{1}	3.58
	58	1.91×10^{1}	2.34
	62	1.29×10^{1}	1.41
	66	8.70	1.02
	70	6.58	8.29×10^{-1}
	74	7.15	7.62×10^{-1}
	78	6.40	7.71×10^{-1}
	82	8.45	8.67×10^{-1}
	86	1.41×10^{1}	1.09
	90	1.42×10^{1}	1.11
	94	1.47×10^{1}	1.18
	98	9.68	9.19×10^{-1}
	102	7.70	8.35×10^{-1}
	106	6.91	8.14×10^{-1}
	110	7.62	8.80×10^{-1}
	114	7.68	8.75×10^{-1}

Continued.

Table A.17 : (Continued)

E'_{cm} (MeV)	θ_{cm} (deg)	$d\sigma/d\Omega$ (μb/sr)	$\Delta d\sigma/d\Omega_{stat}$ (μb/sr)
	118	1.33×10^{1}	1.26
	122	1.93×10^{1}	1.58
	126	2.76×10^{1}	1.91
	130	5.73×10^{1}	3.22
	134	7.32×10^{1}	4.02
	138	1.44×10^{2}	9.30
	142	1.35×10^{2}	1.19×10^{1}
20.92	54	1.17×10^{1}	3.12
(Mar.)	58	1.62×10^{1}	2.91
	62	8.82	1.70
	66	8.39	1.44
	70	9.74	1.42
	74	1.06×10^{1}	1.31
	78	9.05	1.28
	82	1.09×10^{1}	1.39
	86	1.83×10^{1}	1.73
	90	1.88×10^{1}	1.80
	94	1.28×10^{1}	1.45
	98	1.53×10^{1}	1.59
	102	1.02×10^{1}	1.32
	106	9.69	1.34
	110	9.35	1.32
	114	7.14	1.16
	118	1.01×10^{1}	1.48
	122	1.65×10^{1}	1.90
	126	3.82×10^{1}	3.04
	130	5.33×10^{1}	3.90
	134	8.06×10^{1}	5.85
	138	1.08×10^{2}	9.22
	142	6.02×10^{1}	8.19
20.92	54	2.11×10^{1}	5.86

Continued.

Table A.17 : (Continued)

E'_{cm} (MeV)	θ_{cm} (deg)	$d\sigma/d\Omega$ (μb/sr)	$\Delta d\sigma/d\Omega_{stat}$ (μb/sr)
(Apr.)	58	2.39×10^{1}	4.70
	62	1.22×10^{1}	2.48
	66	8.76	1.87
	70	7.63	1.63
	74	8.05	1.52
	78	1.08×10^{1}	1.82
	82	1.04×10^{1}	1.78
	86	1.06×10^{1}	1.71
	90	2.22×10^{1}	2.59
	94	1.84×10^{1}	2.31
	98	1.29×10^{1}	1.94
	102	8.66	1.64
	106	1.01×10^{1}	1.81
	110	1.02×10^{1}	1.92
	114	1.13×10^{1}	2.05
	118	1.15×10^{1}	2.17
	122	1.78×10^{1}	2.75
	126	3.47×10^{1}	4.03
	130	6.38×10^{1}	6.26
	134	8.23×10^{1}	8.44
	138	1.63×10^{2}	1.87×10^{1}
	142	1.16×10^{2}	2.19×10^{1}
21.17	54	1.92×10^{1}	2.74
	58	1.36×10^{1}	1.74
	62	9.44	1.11
	66	7.80	9.60×10^{-1}
	70	8.91	9.40×10^{-1}
	74	5.76	6.79×10^{-1}
	78	6.10	7.51×10^{-1}
	82	7.52	8.15×10^{-1}
	86	1.60×10^{1}	1.14

Continued.

Table A.17 : (Continued)

E'_{cm} (MeV)	θ_{cm} (deg)	$d\sigma/d\Omega$ (μb/sr)	$\Delta d\sigma/d\Omega_{stat}$ (μb/sr)
	90	2.06×10^{1}	1.32
	94	1.89×10^{1}	1.31
	98	1.08×10^{1}	9.71×10^{-1}
	102	7.19	8.04×10^{-1}
	106	7.43	8.36×10^{-1}
	110	1.06×10^{1}	1.07
	114	1.01×10^{1}	1.02
	118	1.03×10^{1}	1.08
	122	1.32×10^{1}	1.25
	126	2.73×10^{1}	1.93
	130	5.59×10^{1}	3.16
	134	8.30×10^{1}	4.38
	138	1.50×10^{2}	9.30
	142	1.64×10^{2}	1.41×10^{1}
21.42	54	2.28×10^{1}	4.31
	58	1.97×10^{1}	2.93
	62	1.55×10^{1}	2.19
	66	8.17	1.40
	70	7.31	1.22
	74	1.09×10^{1}	1.37
	78	1.11×10^{1}	1.42
	82	9.25	1.27
	86	1.39×10^{1}	1.48
	90	1.15×10^{1}	1.42
	94	1.31×10^{1}	1.50
	98	1.09×10^{1}	1.32
	102	1.30×10^{1}	1.48
	106	1.11×10^{1}	1.43
	110	7.91	1.18
	114	7.39	1.23
	118	1.49×10^{1}	1.79

Continued.

Table A.17 : (Continued)

E'_{cm} (MeV)	θ_{cm} (deg)	$d\sigma/d\Omega$ (μb/sr)	$\Delta d\sigma/d\Omega_{stat}$ (μb/sr)
	122	2.14×10^{1}	2.18
	126	2.80×10^{1}	2.53
	130	4.47×10^{1}	3.58
	134	6.33×10^{1}	4.59
	138	8.93×10^{1}	7.89
	142	9.95×10^{1}	1.23×10^{1}
21.67	54	2.94×10^{1}	3.54
	58	2.62×10^{1}	2.25
	62	1.70×10^{1}	1.46
	66	9.24	1.02
	70	5.22	7.24×10^{-1}
	74	5.82	7.10×10^{-1}
	78	1.05×10^{1}	9.67×10^{-1}
	82	1.14×10^{1}	1.01
	86	1.15×10^{1}	9.76×10^{-1}
	90	1.12×10^{1}	1.01
	94	1.24×10^{1}	1.07
	98	1.36×10^{1}	1.04
	102	1.05×10^{1}	9.62×10^{-1}
	106	9.68	9.45×10^{-1}
	110	5.99	7.49×10^{-1}
	114	7.11	8.62×10^{-1}
	118	1.81×10^{1}	1.44
	122	2.75×10^{1}	1.76
	126	4.35×10^{1}	2.40
	130	4.90×10^{1}	2.73
	134	5.71×10^{1}	3.37
	138	9.23×10^{1}	6.56
	142	1.12×10^{2}	1.08×10^{1}
21.92	54	3.32×10^{1}	5.13
(Mar.)	58	2.89×10^{1}	3.39

Continued.

Table A.17 : (Continued)

E'_{cm} (MeV)	θ_{cm} (deg)	$d\sigma/d\Omega$ (μb/sr)	$\Delta d\sigma/d\Omega_{stat}$ (μb/sr)
	62	1.59×10^{1}	2.14
	66	7.86	1.41
	70	1.73	6.12×10^{-1}
	74	5.18	9.80×10^{-1}
	78	1.10×10^{1}	1.48
	82	1.54×10^{1}	1.65
	86	1.90×10^{1}	1.75
	90	2.08×10^{1}	1.94
	94	2.27×10^{1}	2.02
	98	1.83×10^{1}	1.81
	102	1.03×10^{1}	1.42
	106	5.32	1.00
	110	2.89	7.46×10^{-1}
	114	8.94	1.33
	118	1.58×10^{1}	1.81
	122	2.79×10^{1}	2.42
	126	3.17×10^{1}	2.79
	130	3.84×10^{1}	3.47
	134	3.66×10^{1}	3.43
	138	4.99×10^{1}	5.61
	142	5.46×10^{1}	7.72
21.92	54	3.28×10^{1}	6.57
(Apr.)	58	2.84×10^{1}	4.15
	62	2.05×10^{1}	2.93
	66	6.78	1.60
	70	2.94	9.80×10^{-1}
	74	5.89	1.32
	78	1.08×10^{1}	1.88
	82	1.24×10^{1}	1.92
	86	1.86×10^{1}	2.27
	90	1.87×10^{1}	2.46

Continued.

Table A.17 : (Continued)

E'_{cm} (MeV)	θ_{cm} (deg)	$d\sigma/d\Omega$ (μb/sr)	$\Delta d\sigma/d\Omega_{stat}$ (μb/sr)
	94	1.66×10^{1}	2.24
	98	1.63×10^{1}	2.20
	102	1.11×10^{1}	1.87
	106	4.60	1.23
	110	3.17	1.00
	114	8.50	1.73
	118	1.47×10^{1}	2.33
	122	2.95×10^{1}	3.32
	126	4.21×10^{1}	4.49
	130	3.94×10^{1}	4.77
	134	3.51×10^{1}	4.78
	138	6.06×10^{1}	9.71
	142	7.57×10^{1}	1.55×10^{1}
22.17	54	3.63×10^{1}	3.45
	58	2.95×10^{1}	2.31
	62	1.64×10^{1}	1.38
	66	7.99	9.23×10^{-1}
	70	4.34	6.20×10^{-1}
	74	9.37	8.93×10^{-1}
	78	1.24×10^{1}	1.08
	82	1.43×10^{1}	1.12
	86	1.62×10^{1}	1.17
	90	1.67×10^{1}	1.17
	94	1.75×10^{1}	1.24
	98	1.69×10^{1}	1.18
	102	1.69×10^{1}	1.23
	106	9.67	9.35×10^{-1}
	110	5.12	6.84×10^{-1}
	114	7.61	8.51×10^{-1}
	118	1.84×10^{1}	1.40
	122	3.44×10^{1}	1.93

Continued.

Table A.17 : (Continued)

E'_{cm} (MeV)	θ_{cm} (deg)	$d\sigma/d\Omega$ (μb/sr)	$\Delta d\sigma/d\Omega_{stat}$ (μb/sr)
	126	4.27×10^{1}	2.36
	130	4.72×10^{1}	2.71
	134	3.99×10^{1}	2.70
	138	6.05×10^{1}	4.94
	142	7.59×10^{1}	8.71
22.43	54	5.44×10^{1}	6.70
	58	5.30×10^{1}	5.38
	62	3.04×10^{1}	3.46
	66	1.77×10^{1}	2.48
	70	1.21×10^{1}	1.87
	74	2.02×10^{1}	2.22
	78	2.62×10^{1}	2.60
	82	2.09×10^{1}	2.14
	86	1.13×10^{1}	1.52
	90	9.60	1.46
	94	1.49×10^{1}	1.89
	98	2.13×10^{1}	2.17
	102	2.23×10^{1}	2.24
	106	2.27×10^{1}	2.25
	110	7.41	1.33
	114	6.84	1.25
	118	2.62×10^{1}	2.76
	122	5.28×10^{1}	3.96
	126	5.20×10^{1}	3.92
	130	4.37×10^{1}	3.88
	134	3.33×10^{1}	3.83
	138	2.90×10^{1}	4.65
	142	2.96×10^{1}	6.98
22.68	54	5.07×10^{1}	3.90
	58	3.79×10^{1}	2.51
	62	1.97×10^{1}	1.56

Continued.

Table A.17 : (Continued)

E'_{cm} (MeV)	θ_{cm} (deg)	$d\sigma/d\Omega$ (μb/sr)	$\Delta d\sigma/d\Omega_{stat}$ (μb/sr)
	66	9.43	1.06
	70	1.01×10^{1}	9.96×10^{-1}
	74	1.60×10^{1}	1.24
	78	2.16×10^{1}	1.47
	82	1.85×10^{1}	1.31
	86	1.16×10^{1}	9.81×10^{-1}
	90	8.69	8.91×10^{-1}
	94	1.36×10^{1}	1.10
	98	1.82×10^{1}	1.28
	102	2.29×10^{1}	1.49
	106	1.90×10^{1}	1.35
	110	1.28×10^{1}	1.11
	114	9.44	9.73×10^{-1}
	118	2.56×10^{1}	1.72
	122	4.39×10^{1}	2.28
	126	6.22×10^{1}	2.89
	130	5.40×10^{1}	2.84
	134	4.00×10^{1}	2.86
	138	3.93×10^{1}	4.19
	142	4.39×10^{1}	6.09
22.93	54	4.90×10^{1}	5.89
(Mar.)	58	3.05×10^{1}	3.90
	62	2.81×10^{1}	3.51
	66	1.22×10^{1}	1.97
	70	8.65	1.64
	74	1.52×10^{1}	1.96
	78	2.09×10^{1}	2.32
	82	2.13×10^{1}	2.14
	86	1.95×10^{1}	2.02
	90	2.27×10^{1}	2.28
	94	2.25×10^{1}	2.16

Continued.

Table A.17 : (Continued)

E'_{cm} (MeV)	θ_{cm} (deg)	$d\sigma/d\Omega$ (μb/sr)	$\Delta d\sigma/d\Omega_{stat}$ (μb/sr)
	98	1.78×10^{1}	1.83
	102	2.20×10^{1}	2.29
	106	1.50×10^{1}	1.86
	110	8.68	1.41
	114	7.22	1.26
	118	2.13×10^{1}	2.31
	122	3.94×10^{1}	3.31
	126	4.19×10^{1}	3.54
	130	3.65×10^{1}	3.40
	134	2.33×10^{1}	3.09
	138	1.76×10^{1}	3.26
	142	2.68×10^{1}	5.85
22.93	54	4.65×10^{1}	7.09
(Apr.)	58	3.50×10^{1}	4.31
	62	1.84×10^{1}	2.87
	66	1.21×10^{1}	2.14
	70	9.68	1.80
	74	1.24×10^{1}	2.03
	78	2.08×10^{1}	2.67
	82	2.22×10^{1}	2.62
	86	2.65×10^{1}	2.91
	90	1.82×10^{1}	2.44
	94	2.10×10^{1}	2.51
	98	1.91×10^{1}	2.37
	102	1.93×10^{1}	2.55
	106	1.78×10^{1}	2.54
	110	9.75	1.84
	114	7.28	1.59
	118	2.34×10^{1}	3.02
	122	3.69×10^{1}	4.02
	126	5.77×10^{1}	5.23

Continued.

Table A.17 : (Continued)

E'_{cm} (MeV)	θ_{cm} (deg)	$d\sigma/d\Omega$ (μb/sr)	$\Delta d\sigma/d\Omega_{stat}$ (μb/sr)
	130	5.18×10^{1}	5.18
	134	3.71×10^{1}	5.19
	138	1.71×10^{1}	4.41
	142	5.68×10^{1}	1.34×10^{1}
23.18	54	4.03×10^{1}	3.37
	58	3.11×10^{1}	2.25
	62	1.58×10^{1}	1.44
	66	9.94	1.08
	70	6.66	8.26×10^{-1}
	74	1.08×10^{1}	1.04
	78	1.53×10^{1}	1.26
	82	2.34×10^{1}	1.49
	86	2.68×10^{1}	1.62
	90	2.77×10^{1}	1.65
	94	2.61×10^{1}	1.57
	98	1.96×10^{1}	1.34
	102	1.77×10^{1}	1.32
	106	1.17×10^{1}	1.12
	110	8.08	9.32×10^{-1}
	114	1.16×10^{1}	1.13
	118	1.76×10^{1}	1.46
	122	3.21×10^{1}	1.98
	126	4.57×10^{1}	2.58
	130	4.46×10^{1}	2.66
	134	3.81×10^{1}	2.77
	138	3.24×10^{1}	3.36
	142	6.62×10^{1}	7.80
23.43	54	3.89×10^{1}	4.93
	58	2.39×10^{1}	3.17
	62	1.37×10^{1}	2.16
	66	1.04×10^{1}	1.81

Continued.

Table A.17 : (Continued)

E'_{cm} (MeV)	θ_{cm} (deg)	$d\sigma/d\Omega$ (μb/sr)	$\Delta d\sigma/d\Omega_{stat}$ (μb/sr)
	70	6.89	1.44
	74	5.44	1.16
	78	1.13×10^{1}	1.64
	82	1.75×10^{1}	1.88
	86	2.26×10^{1}	2.22
	90	3.29×10^{1}	2.66
	94	2.73×10^{1}	2.27
	98	2.00×10^{1}	1.95
	102	1.20×10^{1}	1.59
	106	1.01×10^{1}	1.48
	110	5.01	1.04
	114	1.10×10^{1}	1.61
	118	1.53×10^{1}	1.94
	122	2.34×10^{1}	2.42
	126	4.89×10^{1}	3.91
	130	4.46×10^{1}	3.67
	134	4.17×10^{1}	3.81
	138	4.49×10^{1}	5.49
	142	8.21×10^{1}	1.15×10^{1}
23.93	54	3.46×10^{1}	4.51
	58	3.44×10^{1}	3.76
	62	2.67×10^{1}	2.85
	66	3.48×10^{1}	3.23
	70	2.07×10^{1}	2.42
	74	1.90×10^{1}	2.21
	78	2.31×10^{1}	2.28
	82	2.73×10^{1}	2.33
	86	4.03×10^{1}	2.74
	90	4.49×10^{1}	3.02
	94	3.91×10^{1}	2.63
	98	3.10×10^{1}	2.39

Continued.

Table A.17 : (Continued)

E'_{cm} (MeV)	θ_{cm} (deg)	$d\sigma/d\Omega$ (μb/sr)	$\Delta d\sigma/d\Omega_{stat}$ (μb/sr)
	102	2.10×10^1	1.98
	106	2.03×10^1	1.94
	110	2.37×10^1	2.14
	114	3.19×10^1	2.59
	118	3.37×10^1	2.69
	122	3.12×10^1	2.75
	126	3.88×10^1	3.17
	130	4.38×10^1	3.46
	134	4.61×10^1	3.84
	138	4.24×10^1	4.65
	142	4.32×10^1	6.59
24.43	54	1.36×10^1	2.66
	58	1.38×10^1	2.23
	62	2.76×10^1	2.81
	66	2.80×10^1	2.75
	70	2.92×10^1	2.85
	74	1.83×10^1	2.11
	78	2.34×10^1	2.28
	82	3.08×10^1	2.41
	86	4.06×10^1	2.77
	90	4.38×10^1	2.81
	94	4.00×10^1	2.55
	98	2.76×10^1	2.14
	102	2.88×10^1	2.31
	106	2.62×10^1	2.15
	110	2.38×10^1	2.02
	114	2.93×10^1	2.41
	118	2.98×10^1	2.46
	122	1.59×10^1	1.85
	126	1.50×10^1	1.86
	130	3.67×10^1	3.12

Continued.

Table A.17 : (Continued)

E'_{cm} (MeV)	θ_{cm} (deg)	$d\sigma/d\Omega$ (μb/sr)	$\Delta d\sigma/d\Omega_{stat}$ (μb/sr)
	134	4.62×10^1	3.62
	138	6.79×10^1	5.89
	142	7.27×10^1	8.23
24.93	54	7.87	2.03
	58	1.15×10^1	2.06
	62	1.47×10^1	2.09
	66	1.99×10^1	2.47
	70	2.22×10^1	2.57
	74	2.40×10^1	2.58
	78	1.99×10^1	2.22
	82	2.18×10^1	2.16
	86	4.33×10^1	3.05
	90	5.01×10^1	3.16
	94	3.70×10^1	2.55
	98	1.98×10^1	1.88
	102	1.98×10^1	1.97
	106	2.30×10^1	2.07
	110	1.93×10^1	1.92
	114	2.31×10^1	2.19
	118	1.75×10^1	1.95
	122	1.05×10^1	1.62
	126	4.92	1.07
	130	2.22×10^1	2.45
	134	4.61×10^1	3.91
	138	5.65×10^1	5.25
	142	5.30×10^1	7.36

Table A.18: Angular distribution for the $^{12}C(^{12}C, ^{12}C[0_2^+] \rightarrow 3\alpha)^{12}C(0_2^+)$ reaction using reliable segments of SAKRA.

E'_{cm} (MeV)	θ_{cm} (deg)	$d\sigma/d\Omega$ (μb/sr)	$\Delta d\sigma/d\Omega_{stat}$ (μb/sr)
18.91	70	0.00	0.00
(Mar.)	74	0.00	0.00
	78	1.98	1.14
	82	4.83×10^{-1}	4.83×10^{-1}
	86	7.01×10^{-1}	4.95×10^{-1}
	90	2.90×10^{-1}	2.90×10^{-1}
	94	2.68×10^{-1}	2.68×10^{-1}
	98	0.00	0.00
	102	0.00	0.00
	106	0.00	0.00
	110	0.00	0.00
	114	0.00	0.00
	118	0.00	0.00
	122	0.00	0.00
	126	0.00	0.00
	130	0.00	0.00
	134	0.00	0.00
	138	0.00	0.00
18.91	70	0.00	0.00
(Apr.)	74	0.00	0.00
	78	3.87	3.87
	82	0.00	0.00
	86	0.00	0.00
	90	0.00	0.00
	94	0.00	0.00
	98	0.00	0.00
	102	0.00	0.00
	106	0.00	0.00
	110	0.00	0.00
	114	0.00	0.00
	118	0.00	0.00
	122	0.00	0.00
	126	0.00	0.00
	130	0.00	0.00
	134	0.00	0.00
	138	0.00	0.00
19.11	70	0.00	0.00
	74	0.00	0.00
	78	1.44	7.20×10^{-1}
	82	7.71×10^{-1}	4.45×10^{-1}
	86	0.00	0.00
	90	5.19×10^{-1}	3.00×10^{-1}
	94	1.58×10^{-1}	1.58×10^{-1}
	98	0.00	0.00
	102	0.00	0.00
	106	0.00	0.00
	110	1.69×10^{-1}	1.69×10^{-1}
	114	0.00	0.00
	118	0.00	0.00
	122	0.00	0.00
	126	0.00	0.00
	130	0.00	0.00
	134	0.00	0.00
	138	0.00	0.00
19.32	70	7.63×10^{-1}	7.63×10^{-1}
	74	8.72×10^{-1}	6.17×10^{-1}
	78	9.57×10^{-1}	5.52×10^{-1}
	82	1.27	5.18×10^{-1}
	86	3.36×10^{-1}	2.38×10^{-1}

Continued.

Table A.18 : (Continued)

Continued.

Table A.18 : (Continued)

E'_{cm} (MeV)	θ_{cm} (deg)	$d\sigma/d\Omega$ (μb/sr)	$\Delta d\sigma/d\Omega_{stat}$ (μb/sr)
	90	4.90×10^{-1}	2.83×10^{-1}
	94	0.00	0.00
	98	1.34×10^{-1}	1.34×10^{-1}
	102	1.34×10^{-1}	1.34×10^{-1}
	106	1.33×10^{-1}	1.33×10^{-1}
	110	0.00	0.00
	114	0.00	0.00
	118	1.94×10^{-1}	1.94×10^{-1}
	122	0.00	0.00
	126	3.02×10^{-1}	3.02×10^{-1}
	130	0.00	0.00
	134	0.00	0.00
	138	0.00	0.00
19.42	70	0.00	0.00
	74	0.00	0.00
	78	9.11×10^{-1}	6.44×10^{-1}
	82	0.00	0.00
	86	5.14×10^{-1}	3.63×10^{-1}
	90	2.36×10^{-1}	2.36×10^{-1}
	94	4.26×10^{-1}	3.01×10^{-1}
	98	2.01×10^{-1}	2.01×10^{-1}
	102	0.00	0.00
	106	0.00	0.00
	110	0.00	0.00
	114	0.00	0.00
	118	0.00	0.00
	122	0.00	0.00
	126	0.00	0.00
	130	0.00	0.00
	134	8.59×10^{-1}	8.59×10^{-1}
	138	0.00	0.00

Continued.

Table A.18 : (Continued)

E'_{cm} (MeV)	θ_{cm} (deg)	$d\sigma/d\Omega$ (μb/sr)	$\Delta d\sigma/d\Omega_{stat}$ (μb/sr)
19.51	70	0.00	0.00
	74	3.40×10^{-1}	3.40×10^{-1}
	78	2.33×10^{-1}	2.33×10^{-1}
	82	3.37×10^{-1}	2.38×10^{-1}
	86	6.97×10^{-1}	3.12×10^{-1}
	90	5.19×10^{-1}	2.59×10^{-1}
	94	2.33×10^{-1}	1.65×10^{-1}
	98	2.19×10^{-1}	1.55×10^{-1}
	102	4.32×10^{-1}	2.16×10^{-1}
	106	1.04×10^{-1}	1.04×10^{-1}
	110	2.21×10^{-1}	1.56×10^{-1}
	114	0.00	0.00
	118	0.00	0.00
	122	0.00	0.00
	126	0.00	0.00
	130	0.00	0.00
	134	0.00	0.00
	138	0.00	0.00
19.72	70	4.58×10^{-1}	4.58×10^{-1}
	74	9.14×10^{-1}	5.28×10^{-1}
	78	1.13	4.63×10^{-1}
	82	9.93×10^{-1}	3.75×10^{-1}
	86	7.83×10^{-1}	3.20×10^{-1}
	90	3.36×10^{-1}	1.94×10^{-1}
	94	1.03×10^{-1}	1.03×10^{-1}
	98	1.91×10^{-1}	1.35×10^{-1}
	102	9.89×10^{-2}	9.89×10^{-2}
	106	0.00	0.00
	110	0.00	0.00
	114	0.00	0.00
	118	0.00	0.00

Continued.

Table A.18 : (Continued)

E'_{cm} (MeV)	θ_{cm} (deg)	$d\sigma/d\Omega$ (μb/sr)	$\Delta d\sigma/d\Omega_{stat}$ (μb/sr)
	122	1.63×10^{-1}	1.63×10^{-1}
	126	2.11×10^{-1}	2.11×10^{-1}
	130	2.96×10^{-1}	2.96×10^{-1}
	134	4.79×10^{-1}	4.79×10^{-1}
	138	8.72×10^{-1}	8.72×10^{-1}
19.92	70	0.00	0.00
(Mar.)	74	1.54	8.87×10^{-1}
	78	1.64	7.33×10^{-1}
	82	1.62	6.59×10^{-1}
	86	7.24×10^{-1}	4.18×10^{-1}
	90	1.08	4.83×10^{-1}
	94	6.12×10^{-1}	3.53×10^{-1}
	98	5.80×10^{-1}	3.35×10^{-1}
	102	3.73×10^{-1}	2.64×10^{-1}
	106	1.89×10^{-1}	1.89×10^{-1}
	110	0.00	0.00
	114	4.23×10^{-1}	2.99×10^{-1}
	118	2.40×10^{-1}	2.40×10^{-1}
	122	0.00	0.00
	126	3.19×10^{-1}	3.19×10^{-1}
	130	8.78×10^{-1}	6.21×10^{-1}
	134	0.00	0.00
	138	1.12	1.12
19.92	70	0.00	0.00
(Apr.)	74	1.05	1.05
	78	0.00	0.00
	82	1.59	9.20×10^{-1}
	86	0.00	0.00
	90	0.00	0.00
	94	8.01×10^{-1}	5.66×10^{-1}
	98	7.65×10^{-1}	5.41×10^{-1}

Continued.

Table A.18 : (Continued)

E'_{cm} (MeV)	θ_{cm} (deg)	$d\sigma/d\Omega$ (μb/sr)	$\Delta d\sigma/d\Omega_{stat}$ (μb/sr)
	102	0.00	0.00
	106	0.00	0.00
	110	0.00	0.00
	114	0.00	0.00
	118	0.00	0.00
	122	0.00	0.00
	126	0.00	0.00
	130	3.45	1.99
	134	0.00	0.00
	138	0.00	0.00
20.17	70	7.41×10^{-1}	5.24×10^{-1}
	74	7.72×10^{-1}	4.46×10^{-1}
	78	1.40	4.93×10^{-1}
	82	9.00×10^{-1}	3.68×10^{-1}
	86	1.06	3.74×10^{-1}
	90	1.10	3.66×10^{-1}
	94	4.51×10^{-1}	2.26×10^{-1}
	98	2.14×10^{-1}	1.51×10^{-1}
	102	5.33×10^{-1}	2.38×10^{-1}
	106	2.22×10^{-1}	1.57×10^{-1}
	110	2.33×10^{-1}	1.65×10^{-1}
	114	1.26×10^{-1}	1.26×10^{-1}
	118	2.96×10^{-1}	2.10×10^{-1}
	122	5.15×10^{-1}	2.97×10^{-1}
	126	1.46	5.54×10^{-1}
	130	6.07×10^{-1}	4.29×10^{-1}
	134	4.51×10^{-1}	4.51×10^{-1}
	138	8.20×10^{-1}	8.20×10^{-1}
20.42	70	1.98	1.14
	74	1.26	7.26×10^{-1}
	78	6.40×10^{-1}	4.53×10^{-1}

Continued.

Table A.18 : (Continued)

E'_{cm} (MeV)	θ_{cm} (deg)	$d\sigma/d\Omega$ (μb/sr)	$\Delta d\sigma/d\Omega_{stat}$ (μb/sr)
	82	2.47	8.22×10^{-1}
	86	1.93	6.81×10^{-1}
	90	1.99	6.62×10^{-1}
	94	6.54×10^{-1}	3.77×10^{-1}
	98	7.96×10^{-1}	3.98×10^{-1}
	102	4.26×10^{-1}	3.01×10^{-1}
	106	0.00	0.00
	110	4.50×10^{-1}	3.18×10^{-1}
	114	0.00	0.00
	118	0.00	0.00
	122	0.00	0.00
	126	7.32×10^{-1}	5.18×10^{-1}
	130	2.83	1.15
	134	1.88	1.09
	138	2.05	1.45
20.67	70	0.00	0.00
	74	1.01	4.11×10^{-1}
	78	8.56×10^{-1}	3.49×10^{-1}
	82	1.16	3.88×10^{-1}
	86	1.67	4.31×10^{-1}
	90	1.44	3.85×10^{-1}
	94	2.07	4.52×10^{-1}
	98	7.87×10^{-1}	2.78×10^{-1}
	102	5.83×10^{-1}	2.38×10^{-1}
	106	2.00×10^{-1}	1.41×10^{-1}
	110	3.05×10^{-1}	1.76×10^{-1}
	114	2.26×10^{-1}	1.60×10^{-1}
	118	2.46×10^{-1}	1.74×10^{-1}
	122	2.74×10^{-1}	1.94×10^{-1}
	126	1.58	5.26×10^{-1}
	130	1.81	6.38×10^{-1}

Continued.

Table A.18 : (Continued)

E'_{cm} (MeV)	θ_{cm} (deg)	$d\sigma/d\Omega$ (μb/sr)	$\Delta d\sigma/d\Omega_{stat}$ (μb/sr)
	134	3.41	1.08
	138	2.74	1.23
20.92	70	1.00	7.09×10^{-1}
(Mar.)	74	1.57	7.03×10^{-1}
	78	1.32	5.90×10^{-1}
	82	1.94	6.86×10^{-1}
	86	2.91	7.78×10^{-1}
	90	2.35	6.77×10^{-1}
	94	1.89	5.99×10^{-1}
	98	2.20	6.35×10^{-1}
	102	1.14	4.64×10^{-1}
	106	5.56×10^{-1}	3.21×10^{-1}
	110	5.85×10^{-1}	3.38×10^{-1}
	114	3.99×10^{-1}	2.82×10^{-1}
	118	0.00	0.00
	122	1.07	5.36×10^{-1}
	126	1.53	6.85×10^{-1}
	130	1.55	7.76×10^{-1}
	134	4.20	1.48
	138	3.09	1.55
20.92	70	8.66×10^{-1}	8.66×10^{-1}
(Apr.)	74	5.64×10^{-1}	5.64×10^{-1}
	78	1.88	9.41×10^{-1}
	82	2.56	1.05
	86	1.13	6.51×10^{-1}
	90	1.05	6.08×10^{-1}
	94	1.36	6.81×10^{-1}
	98	1.27	6.36×10^{-1}
	102	1.01	5.84×10^{-1}
	106	3.34×10^{-1}	3.34×10^{-1}
	110	7.20×10^{-1}	5.09×10^{-1}

Continued.

Table A.18 : (Continued)

E'_{cm} (MeV)	θ_{cm} (deg)	$d\sigma/d\Omega$ (μb/sr)	$\Delta d\sigma/d\Omega_{stat}$ (μb/sr)
	114	0.00	0.00
	118	1.28	7.38×10^{-1}
	122	1.44	8.30×10^{-1}
	126	5.73×10^{-1}	5.73×10^{-1}
	130	7.64×10^{-1}	7.64×10^{-1}
	134	5.44	2.43
	138	3.60	2.54
21.17	70	8.87×10^{-1}	4.44×10^{-1}
	74	1.44	4.80×10^{-1}
	78	1.37	4.33×10^{-1}
	82	2.06	4.86×10^{-1}
	86	3.37	5.96×10^{-1}
	90	3.87	6.12×10^{-1}
	94	1.79	4.11×10^{-1}
	98	2.06	4.40×10^{-1}
	102	1.79	4.10×10^{-1}
	106	1.05	3.17×10^{-1}
	110	3.84×10^{-1}	1.92×10^{-1}
	114	5.30×10^{-1}	2.37×10^{-1}
	118	1.14×10^{-1}	1.14×10^{-1}
	122	6.79×10^{-1}	3.04×10^{-1}
	126	9.90×10^{-1}	4.04×10^{-1}
	130	1.63	5.77×10^{-1}
	134	4.27	1.10
	138	1.48	8.55×10^{-1}
21.42	70	1.14	6.57×10^{-1}
	74	2.64	8.81×10^{-1}
	78	2.08	7.35×10^{-1}
	82	5.75	1.11
	86	4.59	9.36×10^{-1}
	90	7.38	1.17

Continued.

Table A.18 : (Continued)

E'_{cm} (MeV)	θ_{cm} (deg)	$d\sigma/d\Omega$ (μb/sr)	$\Delta d\sigma/d\Omega_{stat}$ (μb/sr)
	94	6.65	1.08
	98	4.57	8.80×10^{-1}
	102	1.82	5.48×10^{-1}
	106	1.05	4.28×10^{-1}
	110	5.44×10^{-1}	3.14×10^{-1}
	114	3.77×10^{-1}	2.66×10^{-1}
	118	0.00	0.00
	122	7.10×10^{-1}	4.10×10^{-1}
	126	8.30×10^{-1}	4.79×10^{-1}
	130	9.94×10^{-1}	5.74×10^{-1}
	134	2.17	9.71×10^{-1}
	138	3.84	1.57
21.67	70	1.38	4.89×10^{-1}
	74	1.44	4.55×10^{-1}
	78	3.17	6.48×10^{-1}
	82	5.45	7.71×10^{-1}
	86	7.11	8.32×10^{-1}
	90	9.68	9.78×10^{-1}
	94	7.41	8.34×10^{-1}
	98	4.98	6.78×10^{-1}
	102	3.50	5.67×10^{-1}
	106	2.23	4.65×10^{-1}
	110	1.93×10^{-1}	1.37×10^{-1}
	114	1.99×10^{-1}	1.41×10^{-1}
	118	7.77×10^{-1}	2.94×10^{-1}
	122	1.34	4.05×10^{-1}
	126	1.74	5.01×10^{-1}
	130	4.44	9.06×10^{-1}
	134	5.46	1.14
	138	5.16	1.43
21.92	70	6.62×10^{-1}	4.68×10^{-1}

Continued.

Table A.18 : (Continued)

E'_{cm} (MeV)	θ_{cm} (deg)	$d\sigma/d\Omega$ (μb/sr)	$\Delta d\sigma/d\Omega_{stat}$ (μb/sr)
(Mar.)	74	1.90	7.18×10^{-1}
	78	5.24	1.17
	82	6.41	1.19
	86	9.85	1.37
	90	1.23×10^{1}	1.55
	94	8.06	1.22
	98	7.33	1.16
	102	3.66	8.18×10^{-1}
	106	9.21×10^{-1}	4.12×10^{-1}
	110	1.87×10^{-1}	1.87×10^{-1}
	114	7.99×10^{-1}	4.00×10^{-1}
	118	6.89×10^{-1}	3.98×10^{-1}
	122	9.85×10^{-1}	4.93×10^{-1}
	126	4.37	1.09
	130	2.86	9.53×10^{-1}
	134	4.15	1.31
	138	2.44	1.22
21.92	70	1.70	9.82×10^{-1}
(Apr.)	74	3.42	1.29
	78	4.09	1.36
	82	5.39	1.44
	86	7.26	1.55
	90	1.02×10^{1}	1.87
	94	1.15×10^{1}	1.95
	98	7.27	1.55
	102	2.92	9.73×10^{-1}
	106	9.86×10^{-1}	5.69×10^{-1}
	110	3.27×10^{-1}	3.27×10^{-1}
	114	1.04	6.00×10^{-1}
	118	1.59	7.93×10^{-1}
	122	4.22×10^{-1}	4.22×10^{-1}

Continued.

Table A.18 : (Continued)

E'_{cm} (MeV)	θ_{cm} (deg)	$d\sigma/d\Omega$ (μb/sr)	$\Delta d\sigma/d\Omega_{stat}$ (μb/sr)
	126	4.50	1.50
	130	2.42	1.21
	134	4.05	1.81
	138	5.34	2.67
22.17	70	1.67	5.03×10^{-1}
	74	1.46	4.41×10^{-1}
	78	2.37	5.30×10^{-1}
	82	5.75	7.61×10^{-1}
	86	8.79	9.16×10^{-1}
	90	1.02×10^{1}	9.86×10^{-1}
	94	8.59	9.05×10^{-1}
	98	6.88	8.10×10^{-1}
	102	5.39	7.27×10^{-1}
	106	1.89	4.23×10^{-1}
	110	1.96×10^{-1}	1.38×10^{-1}
	114	1.61	4.04×10^{-1}
	118	3.00	5.77×10^{-1}
	122	6.71	9.05×10^{-1}
	126	8.40	1.09
	130	7.83	1.14
	134	7.78	1.32
	138	6.70	1.54
22.43	70	2.30	9.37×10^{-1}
	74	1.29	6.45×10^{-1}
	78	2.00	7.57×10^{-1}
	82	8.75	1.46
	86	9.20	1.47
	90	1.17×10^{1}	1.70
	94	8.71	1.43
	98	7.46	1.30
	102	9.32×10^{-1}	4.66×10^{-1}

Continued.

Table A.18 : (Continued)

E'_{cm} (MeV)	θ_{cm} (deg)	$d\sigma/d\Omega$ (μb/sr)	$\Delta d\sigma/d\Omega_{stat}$ (μb/sr)
	106	1.66	6.29×10^{-1}
	110	2.38×10^{-1}	2.38×10^{-1}
	114	2.41	8.03×10^{-1}
	118	4.51	1.13
	122	1.02×10^{1}	1.75
	126	7.42	1.58
	130	6.16	1.59
	134	5.00	1.51
	138	1.42	1.01
22.68	70	1.96	5.43×10^{-1}
	74	8.63×10^{-1}	3.52×10^{-1}
	78	2.32	5.20×10^{-1}
	82	4.47	6.59×10^{-1}
	86	6.66	8.33×10^{-1}
	90	9.00	9.70×10^{-1}
	94	8.97	9.46×10^{-1}
	98	6.67	8.21×10^{-1}
	102	2.05	4.59×10^{-1}
	106	5.23×10^{-1}	2.34×10^{-1}
	110	1.72	4.29×10^{-1}
	114	3.34	6.10×10^{-1}
	118	7.78	9.72×10^{-1}
	122	1.14×10^{1}	1.22
	126	8.43	1.10
	130	7.27	1.10
	134	8.71	1.38
	138	5.37	1.30
22.93	70	2.40	9.07×10^{-1}
(Mar.)	74	9.23×10^{-1}	5.33×10^{-1}
	78	4.99×10^{-1}	3.53×10^{-1}
	82	4.18	9.59×10^{-1}

Continued.

Table A.18 : (Continued)

E'_{cm} (MeV)	θ_{cm} (deg)	$d\sigma/d\Omega$ (μb/sr)	$\Delta d\sigma/d\Omega_{stat}$ (μb/sr)
	86	6.45	1.24
	90	6.62	1.25
	94	7.41	1.27
	98	5.41	1.08
	102	1.11	4.98×10^{-1}
	106	6.94×10^{-1}	4.01×10^{-1}
	110	2.58	7.78×10^{-1}
	114	7.20	1.34
	118	1.16×10^{1}	1.77
	122	1.16×10^{1}	1.84
	126	9.46	1.67
	130	6.76	1.55
	134	1.69	8.45×10^{-1}
	138	2.33	1.16
22.93	70	2.53	1.13
(Apr.)	74	9.85×10^{-1}	6.96×10^{-1}
	78	1.59	7.95×10^{-1}
	82	3.78	1.14
	86	7.96	1.74
	90	6.38	1.55
	94	6.21	1.46
	98	4.64	1.29
	102	1.80	8.06×10^{-1}
	106	1.49	7.45×10^{-1}
	110	3.06	1.08
	114	3.16	1.12
	118	9.60	2.05
	122	1.02×10^{1}	2.12
	126	7.15	1.85
	130	8.92	2.23
	134	7.06	2.23

Continued.

Table A.18 : (Continued)

E'_{cm} (MeV)	θ_{cm} (deg)	$d\sigma/d\Omega$ (μb/sr)	$\Delta d\sigma/d\Omega_{stat}$ (μb/sr)
	138	4.26	2.13
23.18	70	2.97	6.64×10^{-1}
	74	1.11	3.94×10^{-1}
	78	1.72	4.43×10^{-1}
	82	2.92	5.51×10^{-1}
	86	4.44	7.11×10^{-1}
	90	5.64	7.97×10^{-1}
	94	4.01	6.34×10^{-1}
	98	3.14	5.82×10^{-1}
	102	1.56	4.16×10^{-1}
	106	9.24×10^{-1}	3.27×10^{-1}
	110	3.02	5.93×10^{-1}
	114	6.24	8.58×10^{-1}
	118	8.86	1.04
	122	1.02×10^{1}	1.16
	126	6.33	9.34×10^{-1}
	130	8.03	1.16
	134	4.20	9.38×10^{-1}
	138	4.34	1.16
23.43	70	2.55	9.03×10^{-1}
	74	1.19	5.94×10^{-1}
	78	2.18	7.28×10^{-1}
	82	2.76	7.98×10^{-1}
	86	5.44	1.13
	90	6.18	1.21
	94	4.98	1.06
	98	4.54	1.02
	102	1.87	6.60×10^{-1}
	106	2.07	6.88×10^{-1}
	110	3.43	9.16×10^{-1}
	114	7.38	1.35

Continued.

Table A.18 : (Continued)

E'_{cm} (MeV)	θ_{cm} (deg)	$d\sigma/d\Omega$ (μb/sr)	$\Delta d\sigma/d\Omega_{stat}$ (μb/sr)
	118	8.51	1.46
	122	9.60	1.58
	126	7.41	1.45
	130	1.99	8.11×10^{-1}
	134	3.97	1.25
	138	2.68	1.20
23.93	70	1.85	7.55×10^{-1}
	74	1.29	5.79×10^{-1}
	78	1.68	5.95×10^{-1}
	82	2.88	8.00×10^{-1}
	86	4.50	1.01
	90	6.09	1.15
	94	2.66	7.37×10^{-1}
	98	2.33	7.04×10^{-1}
	102	1.30	5.30×10^{-1}
	106	1.49	5.61×10^{-1}
	110	2.11	6.68×10^{-1}
	114	2.90	8.05×10^{-1}
	118	4.38	9.80×10^{-1}
	122	2.87	8.28×10^{-1}
	126	2.61	8.26×10^{-1}
	130	3.57	1.03
	134	2.39	9.02×10^{-1}
	138	6.45	1.72
24.43	70	2.07	7.81×10^{-1}
	74	1.48	6.03×10^{-1}
	78	1.81	6.05×10^{-1}
	82	1.46	5.52×10^{-1}
	86	1.64	5.80×10^{-1}
	90	3.23	8.06×10^{-1}
	94	2.63	7.03×10^{-1}

Continued.

Table A.18 : (Continued)

E'_{cm} (MeV)	θ_{cm} (deg)	$d\sigma/d\Omega$ (μb/sr)	$\Delta d\sigma/d\Omega_{stat}$ (μb/sr)
	98	1.98	6.27×10^{-1}
	102	1.60	5.66×10^{-1}
	106	1.59	5.61×10^{-1}
	110	2.34	6.74×10^{-1}
	114	2.58	7.15×10^{-1}
	118	3.31	8.27×10^{-1}
	122	4.64	1.01
	126	5.31	1.13
	130	4.91	1.16
	134	3.48	1.05
	138	1.68	8.42×10^{-1}
24.93	70	1.67	7.47×10^{-1}
	74	2.63×10^{-1}	2.63×10^{-1}
	78	1.56	5.90×10^{-1}
	82	1.63	6.16×10^{-1}
	86	2.27	7.18×10^{-1}
	90	4.12	9.21×10^{-1}
	94	4.10	9.17×10^{-1}
	98	2.20	6.95×10^{-1}
	102	1.70	6.02×10^{-1}
	106	2.27	6.84×10^{-1}
	110	2.47	7.14×10^{-1}
	114	4.86	1.01
	118	6.45	1.20
	122	9.34	1.48
	126	8.87	1.48
	130	7.56	1.48
	134	4.25	1.18
	138	4.58	1.38

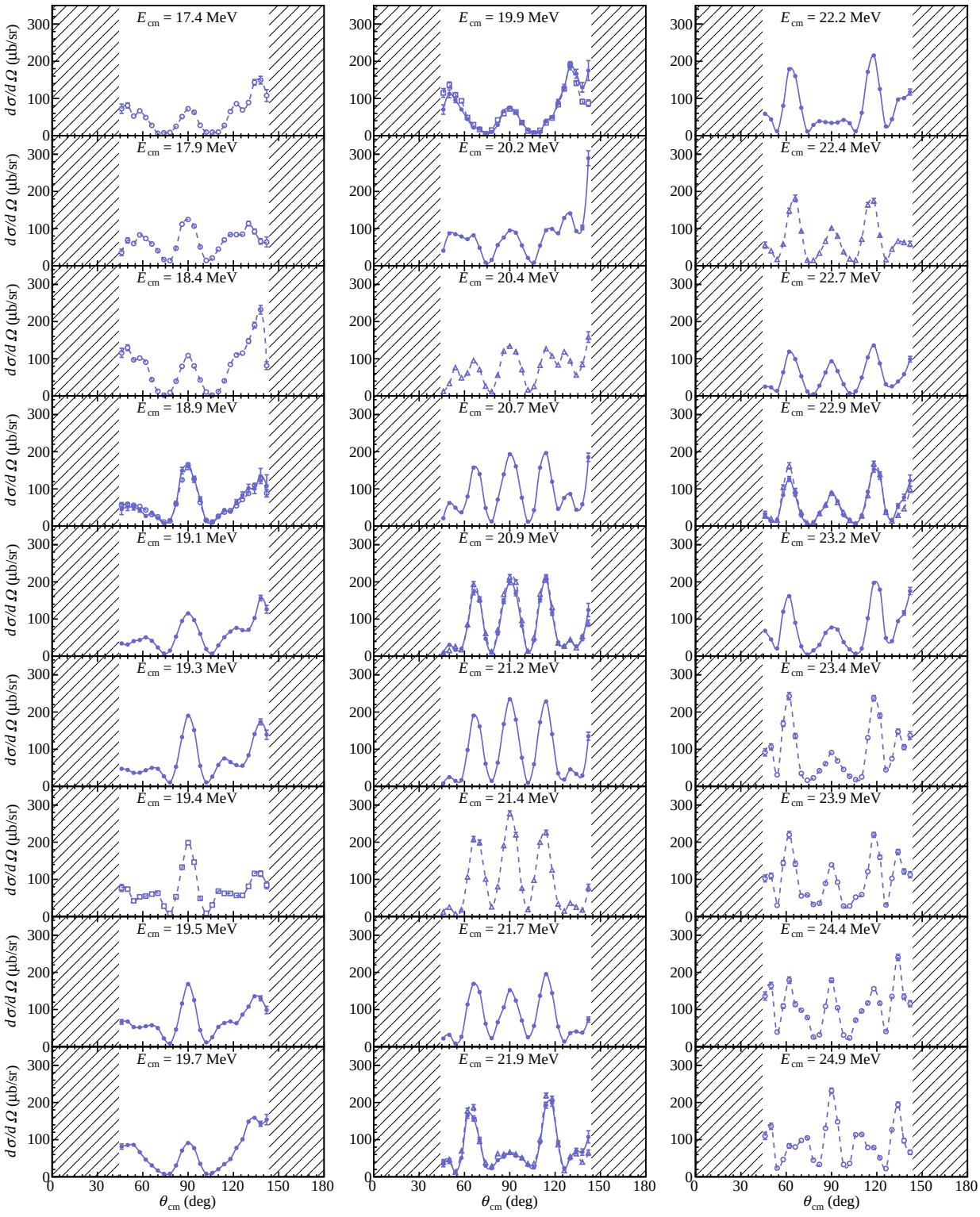

Figure A.1: Angular distributions of the differential cross sections for the $^{12}C + {}^{12}C \rightarrow {}^{12}C(0_2^+) + {}^{12}C(0_1^+)$ reactions.

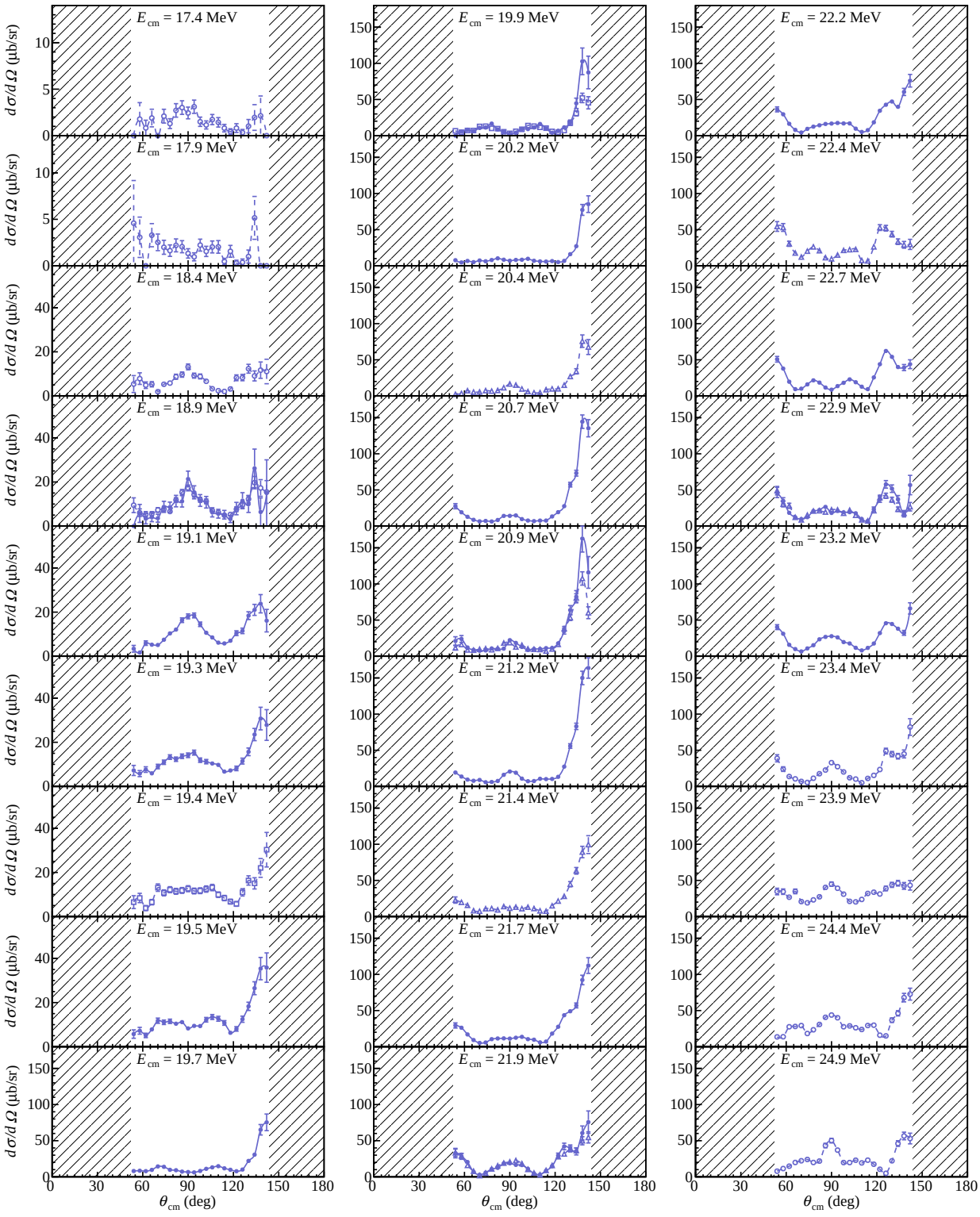

Figure A.2: Angular distributions of the differential cross sections for the $^{12}C + {}^{12}C \rightarrow {}^{12}C(0_2^+) + {}^{12}C(2_1^+)$ reactions.

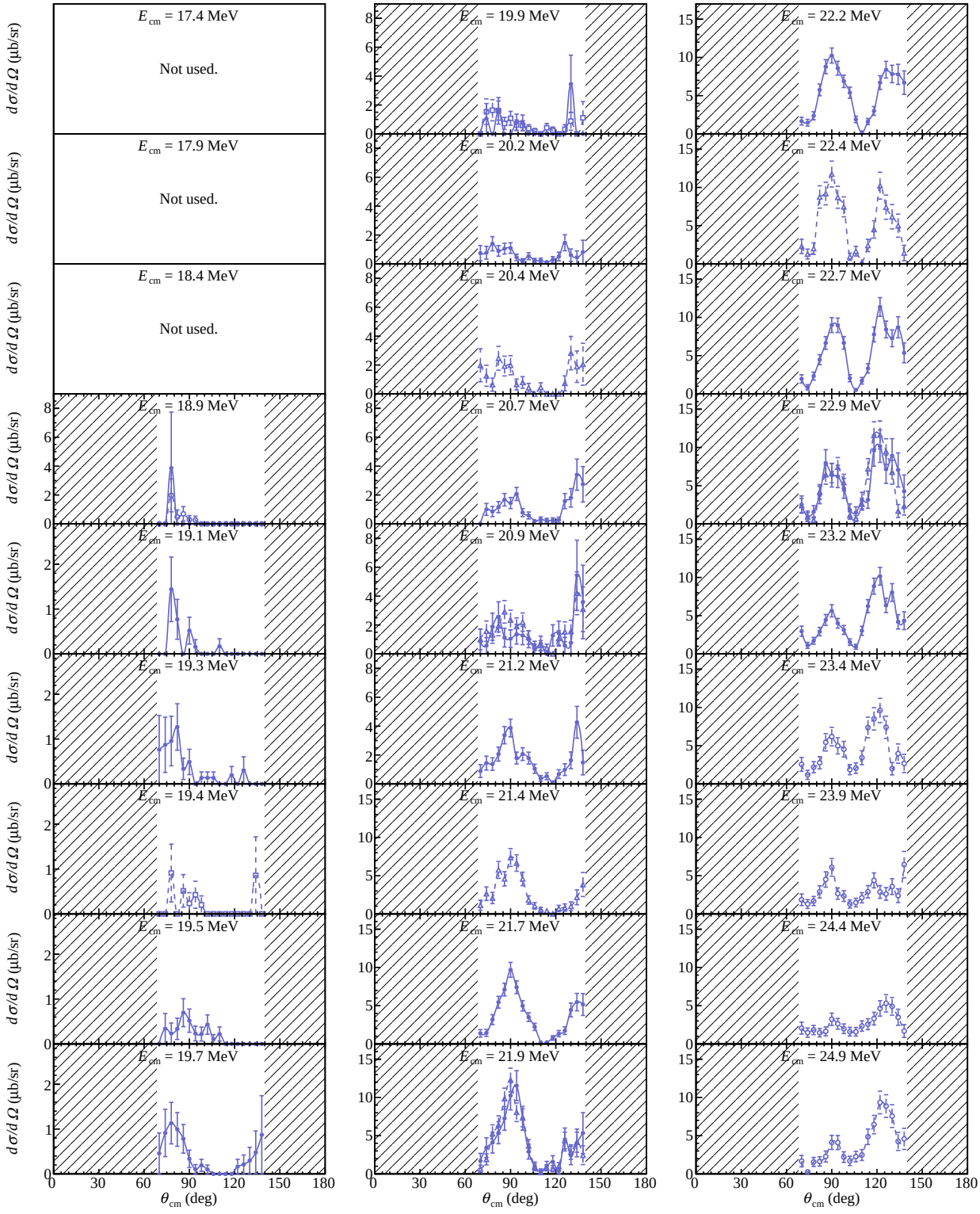

Figure A.3: Angular distributions of the differential cross sections for the $^{12}C + {}^{12}C \rightarrow {}^{12}C(0_2^+) + {}^{12}C(0_2^+)$ reactions.

List of Figures

1.1 Ikeda diagram . . . 2
1.2 Occupation of the single-α orbitals of the Hoyle state of ^{12}C . . . 4
1.3 Density and momentum distribution of the alpha clusters in the ground state and the 0_2^+ state in ^{12}C obtained by the 3α OCM calculation . . . 4
1.4 Cluster fractions X_i in symmetric nuclear matter as a function of the total density n for various temperatures T . . . 5
1.5 Energy levels related to the excitation states of the Hoyle state . . . 6
1.6 Energies of the $k\alpha$-condensed states measured from each $k\alpha$-decay threshold energy . . . 7
1.7 Comparison of energy spectra among experiment, the 4α OCM calculation, and the α + ^{12}C model calculation . . . 8
1.8 Spectroscopic factors S_L^2 of the α + ^{12}C(L_n^π) channels . . . 8
1.9 Excitation function for the ^{12}C(^{12}C, ^{12}C[0_2^+])^{12}C(0_2^+) reaction from [36] . . . 11
1.10 Effective 3α-emission cross section from the fused system (^{24}Mg) . . . 11

2.1 Schematic view and photograph of SAKRA . . . 14
2.2 Schematic diagram of the SAKRA DAQ system . . . 15
2.3 Schematic diagram of the veto circuit . . . 17
2.4 ZLE algorithm description . . . 18
2.5 Schematic diagram of MMM design Si detector . . . 19
2.6 Data of the mixed alpha source (not filtered) . . . 21
2.7 Data of the mixed alpha source (filtered by the LPF) . . . 22
2.8 Data of the mixed alpha source (filtered by the LPF and the shaping filter) . . . 23
2.9 Waveforms and differential waveforms of p, d, and α . . . 23
2.10 Comparison of waveforms and $A_{\max}$ between the experimental configurations . . . 25

2.11 Correlation between the measured energies in the first layer and the second layer 27
2.12 Scatter plots of the A_{max} versus energies 28
2.13 A_{max} spectra at $E = 2.0, 2.5, 3.0 \pm 0.05$ MeV 28
2.14 Scatter plots of A_{max} versus the energy at different segment of SAKRA 30

3.1 Schematic exterior and plane view of the JAEA tandem accelerator facility 32
3.2 Schematic view and photograph of the setup in the scattering chamber 33
3.3 Schematic diagram of the signal processing 34
3.4 Schematic diagram of the trigger production in V2495 35
3.5 A_{max} variation due to the bias shortage 36

4.1 Energy spectra of the mixed alpha source 38
4.2 Examples of acquired waveforms 39
4.3 Correlation between integral and peak ADC 40
4.4 Example of the ohmic-side energy spectra 41
4.5 Typical energy correlation between neighbor strips at the ohmic side in the segment 0 41
4.6 Energy correlation between neighboring strips at the ohmic side including the synchronous noises in the segment 3 41
4.7 Energy distributions at each multiplicity 42
4.8 Result of the synchronous-noise reduction in the segment 3 43
4.9 Energy correlation after the synchronous-noise reduction 43
4.10 Energy correlation between total energy contained in the front- and rear-side strip lists . . . 45
4.11 Schematic diagrams of the 6 types of combinations 46
4.12 Correlation between A_{max} and kinetic energies of decay particles 47
4.13 PID using the correlation between A_{max} and kinetic energies of decay particles 48
4.14 TDC data taken with a pulse generator 49
4.15 Excitation-energy spectrum of ^{12}C reconstructed from the detected 3α particles in the $^{12}C + ^{12}C \rightarrow 3\alpha + X$ reaction 50
4.16 Excitation-energy spectra of the residual ^{12}C 51
4.17 Accepted probability as the function of rear-side energies 52
4.18 Efficiency at each angular bin for $^{12}C + ^{12}C \rightarrow ^{12}C(0^+_2) + ^{12}C(J^\pi_k)$ reactions 53
4.19 Maximum value of the efficiency at each angular bin 54

4.20 Angular acceptance for each $^{12}C^{*}$ + $^{12}C^{*}$ channel 55
4.21 Example of the measured angular distribution of the differential cross sections and the generated simulation data 57
4.22 Angular averaged efficiency 58
4.23 Averaged efficiency over all the solid angles for the inclusive reactions 59
4.24 Previous result of the differential cross sections for the ^{12}C + ^{12}C elastic scattering 60
4.25 Present result of the differential cross sections for the ^{12}C + ^{12}C elastic scattering 60
4.26 Event time stamp distribution at the minimum bias measurement and physics measurement . 61

5.1 Inclusive cross sections using each segment of SAKRA 64
5.2 Inclusive cross sections using reliable segments of SAKRA 65
5.3 Exclusive cross sections using each segment of SAKRA 67
5.4 Exclusive cross sections using reliable segments of SAKRA 68
5.5 Angular distributions for the $^{12}C + {}^{12}C \rightarrow {}^{12}C(0^{+}_{2}) + {}^{12}C(0^{+}_{1})$ reaction and fitting result . . . 70
5.6 Angular distributions for the $^{12}C + {}^{12}C \rightarrow {}^{12}C(0^{+}_{2}) + {}^{12}C(0^{+}_{2})$ reaction and fitting result . . . 72
5.7 Angular distributions for the $^{12}C + {}^{12}C \rightarrow {}^{12}C(0^{+}_{2}) + {}^{12}C(0^{+}_{2})$ reaction at the low-energy side 72

A.1 Angular distributions of the differential cross sections for the $^{12}C + {}^{12}C \rightarrow {}^{12}C(0^{+}_{2}) + {}^{12}C(0^{+}_{1})$ reactions 139
A.2 Angular distributions of the differential cross sections for the $^{12}C + {}^{12}C \rightarrow {}^{12}C(0^{+}_{2}) + {}^{12}C(2^{+}_{1})$ reactions 140
A.3 Angular distributions of the differential cross sections for the $^{12}C + {}^{12}C \rightarrow {}^{12}C(0^{+}_{2}) + {}^{12}C(0^{+}_{2})$ reactions 141

List of Tables

2.1 List of the used conventional modules . . . 16
2.2 Performances of the V1730SB module . . . 16
2.3 Specifications of Mesytec MPR-16/32 and CAEN A1442B preamplifiers . . . 20
2.4 Summary of the experimental configurations . . . 20
2.5 FoM for various nuclides pair at each configuration . . . 24

3.1 Summary of the measurement . . . 31

4.1 Summary of the energy resolution of the ^{148}Gd peak at sigma . . . 37
4.2 Summary of the event types and the gate conditions . . . 39

A.1 $^{12}C(^{12}C, ^{12}C[0^+_2] \rightarrow 3\alpha)X$ reaction at the first beam-time period. . . . 83
A.2 $^{12}C(^{12}C, ^{12}C[0^+_2] \rightarrow 3\alpha)X$ reaction at the second beam-time period. . . . 84
A.3 $^{12}C(^{12}C, ^{12}C[3^-_1] \rightarrow 3\alpha)X$ reaction at the first beam-time period. . . . 86
A.4 $^{12}C(^{12}C, ^{12}C[3^-_1] \rightarrow 3\alpha)X$ reaction at the second beam-time period. . . . 87
A.5 $^{12}C(^{12}C, ^{12}C[0^+_2] \rightarrow 3\alpha)X$ reaction using reliable segments of SAKRA. . . . 89
A.6 $^{12}C(^{12}C, ^{12}C[3^-_1] \rightarrow 3\alpha)X$ reaction using reliable segments of SAKRA. . . . 90
A.7 $^{12}C(^{12}C, ^{12}C[0^+_2] \rightarrow 3\alpha)^{12}C(0^+_1)$ reaction at the first beam-time period. . . . 92
A.8 $^{12}C(^{12}C, ^{12}C[0^+_2] \rightarrow 3\alpha)^{12}C(0^+_1)$ reaction at the second beam-time period. . . . 93
A.9 $^{12}C(^{12}C, ^{12}C[0^+_2] \rightarrow 3\alpha)^{12}C(2^+_1)$ reaction at the first beam-time period. . . . 94
A.10 $^{12}C(^{12}C, ^{12}C[0^+_2] \rightarrow 3\alpha)^{12}C(2^+_1)$ reaction at the second beam-time period. . . . 96
A.11 $^{12}C(^{12}C, ^{12}C[0^+_2] \rightarrow 3\alpha)^{12}C(0^+_2)$ reaction at the first beam-time period. . . . 97
A.12 $^{12}C(^{12}C, ^{12}C[0^+_2] \rightarrow 3\alpha)^{12}C(0^+_2)$ reaction at the second beam-time period. . . . 99
A.13 $^{12}C(^{12}C, ^{12}C[0^+_2] \rightarrow 3\alpha)^{12}C(0^+_1)$ reaction using reliable segments of SAKRA. . . . 101
A.14 $^{12}C(^{12}C, ^{12}C[0^+_2] \rightarrow 3\alpha)^{12}C(2^+_1)$ reaction using reliable segments of SAKRA. . . . 102

A.15 ^{12}C(^{12}C, ^{12}C[0^+_2] → 3α)^{12}C(0^+_2) reaction using reliable segments of SAKRA. 103
A.16 Angular distribution for the ^{12}C(^{12}C, ^{12}C[0^+_2] → 3α)^{12}C(0^+_1) reaction using reliable segments of SAKRA. 105
A.17 Angular distribution for the ^{12}C(^{12}C, ^{12}C[0^+_2] → 3α)^{12}C(2^+_1) reaction using reliable segments of SAKRA. 118
A.18 Angular distribution for the ^{12}C(^{12}C, ^{12}C[0^+_2] → 3α)^{12}C(0^+_2) reaction using reliable segments of SAKRA. 130